

Programa de Doctorado en Ingeniería Matemática,
Estadística e Investigación Operativa

por la

Universidad Complutense de Madrid

y la

Universidad Politécnica de Madrid



**A model for turbulent combustion
simulation of large scale hydrogen
explosions**

Tesis Doctoral

Jorge Yáñez Escanciano

Director

Antonio Souto Iglesias

Año
2015

Tribunal nombrado por el Mgfco. y Excemo. Sr. Rector de la Universidad Politécnica de Madrid, el día _____ de _____ de 2015.

Presidente D. _____

Vocal D. _____

Vocal D. _____

Vocal D. _____

Vocal Secretario D. _____

Realizado el acto de defensa y lectura de la Tesis el día _____ de _____ de 2015, en _____.

Calificación: _____

EL PRESIDENTE

LOS VOCALES

EL VOCAL SECRETARIO

Contents

CONTENTS	VIII
Nomenclature	X
Abstract	XIII
Resumen	XVI
1 INTRODUCTION	1
1.1 Hydrogen economy	1
1.2 Calculation of realistic accident scenarios	2
1.3 Qualitative description of the explosion process	4
1.4 Governing equations	7
1.5 Turbulence modeling	9
1.5.1 General	9
1.5.2 Direct numerical simulation (DNS)	10
1.5.3 Large Eddy Simulations	11
1.5.4 Reynolds Averaged Navier-Stokes equations (RANS)	17
1.5.5 Hybrid models	21
1.5.6 Zonal models	21
1.5.7 Non-dimensional correlations of data	22
1.6 Turbulent combustion modeling	22
1.6.1 General	22

1.6.2	Necessity of the modeling	23
1.6.3	Combustion regimes	25
1.6.4	Thermal radiation	27
1.6.5	Relation of the reaction rate modeling and the turbulence modeling	28
1.6.6	Classical turbulent combustion models	30
1.6.7	Modern turbulent combustion models	32
1.7	Turbulent flame speed	38
1.7.1	Introduction	38
1.7.2	A general formulation of the turbulent burning velocity	39
1.7.3	Laminar burning velocity	42
1.8	H_2 safety and large scale explosions	44
1.8.1	General	44
1.8.2	H_2 safety and combustion for nuclear power plants	48
1.9	Critical considerations of the status of the modeling	49
2	OBJECTIVES	53
3	METHODOLOGY	56
4	COMBUSTION MODEL DEVELOPMENT	58
4.1	Introduction	58
4.2	KYLCOM model outline	59
4.2.1	General	59
4.2.2	Flame propagation model: CREBCOM model	63
4.2.3	Limitations of the KYLCOM model	73
4.3	Calculation of the laminar burning velocity	75
4.3.1	General	75
4.3.2	Laminar burning velocity: temperature dependence	76
4.3.3	Laminar burning velocity: pressure dependence	76
4.3.4	Laminar burning velocity: diluted dependence	77

4.3.5	Laminar burning velocity: holistic phenomenological model strategy	77
4.4	Creation of a database of laminar flame speed	78
4.5	Laminar flame velocity formula: Dependence on the equivalence ratio	84
4.6	Laminar flame velocity formula: Dependence on temperature	85
4.7	Laminar flame velocity formula: Dependence on steam dilution	89
4.8	Laminar flame velocity formula: Dependence on pressure	93
4.8.1	General	93
4.8.2	Pressures lower than 1 bar	93
4.8.3	Pressures higher than 1 bar	94
4.8.4	Summary of the pressure related corrections	95
4.9	Simultaneous influence of all parameters and restrictions in the applicability of the model	98
4.10	Transport properties of gases	100
4.10.1	General	100
4.10.2	Dynamic viscosity	101
4.10.3	Collision integrals $\Omega^{(1,1)*}$ and $\Omega^{(2,2)*}$	102
4.10.4	Diffusion	103
4.10.5	Thermal conductivity	104
5	KYLCOM Model: turbulent velocity correlation and flame instability modeling	106
5.1	Introduction	106
5.2	The DRIVER experiment	107
5.2.1	General	107
5.2.2	Modeling of the initial stage of the combustion	110
5.2.3	The KYLCOM model in the initial stage of the combustion	115
5.2.4	Results	116
5.3	THAI experiment	129
5.3.1	General	129
5.3.2	Description of the experiment	130

5.3.3	Numerical simulations	133
5.3.4	Results for test HD-12	134
5.3.5	Results for test HD-15	142
5.3.6	Results for test HD-22	149
5.3.7	Buoyancy driven flames analysis	152
5.3.8	Analysis with the Borghi diagram	155
5.3.9	Acoustic-parametric instability analysis	157
5.3.10	Effect of the parametric instability in flame dynamics in HD-22	164
6	APPLICATIONS	173
6.1	General	173
6.2	Large scale tunnel	174
6.2.1	General	174
6.2.2	Description of the experiment	174
6.2.3	Results of the simulation	176
6.3	Quiescent dry hydrogen-air mixtures with concentration gradient . .	186
6.3.1	Introduction	186
6.3.2	Description of the experiments	186
6.3.3	Results of the simulation	188
6.4	Vented Combustion	194
6.4.1	Description of the experiment	194
6.4.2	Calculation Results	197
7	Fukushima power plant analysis	202
7.1	Introduction	202
7.2	Evaluation of the amount of hydrogen participating in the explosion	206
7.2.1	Amount of hydrogen generated during the cooling system fail- ure	206
7.2.2	Methodologies for the assessment of the amount of hydrogen exploding	207

7.2.3	Evaluation of the amount of exploding hydrogen based on the speed of the shock wave	208
7.2.4	Evaluation of the amount of hydrogen exploding based on the radius of the combustion products	214
7.3	Qualitative considerations on the hydrogen release from the point of view of combustion science	215
7.3.1	General	215
7.3.2	Comparison with fully closed geometries	217
7.3.3	Acceleration and flame propagation regime in semi-confined layers	217
7.3.4	Size of the H_2 cloud and possibility of existence of detonation in view of the results of the first assessments	218
7.4	Numerical simulations of the explosion	221
7.4.1	Large computational domain calculations	222
7.4.2	Medium scale calculations	234
8	CONCLUSIONS	245
8.1	Conclusions	245
8.2	Contributions	247
8.3	Future work	249
9	LIST OF PUBLICATIONS DURING PhD THESIS WORK	251
9.1	Journal papers:	251
9.2	Conference Papers	253
10	Bibliography	255
A	CONVOLUTION OF THE NAVIER-STOKES EQUATIONS	294
A.1	Derivation of the convoluted equations	294
A.1.1	General	294
A.1.2	Filtering of total density	296
A.1.3	Filtering of momentum equation	296

A.1.4	Filtering of total energy	297
A.2	Summary of results in A.1.1	300
A.3	Definition of Sub-grid Terms	301
A.3.1	Impulse equation	301
A.3.2	Energy Equation	301
A.3.3	Transport equation for chemical species	303
B	MODELING OF THE SUB-GRID TERMS IN LARGE EDDY SIMULATIONS	304
B.1	Modeling the S_{1ij} tensor	304
B.1.1	Eddy-viscosity-eddy-diffusivity model	306
B.1.2	Mixed model	307
B.1.3	Dynamic model	307
B.1.4	Realizability conditions	310
B.1.5	Stability constrains	313
B.2	Modeling the S_{2ij} tensor	314
B.3	Modeling the α_3 term	315
B.4	Modeling the α_4 & α_5 terms	315
B.4.1	Eddy viscosity, eddy diffusivity	315
B.4.2	Mixed model	316
B.4.3	Dynamic eddy-viscosity model	316
B.5	Modeling the term α_6	318
B.6	Modeling the terms α_7 & α_8	319
C	DERIVATION OF THE ACOUSTIC-PARAMETRIC INSTABILITY EQUATION	
	DESCRIBING THE GROWTH RATE	321
C.1	General	321
C.2	Acoustic instability	328
C.3	Parametric instability	331
D	DERIVATION OF THE MODEL FOR THE FLAME WRINKLING EVOLUTION	334
D.1	General	334
D.2	Source term	336

D.3	Flame surface annihilation due to cusps	337
D.4	Formulation in terms of Ξ	340
D.4.1	Annihilation due to cusp (sink contributor)	340
D.4.2	Source term (instability) wrinkling factor	342
D.5	Final equation	343
D.5.1	General	343
D.5.2	Limitations	343

NOMENCLATURE

Latin		Latin	
		D	Diffusion coefficient
		D_{ij}	Mean rate of strain tensor
		D_{Dij}	Deviatoric part of the mean rate of strain tensor
A	Auxiliary variable acoustic parametric instability modeling	D_t	Turbulent Diffusion
A_c	Amplitude of the cellular structure in flame	Da	Damkoehler number
A_c	Area of the flame	e	Total energy
B	Auxiliary variable acoustic parametric instability modeling	E_a	Activation energy
C_1	Auxiliary variable acoustic parametric instability modeling	f	Progress variable
$C_{1k\epsilon}$	$k-\epsilon$ model constant	f_t	Translational partition function
C_2	Auxiliary variable acoustic parametric instability modeling	f_r	Rotational partition function
$C_{2k\epsilon}$	$k-\epsilon$ model constant	f_v	Vibrational partition function
C_D	Eddy-viscosity LES model constant	F	Rotational cumulative distribution function
C_g	KYLCOM auxiliary variable	g	Gravity acceleration
C_h	Eddy conductivity LES model constant	G	Filter function kernel
C_I	Eddy-diffusivity LES model constant	G_p	Level set variable
C_k	$k-\epsilon$ model constant	G_w	Sub-grid scale wrinkling source term
C_L	BML model constant	h	Burned/unburned heat conductivity ratio
C_{vr}	Rotational heat at constant volume	H	Auxiliary variable related to acoustic parametric instability. Heats conductivity ratio integral
C_{vt}	Translational heat at constant volume	j	Diffusion flux
C_{vv}	Vibrational heat at constant volume	J	Auxiliary variable acoustic parametric instability. Heats conductivity ratio integral
C_ϵ	$k-\epsilon$ model constant	I_0	Enhancement factor due to stretching
C_ϵ	sub-grid dissipation LES model constant	k	Turbulent kinetic energy
C_μ	$k-\epsilon$ model constant	\tilde{k}	Dimensionless wavenumber
C_π	Eddy conductivity LES model constant	k_B	Boltzmann constant
		k_0	Pre-exponential factor
		\overline{K}	Source term in Coherent flame model due to stretching
		Ka	Karlovitz number

Latin		Latin	
ℓ	Length of arch	$S_{L,0}$	Laminar burning velocity at reference conditions of pressure and temperature
L	Integral scale of turbulence	$S_{L,air}$	Laminar burning velocity of H_2 -air mixture
L_{ij}	Auxiliary tensor in LES formulation	$S_{L,steam}$	Laminar burning velocity of H_2 -air steam mixture
Le	Lewis number	$S_{L,C}$	Laminar burning velocity corrected
L_{mark}	Markstein length	$S_{L,C}^*$	Laminar burning velocity corrected for enhanced temperature range. Intermediate
M_{ij}	Resolved viscous stress tensor	$S_{L,C}^T$	Laminar burning velocity corrected for enhanced temperature range. Final correction
M	Mach number	$S_{L,C}^{T,dil}$	Laminar burning velocity corrected for enhanced temperature and dilution
Ma	Markstein number	$S_{L,C}^{T,dil,p}$	Laminar burning velocity corrected for enhanced temperature, dilution and pressure
Ma_{sr}	Markstein number due to aerodynamic strain	$S_{L,I}$	Laminar burning velocity of the database
\overline{M}	Merging rate in Coherent flame model	S_{QL}	Quasi-laminar burning velocity
M_i	Molar mass of specie i	S_t	Turbulent burning velocity
N_g	Number of points due to geometry constrains	t	time
N_t	Number of points per turnover	T	Temperature
n	Overall reaction order	T_0	Reference temperature
n_l	Reaction order of the limiting component	T_{ij}	Auxiliary tensor in LES formulation
p	Pressure	T_a	Activation temperature
p_0	Reference pressure	u	Speed
Pe	Peclet number	U_a	Amplitude of acoustic perturbations
Pr	Prandtl number	u'	RMS turbulent velocity
q	Heat flux	W_u	Molar mass of the mixture
\overline{Q}	Quenching rate in Coherent flame model	x	Spatial coordinate
R	Constant of gases	X_α	Molar fractions
R_w	Sub-grid scale wrinkling annihilation	Y_α	Mass fraction
R_f	Radius of flame	Z_r	Rotational relaxation collision number
R_c	Radius of curvature		
Re_λ	Reynolds number based in Taylor micro-scale		
Re_t	Turbulent Reynolds number		
S_{ij}	Rate of strain		
S_{1ij}	Sub-grid scale term LES		
S_{2ij}	Sub-grid scale term LES		
S_{9ij}	Sub-grid scale term LES		
S_{10ij}	Sub-grid scale term LES		
S_L	Laminar burning velocity		

Greek		Greek	
α_t	Flame stretching	λ_n	Wavelength associated to wavenumber n in instabilities for small diameters
α_t	Dependence of laminar burning velocity on temperature	μ	Dynamic viscosity
α_{3-8}	Sub grid terms LES	ν	Cinematic viscosity
β_t	Dependence of laminar burning velocity on pressure	ρ	Density
β	Zeldovich number	Ξ	Surface wrinkling factor
Γ	Gamma function	σ_d	Molecular diameter
γ	Heat capacity ratio	σ	Growth rate
δ_{ij}	Kronecker delta	$\bar{\sigma}$	Dimensionless growth rate
δ	Flame thickness	σ_Y	Sum of the variance of the species
Δ	Filter amplitude	σ_T	Variance of the temperature
Δx	Cell size	Σ	Flame surface density
Δh_a^0	Enthalpy of formation	σ_{ij}	Viscous stress tensor
ε_w	Well depth	τ_{ij}	Reynolds stress tensor
ϵ_r	Small parameter	τ_t	Characteristic turbulent time
ϵ	Turbulent kinetic energy dissipation	Φ	Correction factor
η	Kolmogorov scale	φ	Equivalence ratio
ϑ_{ij}	Auxiliary tensor in LES formulation	χ	Thermal diffusivity
θ	Expansion ratio	ω_a	Reaction rate species
θ_c	Angle of the cusp	ω	Reaction rate species
κ	Wavenumber	ω_{ac}	Circular frequency acoustic perturbation
λ	Thermal conductivity	$\Omega^{(1,1)*}$	Collision integral
λ_c	Wavelength of the cusps	$\Omega^{(2,2)*}$	Collision integral

ABSTRACT

The exhaustion, absolute absence or simply the uncertainty on the amount of the reserves of fossil fuels sources added to the variability of their prices and the increasing instability and difficulties on the supply chain are strong incentives for the development of alternative energy sources and carriers.

The attractiveness of hydrogen in a context that additionally comprehends concerns on pollution and emissions is very high. Due to its excellent environmental impact, the public acceptance of the new energetic vector will depend on the risk associated to its handling and storage. From these, the danger of a severe explosion appears as the major drawback of this alternative fuel.

This thesis investigates the numerical modeling of large scale explosions, focusing on the simulation of turbulent combustion in large domains where the resolution achievable is forcefully limited.

In the introduction, a general description of explosion process is undertaken. It is concluded that the restrictions of resolution makes necessary the modeling of the turbulence and combustion processes. Subsequently, a critical review of the available methodologies for both turbulence and combustion is carried out pointing out their strengths and deficiencies. As a conclusion of this investigation, it appears clear that the only viable methodology for combustion modeling is the utilization of an expression for the turbulent burning velocity to close a balance equation for the combustion progress variable, a model of the *Turbulent flame velocity* kind. Also, that depending on the particular resolution restriction of each problem and on its geometry the utilization of different simulation methodologies,

LES or RANS, is the most adequate solution for modeling the turbulence.

Based on these findings, the candidate undertakes the creation of a combustion model in the framework of *turbulent flame speed* methodology which is able to overcome the deficiencies of the available ones for low resolution problems. Particularly, the model utilizes a heuristic algorithm to maintain the thickness of the flame brush under control, a serious deficiency of the Zimont model.

Under the approach utilized by the candidate, the emphasis of the analysis lays on the accurate determination of the burning velocity, both laminar and turbulent. On one side, the laminar burning velocity is determined through a newly developed correlation which is able to describe the simultaneous influence of the equivalence ratio, temperature, steam dilution and pressure on the laminar burning velocity. The formulation obtained is valid for a larger domain of temperature, steam dilution and pressure than any of the previously available formulations. On the other side, a certain number of turbulent burning velocity correlations are available in the literature. For the selection of the most suitable, they have been compared with experiments and ranked, with the outcome that the formulation due to Schmidt was the most adequate for the conditions studied.

Subsequently, the role of the flame instabilities on the development of explosions is assessed. Their significance appears to be of importance for lean mixtures in which the turbulence intensity remains moderate. These are important conditions which are typical for accidents on Nuclear Power Plants. Therefore, the creation of a model to account for the instabilities, and concretely, the acoustic-parametric instability is undertaken. This encloses the mathematical derivation of the heuristic formulation of Bauwebs et al. for the calculation of the burning velocity enhancement due to flame instabilities as well as the analysis of the stability of flames with respect to a cyclic velocity perturbation. The results are combined to build a model of the acoustic-parametric instability.

The following task in this research has been to apply the model developed to several problems significant for the industrial safety and the subsequent analysis of the results and comparison with the corresponding experimental data was performed. As a part of such task simulations of explosions in a tunnel and explosions

in large containers, with and without gradient of concentration and venting have been carried out. As a general outcome, the validation of the model is achieved, confirming its suitability for the problems addressed.

As a last and final undertaking, a thorough study of the Fukushima-Daiichi catastrophe has been carried out. The analysis performed aims at the determination of the amount of hydrogen participating on the explosion that happened in the reactor one, in contrast with other analysis centered on the amount of hydrogen generated during the accident. As an outcome of the research, it was determined that the most probable amount of hydrogen exploding during the catastrophe was 130 kg. It is remarkable that the combustion of such a small quantity of material can cause tremendous damage. This is an indication of the importance of these types of investigations.

The industrial branches that can benefit from the applications of the model developed in this thesis include the whole future hydrogen economy, as well as nuclear safety both in fusion and fission technology.

RESUMEN

El agotamiento, la ausencia o, simplemente, la incertidumbre sobre la cantidad de las reservas de combustibles fósiles se añaden a la variabilidad de los precios y a la creciente inestabilidad en la cadena de aprovisionamiento para crear fuertes incentivos para el desarrollo de fuentes y vectores energéticos alternativos.

El atractivo de hidrógeno como vector energético es muy alto en un contexto que abarca, además, fuertes inquietudes por parte de la población sobre la contaminación y las emisiones de gases de efecto invernadero. Debido a su excelente impacto ambiental, la aceptación pública del nuevo vector energético dependería, a priori, del control de los riesgos asociados su manipulación y almacenamiento. Entre estos, la existencia de un inegable riesgo de explosión aparece como el principal inconveniente de este combustible alternativo.

Esta tesis investiga la modelización numérica de explosiones en grandes volúmenes, centrándose en la simulación de la combustión turbulenta en grandes dominios de cálculo en los que la resolución que es alcanzable está fuertemente limitada.

En la introducción, se aborda una descripción general de los procesos de explosión. Se concluye que las restricciones en la resolución de los cálculos hacen necesario el modelado de los procesos de turbulencia y de combustión. Posteriormente, se realiza una revisión crítica de las metodologías disponibles tanto para turbulencia como para combustión, que se lleva a cabo señalando las fortalezas, deficiencias e idoneidad de cada una de las metodologías. Como conclusión de esta investigación, se obtiene que la única estrategia viable para el modelado de la

combustión, teniendo en cuenta las limitaciones existentes, es la utilización de una expresión que describa la velocidad de combustión turbulenta en función de distintos parámetros. Este tipo de modelos se denominan *Modelos de velocidad de llama turbulenta* y permiten cerrar una ecuación de balance para la variable de progreso de combustión. Como conclusión también se ha obtenido, que la solución más adecuada para la simulación de la turbulencia es la utilización de diferentes metodologías para la simulación de la turbulencia, LES o RANS, en función de la geometría y de las restricciones en la resolución de cada problema particular.

Sobre la base de estos hallazgos, se crea un modelo de combustión en el marco de los modelos de *velocidad de la llama turbulenta*. La metodología propuesta es capaz de superar las deficiencias existentes en los modelos disponibles para aquellos problemas en los que se precisa realizar cálculos con una resolución moderada o baja. Particularmente, el modelo utiliza un algoritmo heurístico para impedir el crecimiento del espesor de la llama, una deficiencia que lastimaba el célebre modelo de Zimont.

Bajo este enfoque, el énfasis del análisis se centra en la determinación de la velocidad de combustión, tanto laminar como turbulenta.

La velocidad de combustión laminar se determina a través de una nueva formulación capaz de tener en cuenta la influencia simultánea en la velocidad de combustión laminar de la relación de equivalencia, la temperatura, la presión y la dilución con vapor de agua. La formulación obtenida es válida para un dominio de temperaturas, presiones y dilución con vapor de agua más extenso de cualquiera de las formulaciones previamente disponibles.

Por otra parte, el cálculo de la velocidad de combustión turbulenta puede ser abordado mediante el uso de correlaciones que permiten la determinación de esta magnitud en función de distintos parámetros. Con el objetivo de seleccionar la formulación más adecuada, se ha realizado una comparación entre los resultados obtenidos con diversas expresiones y los resultados obtenidos en los experimentos. Se concluye que la ecuación debida a Schmidt es la más adecuada teniendo en cuenta las condiciones del estudio.

A continuación, se analiza la importancia de las inestabilidades de la llama en la

propagación de los frentes de combustión. Su relevancia resulta significativa para mezclas pobres en combustible en las que la intensidad de la turbulencia permanece moderada. Estas condiciones son importantes dado que son habituales en los accidentes que ocurren en las centrales nucleares. Por ello, se lleva a cabo la creación de un modelo que permita estimar el efecto de las inestabilidades, y en concreto de la inestabilidad acústica-paramétrica, en la velocidad de propagación de llama. El modelado incluye la derivación matemática de la formulación heurística de Bauwebs et al. para el cálculo de la incremento de la velocidad de combustión debido a las inestabilidades de la llama, así como el análisis de la estabilidad de las llamas con respecto a una perturbación cíclica. Por último, los resultados se combinan para concluir el modelado de la inestabilidad acústica-paramétrica.

Tras finalizar esta fase, la investigación se centro en la aplicación del modelo desarrollado en varios problemas de importancia para la seguridad industrial y el posterior análisis de los resultados y la comparación de los mismos con los datos experimentales correspondientes. Concretamente, se abordó la simulación de explosiones en túneles y en contenedores, con y sin gradiente de concentración y ventilación. Como resultados generales, se logra validar el modelo confirmando su idoneidad para estos problemas.

Como última tarea, se ha realizado un análisis en profundidad de la catástrofe de Fukushima-Daiichi. El objetivo del análisis es determinar la cantidad de hidrógeno que explotó en el reactor número uno, en contraste con los otros estudios sobre el tema que se han centrado en la determinación de la cantidad de hidrógeno generado durante el accidente. Como resultado de la investigación, se determinó que la cantidad más probable de hidrógeno que fue consumida durante la explosión fue de 130 kg. Es un hecho notable el que la combustión de una relativamente pequeña cantidad de hidrógeno pueda causar un daño tan significativo. Esta es una muestra de la importancia de este tipo de investigaciones.

Las ramas de la industria para las que el modelo desarrollado será de interés abarca la totalidad de la futura economía de hidrógeno (pilas de combustible, vehículos, almacenamiento energético, etc) con un impacto especial en los sectores del transporte y la energía nuclear, tanto para las tecnologías de fisión y fusión.

Chapter 1

INTRODUCTION

1.1 Hydrogen economy

The use of hydrogen in parallel to its industrial and economic importance is expected to grow increasingly in the near future (Argonne National Laboratory, 2013), (Evers, 2013). The difficulties on supply of fossil fuels, its uncontrolled prices and the uncertain reserves are strong incentives for the development of alternative energy sources and energy carriers. Global warming and pollution associated with fossil fuel usage are further significant environmental and societal problems that push this tendency.

In this global context, the attractiveness of hydrogen lies on the variety of methods available for its production and its long-term viability (Damen et al., 2006) (Damen et al., 2007). Such methodologies enclose, among others, its generation from fossil fuels, biomass, wind, solar and nuclear power. An additional, but very significant advantage is the existence of numerous methodologies to produce energy from hydrogen, almost with zero harmful emissions. Among these highly efficient technologies, internal combustion engines, gas turbines and fuel cells appear as the most viable choices.

These aspects can be enclosed in the concept of *hydrogen economy* which basically stands for a societal energy system based on the extensive use of hydrogen

as energy storage and transportation medium.

Nevertheless, the future public acceptance of this new energetic vector will depend not only on its excellent environmental impact, but also on the risk management of its handling and storage, as the danger of explosions appears as the major drawback posed by this alternative fuel. Most significantly, an unequivocal example of the importance of societal issues on the energy supply is the acceptance of nuclear energy. From the initial fascination that created in the fifties, public opinion has evolved into the deepest public rejection in several countries (80% of the Austrians, 43% of the Germans and 37 % Spaniards appear to be against nuclear power (European Comision, 2007)).

A mean of addressing the safety issues of hydrogen manipulation is to perform experiments and/or simulations of accident scenarios involving explosions. The data obtained can be immediately utilized to analyze the propagation of the blast, study the suitability of the structural design, perform an assessment of the inherent risk and finally implement measures to minimize the impact. Experiments can be used to find the resulting over-pressures for a given set of parameters. However, reliable simulations of a scenario can provide data on the pressure loads resulting from explosion processes faster and cheaper than experiments.

The combustion regimes that can be expected to be found in hydrogen explosions can be ranged from slow laminar flames to deflagration-to-detonation transition and even to detonation. Its strength depends on a large range of parameters both related to the geometry (size, confinement, obstructions, presence of generators of turbulence) and to the gas mixtures (composition, quantity).

1.2 Calculation of realistic accident scenarios

The performance of deflagration calculations of realistic accidents occurring in industrial sites, cities, etc. which may involve risk for life and property has substantial implications in terms of the resolution achievable (Movahed-Shariat-Panahi, 2012). This is especially significant in large scale calculations where the resolution is forcefully limited with the present computational resources. This may pose re-

strictions to the calculations that are feasible nowadays that can be nevertheless overcome through the adequate modeling of turbulence and combustion.

To be applicable in the praxis, the models must handle the widest possible range of compositions, turbulence intensities and be appropriate to simulate interaction with complex geometries. Therefore, any practical methodology should be able to avoid resolving the flame front providing good mass consumption and energy release which mimic flame propagation.

Some insight on the problematic posed by large scale calculations can be obtained by studying the different scales participating in the combustion process (see Arpaci (1995)). This involves the comparison of two sets of magnitudes. On one hand, the Kolmogorov, Taylor and the integral scales of the turbulence, the thickness of the boundary layer and the thickness of the flame front describe the physical scales of the phenomena. On the other, the global dimension magnitude of the problem and the size of the numerical grid represent the macroscopic frames and the feasible numerical description of its details. The difficulties in the modeling arise from the disparity of these scales $O(10^{-4})$ m for the microscopic processes and $O(10^2)$ m for the macroscopic.

Let us begin with the scales of the combustion. Certainly, combustion simulations should provide a representation of the combustion processes that include location and surface area of the flame. Nevertheless, the flame thickness $O(10^{-4})$ $O(10^{-5})$ m is going to be forcefully much smaller than the grid used in large scale calculations, a fact that forces the necessity of the combustion modeling. Also, this fact implies that much of the flame details will remain unresolved.

Let's study now the scales involved in the turbulence. The Kolmogorov and Taylor scales of the turbulence are always much smaller than the size of the grid in practical applications. The integral turbulence scale may be, depending on the problem, smaller or larger than the grid resolution. In problems in which walls are present, the integral scale of the turbulence is almost always smaller than the grid elements, specially after obstacles or in the vicinity of walls. The thickness of the boundary layer is, in most cases, thinner than the grid. Thus, turbulence modeling is required to remedy this difficulty.

The geometry is also usually represented in a coarse manner and, for very coarse resolutions, even in an incomplete manner. This constraint not only limits the accuracy of the calculation but even implies a serious limit on the level of detail that the geometrical representation of the reality may attain.

Additionally, the coupling of turbulence with combustion is known to be very important. The strength of an explosion depends on the composition of the gases involved, the velocity of the flame, the expansion ratio (relation between the density of the reactants and the products) and the interaction with the surrounding environment. The burning rate depends largely on the turbulence intensity and its characteristics size. Therefore, inaccuracies in the determination of these magnitudes may strongly affect the final precision achieved. Those inaccuracies may be exacerbated by the fact that most turbulence models apply, and were derived, considering incompressible stationary flows. Moreover, its response may be significantly dependent on the grid resolution and/or initial conditions. The turbulence model must be then selected so that it produces a representative turbulence field in the presence of reactive compressible flows.

Furthermore, the expansion ratio depends on the thermodynamic characteristics of the gases, both products and reactants, involved in the explosion. The products composition is then dependent on the final equilibrium composition which in turn depends on the final conditions reached in the problem.

1.3 Qualitative description of the explosion process

Several stages are successively reached in an explosion propagating in a pre-mixed cloud of fuel. Very often, a weak source, like a spark, produces the ignition of the reactive mixture. The flame starts out as a slow combustion wave with a velocity comprised between several centimeters and several meters per second. In the absence of turbulizers and confinement, the flame will not suffer strong accelerations, and the overpressure generated will remain moderate. Under those circum-

stances, the main sources of flame acceleration are the flame instabilities, the turbulence generated by the flame itself, the interaction with the ground surface and the flame folding. Nevertheless, in buildings, industrial facilities and any other realistic environment, obstruction and confinement will likely exist due to the existence of rooms, closed spaces, equipment, pipes and any other kind of obstacle or enclosure of any type. The expansion of the gas, in close interaction with the obstacles, generates turbulence that in a feedback mechanism increases the effective burning rate generating a faster expansion. This mechanism causes flame acceleration, high explosion pressures and under certain circumstances transition to detonation.

The strength of an explosion depends on many circumstances (Molkov et al., 2008b). Some of the most significant are the concentration of fuel, the size of the fuel cloud, the presence of dilutants, the location of the ignition point, the initial levels of turbulence, the location and size of obstacles, the degree of obstruction and the size, location and type of venting areas.

The combination of those factors will determine the effect and consequences of an explosion characterized by the resulting overpressures.

The main causes of a pressure built up are the degree of confinement (that describes whether the products can be discharged in the surrounding atmosphere) and the speed of the propagating flame.

In a problem which contains a certain degree of obstruction the flame may very likely accelerate to velocities of several hundred meters per second. The increased burning rate is caused by wrinkling of the flame front by turbulent eddies. Additionally, an increased transport of heat and mass appears at the reaction front due to the turbulent mixing, rising even more the consumption rate. Turbulence is then generated by the interaction of the flow with the structural elements creating a feed-back process. Figure 1.1 illustrates the development of the process.

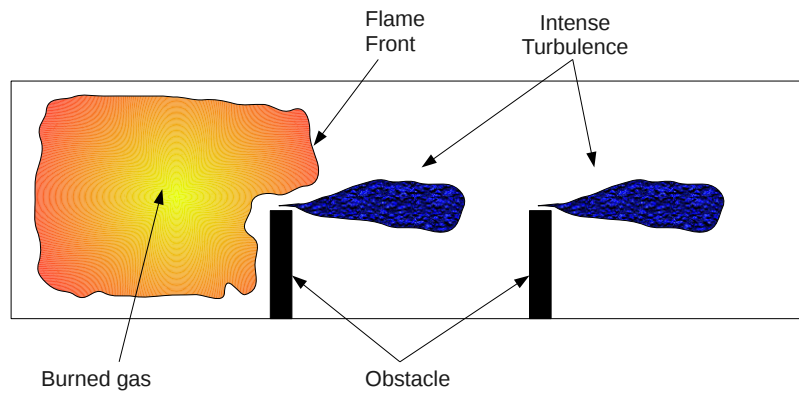


Figure 1.1: Interaction between expanding gases and turbulence generated by obstacles in a closed channel.

The flame causes the consumption of the reactants generating combustion products and creating a strong gas expansion which in turn pushes the flame, and the reactants, ahead and creates turbulence in the latter. The propagation of the flame inside this turbulent field causes a dramatic increase of the burning rate, augmenting both the velocity of the flow and the intensity of the turbulence ahead of the flame. The increased burning velocity causes a rise in the pressure generated by the explosion. Therefore, the acceleration of a flame due to the interaction with repeated obstacles constitutes a strong positive feedback loop which is represented in Figure 1.2.

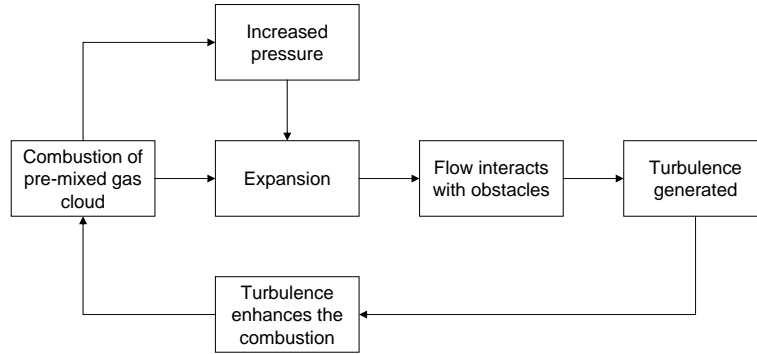


Figure 1.2: Positive feedback loop of flame acceleration due to turbulence, expansion and interaction with obstacles.

Two competing mechanisms govern the pressure increments in a partially confined explosion. On one hand, the flame accelerates due to an enhanced burning rate created by the turbulence generated when the flow overcomes the obstacles, producing a very significant increment of the pressure. On the other hand, venting provides some pressure relief reducing the feedback mechanism described in the previous paragraph. The interaction between both mechanisms is complex. The balance between them provides the final effects of the explosion which can be determined carrying out experiments or performing a fluid dynamics calculation.

1.4 Governing equations

Turbulent combustion modeling is a multidisciplinary topic in which fluid mechanics, chemistry and thermodynamics influence each other. In order to perform realistic analysis, numerical solution of the reactive Navier-Stokes equations is necessary. This adds the numerical resolution of partial differential equations to the topics of especial interest.

The Navier-Stokes equations for the reactive flows can be formulated (Warnatz

et al., 1999) as

$$\frac{\partial \rho}{\partial t} + \frac{\partial \rho u_j}{\partial x_j} = 0, \quad (1.1)$$

$$\frac{\partial \rho u_i}{\partial t} + \frac{\partial}{\partial x_j} (\rho u_i u_j + p \delta_{ij}) = \frac{\partial \sigma_{ij}}{\partial x_j} + \rho g_i, \quad (1.2)$$

$$\frac{\partial \rho e}{\partial t} + \frac{\partial}{\partial x_i} ((\rho e + p) u_i) = \frac{\partial u_j \sigma_{ij} - q_i}{\partial x_i} + \rho g_i u_i, \quad (1.3)$$

$$\frac{\partial \rho Y_\alpha}{\partial t} + \frac{\partial \rho Y_\alpha u_i}{\partial x_i} = \frac{\partial}{\partial x_i} (j_i) + \rho \omega_\alpha. \quad (1.4)$$

where ρ is the density, u the velocity, p the pressure, σ_{ij} the viscous stress tensor, g the acceleration, e the total specific energy, Y_α the mass fraction of the α species, j the diffusion flux and ω_α the reaction rate rate, where $\alpha = 1 \dots N_{\text{species}}$ ¹. The term ω_α is a crucial magnitude for this thesis and will be treated in detail in section 1.6.

These equations must be closed with expressions for the species molecular fluxes, heat fluxes, viscous forces and chemical kinetics.

Assuming that the fluids are Newtonian and that bulk viscosity can be neglected, the shear stress tensor reads

$$\sigma_{ij} = 2\mu S_{ij} - 2/3\mu \delta_{ij} S_{kk}, \quad (1.5)$$

with the rate of strain, tensor S being

$$S_{ij} = \frac{1}{2} \left(\frac{\partial u_i}{\partial x_j} + \frac{\partial u_j}{\partial x_i} \right). \quad (1.6)$$

The heat flux is assumed to be modeled by Fourier's law

$$q_j \approx -\lambda \frac{\partial T}{\partial x_j}, \quad (1.7)$$

where λ , μ are respectively the thermal conductivity and the dynamic viscosity.

¹If one transport equation is utilized for each species, the continuity equations could not be taken into account as $\sum_{\alpha=1}^{N_{\text{species}}} Y_\alpha = 1$.

Diffusion is assumed to be modeled with the Fick's law

$$j_i \approx -\rho D_\alpha \frac{\partial Y_\alpha}{\partial x_i}, \quad (1.8)$$

where D_α is the diffusivity of the specie α in the mixture.

If no turbulence or combustion modeling is considered, the Navier-Stokes equations and the scalar mixing reaction equations must be solved exactly. This implies that the whole time and length scales must be fully resolved, a methodology which is called Direct Numerical Simulation (DNS). Clearly this method is computationally intensive and given the current capabilities feasible only for moderate Reynolds number flows and simple geometries.

This difficulty can be overcome by averaging, or filtering, the conservation equations to describe only the mean, or low frequency, components of the flow field. In such an approach, the fluctuations are incorporated inside mean quantities, and are not described by the simulation. The fields obtained in such a way are described by its mean (or filtered) value and its fluctuating part. For an arbitrary variable ϕ , $\phi = \bar{\phi} + \phi'$. If the equations (1.1)-(1.4) are averaged (or filtered), ensemble terms like $\overline{\rho \phi \varphi} = \overline{\rho (\bar{\phi} + \phi') (\bar{\varphi} + \varphi')}$ appear and should be modeled. The closure of the ensemble terms of the kind $\overline{\rho \phi \varphi}$, or alternatively just the fluctuations, is the object of turbulence modeling while the closure of the averaged (or filtered) reaction rate $\overline{\rho \omega_a}$ is the goal of the combustion modeling.

1.5 Turbulence modeling

1.5.1 General

Turbulence is the most important non-chemical process that determines the severity of an explosion (Poinsot and Veynante, 2001), (Kadowaki and Hasegawaba, 2005). Depending on the problem considered and the accuracy required, different simulation methods should be used. They can be classified according to different criteria: Rodi (2000), Warnatz et al. (1999) or Nallasamy (1987) devised a taxonomy

taking into account the number of equations utilized in the modeling. Pope (2000) suggested a sorting focusing on the level of description, completeness, utilization cost, range of applicability and accuracy. For our review, the taxonomy due to Kline et al. (1978) has been considered according to which the simulation methods are categorized studying the spectral decomposition of the turbulence into modeled and calculated parts (Landau and Lifshitz, 1987). Following Kline, the different methods can be grouped in the next categories:

1. Direct Numerical Simulations.
2. Large Eddy Simulations.
3. Reynolds Averaged Navier-Stokes equations
4. Hybrid models.
5. Zonal models.
6. Non dimensional correlations of data.

Let's briefly review the most salient characteristics of these modeling methodologies.

1.5.2 Direct numerical simulation (DNS)

DNS method is based on the resolution the whole spectrum of the turbulence (Lesieur, 2008) considering a frequency range broad enough to enclose the large scales eddies, containing most of the energy, and the energy dissipation scales. Those requirements pose severe constraints on the computational mesh and domain. The computational domain has to be taken large enough as to contain the largest eddies, with a size similar to the integral scale of the turbulence, L . At the same time, the resolution must be fine enough to resolve the smallest eddies, of the order of the Kolmogorov length scale ($\Delta x \approx \eta$).

The previous considerations imply a dependence of the number of cells of the mesh on the Reynolds number. The number of points necessary to mesh a line of

size L is $N_g = L/\Delta x \approx L/\eta \propto Re_\lambda^{3/2}$ (Pope, 2000), where L is the integral scale of the turbulence, η the Kolmogorov scale and λ the Taylor scale.

This constraint is even more severe in three dimensional simulations, in which the number of points necessary to mesh a cube of edge L , N_g are $N_g \propto Re_\lambda^{9/2}$. Additionally, for unsteady flow fields, it is necessary to compute at least one eddy turnover time. This poses an extra constraint on the time integration, as it is necessary, for numerical reasons (CFL condition (LeVeque, 2002)), that the time step remains shorter than the cell cross over time. Finally, the number of time integrations per eddy turnover, N_t , will be $N_t \propto Re_\lambda^{3/2}$. The total number of operations per turnover results to be $N = N_g N_t \propto Re_\lambda^6$.

The limitation in the computing due to memory requirements and operations will be less restrictive with the advancement of computer architecture and improvements in computational speed and memory. Therefore, DNS methodology is experimenting an increasing expansion that has been reviewed by Moin and Mahesh (1998) and for combustion applications by Vervisch and Poinot (1998) and Westbrook et al. (2005). The maximum capabilities are reported to be of the $O(10^{12})$ mesh elements (Chen, 2011) which is a limitation that makes that this technique is still far away from practical applications.

1.5.3 Large Eddy Simulations

Large Eddy simulations (LES) were first developed to compute meteorological flows in the early sixties by Smagorinsky (1963). LES is a methodology in which large scale eddies carrying a significant amount of kinetic energy are resolved numerically in the numerical mesh while the dissipation scales and a great amount of the inertial cascade are substituted by a sub-grid model. The methodology is based on the fact that the large scales are directly affected by the boundary conditions and thus are peculiar to the particular problem treated whilst the isotropic inertial range is universal (Sagaut, 2001), see Figure 1.3. Once this universality is ascertained, it is considered that the effect of the sub-grid scales (SGS) on the resolved ones can be specified by a small number of parameters which are the model itself.

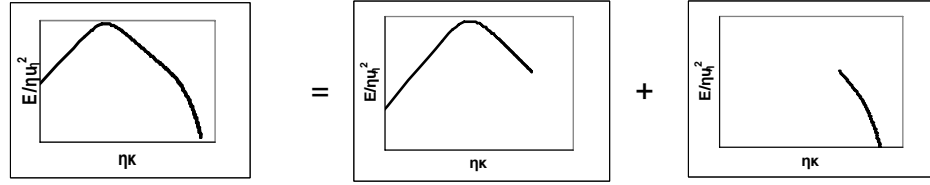


Figure 1.3: Spectrum resolved and simulated in the LES simulation method (Sagaut, 2001). Dimensionless kinetic energy of the turbulence, $E/\eta u_\eta^2$, versus dimensionless wavenumber, $\eta\kappa$, with η the Kolmogorov scale.

We may reformulate the concept of LES: when a problem is sampled on a discrete grid, Large Eddy Simulation technique consists on resolving the Navier-Stokes equations on this grid (see, Figure 1.4) making assumptions on the scales too small to be represented.

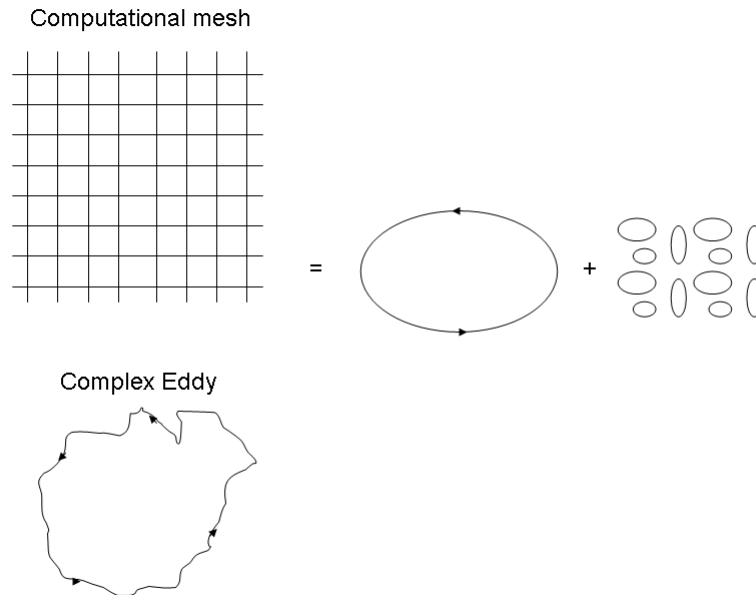


Figure 1.4: Large Eddy simulation principles. Two dimensional example. Complex large eddy is decomposed in resolvable scale and sub grid scale.

Thus, in LES, the equations of the resolved scales that govern the flow should be deduced. This can be achieved by convoluting the Navier-Stokes equations with a predefined filter which eliminates the dissipative scales (high frequencies). An important requirement for LES is that the cut-off wave-number of the filter must be contained in the inertial range of the energy spectrum (in Figure 1.3 the domain where $E/\eta u_\eta^2$ decreases linearly with $\eta\kappa$). As stated by Jimenez (2003), the stresses are carried by eddies whose scales are at most one order of magnitude smaller than the integral scale of the turbulence, L . To include them, it is hence required that $\Delta x < L/10$ and therefore around 1000 points are required per cubic integral scale. Although this restriction is in many cases severe, it is important to underline that this condition, which represents a constrain in terms of resolution, is independent of the Re number. This makes the methodology applicable for the problems in which the comparison between the grid and the integral scale of the turbulence is convenient in terms of resolution. Great number of studies of premixed combustion utilize the LES methodology. Among others, for its relevance for the topic we are treating it is possible to cite (Molkov et al., 2007b), (Molkov et al., 2007a).

The numerical schemes used to solve LES equations introduce an additional separation between scales, see Figure 1.5, dividing the frequency domain in three ranges: a) well resolved (low frequencies); b) non-resolved (high frequencies); and c) an intermediate region of poorly-resolved frequencies. Their spectral resolution induces a high wave numbers area close to the cut off wave number that although represented on the mesh is poorly resolved as stated in the Nyquist Theorem. This figure serves to illustrate the requirements posed by LES to the numerical schemes, which rise from the necessity to solve correctly and accurately the range of the spectrum previously discussed (Berselli et al., 2005). In the Figure, we have represented the cutoff wavenumber, $\kappa_c \eta$ where κ_c can be obtained directly from the numerical resolution Δx as $\kappa_c = 2\pi/\Delta x$, and that separates the resolved from the unresolved wavenumbers. Immediately adjacent is the poorly resolved zone. A complete review on numerical issues related with LES can be found in (Lele, 1992).

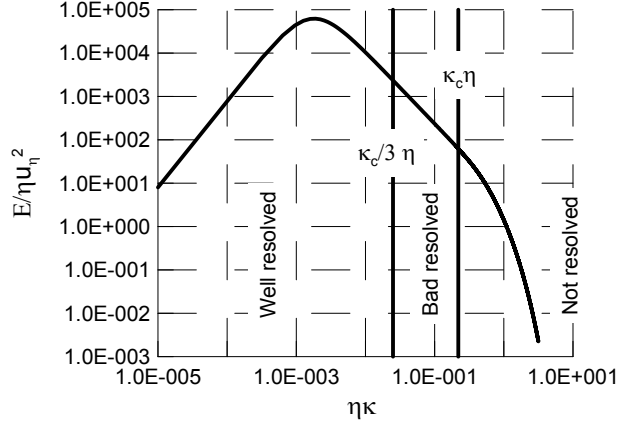


Figure 1.5: Turbulent kinetic energy spectrum. Dimensionless energy $E/\eta u_\eta^2$ vs. cutoff wavenumber $\kappa_c \eta$ for the mesh. Visible are the non-resolved, well and partially resolved frequencies. Figure obtained for a fluid with integral scale of the turbulence $L=0.5$ m, viscosity $\nu=10^{-5}$ m^2/s and turbulent kinetic energy dissipation $\varepsilon=0.1$ m^2/s^3 .

We have already mentioned that, in order to obtain the governing equations for the grid scale motions, the system balance equations (1.1)-(1.4) should be filtered with a convolution kernel G . For an arbitrary variable ϕ the convoluted one $\bar{\phi}$ is obtained,

$$\bar{\phi}(\vec{x}, t) = \frac{1}{\Delta} \int_{-\infty}^{+\infty} \phi(\vec{x}, t) G\left(\frac{\vec{x}-\vec{\xi}}{\Delta}, t\right) d^3 \xi. \quad (1.9)$$

We may now notice that filtering is performed by three superimposed methods: a) the numerical method; b) the mesh, which we have already have shown that works like an special class of filtering; and c) the explicit filtering (eq. (1.9)). Certainly, these three filters have also three differentiate scales. This imposes constraints on the numerical methodologies reviewed by Berselli et al. (2005).

Even if the results of the convolution are known (Garnier et al., 2009), detailed derivation of the system of equations is necessary to obtain a coherent system, and avoid incomplete formulations. Ignoring this step usually has as consequence the unaware neglect of terms and/or the utilization of non-adequate models. The results of the application of the convolution to the Navier-Stokes equations for the

reactive systems is obtained in Annex A. The final equations are:

$$\frac{\partial \bar{\rho}}{\partial t} = -\frac{\partial \bar{\rho} \tilde{u}_j}{\partial x_j}, \quad (1.10)$$

$$\frac{\partial \bar{\rho} \tilde{u}_i}{\partial t} = -\frac{\partial}{\partial x_i} (\bar{\rho} \tilde{u}_i \tilde{u}_j + p \delta_{ij}) + \frac{\partial \check{\sigma}_{ij}}{\partial x_i} + \bar{\rho} g + S_{1,ij} + S_{2,ij}, \quad (1.11)$$

$$\begin{aligned} \frac{\partial \bar{\rho} \check{e}}{\partial t} = & -\frac{\partial}{\partial x_i} ((\bar{\rho} \check{e} + p) \tilde{u}_i) + \frac{\partial \tilde{u}_j \check{\sigma}_{ij} - \bar{q}_i}{\partial x_i} + \bar{\rho} g_j \tilde{u}_i + \\ & + \alpha_3 + \alpha_4 + \alpha_5 + \alpha_6 + \alpha_7 + \alpha_8, \end{aligned} \quad (1.12)$$

$$\frac{\partial \bar{\rho} \tilde{Y}_a}{\partial t} = -\frac{\partial \bar{\rho} \tilde{Y}_a \tilde{u}_i}{\partial x_i} + \frac{\partial}{\partial x_i} \left(\tilde{D} \frac{\partial \tilde{Y}_a}{\partial x_i} \right) + \tilde{\omega}_a + S_9 + S_{10}, \quad (1.13)$$

where $S_{1,ij}$, $S_{2,ij}$, $\alpha_1 - \alpha_8$ & S_9 , S_{10} are the sub-grid terms, whose meaning is summarized in Table 1.1. Super-indexes represent different filtering levels. The reader is referred to Appendix A for more details.

Table 1.1: Summary of Sub Grid Scale Terms.

Name	Definition	Effect
Sub-grid stress term	$S_{1,ij} = -\frac{\partial}{\partial x_i} (\bar{\rho} \tau_{ij})$	Stress tensor modeling
Sub-grid viscous stress	$S_{2,ij} = \frac{\partial}{\partial x_i} (\overline{\sigma_{ij}} - \bar{\sigma}_{ij})$	Non-linearity the viscous stress tensors
Sub-grid turbulent stress on the scalar level	$\alpha_3 = \tilde{u}_i \frac{\partial \bar{\rho} \tau_{ij}}{\partial x_j}$	Kinetic energy transfer from resolved to unresolved scales
Sub-grid total velocity pressure	$\alpha_4 = -\frac{1}{\gamma-1} \frac{\partial}{\partial x_i} (\overline{p u_i} - \bar{p} \tilde{u}_i)$	Sub-grid turbulence effect on the conduction of heat on the resolved scales.
Sub-grid pressure dilatation term	$\alpha_5 = -\left(\overline{p \frac{\partial u_j}{\partial x_j}} - \bar{p} \frac{\partial \tilde{u}_j}{\partial x_j} \right)$	Pure compressibility effect
Sub-grid dissipation rate	$\alpha_6 = \overline{\sigma_{ij} \frac{\partial u_i}{\partial x_j}} - \overline{\sigma_{ij}} \frac{\partial \tilde{u}_i}{\partial x_j}$	Energy converted in internal energy due to viscous dissipation
Viscous stress non-linearities term	$\alpha_7 = \frac{\partial}{\partial x_j} (\bar{\sigma}_{ij} \tilde{u}_i - \bar{\sigma}_{ij} \tilde{u}_i)$	Viscous stress non-linearities
Sub-grid heat conduction term	$\alpha_8 = -\frac{\partial}{\partial x_j} (\bar{q}_j - \hat{q}_j)$	Non-linearities of the heat flux
Sub grid turbulent species flux	$S_9 = -\frac{\partial}{\partial x_i} (\bar{\rho} (\widetilde{u_i Y_\alpha} - \tilde{u}_i \tilde{Y}_\alpha))$	Turbulent species transport
Sub grid viscous diffusion term	$S_{10} = \frac{\partial}{\partial x_i} \left(\rho D \frac{\partial Y_\alpha}{\partial x_i} - \bar{\rho} \tilde{D} \frac{\partial \tilde{Y}_\alpha}{\partial x_i} \right)$	Non-linearities of diffusion flux

Numerous strategies to perform the closure of the SGS appearing in Table 1.1 terms have been developed and each of them leads to a different branch of models. Due to the strong efforts carried out in the last decades a vast number of them can be found in the devoted literature (Vreman, 1995), (Sagaut, 2001), (Lesieur et al., 2005), (Fröhlich, 2006), (Garnier et al., 2009). For this reason it is difficult to find or even to provide a comprehensive classification of LES methodologies for reactive

mixtures in the literature. It is nevertheless possible to create a classification of the models considering the modeling of the sub-grid stress tensor (Sagaut, 2001). It should be pointed out that in the incompressible formulation this tensor is the main object of LES.

The different trends could be classified in two main approaches: *Structural* and *Functional* modeling. *Structural* modeling consists of constructing the best approximation of sub-grid stress tensor by the evaluation of the filtered velocity as a series expansion. *Functional* modeling consists of calculating the action of the sub-grid terms on the filtered velocity, disregarding the sub-grid stress tensor itself.

Figure 1.6 contains a general overview of the different methodologies. Its complexity reflects the abundance of calculation approaches.

Inside the *Functional* methodology, two main processes should be modeled: the transmission of energy from the low to the high wave-numbers and viceversa, the so called back-scatter (see Figure 1.5). Differentiated models for each of these phenomena exist. In addition, it is possible to distinguish two approaches, depending on whether the turbulence interaction is resolved in the physical or in the spectral space.

The functional approach is the one chosen by most previous works concerning combustion (Luo, 2001), (Vreman, 1995), (Fureby, 1996). The methodology selected follows thus this approach, which is widely acknowledged. A detailed mathematical modeling of the LES sub-grid terms can be found in Annex B.

For the practical application that will be later presented, LES will be utilized whenever the resolution requirements for the method make it possible. That is, whenever the resolution make possible to resolve the most of the kinetic energy carried by the eddies.

1.5.4 Reynolds Averaged Navier-Stokes equations (RANS)

RANS is the most utilized and widespread simulation methodology for turbulent flows (Pope, 2000; Jimenez, 2003). The main aspects of the methodology consists of separating the independent variables in a mean and a fluctuating part. The

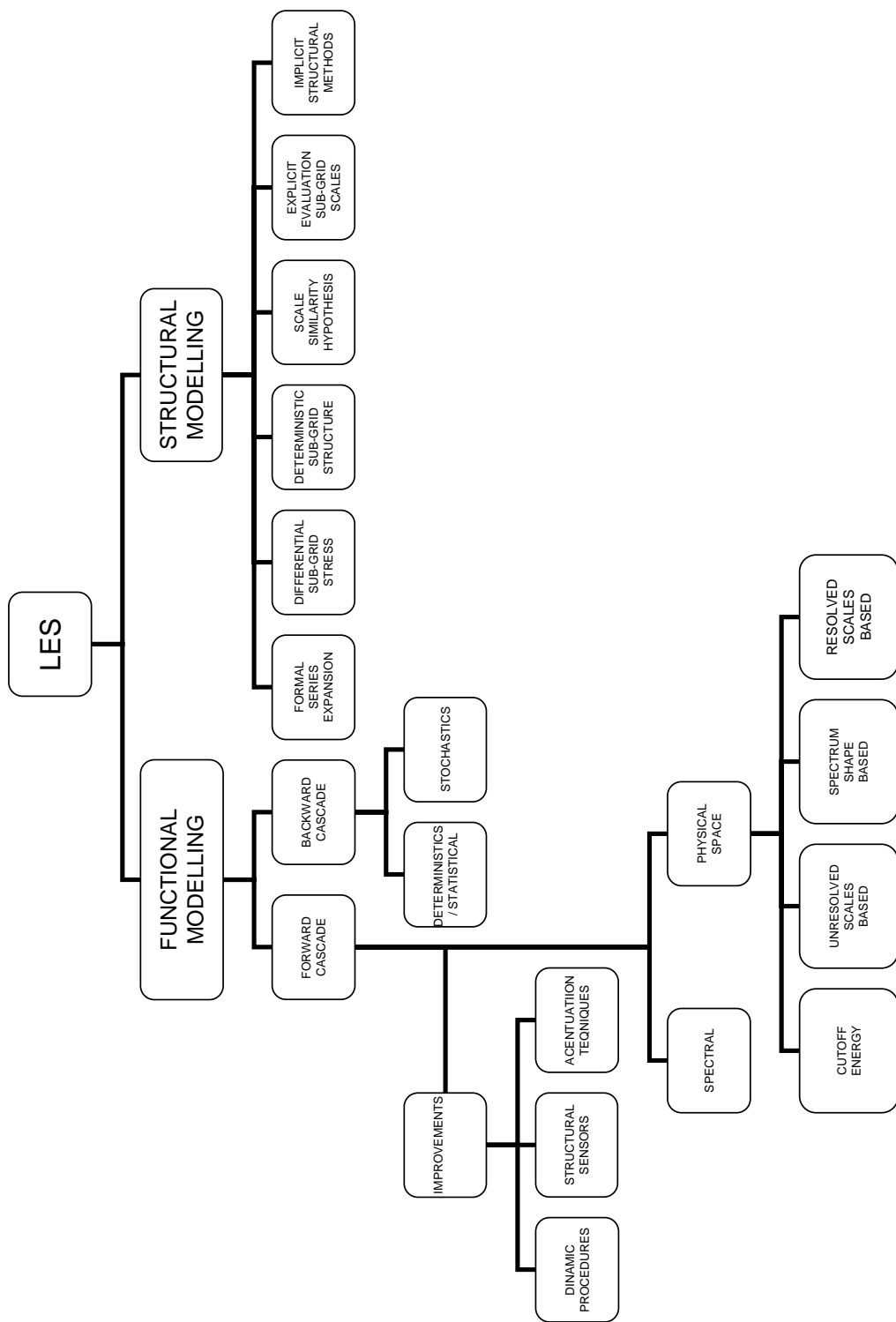


Figure 1.6: General description of the Large Eddy Simulation modeling methodologies.

equations obtained applying this methodology contain additional terms describing the interaction between the fluctuating and the mean motions. Such terms, i.e. the Reynolds stresses, are not *closed* and a model has to be postulated in order to achieve such *closure*.

Contrary to LES, this methodology tries to model all the turbulent scales, including the non-universal ones. Therefore, the model is not universal and must be *ad hoc* adapted (Jimenez, 2003).

The RANS models are better suited to handle stationary than unsteady problems. It is not necessary to consider temporal requirements or perturbations if only the stationary solution is needed. RANS methodologies also model large scales implying that the requirements of spatial resolution are significantly lighter (one or two orders of magnitude) than in LES calculations (Jimenez, 2003). The total volumetric gain results to be from three to six orders of magnitude on spatial resolution a notable descent in the resolution constrains. Nevertheless, RANS methods perform poorly in non-equilibrium situations and require calibration of the constants against experiments or LES. RANS model will be utilized later in this thesis to compute complex hydrogen combustion flows for which LES model becomes too demanding.

Because of its relevance, we may introduce now the $k - \varepsilon$ model that was created originally by Jones and Launder (1972). It is a two equations model in which transport equations are solved for two quantities relevant for turbulence, the turbulent kinetic energy and the dissipation of energy. $k - \varepsilon$ belongs to the kind of models in which the Reynolds stresses are calculated with the turbulent viscosity assumption (Boussinesq assumption). This assumption states that the deviatoric part of the Reynolds stresses are proportional to the mean rate of strain.

As previously stated, under RANS methodologies a magnitude is described by its mean and its fluctuating part. Averaging of the Navier-Stokes equations (1.1)-(1.4) yields the standard set of equations for RANS for mass, momentum, energy and species,

$$(\bar{\rho})_t + (\bar{\rho} \bar{u}_j)_{x_j} = 0, \quad (1.14)$$

$$(\bar{\rho} \bar{u}_j)_t + (\bar{\rho} \bar{u}_i \bar{u}_j)_{x_j} = \bar{\rho} g_j - \bar{p}_{x_j} + M_{ij,x_j}, \quad (1.15)$$

$$(\bar{\rho} \bar{e})_t + ((\bar{\rho} \bar{e} + \bar{p}) \bar{u}_j)_{x_j} = \bar{\rho} g_j \bar{u}_j + \bar{u}_i M_{ij,x_j} + \quad (1.16)$$

$$+ \left(\frac{\bar{\mu}}{C_h} \left(\bar{e} - \frac{1}{2} \bar{u}_i \bar{u}_j + \frac{\bar{p}}{\bar{\rho}} \right)_{x_j} \right)_{x_j} + B + \rho \varepsilon, \quad (1.17)$$

$$(\bar{\rho} \bar{Y}_\alpha)_t + (\bar{\rho} \bar{Y}_\alpha \bar{u}_j)_{x_j} = \left(\frac{\bar{\mu}}{C_{f_\alpha}} \bar{Y}_{\alpha,x_j} \right)_{x_j} + \bar{\omega}_\alpha, \quad (1.18)$$

where $\alpha = 1 \dots N_{\text{species}}$ with the auxiliary variables

$$M_{ij} = -\frac{2}{3} \delta_{ij} (\bar{\rho} \bar{k} + \bar{\mu} \bar{u}_{r,x_r}) + \bar{\mu} (\bar{u}_{i,x_j} + \bar{u}_{j,x_i}), \quad (1.19)$$

$$S = \bar{u}_{i,x_j} M_{ij} - B, \quad (1.20)$$

$$B = \frac{\bar{\mu}}{C_\rho} \frac{1}{\bar{\rho}^2} \bar{\rho}_{x_r} \bar{p}_{x_r}. \quad (1.21)$$

The standard $k - \varepsilon$ model is formulated by the following equations

$$(\bar{\rho} \bar{k})_t + (\bar{\rho} \bar{k} \bar{u}_j)_{x_j} = S - \bar{\rho} \bar{\varepsilon} + \left(\frac{\bar{\mu}}{C_k} \bar{k}_{x_j} \right)_{x_j}, \quad (1.22)$$

$$(\bar{\rho} \bar{\varepsilon})_t + (\bar{\rho} \bar{\varepsilon} \bar{u}_j)_{x_j} = \frac{\bar{\varepsilon}}{\bar{k}} [C_{1k\epsilon} S - C_{2k\epsilon} \bar{\rho} \bar{\varepsilon}] + \left(\frac{\bar{\mu}}{C_\epsilon} \bar{\varepsilon}_{x_j} \right)_{x_j}, \quad (1.23)$$

and the turbulent viscosity

$$\bar{\mu}_t = \bar{\mu} + C_\mu \frac{\bar{k}^2}{\bar{\varepsilon}}. \quad (1.24)$$

Launer and Sharma (1974) provided an improved set of constants for the model, calibrated for tubes and shown in table 1.2

Table 1.2: Constants set for the Standard k- ϵ method (Launer and Sharma, 1974).

C_μ	C_1	C_2	C_k	C_ϵ	C_{f_α}
0.09	1.44	1.92	1.0	1.3	1.

1.5.5 Hybrid models

Hybrid models consist of mixing two or several models in different regions of the calculation domain. Each model is applied inside its validity region or in the location in which it is expected to provide better accuracy than the others (Spalart, 2009).

A typical example of these models could be the combination of LES and RANS, the classical *Detached eddy simulation* (Strelets, 2001) in which LES is utilized as soon as its requirements are fulfilled. The biggest advantage of these models is the capability to treat the boundary layers utilizing RANS methods while the separated regions are addressed by LES methodologies (Spalart, 1997). The DES methodologies are shown as a way to close the gap between the considerable requirements in terms of resolution of LES methodologies and the lack of physical basis of RANS methodologies. Models that can be included in the DES category are the wall-modeled LES (WMLES) (Shur et al., 2008) and the delayed detached-eddy simulation (DDES) (Spalart et al., 2006).

Alternatively, hybrid models can also provide the coupling of two RANS models to benefit from the best characteristics of each in a certain domain of calculation. In this sense, the best example is the Shear Stress Transport (SST) model (Menter, 1993), (Menter, 1994) which is based on the combination of two RANS models, namely $k - \epsilon$ and $k - \omega$ (Wilcox, 1998).

1.5.6 Zonal models

The Zonal models provide an engineering approach to a particular kind of fluid or a specific flow in an area of interest. Computing cost is very reduced. They are now obsolete but can be extremely useful for some particular cases. Typical examples of these methodologies are e.g. explicit algebraic expressions for the turbulence heat exchange coefficient and the length formula of Prandtl and von Kármán (Pope, 2000).

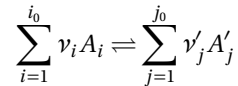
1.5.7 Non-dimensional correlations of data

Non-dimensional correlations of data are methodologies in which e.g. the non-dimensional skin friction coefficient is approximated as a function of suitable non-dimensional numbers. They are extremely useful but limited to the particular class of flows for which they are defined. When not available, the correlations are credited to be expensive to be obtained. Today, they are extensively utilized in the treatment of two phase media e.g. (Yarin et al., 2004).

1.6 Turbulent combustion modeling

1.6.1 General

The stoichiometric equation that describe a chemical system having only one reaction reads



where A_i and A'_j are the chemical symbols of reagents and products, and ν_i ν'_j are the corresponding stoichiometric coefficients. The transition from the initial to the final state is characterized by the chemical reaction rates for the various components of the reacting medium, defined following Zeldovich et al. (1985), as

$$\omega_i = \nu_i \frac{1}{V} \frac{dN_i}{dt}$$

describing the amount of molecules N_i of the i -specie created (or consumed) per unit of time in the volume V . The concentrations of species appearing in the equation (1.13) or its averaged counterpart eq. (1.18) can be expressed in different units being the most usual the molar fractions, the mass fractions and the mass densities or the molar densities of concentrations (Martinez, 1992). The consumption rates must be simply written in the corresponding, but clearly all of them are equivalent, e.g.

$$\frac{M_i}{V \rho N_A} \frac{dN_i}{dt} = \frac{dY_i}{dt}$$

where M_i is the molar mass and N_A is the number of Avogadro.

For a known initial concentration, the eq. (1.18) can be conveniently written utilizing the so called progress variable, f , which describes the evolutions of a reaction taking the value zero for a fresh mixture, one for a completed reaction and intermediate values in between. Knowing the values of the initial concentrations $(Y_{1_0}, \dots, Y_{n_0})$, using the progress variable f , taking into account that $\omega_i/\nu_i = \omega_j/\nu_j = \omega$ (ω already written in terms of f , $\omega = df/dt$ due to the chemical reaction) and, the set of equations (1.18) can be converted to the form

$$\frac{\partial \bar{\rho} \bar{f}}{\partial t} + \frac{\partial \bar{\rho} \bar{f} \bar{u}_i}{\partial x_i} = \frac{\partial}{\partial x_i} \left(\bar{\rho} \bar{D} \frac{\partial \bar{f}}{\partial x_i} \right) + \bar{\rho} \bar{\omega}. \quad (1.25)$$

which is convenient for modeling reactions considering single step chemistry.

1.6.2 Necessity of the modeling

The reaction rate, ω , is a highly non-linear function of several variables. Due to this non-linearity, the mean value of the reaction rate is not equal to the value of this magnitude calculated from the mean value of the variables. We may clarify this point. If e.g. a second order reaction is considered,



the combustion rate results to be, in terms of the mass fractions

$$\bar{\omega}_A = \bar{\omega}_B = -\bar{k} \bar{Y}_A \bar{Y}_B, \quad (1.27)$$

where \bar{Y}_A, \bar{Y}_B are mass fractions and the reaction rate coefficient k is expressed with the Arrhenius formula (House, 2007) as

$$k = k_0 \exp\left(-\frac{T_a}{T}\right), \quad (1.28)$$

where T_a is the activation temperature $T_a = E_a/R$.

We may now express the variables in terms of mean and fluctuating parts and make an expansion for the fluctuating terms. The formula

$$\begin{aligned}\bar{\omega}_A = \bar{\omega}_B = & -k_0 \bar{Y}_A \bar{Y}_B \exp\left(-\frac{T_a}{\bar{T}}\right) \cdot \left[1 + \frac{\overline{Y'_A Y'_B}}{\bar{Y}_A \bar{Y}_B} + \right. \\ & + P_1\left(\frac{T_a}{\bar{T}}\right) \left(\frac{\overline{Y'_A T'}}{\bar{Y}_A \bar{T}} + \frac{\overline{Y'_B T'}}{\bar{Y}_B \bar{T}} \right) + P_1\left(\frac{T_a}{\bar{T}}\right) \frac{\bar{T}'^2}{\bar{T}^2} + \\ & \left. + P_1\left(\frac{T_a}{\bar{T}}\right) \left(\frac{\overline{Y'_A T'^2}}{\bar{Y}_A \bar{T}^2} + \frac{\overline{Y'_B T'^2}}{\bar{Y}_B \bar{T}^2} \right) + P_3\left(\frac{T_a}{\bar{T}}\right) \frac{\bar{T}'^3}{\bar{T}^3} + \dots \right],\end{aligned}\quad (1.29)$$

is obtained, where P_1, P_2, P_3 represent polynomials of T_a/\bar{T} .

In such an approach for the description of the mean reaction rate, balance equations are required for every of the moments $\overline{T'Y'_a}$ in order to close the formulation. Those equations contain, in turn, non-closed terms and a good approximation of the formula (1.29) requires a large numbers of models to be taken into account. Additionally, and due to the non-linearity of the exponential term, the equation is only valid for the cases in which $T'/\bar{T} \ll 1$. Good results have been reported for this intuitive formulation exclusively for very slow reactions (Borghi, 1975) with small activation temperature. Nevertheless, the fluctuations, especially of temperature, can be very large (consider the temperature differences existing between fresh gases and the products of the reaction) and the applicability of the methods based in expansions is very restricted, being inadequate to the cases of premixed and diffusion turbulent flames.

Therefore, combustion modeling, and concretely turbulent combustion modeling, has been the subject of an extensive research in the last decades. Since the pioneering work of Damköhler (1940), an intensive work has been performed and much advancement achieved. Without intending to be exhaustive, several reference contributions to the combustion science due to Zeldovich et al. (1985), Liñan and Williams (1993), Williams (1994) and the more contemporary text due to Glassman and Yetter (2008) could be mentioned because of their relevance.

1.6.3 Combustion regimes

The purpose of a combustion model for pre-mixed combustion is to convert reactants to products at a rate and in a location similar to that of the real flame in a similar reaction area.

For pre-mixed flames, several regimes of combustion have been identified by Borghi (1988) based on comparison of turbulence and chemistry scales (see Figure 1.7). Three magnitudes summarize those comparisons: a) the turbulent Reynolds number $Re_t = u' L / \nu$ which weighs the turbulent transport to the viscous forces; b) the Damkoehler number $Da = \tau_t / \tau_c$ which compares the turbulent and the chemical time scales; and finally c) the Karlovitz number $Ka = \tau_c / \tau_\nu$ which balances the chemical time and the dissipation time of the turbulence.

In the diagram, the different combustion regimes are assigned to separate regions:

1. The *laminar regime* was identified to exist for $Re_t < 1$.
2. For $Ka < 1$ the *flamelet regime* was determined. A flamelet, following Peters (2000), is a layer that contains a preheat and reaction zone and has gradients in the normal direction that are larger than in the transverse, and a molecular diffusivity that is much larger than the turbulent diffusivity within the layer. This is characterized by turbulent times larger than chemical ones. Inside the *flamelet regime*, two subdivisions are recognized comparing the intensity of the turbulence represented by u' and the laminar burning velocity S_L .
 - (a) The *wrinkled flamelets regime* $u' / S_L < 1$ exists if the laminar propagation is predominant and the turbulence interaction remains limited.
 - (b) The *wrinkled flamelets regime with pockets* appears if $u' / S_L > 1$ representing turbulence preponderance.
3. For flames with $1 < Ka < 100$ *thickened-wrinkled flames* arise and the turbulent motions thicken the flame pre-heat zone but do not affect the zone of reaction.

4. Finally, *thickened flames* appear in the cases in which the reaction zone is also affected by turbulence.

It has to be noted that the areas in which the Borghi diagram is divided have dissimilar denominations in different sources, see e.g. Dorofeev (2008), Ciccarelli and Dorofeev (2008), Lipatnikov and Chomiak (2002), Warnatz et al. (1999), Peters (2000), etc.

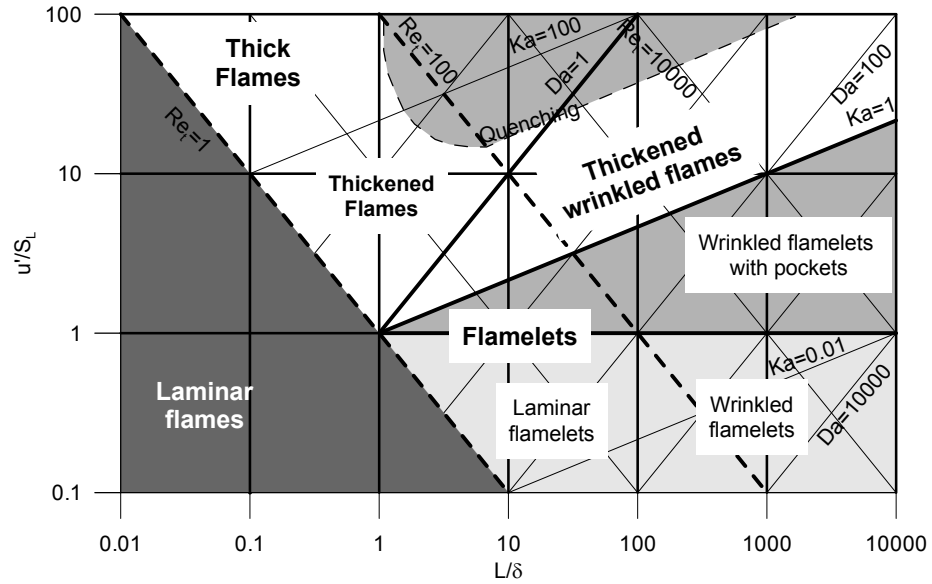


Figure 1.7: Turbulent premixed combustion diagram. In the abscissa, the integral scale of turbulence made dimensionless utilizing the flame thickness. In ordinates the ratio of the RMS intensity of turbulence and the laminar burning velocity.

Two significant extension to the classical Borghi diagram may be mentioned:

1. Different numerical and experimental investigations (Veynante and Vervisch, 2002) allow inferring that the classical Klimov-Williams criterion, $Ka = 1$, for the existence of the flamelet regime must not be strictly interpreted. Following these authors the existence of the flamelet regime seems to be guaranteed

if $Ka < 100$ (region below $Ka = 100$ in the Figure 1.7)². With this enlarged criterion, the domain of existence of the flamelet regime covers the most of the cases of practical interest, with *thickened flames* reduced to uncommon conditions (Veynante and Vervisch, 2002). Certainly, with common fuels, the eddies do not penetrate in the reaction zone of the flame and thus the *Thickened flames* and *Thickened wrinkled flames* can be disregarded for the modeling that will consider flamelet regime exclusively.

2. The second significant extension to the *classical* region division was proposed by Poinso et al. (1991) and is constituted by the upper gray peninsula in the Figure 1.7. This region represents the conditions in which the *quenching* of the flame will happen. Certainly, this region can be characterized in its linear part, for $Re_t > 100$, by the surprisingly simple criteria $Ka \gtrsim 20$ (see ³)

1.6.4 Thermal radiation

It would be pertinent to finalize this section saying a few words about radiation. The radiative heat transfer and its interaction with turbulence has been the subject of several investigations (Modest, 1993), (Siegel and Howell, 1992). For the accuracy necessary for the industrial safety purposes, the thermal radiation can be neglected in first approach. This assumption is equivalent to considering the gaseous media as transparent, a statement that is completely realistic for the fuel and air but less adequate for the steam, product of the reaction (for the absorbance of the different species see e.g. (Zeldovich and Raizer, 2002) and particularly for the steam see (Leckner, 1972)).

²in terms of u'/S_L and L/δ in the turbulent flames region this means

$$\log_{10}(u'/S_L) < \frac{2}{3} \log_{10}(Ka) + \frac{1}{3} \log_{10}(L/\delta)$$

³The Karlovitz number utilized here has been the one defined by Lipatnikov and Chomiak (2010) as $Ka = (u'/S_L)^{3/2}(\delta/L)^{1/2}$

1.6.5 Relation of the reaction rate modeling and the turbulence modeling

In this section 1.6.1, the modeling of the reaction rate, ω , have been studied utilizing the eq. (1.25). Because in low resolution applications, historically RANS have been more often applied, we have exhibit and center our attention on the RANS formulation of the progress variable equation. For functional LES modeling, historically most of the sub grid terms appearing in the equations have been ignored and similar equations to RANS have been utilized.

Nevertheless, there is an alternative manner of express the progress variable equation, utilizing the transport set of equations for the mass fractions (Y_1, \dots, Y_n) equations (1.4) and a fictitious species Z that will be equal to one of the reactive species at initial time, i.e. $Z = Y_{1_0}$, will be transported in the same conditions as the other scalars but will suffer no chemical transformations $\omega_Z = 0$. Under such an approach the equation (1.25) is never utilized. Instead of it the set of equations (1.13) for LES or 1.18 for RANS are utilized.

We have already mentioned in the introduction of section 1.6.1 that $\omega_i/\nu_i = \omega_j/\nu_j = \omega$ and that all the forms of the reaction rate are equivalent. Utilizing the initial concentrations (Y_{1_u}, \dots, Y_{n_u}) we may study the chemical evolution of our system in a simplified manner utilizing a single reaction rate, see Figure 1.8. From the initial concentration, the chemical system evolves along a curve (mono-parametric system) until the exhaustion of the fuel, here represented by subindex 1. The final status, (Y_{1_f}, \dots, Y_{n_f}) lies then in the horizontal plane (or hyper-plane in case of more components).

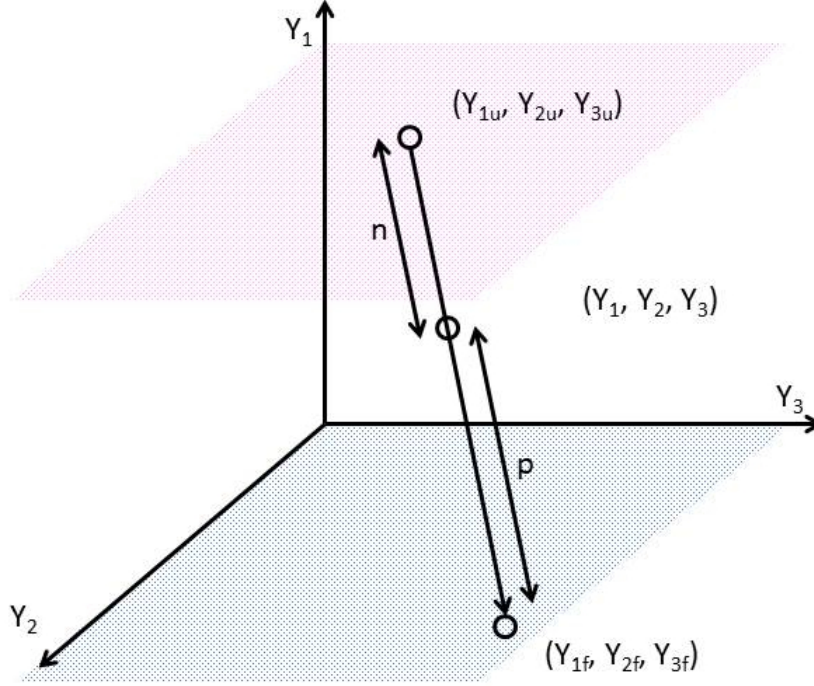


Figure 1.8: Diagram of concentrations illustrating the path followed by a particle in the concentrations space of a three dimensional mixture. Sub-index 0 designate the fuel. Initial fuel concentration is marked by the pink plane. Final position lies in the horizontal blue plane (fuel exhausted).

For each intermediate position, we may calculate the progress variable f as a function of the set Z and (Y_1, \dots, Y_n) as

$$n = \max \left(\frac{Z - Y_0}{\nu_0 M_0}, \max_{i \in [1, N_{\text{species}}] \mid \nu_i > 0} \left(-\frac{Y_i}{\nu_i M_i} \right) \right), \quad (1.30)$$

$$p = \min_{i \in [1, N_{\text{species}}] \mid \nu_i < 0} \left(-\frac{Y_i}{\nu_i M_i} \right), \quad (1.31)$$

$$f = \frac{n}{n - p}. \quad (1.32)$$

The meaning of the auxiliary variables, n and p , is easy understandable. n represents how much have the system advanced (in terms of the length of the curve)

from the initial concentrations. p represents how much can still advance until exhaustion or equilibrium. $p - n$ is the total length of the curve from the initial concentration until the final status.

We may now explicitly write down the relation between the reaction rate given in terms of the mass fractions and in terms of the progress variable. That is,

$$\frac{dY_i}{dt} = \nu_i M_i p(Y_1, \dots, Y_n) \frac{df}{dt}. \quad (1.33)$$

For the rest of this thesis, we will keep the formulation of eq. (1.25) that because of its simplicity is more illustrative. Taking into account the last formula is easy to see that the curve of Figure 1.8 is a straight line of direction $(\nu_1 M_1, \dots, \nu_i M_i, \dots, \nu_n M_n)$.

1.6.6 Classical turbulent combustion models

1.6.6.1 General

A set of the classical models for turbulent combustion may enclose the Eddy Dissipation Model presented by Magnussen and Hjertager (1976) and the Eddy Break Up model (EBU) due to Spalding (1971). Although their physical content is rather limited (Peters, 1999) recent practical applications of the former in the nuclear industry are documented (Kotchourko, 2005), (Bielert et al., 2001), (Kotchourko et al., 1999a) and (Bentaib et al., 2007). This suggest we may shortly review them.

1.6.6.2 Eddy dissipation model

Eddy dissipation model is based on the fact that the chemical reaction and its interaction with turbulent mixing greatly determines the propagation of turbulent flames. In many applications, the chemical reaction can be considered infinitely fast compared to the turbulent mixing process (equivalent to $Da \approx \infty$). In this case, the turbulent mixing of fuel and oxidizer is the unique limiter of the progress of the reaction and completely defines the combustion process. That means that the reaction rate has to be dependent on the timescale of turbulent mixing. This suggest that for one single step reaction the reaction rate is determined as the mini-

mum of the following three reaction rates, valid for products ω_p , fuel ω_f and comburent ω_o

$$\bar{\omega} = \min(\omega_f, \omega_o, \omega_p), \quad (1.34)$$

where each of the reaction rates is

$$\omega_f = A \frac{\epsilon}{k} Y_f, \quad \omega_o = A \frac{\epsilon}{k} \frac{1}{r_f} Y_o, \quad \omega_p = AB \frac{\epsilon}{k} \frac{1}{1 + r_f} Y_p, \quad (1.35)$$

where the symbol r_f represents the stoichiometric ratio $r_f = \mu_o \nu_o / \mu_f \nu_f$, Y_n is the corresponding mass fraction of fuel, products and comburent, k the turbulent kinetic energy, ϵ the turbulent kinetic energy dissipation and A and B constants of the model.

1.6.6.3 Eddy Break Up

The Standard and Modified Eddy Break Up (EBU) model also apply to the limiting case of very fast chemistry. In this limiting case, the reaction zone is described as a mixture of pure burned and unburned regions (Warnatz et al., 1999). The formulation tries to describe the rate that governs the breakup of domains of unburned gas into smaller fragments. The fragments are in close contact with hot burned gases and thus react almost immediately. Therefore, the EBU model could be interpreted as a limit case inside the so called *Presumed PDF Method* firstly proposed by Mao and Toor (1970). The limiting case represented by EBU model would then be consistent with a probability density function in which only two peaks are non-zero (Borghi, 1988). Those peaks correspond to the cases in which Y_α is equal to 0 or Y_α^0 , the initial mass fraction.

The modified EBU model extends the standard EBU model by taking into account the distinction between the movements of the flamelets and the turbulent flow. It has been shown by Borghi (1988) that the mean reaction rate strongly depends on the ratio of the turbulent kinetic energy k to the laminar flame velocity S_L when $k^{1/2}$ is of the order of S_L , namely when the reaction rate is controlled not only by the mixing of turbulence (related to k), but also is influenced by the flamelet

properties (related to S_L). This is the basis of the modified model, in which the corresponding dependence on $k^{1/2}/S_L$ has been taken into account.

1.6.7 Modern turbulent combustion models

1.6.7.1 General

Following Lipatnikov and Chomiak (2002) the modern turbulent combustion models can be classified in two main groups, the models studying the *turbulent flame speed* and the models considering the *structure of the flame*. Although the two techniques should not be considered to be separate, the main difference lies on whether the emphasis of the model is on modeling the turbulent flame speed or on modeling any other characteristic of the flame, like e.g. its stretching, etc.

1.6.7.2 Structure of the flame models

1.6.7.2.1 General

Several models may be enclosed in the scope considered in the *structure of the flame* research, (Lipatnikov and Chomiak, 2002), (Peters, 2000). Among them, the Bray-Moss-Libby (BML) model (Bray, 1995), (Bray, 1996), the Coherent Flame Model (CFM) (Meneveau and Poinso, 1991) and its enhancements and applications, e.g. (Trouvé and Poinso, 1994) (Bray, 1995), (Bray, 1996) and the methodologies based on the treatment of the statistical momentum of the reactive variables, the pdf, or based on a presumed pdf-model, can be cited.

The BML models consider a closure for the $\overline{\omega}$ rate (Bray, 1996) of the type,

$$\overline{\rho\omega} = \rho_u I_0 S_L \Sigma, \quad (1.36)$$

where ρ_u is the density of the reactants, I_0 accounts for the effect of stretching and Σ is the flame surface density. A closure for the flame surface density is provided

considering an infinitely thin flamelet (Libby and Williams, 1994) to be

$$\Sigma = C_L \frac{u'}{LS_L} \bar{f}(1 - \bar{f}), \quad (1.37)$$

where C_L is a coefficient whose formulation can be retrieved in (Libby and Williams, 1994) or in Veynante and Vervisch (2002), f the progress variable, L the integral scale of the turbulence and S_L the laminar burning velocity.

Alternatively, if an additional balance equation for the mean flamelet surface density is utilized in order to close the eq. (1.36) then the model strategy derives into the *Coherent Flame Model* approach (see (Meneveau and Poinso, 1991), (Duclos et al., 1993) and Peters (2000)).

1.6.7.2.2 Methodologies based on the treatment of the statistical moments of the reactive variables

An alternative branch of the *structure of flame* models are those based on the study of the statistical distribution of the variables. This category can be in turn divided in different sub-sets.

The first group is based on the full joint pdf of the velocity of viscous dissipation and a reactive scalar (Pope, 2000). The resulting transport equation contains several non-closed terms that pose serious modeling difficulties. Additionally, require very significant calculation resources resulting in solutions which are usually obtained utilizing the Monte Carlo method (Pope and Cheng, 1986).

The moments method is based on the calculation of the first few statistical moments of the variables. In order to evaluate the moments of a non-linear function of several random variables, the joint pdf of these variables should be known (see equation (1.29)). Thus, transport equations and closures for the join pdf would be required representing no advantage from the full joint pdf methodology.

Still, a third methodology is available, the so called presumed pdf approach. In it, the probability density function is prescribed, e.g. β -pdf shape (Girimaji, 1991), (Baurle and Girimaji, 2003), based on the knowledge of the first two moments, i.e.,

average and variance of the variables. Thus,

$$\bar{\omega} = \int \omega P(\bar{T}, \bar{Y}_1, \dots, \bar{Y}_{ns}) dTDY \approx \int \omega P(\bar{T}, \sigma_T) P(\bar{Y}_1, \dots, \bar{Y}_{ns}, \sigma_Y) dTDY, \quad (1.38)$$

where σ_T is the variance of the temperature and σ_Y the sum of the variances of the different species and P the *a priori* assumed pdf. The calculation of σ_T and σ_Y require the solution of a scalar balance equation for each of them.

1.6.7.3 Turbulent flame speed models

The *turbulent flame speed* category encloses two main branches. The first, the *level set approach*, also called the *G-equation*, utilizes a non-reactive variable describing a set of levels, and is due to Peters (2000). The second, uses some expression for the turbulent burning velocity to close a balance equation for the combustion progress variable (Zimont (1977)).

The *level set approach* model treats the gases as a non-reacting and constant density species inside a turbulence velocity field determined by the averaged (or filtered) Navier Stokes equations. The quantity G_p is a scalar without any physical significance. Defining arbitrarily the value $G_p(x, t) = G_{0p}$ as the position of the flame in time $t = t_0$, the propagation of the flame can be traced dividing the calculation domain in two regions: $G_p < G_{0p}$ for the reactants and $G_p > G_{0p}$ for the products. The G-Equation can be written (Peters, 2000)

$$\frac{\partial G_p}{\partial t} + u_i \frac{\partial G_p}{\partial x_i} = S_L |\nabla G_p| - S_L L_{mark} \kappa |\nabla G_p| - L_{mark} S |\nabla G_p|, \quad (1.39)$$

where L_{mark} is the Markstein Length, $\kappa = \nabla \cdot n$ the curvature and $S = -n \cdot \nabla v \cdot n$ the strain. The normal to the surface can be obtained as $n = \nabla G / |\nabla G|$.

The extended model by Zimont (1977), also called *gradient model*, considers the eq. 1.25 for the progress reaction variable and provides the following closure for the mean combustion progress variable

$$\bar{\omega} = \rho_u S_t |\nabla \bar{f}|. \quad (1.40)$$

The model reads

$$\frac{\partial \bar{\rho} \bar{f}}{\partial t} + \frac{\partial \bar{\rho} \bar{f} \bar{u}_i}{\partial x_i} = \frac{\partial}{\partial x_i} \left(\bar{D} \bar{\rho} \frac{\partial \bar{f}}{\partial x_i} \right) + \rho_u S_t |\nabla \bar{f}|. \quad (1.41)$$

The last equation can be probably called the *workhorse* of the combustion modeling in recent years. Zimont developed its model trying to reproduce independently the behavior of the flame brush thickness and the burning rate and at the same time giving an especial emphasis to the turbulent flame speed. Considering the planar, constant density flame in a system of coordinates moving with velocity S_t eq. (1.41) reduces to $(\bar{\rho} \bar{f})_t = (\bar{D}(\bar{f})_x)_x$. Thus, equation (1.41) provides an increasing flame brush thickness controlled by the turbulent diffusion. This is in agreement with observations that indicate that the brush thickness is determined by large-scale eddies. In a planar case, integration from $-\infty$ to $+\infty$ of eq. (1.41), renders a mass burning rate of value $\rho_u S_t$. Thus, the diffusion term does not affect the predicted propagation velocity and the brush thickness is independent of the burning rate. Taking into account that the burning rate is mainly controlled by small eddies, the model correctly reproduces the separation of scales of the two phenomena.

The great advantage of the Zimont methodology is the possibility of reducing the problem of combustion modeling to the determination of the turbulent burning rate, offering the possibility of utilizing the experimental and theoretical analysis available for the latter for the obtaining of the final solution. The simplification of the problem so achieved is enormous, changing from a three dimensional phenomena to a one dimensional one in which experiments are at disposal.

1.6.7.4 Alternative classifications methodologies

The strong dependence of the turbulent combustion on the turbulence, suggests to classify the models taking into account the methodology that was used to model turbulence. This alternative classification was utilized also by Lipatnikov and Chomiak (2002), Peters (2000) and Driscoll (2008). Following this methodology, the turbulent combustion models can be classified in groups such as RANS, LES and

DNS depending on the technique utilized. Among the significant models applying RANS the Coherent Flamelet Model (Veynante et al., 1994), the Surface Density Balance Equation (Trouvé and Poinso, 1994) and the level set approach (G-Equation) by Peters (2000) can be mentioned. The most prominent LES methodologies are the ones based on the flame surface density equation (Weller et al., 1998), (Charlette et al., 2002) and the application of the Surface Density Balance Equation to the Large Eddy Simulation (Pitsch, 2005). Direct numerical simulations DNS were restricted mainly to burners, e.g. (Bell et al., 2006).

Finally, it has to be remarked that a final way to classify the turbulent models can be to take into account the existence, or not, of a transport equation for the flame surface density. Taking into account this classification (Driscoll, 2008), the models belonging to the first category, can be listed to be the BML (Bray and Moss, 1977), the stochastic particle (Monte Carlo) model (Pope and Cheng, 1986), Fractal Theory (Lindstedt and Vaos, 1999), (Bychkov and Liberman, 2000) and the aforementioned Zimont model (Lipatnikov and Chomiak, 2002).

1.6.7.5 Final remarks and summary of the classification of the models for turbulent combustion

Taking into account the objective of our investigation, the first classification due to Lipatnikov, section 1.6.7.1, appears to provide a reasonable clear view in the problem we are dealing with. The diagram of Figure 4.1 has been created to illustrate this classification.

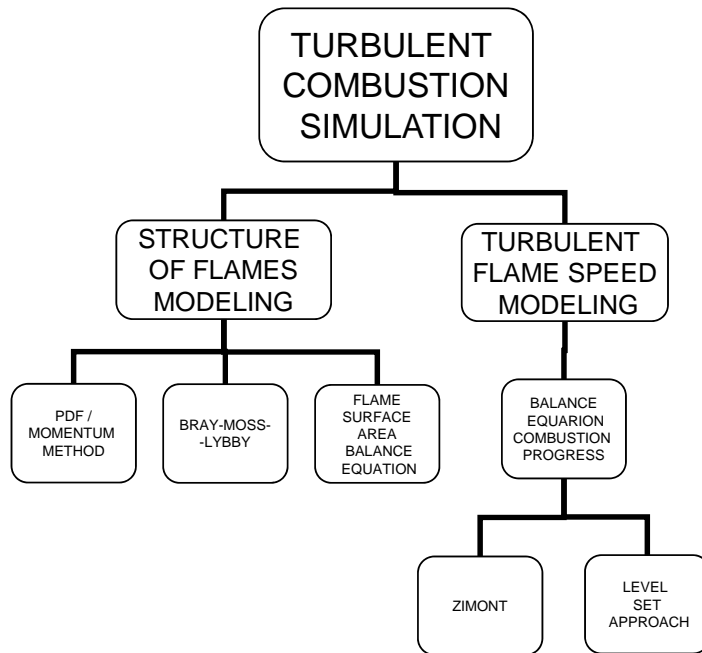


Figure 1.9: Classification of turbulent combustion models, following Lipatnikov and Chomiak (2002).

The first branch in the Figure 4.1, the models belonging to the *structure of the flame*, has been mainly utilized in fundamental research. The second branch, the *flame speed modeling* has been strongly utilized in recent years (Lipatnikov and Chomiak, 2002) due to practical necessities to solve realistic problems. Within this last trend, the methodology consisting in *closing a balance equation for the progress variable using some expression to evaluate the turbulent flame speed*, (see section 1.6.7.3) has been reported to be used with success (Lipatnikov and Chomiak, 2002) in practical applications. Under the last methodology, the calculation of the local value of the turbulent flame velocity becomes the key element of the models under consideration. This problem is reviewed next.

1.7 Turbulent flame speed

1.7.1 Introduction

In previous sections the terms *turbulent burning velocity* and *turbulent flame speed* have been utilized indiscriminately, which, for the purposes of present research, is adequate. However, there are subtle differences between them worth discussing: In fact, these concepts may often be inaccurately defined in the literature:

Turbulent flame speed corresponds to the temporal change of location of a reference surface, arbitrarily fixed inside the flame brush and determined by a given chemical composition or temperature, with respect to the unburned mixture. In principle, the *turbulent flame speed* is not a well-defined quantity because velocities corresponding to different locations inside the flame brush are different due to the growth of the brush thickness.

Turbulent burning velocity can be defined as the mass burning rate per unit flame surface area divided by the density of the reactants. Utilizing the integral mass burning rate as the most accurate measurement of the mass burning rate, $S_T = \frac{1}{\rho_u} \frac{d}{dt} \left(\int_{-\infty}^{\infty} \rho f dx \right)$ (Lipatnikov and Chomiak, 2002). Still this definition is not unique and can be contemplated as a global or a local point-wise dependent quantity.

For the purposes of large scale analysis, and taking into account its accuracy, both concepts will be indistinctly utilized. It has to be remarked that difference between them in the scales we are considering is negligible. Nevertheless, it is important to note the differences.

1.7.2 A general formulation of the turbulent burning velocity

Under general conditions, the turbulent burning velocity S_t can be described (Driscoll, 2008), (Dorofeev, 2008) by a correlation of the type

$$S_t/S_L = f(u'/S_L, L/\delta, Ma). \quad (1.42)$$

where:

1. S_L is the laminar burning velocity, the speed of the planar, steadily propagating, laminar flame with respect to the unburned mixture.
2. u' is the root mean square of the fluctuating part of the the velocity $u' = \langle (u - \langle u \rangle)^2 \rangle^{1/2}$ (Pope, 2000).
3. L the integral scale of the turbulence.

Properly written, the integral scale of the turbulence is defined by Pope (2000) as the $L_{ii}(\vec{x}, t) = \frac{1}{\langle u_i(\vec{x}, t) u_i(\vec{x}, t) \rangle} \int_0^\infty \langle u_i(\vec{x} + r \vec{e}_i, t) u_i(\vec{x}, t) \rangle dr$ which following the same author characterizes the biggest eddies. Nevertheless, the lengthscale characterizing the biggest eddies, $L = k^{3/2}/\varepsilon$ is utilized in the most of the formulations (Lipatnikov and Chomiak, 2002), by an abuse of notation.

4. δ is the thermal thickness of the laminar flame of the order of $\delta \approx \chi/S_L$ (Zeldovich et al., 1985).

Following Jarosinski (1984), there are three usual and arbitrary definitions of flame thickness

- (a) The well known, so-called *characteristic thickness* defined as $\delta = \chi/S_L$ where χ is the thermal conductivity. The dimensional quantity δ is a measure of the thickness within which the unburned mixture is heated to the ignition temperature by the reaction zone (see Figure 1.10, marked with a Δ).

-
- (b) In its second definition, similar to the first one, the preheat zone is restricted to the region between the region of ignition temperature and the point where the temperature has risen by just 1%, from which it follows that the thickness of the preheat zone is 4.6δ (in the Figure 1.10 denoted as 4.6Δ).
- (c) In its third definition, the flame thickness is the ratio between the maximum temperature difference and the maximum temperature gradient which occurs at the point of inflection of the profile,

$$b = \frac{T_u - T_u}{\left. \frac{dT}{dz} \right|_{\max}}, \quad (1.43)$$

where z is a coordinate normal to the flame front, and the subscripts b and u mean burned and unburned, respectively.

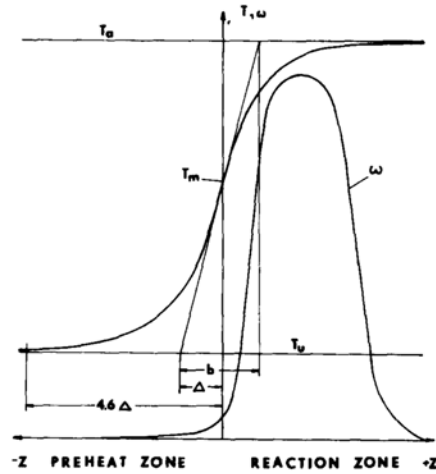


Figure 1.10: Temperature profile across the flame front, obtained from (Jarosinski, 1984)

In this thesis, the first definition will be utilized because of its simplicity.

-
5. Ma the Markstein number, defined as the coefficient of proportionality between the velocities of a planar laminar flame front S_{L_0} , and a perturbed one, S_L , with a curvature R , $Ma = \frac{S_L - S_{L_0}}{S_{L_0}} \frac{R}{\delta}$, see (Zeldovich et al., 1985)

The expression (1.42) provides the effect of the turbulence on the burning velocity dependent on the laminar flame speed and on the molecular transport parameters of the gaseous mixtures. Several concrete formulations of the function f will be considered in section 4.2.1 analyzing in detail their performance. Afterwards, a formulation of this kind will be utilized for the simulations that will appear in the rest of this thesis. Therefore, no concrete details are necessary for the moment. It is enough to say that the turbulent burning velocity has been experimentally investigated by different researchers, and a significant number of formulations for S_t have been suggested by processing measured data or by mathematical analysis (Lewis and von Elbe, 1987), (Peters, 1999), (Dorofeev, 2008), (Schmid et al., 1998).

Nevertheless it is important to understand the limitations of the formulation (1.42). Concretely, equations of this type disregard flame stretching and quenching (extinction due to heat losses, strain, stretch, etc) which may be considered through the introduction of the factor I_0 (Bradley et al., 1992) yielding

$$S_t/S_L = I_0 f(u'/S_L, L/\delta, Ma). \quad (1.44)$$

Very strong efforts for the determination of the variables and criteria controlling the quenching process have been performed in the last years. Since the initial works (Bradley et al., 1992) and the celebrated *How fast can we burn?* by Bradley (1992), a series of papers have expanded the theory of combustion on quenching (Bradley et al., 2003), (Bradley et al., 2007b), (Bradley et al., 2009). The state-of-the-art theories correlate the probability of quenching with some limiting stretch factor which also depends on the combustion properties of the mixture (Bradley et al., 2005). Still some variables involved in the last studies cannot be theoretically predicted and must be experimentally determined.

There are powerful reasons to disregard quenching in the simulation of large scale explosions. The opinion of the candidate is that even with the enormous progress reached in the last years, quenching remains a matter of fundamental research even for problems involving laboratory scales (see e.g. Sanchez-Sanz (2012)), and that the understanding of the mechanisms yielding to extinction is far from being fully understood. Thus, the modeling of such a factor for large scale explosions has not been considered in this work.

1.7.3 Laminar burning velocity

The laminar flame speed is one of the main characteristics of combustible gases. It represents the velocity of the chemical reaction wave governed by the diffusion and the thermal conductivity of the gas. The accurate determination of the laminar burning velocity is a *condicio sine qua non* for the evaluation of the eq. (1.42). Its finding is usually based either on the analysis of direct experimental data or on the performance of calculations utilizing detailed reaction mechanisms for the description of the chemical reactions. Such mechanisms consider the chemical kinetics of each of the multiple elementary reactions with different degrees of complexity.

Major efforts have been carried out for obtaining measurements of the laminar burning velocity (Iijima and Takeno, 1986), (Koroll et al., 1993), (Dowdy et al., 1990), (Takahashi et al., 2001), (Tse et al., 2000), (Verhelst and Sierens, 2007).

Different mechanisms describing the combustion of hydrogen in air have been proposed by several research groups. Significant contributions can be attributed to Maas and Warnatz (1988), Müller et al. (2011), Li et al. (2004), O Conaire et al. (2004), Konnov (2008) and Hong et al. (2011). Some of these mechanisms have been implemented on available specialized numerical codes like INSFLA (Maas and Warnatz, 1988), (Maas and Warnatz, 1988) or Cantera (Goodwin, 2001).

Even if combustion systems are characterized by multi step chemistry, it is often necessary to characterize the basic flame properties by a one-step overall reaction. In such case, instead of looking for explicit experimental data or performing

detailed simulations, it is usually feasible to rely on the approximation of the existent verified data. The laminar flame speed in this case will depend on several variables characterizing the mixture, e.g. heat conductivity, reaction order, activation energy, temperature of the mixture, etc. (Zeldovich et al., 1985), (Yanez et al., 2012c)⁴. All those dependences can be summarized utilizing the Frank-Kamenetskii and Zeldovich (Zeldovich et al., 1985) classic formulation for the laminar flame velocity for gas mixtures with Lewis number equal to one. The formulation was extended to $Le \neq 1$ by Clavin in (Clavin, 1985) and contains some simplifying assumptions. Concretely, it was assumed that the flame front was isobaric ($M \ll 1$), that an asymptotic expansion for β , the Zeldovich number can be performed (considering $\beta \gg 1$) and that the consumption rate depends exclusively on a chemical component, the so called limiting component.

The Zeldovich number

$$\beta = E_a(T_b - T_u)/2RT_b^2, \quad (1.45)$$

where E_a is the activation energy, T_b the temperature of the burned gases, T_u the temperature of the reactants and R is the constant of the gases, compares the thickness of the pre-heating zone of flame related to the extension of its reaction zone. So that the assumption taken ($\beta \gg 1$) is equivalent to count upon an infinitely thin reaction range (compared with the preheating zone) and thus an infinitely fast reaction. Under such circumstances, and denominating l the limiting component,

$$S_L = \frac{\rho_b}{\rho_u} \sqrt{2\chi_b \nu k_0 Le^{n_l} (X_{l,u})^{n_l-1} \left(\frac{\rho_b}{W_u}\right)^{n_l-1} e^{-\frac{E}{RT_b}} \frac{\Gamma_{n_l+1}}{\beta^{n_l+1}}}, \quad (1.46)$$

where χ_b is the thermal diffusivity of the products, ν is the kinematic viscosity, k_0 the pre-exponential factor, Le the Lewis number, $X_{l,u}$ the molar fraction of the unburned limiter component, n_l the reaction order of the limiting component, W_u the molar mass of the unburned mixture, Γ the gamma function and β the Zeldovich number.

⁴Co-authored

The knowledge of the flame parameters under the assumption of one-step overall reaction is very important. The known theoretical description of the response of flames to straining, stretching and quenching (e.g. Bradley et al. (2007b)) as well as the theory of flame stability (Bychkov and Liberman, 2000) rely on this simplifying assumption. Under this hypothesis, the analytical formulations describing each corresponding phenomenon are given as a function of the flame properties. These are, among others, the laminar flame speed, the flame thickness, the overall activation energy, the adiabatic flame temperature, the Lewis number, the expansion ratio, the Zeldovich number and the Markstein number. Even if only a prediction of a worst case scenario is required (highest turbulent flame speed and combustion pressure), some of the formulations existing, e.g. (Dorofeev et al., 2001), will rely on the knowledge of the overall flame parameters. The same flame characteristics (Dorofeev et al., 2001) are used to determine the ability of the flame to propagate with nearly sonic velocity, a fact that may lead to detonation transition.

The general formulation for the dependencies of the turbulent burning velocity (eq. (1.42)) contains still another important indirect dependence on the molecular transport coefficients (Brown et al., 2011). Molecular transport will affect the flame brush thickness, extinction, flammability limits, flame stability and even flame interaction with turbulence (Lipatnikov and Chomiak, 2005). Even if the molecular transport properties are known with great accuracy since the fifties (Wilke, 1950), (Hirschfelder et al., 1954), its effect on combustion is still poorly understood. This is of special interest for hydrogen where the coefficient of the molecular diffusion in fuel and products, and the heat conductivity, are very high. Maximum care for the determination of the molecular transport coefficient should hence be taken.

1.8 H_2 safety and large scale explosions

1.8.1 General

The necessity of the prediction of large scale explosions involving H_2 is intimately linked with the safety of facilities utilizing it. Major fields in which H_2 is to be found

nowadays include its production (including electrolyzers, thermal methodologies, photocatalysis, biological methods); its storage; the energy production from it (fuel cells, internal combustion engines); its use in transportation, land, aerospace applications, etc. Hydrogen safety appears as an issue that should be addressed in each of those applications. The expansion of the activity in each of the mentioned fields increases in parallel the necessity of the assessment of risk of explosion of the procedures involved.

The studies related to the hydrogen safety in realistic environments can be divided into two major groups: the investigations surveying distribution of the gas and those analyzing its combustion. At the same time, most of the analysis can be classified, generating a matrix, taking into account the particular accident scenario addressed.

Several techniques exist for the storage of hydrogen (Hottinen, 2001). In general they can be classified as storage in gaseous or liquid form inside pressure vessels or inclusion in metal hydrides host lattices. The failure of the vessel in the first two techniques will imply, excluding catastrophic failure, the formation of a crack and the subsequent leakage (Molkov and Bragin, 2009) in form of a jet (Molkov et al., 2009). The formation of jets arising from small cracks has been studied by Xiao et al. (2011) who investigated the dynamic blow-down process of a high pressure gaseous hydrogen reservoir. Jets emerging from larger cracks have been experimentally analyzed by Royle and Willoughby (2011), Brennan et al. (2009b) while the formation of the resulting burnable hydrogen-air cloud was studied by Ramamurthi et al. (2009), Makarov and Molkov (2010).

The ensuing releases can be classified, far away of the discharge point, as *plumes* if they are driven by buoyancy and proper jets if the momentum is predominant (Chen and Rodi, 1980). The latter have been analyzed by Hourri et al. (2011) and Veser et al. (2011) while studies about the plumes were undertaken by Chernyavsky et al. (2009), Fardisi and Karim (2009), Sanchez-Sanz et al. (2010). As a mitigation measure against unintended releases of hydrogen in form of jets, the construction of contention barriers appears as a convincing methodology. Investigations considering the interaction between jets and walls have been performed by Houf and

his co-workers (Houf et al., 2011), (Houf et al., 2010), (Schefer et al., 2009) and (Houf et al., 2009) with the final aim of finding some criteria for the dimensioning of the barriers in order to attain an effective contention of the release.

Hydrogen releases can appear in confined, partially confined and open environments (García et al., 2010)⁵. In obstructed, confined and/or partially confined spaces, the pressure loads arising from an eventual explosion result to be larger. Therefore, confined environments have received a special attention in recent years. In a closed space, due to buoyancy, a hydrogen release tends to stratify creating areas with high degree of concentration. The effects of the buoyancy on the hydrogen distribution have been recently studied by Prasad et al. (2011), Matsuura et al. (2008), Lacome et al. (2011), Cariteau et al. (2011b), Schefer et al. (2008), Houf and Schefer (2008), Matsuura (2009), Venetsanos et al. (2011) with the common aim of analyzing the potential for deflagration associated with the release.

An approach to minimize the hydrogen accumulation, thus limiting the risk of a potential explosion, consists on carrying out the ventilation of the space where a release has appeared (Brennan et al., 2009a)⁵, (Brennan et al., 2011)⁵. Two techniques seem to be possible: natural and forced ventilation. Assessments of the effectiveness of natural ventilation as a passive measure for the reduction of hydrogen concentrations were performed by Barley and Gawlik (2009) and Prasad et al. (2010) while analysis of the effect of forced ventilation can be found in (Papanikolaou et al., 2011) and (Matsuura et al., 2010).

Some confined configurations have attracted much attention due to the significance of the potential hazard for the public. Those configurations are the interior of a vehicle, a garage and a transportation tunnel.

The distribution of hydrogen leakage into the interior in an automobile has been studied experimentally by Ekoto et al. (2011) and numerically by Liu and Schreiber (2008). More studies have been performed into this field, concretely in combustion, but due to confidentiality reasons they cannot be found in the literature. For the vehicle garages, experimental studies including hydrogen stratification, the effect of the ventilation and the required sizes of the openings can be

⁵Co-authored by the author of this dissertation

found in the work undertaken by Merilo et al. (2011), Cariteau et al. (2011a) and Gupta et al. (2009) while numerical analysis of the same matter have been carried out by Pitts et al. (2012), Papanikolaou et al. (2010), Saffers et al. (2011) and Venetsanos et al. (2009). Regarding the tunnels, releases from the vehicles and the subsequent formation of burnable clouds have been numerically investigated by Houf et al. (2012), Middha and Hansen (2009) while explosions in an scaled tunnel obtained from a premixed gas clouds was experimentally investigated by Groethe et al. (2007) and subsequently numerically assessed by Baraldi et al. (2009) and Molkov et al. (2008a).

Due to buoyancy, hydrogen discharges and explosions in open spaces (Molkov et al., 2006b) have received in recent years less attention than those occurring in closed environments. Nevertheless, it is possible to find information referred to the calculation of the safety distances (Dorofeev, 2007). Among the accident scenarios happening in open spaces, hydrogen refueling station appears as the most significant one. The requirement for a high level of safeguards and integrity due to the high amount of hydrogen stored, location inside populated areas and strong interaction with the public represents an important security challenge. Leaks in dispensers and subsequent jet formation inside the dispensing area has been analyzed by Shirvill et al. (2012) and Kikukawa (2008) to evaluate the accumulation of hydrogen under the canopy of the station. Experimental studies on hydrogen explosions in a model of a station have been carried out by Tanaka et al. (2007) with the aim of investigating the hydrogen outflow, dispersion and subsequent explosion behavior. Several numerical simulations of accidents involving combustion have been recently reported. Wen et al. (2010) studied the release in form of a jet and its ignition in the refueling environment while Makarov et al. (2009)⁶ analyzed the worst case of an explosion of a pre-mixed stoichiometric cloud. Additionally, separation distances in this particular environment were studied by LaChance (2009) while risk assessment was carried out by Casamirra et al. (2009) and Kikukawa et al. (2009).

As a chapter appart we may consider the detonation (Fickett and Davis, 1979)

⁶Co-authored by the author of this thesis

that should be considered the most dangerous combustion regime from the point of view of the overpressures that can be reached. During the last decades numerous studies, e.g., (Lee, 2008), (Shepherd, 2009), (Williams et al., 1996) have been dedicated to this matter. As a consequence, a high degree of physical knowledge of the phenomenon has been achieved. As detonation is usually considered as a worst case scenario in Hydrogen safety, the importance of the reliability of the simulation is particularly high. Therefore, detailed comparisons of the simulations against large scale experiments have been performed in tubes (Oran et al., 1992), (Redlinger, 2008) and against the *Rocket Strike tube* (RUT by its initials in Russian) facility experiments (Yanez et al., 2011b)⁷, (Zbikowski et al., 2010).

1.8.2 H_2 safety and combustion for nuclear power plants

Still hydrogen safety has a major domain that must be reviewed. In nuclear power plants, severe accidents can cause the generation of large amounts of hydrogen (Abou-Rjeily et al., 2011) whose deflagration can endanger the integrity of the containment. The early degradation of the core implies the generation of hydrogen by oxidation of the zirconium cladding with water steam at high temperatures and its subsequent release inside the containment building. In a major accident, during the subsequent phase, the interaction of the molten core with the concrete at high temperature produces the decomposition of the latter generating water and carbon dioxide. The gases released penetrate in the corium to generate carbon monoxide and, by oxidation of the metals inside the corium, hydrogen. Besides, the radiolysis of water, which occurs both in normal operation and accident conditions involves the decomposition of water molecules by radiation with result of production of hydrogen and oxygen in stoichiometric proportion.

Activities related to hydrogen safety for nuclear power plants are promoted by the International Atomic Energy Agency and the Nuclear Energy Agency. An excellent review of the state of the art concerning distribution and combustion of hydrogen for nuclear reactor safety has been sponsored by NEA (Breitung et al.,

⁷Co-authored article

1999). Since the appearance of this report, the NEA activity in this field has been centered in the ISP-49 program and the *Computational fluid dynamics for nuclear reactor safety* conferences, see e.g. (Yanez et al., 2010b)⁸.

Due to the non-scalability of the combustion and the big volume of the containment, and also because of the high importance of the results obtained, validation of the numerical codes utilized for the analysis is a very important issue for nuclear safety (Breitung et al., 2005), (Baraldi et al., 2007) and (Visser et al., 2012). Dispersion of hydrogen inside the containment can be found in (Kudriakov et al., 2008) and (Prabhudharwadkar et al., 2011c) while its subsequent calculations of combustion providing the pressure loads suffered by the containment building can be found in (Dimmelmeier et al., 2012), (Manninen et al., 2002), (Redlinger, 2008), (Yanez et al., 2012a)⁹.

A remaining thematic of major interest for hydrogen safety inside the nuclear environment are the mitigation measures in case of severe accidents. The reduction of hydrogen concentration from the containment atmosphere during an accident can be achieved through the use of passive catalytic recombiners. The detailed numerical analysis of the operation and performance assessment of catalytic recombiners can be found in e.g. (Prabhudharwadkar et al., 2011a), (Prabhudharwadkar et al., 2011b) and (Heitsch, 2000). The simulation of the recombiners utilization in the atmosphere generated in the containment was performed by Royl et al. (2006).

1.9 Critical considerations of the status of the modeling

From this state of the art, it has become clear that, for large scale calculations, the utilization of a turbulent model is a necessity. It is the opinion of the candidate that selection between the RANS and LES methodologies depends exclusively on the particular characteristics of the problem. LES would represent the most desirable

⁸Co-authored article

⁹Co-authored article

methodology while for those problems in which the resolution requirements will not be fulfilled, RANS methodologies should be utilized.

It is possible to assess the limitations of RANS methodologies taking into account the workhorse of this methodology, the $k - \epsilon$ method. We may now review some of them. $k - \epsilon$ assumes that the anisotropy tensor is aligned with mean of strain tensor. This extreme is reported not to occur even in simple flows (homogeneous shear flow (Pope, 2000)). As a consequence, Reynolds stress anisotropies are non-accurately resolved. Moreover, the model provides a wrong value of the von Kármán constant in the log-law region of the boundary layer. Thus, a set of modifications of this model in the regions close to the walls is necessary and can be found in the literature (Rodi and Mansour, 1993). Furthermore, $k - \epsilon$ is reported not to take into account intermittency. The values of the constant selected as a standard represent a compromise. Adjustment of the coefficients of the model may provide an improvement of the solution for every particular flow (Jimenez, 2003). Besides $k - \epsilon$ model was not intended to deal with transient flows. The initial values of turbulent intensity and dissipation should be fixed so that their effect on the transient phenomena will be negligible or at least minimal. Even higher limitations arise for this model when it is applied to reactive flows. These concerns apply specifically to the effects of dilatation on the turbulence field due to chemical reactions which has been extensively discussed in references (Chomiak and J.R., 1995), (Bray, 1996), (Grimsmo, 1991).

Concerning LES, the major drawback lays on the own definition of the methodology, which requires that large eddies should be resolved, posing important restrictions for the applicability of the model close to walls (Frölich, 2006). Certainly, in the boundary layers the typical eddy size descends significantly increasing the cost of use. Thus, it must be foreseen that expenditure of time and resources is significantly higher in LES than in RANS calculations (Pope, 2000).

The hybrid models, although they represent an interesting compromise between the two main methodologies discussed are still in an early stage of evolution and, in the opinion of the candidate, some time is still necessary for the maturity of these methodologies.

As far as combustion is concerned, we may mention that classic combustion models (Eddy dissipation model, Eddy break up) are based on intuitive, or even empirical, arguments and are obtained for modeling combustion events based on the asymptotic assumption of chemistry being infinitely fast. The behavior of the models fulfilling such assumptions can be summarized under the motto *mixed is burn* which clearly illustrates the validity domain of such assumption, namely very reactive mixtures inside an environment with strong turbulence (Peters, 2000). These severe shortcomings are shared by the Bray-Moss-Libby model and was the reason of the development culminating into the Coherent Flame Model approach.

The Coherent Flame Model shares the limitations of most of the models not based on *turbulent flame velocity* methodologies. Assumptions performed in the derivation of the modeling of the non-closed terms restrict its validity to the limited sizes, 10 to 100 times the laboratory scale (Driscoll, 2008). That implies that this methodology is normally applied to small combustion devices like burners.

An accurate prediction of mean chemical consumption rates under presumed pdf approach is based on a good prediction of the required second-order statistical moments. The calculation of the variances requires the solution of one transport equation for each of these magnitudes that in turn contain non-closed terms that must be modeled. Different approaches have been developed to try to close them, including the usual gradient-type approximation, yielding only partial success (Gerlinger, 2003) comprehending the tries performed by the author.

Although the level set approach enjoys multiple advantages (Peters, 2000) it requires computation effort focused on resolving the interface structure (e.g. equation (1.39) requires the calculation of the curvature of the interface). This is clearly in contradiction with the necessities of large scales calculations in which the interfaces are necessarily poorly resolved.

Limitations of the extended Zimont model for the large scale calculations arise from its own design. In this model, the flame brush thickness is controlled by the turbulent diffusion. In the formulation generally adopted, see equation (1.41), the mathematical expression yields a growing mean flame brush thickness. This characteristic, which was desired by Zimont, limits the applicability of the model for

coarse meshes. The minimal thickness of the calculated brush, a calculation cell, strongly overestimates, by several orders of magnitude, a realistic assessment of the thickness of the brush. A constantly increasing brush, even at low rate, inevitably evolves to thicknesses of several calculation cells, which for large scale calculation may represent several meters, producing an unacceptable overestimation of this magnitude. Still, it is clear that the simplification of the problem achieved through the use of *turbulent flame speed* approaches offers a big potential for the modeling and should be adopted in the opinion of the candidate.

Taking into account the previous critical rationale the goals of this thesis have been set in detail in chapter 2. To achieve the objectives set, the work was organized as orderly and briefly sketched in chapter 3. Taking into account the review made in this Introduction, the focus was initially set in *Combustion Modeling* (Chapter 4) where the modeling of *Flame Propagation*, *Laminar Burning Velocity* and *Turbulent Burning Velocity* are discussed in detail. The results achieved are complemented with additional modeling connected with some particular experiments in chapter 5. Between other topics, flame instabilities are modeled in this chapter. Finally, the model set up is then applied to large scale significant problems in chapter 6. This set of applications is complemented with an analysis of the explosion that occurred in the Fukushima Power Plant during its unfortunate accident.

Chapter 2

OBJECTIVES

The demand for a hydrogen combustion model capable of producing accurate results in calculations performed with coarse resolution is certain taking into account the large number of applications in which hydrogen safety assessments are required.

The main purpose of this work is to improve the modeling of the explosion processes in realistic large scale hydrogen combustion events, which may cause personal and material damage, obtaining reliable, accurate results for practical applications. The targeted application branches that will benefit from the applications of this model will include the whole future hydrogen economy, transportation, and nuclear safety both in fusion (ITER) and fission technology.

This global objective will be pursued in this thesis through other more specific:

1. The creation of a combustion model which is able to overcome the existing deficiencies of the available ones for large scales implying low resolution numerical solutions.
 - (a) Following the rationale developed in the introduction, the approach should be based in the *turbulent flame speed* methodology and ought to utilize its significant potential for simplification .
 - (b) The model should utilize a heuristic algorithm to maintain the thick-

ness of the flame brush under control, thus overcoming the deficiencies of the Zimont model (Zimont, 1977; Lipatnikov and Chomiak, 2002).

In the frames of *turbulent flame speed* methodology the emphasis of the development of the approach should lay on the accurate determination of the burning velocity.

2. A certain number of flame velocity correlations are available for the determination of the turbulent burning velocity in the literature. For the selection of the most suitable they have to be ranked.
3. The turbulent burning velocity strongly depends on the laminar flame velocity. This makes the accurate determination of the laminar flame velocity necessary in the whole domain conditions of interest for the calculations. Two aspects will be contemplated
 - (a) The development of a laminar burning velocity formula which is able to describe the simultaneous influence of the equivalence ratio, temperature, steam dilution and pressure on the laminar burning velocity is necessary. Such correlation should be numerically efficient.
 - (b) Dependence on the molecular transport coefficients appears explicitly in the formulations for the turbulent and laminar burning velocity. The efficient calculation of such variables utilizing the predictions of the kinetic theory of gases should be undertaken.
4. The influence of the flame instabilities is of significant importance for the development of explosions. This is of special importance when lean mixtures in which propagation regimes remain moderate are involved. The creation of a model to account for them is necessary.
 - (a) It has been proven that the acoustic-parametric instability plays a significant role in typical accidental conditions for Nuclear Safety. Thus accounting for such an instability was undertaken.

5. A validation of the model built will be undertaken. The benchmarks should comprehend several experiments, significant for the H_2 safety, and should allow to draw conclusions about the suitability and validity of the model on large scale problems.

- (a) It is our objective to carry out simulations and obtain high quality predictions in the area of transportation and nuclear safety as those are the fields in which this thematic reaches its largest importance.
- (b) As a final undertaken, we have the objective of analyzing the most and sadly famous accident happening during the last years involving hydrogen explosion. This is namely, the Fukushima-Daiichi catastrophe.

In regards of the fitting of the objectives of this thesis with those of the IMEIO doctoral program, this thesis should be understood to lay inside the *Mathematics for the engineering* topic. In this sense it is significant to underline that the objectives mentioned above are related to the development of modeling in the fields of fluid mechanics and physics of combustion. This modeling should be considered in conjunction with the solution of the set of conservation laws including the Navier-Stokes equation formulation for the analysis and numerical simulation of problems related to the industrial engineering.

Chapter 3

METHODOLOGY

The thesis is organized with respect to the objectives of Chapter 2 as follows:

1. The study a creation of a combustion model is carried out in chapter 4.
 - (a) The description of the new combustion model created by the author intended for low resolution problems which is carried out 4.2
 - (b) The description of the phenomenological correlations available in the literature for the turbulent burning velocity, which is presented in section 4.2
 - (c) The newly developed correlation for the laminar burning velocity which is able to describe the simultaneous influence of the equivalence ratio, temperature, steam dilution and pressure in this magnitude is presented in section 4.3
 - (d) The efficient determination of the molecular transport coefficients utilizing the predictions of the kinetic theory of gases is performed in section 4.10
2. Additional model development undertaken to add an extra refinement and accuracy to the methodology is carried out in Chapter 5. This concerns as-

pects of combustion that cannot be related specifically to the previous chapter because are connected with some particular experiments.

- (a) The ranking of the phenomenological correlations for the turbulent burning velocity is presented in chapter 5.2
 - (b) The modeling of the flame instabilities, and concretely the acoustic-parametric instability, is performed in section 5.3.1.
3. The application of the model created to several problems significant for the hydrogen safety and the consequent analysis of the results and comparison with the corresponding experimental data is performed in chapter 6. The model will be implemented as a part of *COM3D*, an in-house, finite differences, cartesian grid parallelized C++ research code. Utilization of a research code, instead of a commercial one, allows for whole flexibility and unrestricted creativity for the physical modeling and code development. On the other hand, the publication of the achievements will allow for implementation in commercial codes.
- (a) The simulations of explosions in a tunnel and the validation of the results obtained with experimental data are undertaken in section 6.2.
 - (b) Explosions in large containers in conditions significant for the nuclear safety are analyzed in sections, 6.3 and 6.4.
 - (c) The Fukushima Daiichi catastrophe is thoroughly studied and analyzed in Chapter 7

Chapter 4

COMBUSTION MODEL DEVELOPMENT

4.1 Introduction

A predictive, reliable and robust model for multi-dimensional simulation of large scale explosions, usually with very limited resolution, which can be applied in engineering simulations has not been yet elaborated and is strongly desirable.

In the rationale performed in previous chapters of this thesis, it has been inferred that the only viable approximation in order to solve problems where the resolution is necessarily limited is the *turbulent flame speed* methodology. It can be also mentioned that, forest fires, or wildfires, are the most extensive fire events to be usual in the nature and can be as extensive as several hundred kilometers. Thus, the coupling of a flame propagation method applying to forest fires and *turbulent flame speed* approximation could be, at least *a priori*, an appropriate modeling for large scale low resolution problems.

Maybe the most remarkable advantage of the flame speed approach is the possibility of reducing the problem of combustion modeling to the determination of the turbulent burning rate, using phenomenological knowledge for its determination.

The purpose of the KYLCOM model is to exploit this possibility to the extreme.

The KYLCOM model (Yanez et al., 2010c), as others in *flame speed* approach (see section 1.6.7.3), has two relatively independent parts: the first one is responsible for the correct evaluation of the turbulent flame speed in the current local conditions, and the second is responsible for the corresponding flame propagation in the simulated media.

The model is based on a variation of the forest fire algorithm (Chen and Bak, 1990) which is utilized to make the flame propagate with a burning speed estimated from an algebraic expression. A phenomenological expression, taking into account local temporal and spatial characteristics of the fluid such as, turbulence level, transport coefficients, other mixture properties, etc., is employed to calculate the flame velocity.

The forest fire CREBCOM algorithm (Efimenko and Dorofeev, 2001) is used to provide flame advancement mechanism in the course of time integration. CREBCOM model applications examples can be found in e.g. (Efimenko and Dorofeev, 2001), (Bielert et al., 2002a), (Bielert et al., 2002b), (Bielert et al., 2003b) and (Bielert et al., 2003a).

In this chapter, the KYLCOM model is first described, including the proposed turbulent flame velocity correlation and the flame propagation model. Second, since the laminar burning velocity is a crucial factor in the turbulent burning velocity, a specific section is dedicated to its estimation. Finally, the transport properties of gases (viscosity, collision integrals, thermal diffusivity, etc.) are discussed because their determination is itself a challenging topic and affect the definition of the laminar flame speed.

4.2 KYLCOM model outline

4.2.1 General

For the last decades, intensive efforts have been made to gain the knowledge required to predict turbulent flame velocity under different conditions. The deduced

relations take into account the influence of turbulence, integral length of turbulence, Lewis number, stretching of flame, etc. on the combustion rate. The formulations are expressed in terms of the characteristics of fresh gases and differ significantly in their complexity, set of parameters and range of applicability. A selection of the most prominent correlations is included in Table 4.1.

Table 4.1: Closures employed for the burning velocity calculation.

Designation	Closure	Ref.
Kawanabe	$S_t = S_L \left(1 + 1.25 \left(\frac{u'}{S_L} \right) \right)^{0.7}$	(Kawanabe et al., 1998)
Peters	$S_t = S_L \left(1 + \frac{0.39}{2} \frac{L \cdot S_L}{\chi} \left(\sqrt{1 + 20.5 \frac{\chi u'}{L \cdot S_L^2}} - 1 \right) \right)$	(Peters, 1999)
Bradley	$S_t = S_L \left(\sqrt{\frac{u'}{S_L}} \left(\frac{L S_L}{\chi} \right)^{\frac{1}{6}} \right)$	(Dorofeev, 2008)
Zimont	$S_t = u' \left(\frac{L S_L^2}{u' \chi} \right)$	(Zimont and Mesheriakov, 1988)
Schmid	$S_t = S_L + \frac{u'}{\sqrt{1 + \frac{1}{D a^2}}}$	(Schmid et al., 1998)
Weller	$S_t = S_L + S_L \sqrt{\frac{u'}{u' + S_L}} \left(1 - e^{-\frac{S_L t}{\tau_0 (u' + S_L)}} \right) \cdot \left(1 - e^{-\frac{t}{\tau_0}} \right) \left(\frac{u'}{S_L} \right)^{\frac{5}{6}}$	(Weller et al., 1998)
Lewis	$S_t = S_L \left(\sqrt{1 + 16 \frac{u'}{S_L}} + \left(1 - e^{-\frac{u'}{S_L}} \right) \frac{\theta - 1}{\sqrt{3}} \right)$	(Lewis and von Elbe, 1987)
Leeds	$S_{t1} = S_L + 0.96 S_L^{0.284} u'^{0.912} L^{0.196} \chi^{-0.196}$ $S_{t2} = 0.96 S_L^{0.784} u'^{0.412} L^{0.196} \chi^{-0.196}$ $S_t = \min(S_{t1}, S_{t2})$	(Bradley et al., 1992), (Arntzen, 1998)

Among the formulae in Table 4.1 a specific clarification is required by the Leeds

formula (last one of the list) with Arntzen modification¹. In Bradley et al. (1992) the correlation

$$S_{t_2} = 0.88u'(KaLe)^{-0.3}, \quad (4.1)$$

which corresponds to the formula S_{t_2} in the line corresponding to Leeds in Table 4.1 was proposed². Nevertheless, the applicability limit of such equation corresponds to relative high turbulence and thick flames, $KaLe < 38$, $Re_t/Le < 6000$ and provides not so accurate results for moderate turbulence intensities. Therefore, the model was complemented, to study moderate turbulence intensities, with a second equation the correlation of Gulder (1991),

$$S_t = S_L \left(1 + 0.7(u'/S_L)^{\frac{3}{4}} (L/\delta)^{\frac{1}{4}} \right). \quad (4.2)$$

To utilize each of the formulas in the areas where they provide better results, the condition $S_t = \min(S_{t_1}, S_{t_2})$ was given. The formula however suffered a second modification, as an alternative equivalent formulation developed by Arntzen (1998) was chosen for S_{t_1} (S_{t_1} formula in Table 4.1). This was the version utilized in the study reported in 5.2

The utilization of separated domains of turbulence intensities for different correlations was further explored by the same authors. Another version of this model is available in the literature, containing a third expression which limits the flame velocity for high levels of turbulence (Arntzen, 1998), (Skjold et al., 2006). Under this methodology, one expression will be utilized for moderate turbulence intensities, S_{t_1} , a second one for intense turbulence, S_{t_2} and a third for very intense, S_{t_3} .

¹Which is very relevant because of its popularity, as it was implemented in the FLACS code (Bakke and Hjertager, 1986)

²formula 4.1 is the formulation in function of u' , Ka , Le . Eq. S_{t_2} in table 4.1 is the same but reformulated in terms of u' , S_L , L_m and χ .

The expression reads then,

$$S_{t1} = S_L + 0.96 \cdot S_L^{0.284} u'^{0.912} L^{0.196} \chi^{-0.196}, \quad (4.3)$$

$$S_{t2} = 0.96 \cdot S_L^{0.784} u'^{0.412} L^{0.196} \chi^{-0.196}, \quad (4.4)$$

$$S_{t3} = 3.0 \cdot S_L^{1.25} L^{0.333} \chi^{-0.333}, \quad (4.5)$$

and finally are coupled with the expression,

$$S_t = \min(S_{t1}, S_{t2}, S_{t3}). \quad (4.6)$$

4.2.2 Flame propagation model: CREBCOM model

4.2.2.1 General

Once the burning velocity is has been estimated, the corresponding flame front propagation is provided by the CREBCOM method. CREBCOM model belongs to the category of Forest Fire models pioneered by Bak et al. (1990). The original CREBCOM algorithm formulation was judged unsatisfactory and the CREBCOM variation due to Efimenko and Dorofeev (2001) has been extended in this thesis to include dependence of mass consumption rate³, $\bar{\omega}$, on remaining fuel concentration, expressed as $(1 - \bar{f})$.

The method is based on the solution of a transport equation for the progress variable f , a normalized burned out mixture fraction (see section 1.6.1),

$$\frac{\partial \bar{\rho} \bar{f}}{\partial t} + \frac{\partial \bar{\rho} u_i \bar{f}}{\partial x_i} = \frac{\partial}{\partial x_i} \left(\bar{\rho} \bar{D}_t \frac{\partial \bar{f}}{\partial x_i} \right) + \bar{\rho} \bar{\omega}. \quad (4.7)$$

The main characteristic of this model is that a cell is supposed to start burning when one or more of the surrounding cells is already consumed above a threshold.

As discussed in section 1.6.1, the progress variable of the reaction is equal to 0 for the fresh mixtures and to 1 for the completed reaction.

As a measure of the burnout in the CREBCOM algorithm, the following control

³The formulation in terms of the progress variable, f , presented in section 1.6.1 is utilized here

parameter $F_{i,j,k}$ is used

$$F_{i,j,k} = \bar{f}_{i+1,j,k}^2 + \bar{f}_{i-1,j,k}^2 + \bar{f}_{i,j+1,k}^2 + \bar{f}_{i,j-1,k}^2 + \bar{f}_{i,j,k+1}^2 + \bar{f}_{i,j,k-1}^2 - 3\bar{f}_{i,j,k}^2. \quad (4.8)$$

If the value of $F_{i,j,k}$ for the current cell (i, j, k) exceeds the critical quantity of 0.25 a cell is considered to be burning, otherwise it remains unignited. The chemical reaction rate considered under the CREBCOM methodology is

$$\bar{\omega}_{i,j,k} = \begin{cases} \frac{S_{i,j,k}}{\Delta x} (1 - \bar{f}_{i,j,k}) & F_{i,j,k} > \left(\frac{1}{2}\right)^2 \\ 0 & F_{i,j,k} < \left(\frac{1}{2}\right)^2 \end{cases}, \quad (4.9)$$

where Δx is the cell size, and S a magnitude related to the propagation velocity, to be treated in detail, and the expansion of the gases θ .

The $(1 - \bar{f}_{i,j,k})$ dependence in the reaction rate was included into the original CREBCOM formulation⁴ (Efimenko and Dorofeev, 2001) to provide the softer convergence to the equilibrium composition represented by the eq. (4.9). The thickness of the flame is approximately of two cells both in original and modified CREBCOM models (respectively considering or not the dependence on $(1 - \bar{f})$ in 4.9). One important limitation of this proposed model is that in its present form, the applicability of the algorithm is restricted to structured cubic grids.

It is now necessary to make a comment on the discrete nature of the control parameter eq. (4.8) and the model equations (4.9) compared with the transport equation (4.7) which is continuous. The model consists of a regular grid of cells in three dimensions. Each of the cells can be in a infinite number of states $f \in [0, 1]$. In time $t + 1$, the cells change their status according to the fixed rule described by eq. (4.8) and (4.9) that determines the new state of each cell in terms of the current

⁴In its original formulation

$$\bar{\omega}_{i,j,k} = \begin{cases} \frac{S}{\Delta x} & F_{i,j,k} > \left(\frac{1}{2}\right)^2 \\ 0 & F_{i,j,k} < \left(\frac{1}{2}\right)^2 \end{cases},$$

with the speed parameter S a constant in the whole calculation domain and time that was adjusted by comparison with experiments (Efimenko and Dorofeev, 2001).

state of the cell and the states of the cells in its neighborhood. The rule for updating the state of cells is the same for each cell and does not change over time, and is applied to the whole grid simultaneously (synchronously). This is the definition of a *non-discrete cellular automaton*⁵, see e.g. (Alonso-Sanz, 2009). With the cells interactions considered in eq. (4.8) the neighborhood considered is of *Moore* type. Cellular Automaton are a vast topic that lies out of the scope of this thesis. Interested readers are referred to the *ambitious* work of Wolfram (2002) and for chemical applications to Kier et al. (2014). Still, it is necessary to note that the somehow non-rigorous mixture of discrete and continuous formulations complicate the notation (absence or not of indexes i, j, k).

4.2.2.2 One dimensional case

The way in which the algorithm operates will be easily understood with the help of a simple example considering a planar flame moving in the direction of the X axis. A cell with coordinates (i, j, k) is about to start burning but still $f_{i,j,k} = 0$. In the neighboring cells the values of the progress variable are

$$\bar{f}_{i,j,k} = \bar{f}_{i,j,k+1} = \bar{f}_{i,j,k-1} = \bar{f}_{i,j+1,k} = \bar{f}_{i,j-1,k} = 0, \quad \bar{f}_{i-1,j,k} \neq 0. \quad (4.10)$$

The burning rate in eq. (4.9) simplifies to

$$\bar{\omega}_{i,j,k} = \frac{S_{i,j,k}}{\Delta x} (1 - \bar{f}_{i,j,k}), \quad (4.11)$$

if $\bar{f}_{i-1,j,k} > \frac{1}{2}$ and zero otherwise. The criteria can be then summarized in one dimension stating that a cell starts burning when the previous cell has already burnt half of the fuel.

⁵The rigorous definition of a cellular automata requires the possible status of the values of variable f to be discrete too.

Once the cell (i, j, k) starts consuming⁶

$$\frac{d\bar{f}}{dt} = \frac{S}{\Delta x} (1 - \bar{f}). \quad (4.12)$$

Operating,

$$\frac{d\bar{f}}{1 - \bar{f}} = \frac{S}{\Delta x} dt, \quad (4.13)$$

and integrating

$$-\ln(1 - \bar{f}) \Big|_0^{\bar{f}} = \frac{S}{\Delta x} t. \quad (4.14)$$

Expressing it in exponential terms,

$$1 - \bar{f} = \exp\left(\frac{-t \cdot S}{\Delta x}\right). \quad (4.15)$$

And thus, the time dependent solution of the progress variable (recovering the i, j, k indexing) is

$$\bar{f}_{(i,j,k)}(t) = 1 - \exp\left(\frac{-t \cdot S_{(i,j,k)}}{\Delta x}\right). \quad (4.16)$$

The time required to burn out half of the reactants contained in the considered volume, τ , necessary to verify the criterion represented by eq. (4.8) is equal to

$$\tau_{i,j,k} = \ln(2) \frac{\Delta x}{S_{i,j,k}}, \quad (4.17)$$

moment in which the flame propagates to the adjacent cell of coordinates $(i + 1, j, k)$. Thus, the flame speed relatively to the gas motion induced by the method is equal to

$$\frac{\Delta x}{\tau_{i,j,k}} = \frac{S_{i,j,k}}{\ln(2)}. \quad (4.18)$$

The introduction of the calculation cell size in the equation (4.9) makes the propagation velocity obtained with the algorithm independent on grid size.

It is important to underline that, contrary to the Zimont model, under the KYL-COM methodology, the flame brush thickness is independent of time scales. In

⁶The diffusive fluxes are now disregarded. The relative motion of the flame to the moving flow is now the focus of the interest

absence of motion (convection) the previous rationale have shown that the value $(1 - f)$ reduces in $\frac{1}{2}$ in the first consumption cell. This induces a constant flame brush thickness. For gradient method, see eq. (1.41), there exists no internal mechanism to reduce the thickness with time.

The balance equation (4.7) provides for the convection of the progress variable with the fluid motion. The turbulent diffusion included in the model provides also transport due to the turbulence but does not influence the flame brush, which is exclusively controlled by the reaction rate. The CREBCOM algorithm provides a spherical flame propagation, for every cell, with respect to the unburned mixture.

4.2.2.3 Propagation velocity

It is still necessary to properly define the dependencies of S . Let us consider a planar flame in a reference system attached to the flame. On one side of the flame there exists exclusively fresh mixture with velocity S_t relative to the flame. On the other side of the flame, only burned gas with velocity equal to θS_t is present. This means that the motion suffers an enhancement of a factor θ through the flame.

If for simplicity the auxiliary variable $\zeta = \theta - 1$ is considered and the assumption, valid for slow flames (Catlin and Lindstedt, 1991),

$$\rho = \frac{\rho_0}{1 + \zeta f} \quad (4.19)$$

and

$$V = V_0(1 + \zeta f) \quad (4.20)$$

is made, the density and velocity are expressed as functions of the fresh status and the progress of the reaction.

In the next sections, 4.2.2.3.1, 4.2.2.3.2 and 4.2.2.3.4, we will make use of previous expressions to obtain approximations of the form of the dependence $S = S(\theta, S_t)$, and finally we will estimate the final functional from numerical experiments

4.2.2.3.1 First approximation method

With the assumptions contained in eq. (4.19) and (4.20), Table 4.2 can be constructed to illustrate the variables evolution across the flame. Certainly, it is applied that $V_0 \approx S_0$,

Table 4.2: Variables in the two first cells after flame arrival.

	Cell i	Cell i+1	Cell i+2
Progress variable	$f_i \approx 0$	$0 < f_{i+1} < 0.5$	$0.5 < f_{i+2} < 1$
Velocity	$V_i \approx S_0$	$V_{i+1} \approx (1 + \zeta f_{i+1}) S_0$	$V_{i+2} \approx (1 + \zeta f_{i+2}) S_0$
Density	$\rho_i \approx \rho_i$	$\rho_{i+1} \approx \frac{\rho_0}{(1 + \zeta f_{i+1})}$	$\rho_{i+2} \approx \frac{\rho_0}{(1 + \zeta f_{i+2})}$

In stationary state, the net flux of fresh mixture $\approx (f_{i+1} - f_i) V_{i+1} \rho_{i+1}$ should be equal to chemical consumption rate $\Delta x \omega_{i+1} \rho_{i+1}$. The numerical approximation of an advective flux depends on implementation details, particularly on the hydrodynamic solver. However, it is possible to try to estimate this flux in a simple case.

Table 4.2 and the approximate balance of masses $(f_{i+1} - f_i) V_{i+1} \rho_{i+1} \approx \Delta x \omega_{i+1} \rho_{i+1}$ allows formulating the evolution of the flame across the flame as a set of equations

$$\begin{aligned}
 S \frac{1 - f_1}{1 + \zeta f_1} &= (f_1 - f_0) S_t, \\
 S \frac{1 - f_2}{1 + \zeta f_2} &= (f_2 - f_1) S_t, \\
 &\vdots \\
 S \frac{1 - f_{i+1}}{1 + \zeta f_{i+1}} &= (f_{i+1} - f_i) S_t.
 \end{aligned} \tag{4.21}$$

Let study the cell $i + 1$ considering that it start to burn. This immediately means

$f_i = 0$ and f_{i+1} . Let call $i = 0$ for simplicity. We have thus,

$$S \frac{1-f_1}{1+\zeta f_1} = (f_1) S_t, \quad (4.22)$$

$$S \frac{1-0.5}{1+\zeta 0.5} = (0.5-f_1) S_t, \quad (4.23)$$

From the last equations, we may deduce immediately that

$$f_1 = \frac{1}{2} - \frac{1}{\theta+1} \frac{S}{S_t}. \quad (4.24)$$

and eliminating f_1 ,

$$S = \frac{1}{8} \left(-(1+3\theta) + \sqrt{(1+3\theta)^2 + 4(2\theta+2)} \right) (\theta+1) S_t \quad (4.25)$$

Last expression may be rewritten supposing that θ is big (for H_2 -air mixtures is of the order of 6) as,

$$\begin{aligned} S &= \frac{1}{8} (\theta+1)(1+3\theta) \left(-1 + \sqrt{1 + \frac{4(2\theta+2)}{(1+3\theta)^2}} \right) S_t \approx \\ &\approx \frac{1}{8} (\theta+1)(1+3\theta) \frac{8}{2} \frac{(\theta+1)}{(1+3\theta)^2} S_t = \frac{1}{2} \frac{(\theta+1)^2}{1+3\theta} S_t \approx \\ &\approx \left(\frac{1}{6} \theta + \frac{7}{18} \right) S_t \end{aligned} \quad (4.26)$$

4.2.2.3.2 Second approximation method

Let estimate a second approximation for the relation $S = S(S_t, \theta)$ starting from the equation (4.7). As this section is just a digression on the form of the functional $S = S(\theta, S_t)$ for simplicity the over-bars are dropped. For the domain for which we have already combustion eq. (4.7) reads

$$\frac{\partial \rho f}{\partial t} + \frac{\partial \rho u_i f}{\partial x_i} = \frac{\partial}{\partial x_i} \left(\rho D_t \frac{\partial f}{\partial x_i} \right) + \rho \frac{S}{\Delta x} (1-f). \quad (4.27)$$

Let suppose it is verified that $D_t \ll S\Delta x$ what is always true for big enough Δx .

Thus,

$$\frac{\partial \rho f}{\partial t} + \frac{\partial \rho u_i f}{\partial x_i} = \rho \frac{S}{\Delta x} (1-f). \quad (4.28)$$

and let us look for an stationary solution $\partial \bar{\rho} f / \partial t = 0$. Utilizing the continuity equation in 1D and dividing by $\bar{\rho}$,

$$u \frac{df}{dx} = \frac{S}{\Delta x} (1-f). \quad (4.29)$$

Recovering from table 4.2, $u = S_t(1 + \zeta f)$ and operating $u = (\theta - (\theta - 1)(1 - f))S_t$.

Substituting,

$$\frac{df}{dx} = \frac{S}{\Delta x(\theta - (\theta - 1)(1 - f))S_t} (1-f). \quad (4.30)$$

We are going to integrate this expression. Let define $h = 1 - f$. Then, $df = dx = -dh/dx$ and thus,

$$\frac{dh}{dx} = \frac{S}{\Delta x S_t} \frac{h}{\theta - (\theta - 1)h}. \quad (4.31)$$

When the cell $i + 1$ starts to burn, in its right border at $x = 0$ where the mixture is fresh $f = 0$ and thus $h = 1$. On the cell $i + 2$, as cell $i + 1$ is starting to burn the average value of the progress variable is $\bar{f} = 1/2$. So for $x = \Delta x$ we may suppose that $f \approx 1/2$. Operating

$$\frac{\theta - (\theta - 1)h}{h} dh = \frac{S}{\Delta x S_t} dx, \quad (4.32)$$

which can be immediately integrated to give,

$$S = \left[\left(\ln(2) - \frac{1}{2} \right) \theta + \frac{1}{2} \right] S_t. \quad (4.33)$$

4.2.2.3.3 Relation between the second approximation method and the flame brush thickness

We may now consider this last results in relation with the thickness of the flame

brush. Let us integrate (4.32),

$$\int_1^h \frac{\theta - (\theta - 1)h}{h} dh = \int_0^x \frac{S}{\Delta x S_t} dx, \quad (4.34)$$

which after operating and recovering f formulation results,

$$\frac{S}{S_t \theta} \frac{x}{\Delta x} = \ln(1 - f) - \frac{\theta - 1}{\theta} f \quad (4.35)$$

The first fraction transforms to,

$$\frac{S}{S_t \theta} = \frac{\left(\ln(2) - \frac{1}{2}\right)\theta + \frac{1}{2}}{\theta} \quad (4.36)$$

which is a variable depending only on the expansion ratio, a function of the gaseous mixture. Let define the variable, \tilde{x} as a dimensionless re-scaled coordinate,

$$\tilde{x} = \frac{\left(\ln(2) - \frac{1}{2}\right)\theta + \frac{1}{2}}{\theta} \frac{x}{\Delta x}. \quad (4.37)$$

In this new variable,

$$\tilde{x} = \ln(1 - f) - \frac{\theta - 1}{\theta} f, \quad (4.38)$$

that can be immediately plotted to deliver,

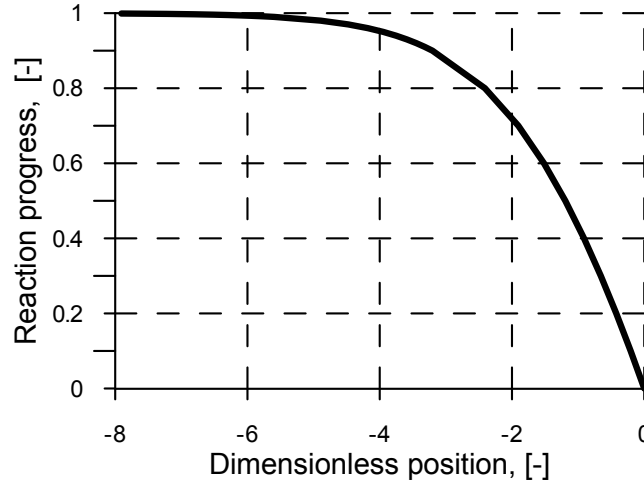


Figure 4.1: Progress of the reaction as a function of the dimensionless coordinate.

In dimensional, non-scaled coordinates, the flame thickness just elongates or contracts as a function of θ and Δx .

We may reformulate the condition we utilize to express the indifference from the diffusion, $D_t \ll S\Delta x$, dividing in both sides by $(\Delta x)^2$ and multiplying by the numerical integration time Δt . Doing this we obtain,

$$\frac{\Delta t D_t}{(\Delta x)^2} \ll \left[\left(\ln(2) - \frac{1}{2} \right) \theta + \frac{1}{2} \right] \frac{S_t \Delta t}{\Delta x}, \quad (4.39)$$

so that the *Diffusion number* is much smaller than the *Courant number* based on the Turbulent burning velocity.

4.2.2.3.4 Realistic estimation of the dependence $S = S(\theta, S_t)$

Due to numerical errors associated, e.g., the non-sharp interface between reactants and products, the S dependence has to be individually calibrated for each implementation. The results of the numerical experiments performed for a matrix of mixture concentrations, temperatures and pressures, allow re-writing the previ-

ous expression as a linear function of the expansion ratio

$$S = (A \cdot \theta + B) S_t. \quad (4.40)$$

The values, $A = 0.243$ and $B = 0.375$ resulted from one dimensional testing. Different shock capturing hydrodynamic solvers (TVD, AUSM+) produce negligible variations for the value of the constants.

The relations selected closure models included in Table 4.1 are functions of fresh gases characteristics. Therefore, such formulae, and thus S must not be recalculated during and after the flame arrival. For cells starting to burn, the last S value is stored and transported, through the flame thickness, with the equation

$$\frac{\partial \rho S}{\partial t} + \frac{\partial \rho u_i S}{\partial x_i} = 0, \quad (4.41)$$

to take into account the motion of the mixture. The meaning of the equation (4.41) can be better understood rewriting it, with the help of the continuity equation as

$$\frac{\partial S}{\partial t} + u_i \frac{\partial S}{\partial x_i} = 0, \quad (4.42)$$

which is the derivative along a flow-line. The variable S which is a function of time and position should be transported across the thickness of the flame as the magnitude is dependent on fresh conditions only (its recalculation inside the flame at elevated temperatures will strongly deviate from realistic values).

The boundary between burnt and unburnt species has been established in one percent of products present in the mixture. The only area in which the transported S is significant is just the flame thickness. For this reason, the candidate thinks that the diffusion of ρS is a secondary process and that can be neglected.

4.2.3 Limitations of the KYLCOM model

In its present status of development, the KYLCOM model can be applied to combustion problems in which the combustion processes are mainly driven by turbu-

lent flow. Naturally, the model is limited by the assumptions made in used turbulent flame speed correlations (see refs. shown in Table 4.1). Particularly, an intrinsic dependence on the validity of turbulence Reynolds stresses model exists, as the formulae rely on an accurate description of the turbulence (its intensity, integral length, decay, etc.).

It should be emphasized that the current model does not allow for the effects of flame wrinkling due to instabilities. Therefore, noticeable under-prediction of flame velocity might be expected in cases in which such processes are significant. Further modeling in this thematic will be carried out in section 5.3.9. Additionally, the capabilities of the model to correctly predict the transition from laminar to turbulent regime will depend on the ability of the turbulence model to do so.

The results due to Bradley et al. (2008) or Bradley et al. (2007b) reveal that the turbulent burning velocity increases with a growth of the turbulent flame velocity until it attains a maximum. Thereafter, it decreases as flame quenching starts to dominate the combustion process. The dependence of flame velocity on turbulence intensity for such flames is complex and is mostly determined by the strained Markstein number (for the definition of this magnitude and further details, refer to (Bradley et al., 2008)). In the phenomenological correlations shown in Table 4.1 an augment in turbulent speed always enhances the turbulent burning velocity. Therefore, spurious flame accelerations may result from intense and unrealistic feedback between turbulence generation and products expansion.

The modeling of the quenching phenomenon in low resolution problems taking into account the degree of development of the experimental investigations (see the Leeds University (Bradley et al., 2008), the leading group in this matter) would lead to unreliable models, taking into account the opinion of the candidate. Thus, the quenching phenomena will not be included into the actual version of KYLCOM model centering our attention in the modeling of other phenomena, see Chapter 5.

4.3 Calculation of the laminar burning velocity

4.3.1 General

It was already mentioned, see section 1.6.7.3, that under the *flame velocity modeling* trend (see e.g. (Lipatnikov and Chomiak, 2002)), to which KYLCOM model belongs, the emphasis of the methodology is given to the propagation velocity of the flame. The turbulent burning velocity, see the digression in section 1.7 and the formulations contained in Table 4.1 has a strong dependence on the laminar burning velocity, which is a key characteristic of the combustion processes and should be calculated for each numerical cell and time step. The direct application of a detailed chemistry to determine the laminar burning velocity coupling a combustion code with a specialized library, like *Cantera* capable of such calculations, is in the opinion of the candidate unpractical. It must be taken into account that, under the modeling adopted, the calculation of the laminar burning velocity must be carried out for each numerical cell and time. The numerical overhead resulting from this is overwhelming, as the evaluation of the laminar burning velocity is in many cases not fast (seconds or even minutes, depending of the concentration and conditions). Tabulation or creation of a model for this variable is then necessary.

The laminar burning velocity, to which the last part of the introduction section 1.7 is devoted, is in general a function of the temperature, pressure and the chemical species concentrations.

For convenience, the composition of the fuel is going to be characterized by the fuel equivalence ratio, that can be written as a function of the mass fractions,

$$\varphi = \frac{\frac{y_{fuel}}{y_{air}}}{\frac{y_{fuel,stoichiometric}}{y_{air,stoichiometric}}}. \quad (4.43)$$

This variable intuitively divides the fuel concentration domain into lean, $\varphi < 1$, rich, $\varphi > 1$ and stoichiometric, $\varphi = 1$, regions.

The laminar flame speed dependence on pressure, temperature and fuel com-

position in hydrogen-air-steam mixtures is mostly characterized by the power function,

$$S_L(\varphi, T, p) = S_{L,0}(\varphi) \cdot (T/T_0)^{\alpha_t} (p/p_0)^{\beta_t}. \quad (4.44)$$

4.3.2 Laminar burning velocity: temperature dependence

Let us explore the temperature and pressure dependence of the laminar burning velocity. A rise of the temperature of the reactants enhances the reaction rate. Iijima and Takeno (1986) found that the exponent α_t depends on the equivalence ratio, ϕ , and proposed a formula, deduced from their experimental data, which is valid between 291 K and 500 K. Hu et al. (2009) observed both in measurements and in calculations with the CHEMKIN code (Kee et al., 1989), that the exponent α_t depends on temperature in a wide range. Koroll et al. (1993) extended the correlation (4.44) including the variation of the thermal conductivity λ , obtaining,

$$S_{L,air}(\varphi, T) = S_{L,air,298}(\varphi) \sqrt{\frac{\lambda_{air}(T)}{\lambda_{air}(298)}} \left(\frac{T}{298}\right)^{n_t}, \quad (4.45)$$

where

$$n_t = \begin{cases} 1.571 + 0.3839(0.42 - X_{H_2,air}) & X_{H_2,air} < 0.42 \\ 1.571 - 0.2476(0.42 - X_{H_2,air}) & X_{H_2,air} > 0.42 \end{cases}. \quad (4.46)$$

4.3.3 Laminar burning velocity: pressure dependence

The variations of the pressure have a more complex influence on the laminar flame speed. In their study, Behrendt and Warnatz (1985) found that the flame speed of a stoichiometric hydrogen-air mixture grows with increasing pressure ($\beta_p > 0$) up to one bar. At this value it reaches a maximum ($\beta_p = 0$) and decreases for higher pressures ($\beta_p < 0$). Consequently, the pressure exponent depends on pressure itself. Furthermore, the pressure exponent in their data also depends on the nitrogen dilution. Shebeko et al. (1995) realized that an increase of temperature will shift the pressure in which a maximum of $S_L|_T$ is obtained to higher values and inferred that

the pressure exponent is also a function of temperature.

Iijima and Takeno (1986) proposed an expression for the exponent which depends linearly on the equivalence ratio. Based on their measurements, Verhelst and Sierens (2007) tried to improve the results of Iijima and Takeno (1986) suggesting a dependence that leads to a change of sign at $\varphi = 0.4$. Using the results obtained with CHEMKIN (Kee et al., 1989), Hu et al. (2009) created a correlation valid at ambient temperature between 1 and 80 bar. Thus, the discussed formulas consider the pressure exponent either as a function of the equivalence ratio or of pressure, disregarding the complex dependencies of β_p on equivalence ratio, temperature, pressure, and diluting concentration.

4.3.4 Laminar burning velocity: diluted dependence

Mixtures diluted by nitrogen or steam have lower flame temperatures than undiluted ones. These diluents in general slow down diffusion processes and steam in particular affects the reaction kinetics reducing the laminar flame speed (Le Cong and Dagaut, 2008). This influence was quantified by Koroll et al. (1993) measuring the laminar flame speed of hydrogen-air mixtures with H_2 concentrations from 9 to 70 mol % and steam dilution up to 42 mol %. With the results obtained, a correlation, which takes into account the change of thermal conductivity due to dilution, was created by Korol,

$$S_{L,steam}(\varphi, T, X_{H_2O}) = S_{L,air}(\varphi, T) \sqrt{\frac{\lambda_{steam}(T)}{\lambda_{air}(T)}} \left(1 - \frac{X_{H_2O}}{X_{H_2O,flam}}\right). \quad (4.47)$$

4.3.5 Laminar burning velocity: holistic phenomenological model strategy

The strategy followed for obtaining a correlation with a wide validity domain implies the determination of the laminar flame speed at the reference pressure and temperature (see Table 4.3). Then, a correction is implemented to take into account the effect of temperature and pressure deviations and the dilution by steam.

The dependence of the laminar flame speed on the equivalence ratio at reference conditions, $T_0 = 300\text{ K}$ and $p_0 = 1\text{ bar}$, is approximated by a cubic spline interpolation adjusted to match the data points calculated with a detailed chemistry mechanism inside the concentration interval bounded by the flammability limits provided by Kuznetsov et al. (2011b). The conditions of the initial reactive mixture were varied from 200 K to the autoignition for temperature (Kuznetsov and Redlinger, 2008), from 0.1 to 31 bar for the pressure. To study the influence of the steam, dilutions ranging from dry up to the complete inhibition of the mixture combustion were used. Hydrogen concentration was changed within flammability limits (Kuznetsov et al., 2011b). The results obtained were summarized in (Szabó et al., 2012a,b)⁷. They are validated against a specifically created database, which is discussed next.

4.4 Creation of a database of laminar flame speed

The speed of a laminar, flat and steadily propagating flame was calculated for different mixture compositions, temperatures and pressures with the detailed reaction mechanism of Warnatz and Maas (1988) implemented in the computer code INSFLA (Maas, 1988), (Maas and Warnatz, 1988). INSFLA simulates one dimensional, non-stationary, laminar, reactive flow by solving the conservation equations of total mass, species mass, momentum and energy. It uses reduced or detailed chemistry as well as detailed transport mechanism.

The calculations were divided in two main groups. Firstly, 2049 hydrogen-air mixtures were analyzed with hydrogen compositions between 3% and 75%, temperatures between 200 K and the autoignition limit (see (Kuznetsov and Redlinger, 2008), (Brown et al., 1997), (Zabetakis, 1965)) and pressures between 0.1 and 31 bar. Secondly, 2324 steam diluted hydrogen-air mixtures were considered, with steam concentrations up to 59 mol%, between 300 K and the autoignition temperature

⁷Co-authored by the author of this thesis

and pressures between 0.1 and 10 bar.

Figure 4.2 shows the comparison of the laminar burning velocity data obtained at 300 °C and 1 bar with the INSFLA code and selected cited experiments from the literature.

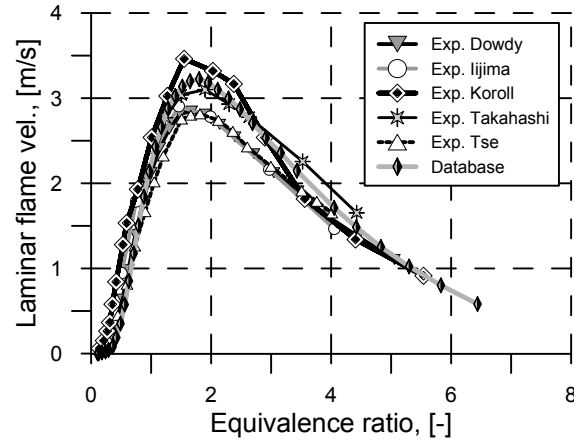


Figure 4.2: Laminar flame speed dependence on equivalence ratio, $(y_{fuel}/y_{air})/(y_{fuel,stoich}/y_{air,stoich})$, at 300 K and 1 bar. Comparison of INSFLA data with experimental results by Iijima and Takeno (1986), Koroll et al. (1993), Dowdy et al. (1990), Takahashi et al. (2001) and Tse et al. (2000).

As can be appreciated, a moderate spread exists in the experimental results of the different authors. The dispersion, in relative terms, is especially important in the area of lean mixtures where, in spite of the virtual coincidence of the values (see Figure 4.2, equivalence ratio approaching 0), large relative differences, of up to 100%, can be observed.

Marinov et al. (1995) proposed that such differences were related to the fact that data for stretched and unstretched flames had been provided, explicitly or implicitly, by the experimentalists. As a matter of fact, the stretching was unconsidered by Koroll et al. (1993), probably disregarded by Iijima and Takeno (1986) and Takahashi et al. (2001), and taken into account by Dowdy et al. (1990) and Tse et al.

(2000). An estimation for laminar flame speed over prediction can be found in (Lamoureux et al., 2002) where it was ascertained that for equivalence ratios larger than one over predictions of 0.5 m/s are to be expected if flame stretch is not taken into account.

Chaumeix (2010) and Bradley et al. (2007a) performed a similar analysis of laminar flame speed with different detailed reaction mechanisms and showed a similar scatter in their results. A review and comparison of reaction mechanisms well adapted for high temperatures and pressures can be found in Stroehle and Myhrvold (2007) where these authors perform an analysis of limitations and virtues of different schemes.

Regarding the database values, they accurately follow the trends suggested by the experiments. In these regards, the selection of the Maas-Warnatz mechanism (the one implemented in INSFLA) was motivated because, in spite of its *maturity*, it is able to provide convergent solutions in a relatively wide range of pressures, temperatures and steam concentrations.

A further assessment of the suitability of the choice for the goals pursued can be carried out comparing the laminar flames speeds obtained utilizing different mechanisms within the pressure and temperatures in the range of interest. The steam content was also varied between 0 and 85 vol. %. Figures 4.3 and 4.4 show that the results obtained with the Maas-Warnatz mechanism appear in an intermediate position in comparison with calculations using Mueller and Li mechanism thought closer to the latter. Additionally, it is shown that the total scatter between the Maas-Warnatz, Mueller and Li mechanisms remains moderate. Furthermore, the candidate considers the Maas-Warnatz mechanism preferable to Li's for hydrogen-air-steam mixtures as the latter disregards nitrogen species and compounds.

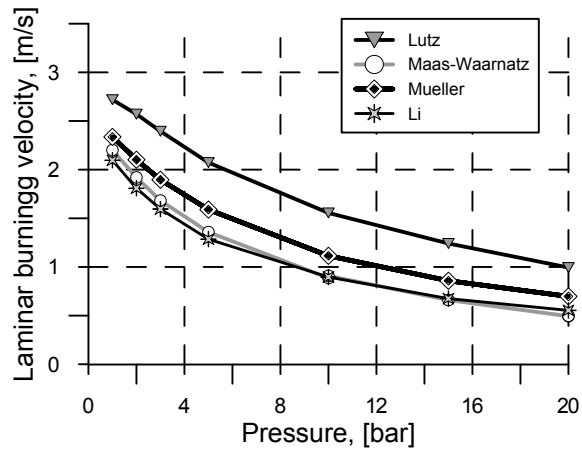


Figure 4.3: Laminar flame speed vs. pressure at a temperature of 373 K with a dilution of 12.9 % H_2O in a stoichiometric H_2 -air-mixture. Detailed chemical schemes by Lutz et al. (1996), Maas (1988), Müller et al. (2011) and Li et al. (2004). Data corresponding to Li and Mass-Waarnatz almost superpose.

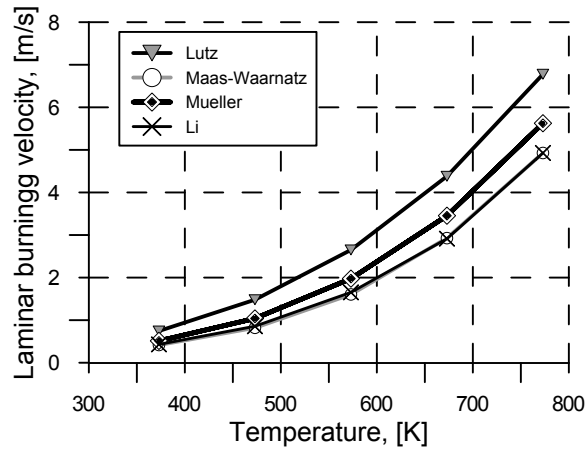


Figure 4.4: Laminar flame speed vs. temperature at 1 bar with a dilution of 37.2 % H_2O in a stoichiometric H_2 -air-mixture. Detailed chemical schemes of Lutz et al. (1996), Maas (1988), Müller et al. (2011) and Li et al. (2004). Data corresponding to Li and Mass-Waarnatz almost superpose.

The laminar flame speed obtained with the INSFLA code is compared to experimental results in Figure 4.5. An excellent agreement is shown with the data obtained by Behrendt and Warnatz (1985) and up to 600 K also with the results obtained with CHEMKIN by Hu et al. (2009).

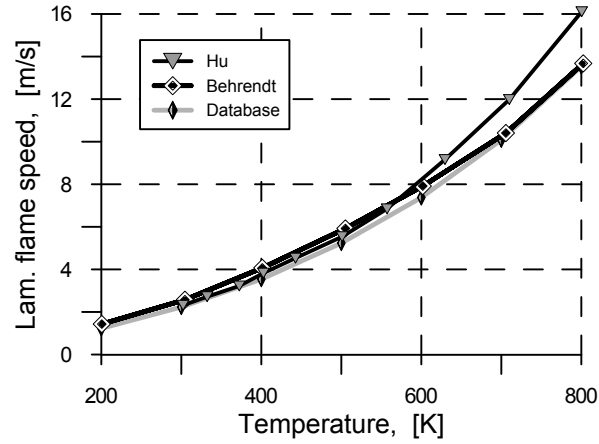


Figure 4.5: Laminar flame speed vs. temperature of a stoichiometric H_2 -air-mixture at 1 bar. Values of the database were compared to data obtained by Hu et al. (2009) and Behrendt and Warnatz (1985).

The curves plotted in Figure 4.6 represent the data obtained with INSFLA code compared with the values calculated using equation (4.44) with Hu et al. (2009) formulation for the exponents. The results obtained in the INSFLA calculations are less than 20% higher than the values delivered by formula (4.44) in the domain of interest. Both curves show similar shapes and have a negative slope that corresponds to a negative pressure exponent between 3 bar and 100 bar. Between 0.8 bar and 3 bar, the values obtained from simulations with INSFLA are nearly pressure independent ($\beta_p = 0$). For pressures lower than 0.8 bar, an increase of pressure implies an increase of laminar flame speed. The described laminar flame speed dependence on pressure is in agreement with the observations contained in Behrendt and Warnatz (1985).

The validity of the data obtained from calculations with INSFLA close to the flammability limits is doubtful, see Figure 4.2 and Figure 4.6 for the lower flammability limit. For hydrogen-air mixtures the lower flammability limit corresponds to around 4% vol. H_2 which in terms of equivalence ratio is in the vicinity of $\varphi \approx 0.1$, although exact value will depend on T , and P . The upper flammability limit corresponds to 75% vol. H_2 -air which in terms of equivalence ratio gives $\varphi \approx 7$. Close to this values, it has been observed that the results of the calculations performed with INSFLA show an unpredictable and erratic separation from the expected outcome based on the data from other authors, e.g., Kuznetsov et al. (2011b). A possible reason can be an inconsistent accounting of the quenching processes (Maas, 2010). For this reason, it should be admitted that close to flammability limits the results of calculations should not be considered as fully reliable.

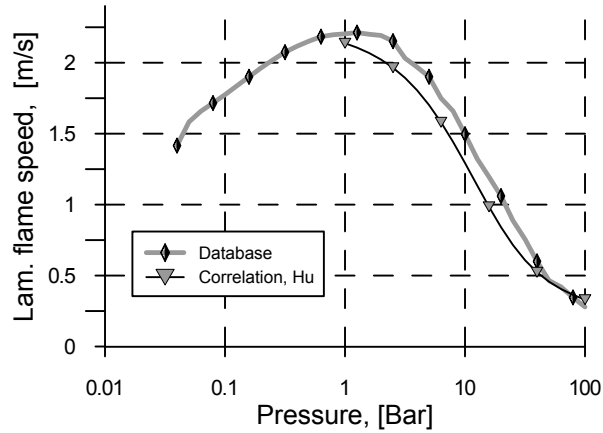


Figure 4.6: Laminar burning velocity of a stoichiometric H_2 -air-mixture at 298 K depending on pressure. Database obtained utilizing INSFLA code and data obtained from Hu et al. (2009).

4.5 Laminar flame velocity formula: Dependence on the equivalence ratio

At this stage, the formula for S_L is

$$S_{L,air}(\varphi, T) = S_{L,air,298}(\varphi) \sqrt{\frac{\lambda_{air}(T)}{\lambda_{air}(298)}} \left(\frac{T}{298}\right)^{n_t},$$

due to Koroll et al. (1993). We may start our modeling by approximating $S_{L,air,298}(\varphi)$ ⁸ the dependence of the laminar flame speed on the equivalence ratio at reference conditions, $T_0 = 300K$ and $P_0 = 1.bar$ (see Table 4.3 and *Database curve* in Figure 4.2). This was approximated by a cubic spline interpolation of the data points calculated with INSFLA and in between the flammability limits given by Kuznetsov et al. (2011b).

Table 4.3: Laminar flame speed at reference conditions 300 K and 1 bar obtained in calculations with INSFLA code.

φ	$S_{L,0}$ [m/s]	φ	$S_{L,0}$ [m/s]	φ	$S_{L,0}$ [m/s]
0.12	0.007	0.97	2.13	2.68	2.70
0.17	0.014	1.06	2.43	2.91	2.53
0.23	0.024	1.17	2.66	3.15	2.35
0.29	0.041	1.28	2.88	3.42	2.14
0.35	0.082	1.39	3.02	4.05	1.71
0.42	0.18	1.52	3.13	4.42	1.48
0.48	0.35	1.65	3.20	4.83	1.25
0.55	0.57	1.79	3.22	5.29	1.02
0.63	0.85	1.94	3.18	5.82	0.80
0.71	1.17	2.11	3.09	6.43	0.58
0.79	1.50	2.28	2.99		
0.88	1.84	2.47	2.87		

⁸with the use of the sub index *air* it is emphasized that we deal with undiluted mixtures, that do not contain extra steam, N_2 , etc.

4.6 Laminar flame velocity formula: Dependence on temperature

The temperature dependence of the laminar flame velocity is based on correlation (4.45)

$$S_{L,air}(\varphi, T) = S_{L,air,298}(\varphi) \sqrt{\frac{\lambda_{air}(T)}{\lambda_{air}(298)}} \left(\frac{T}{298}\right)^{n_t},$$

which was evaluated for a wide range of mixture compositions and conditions at one bar. The results obtained, $S_{L,air}(\varphi, T)$, has been correlated with the database values, $S_{L,I}(\varphi, T)$, at different temperatures, see Figure 4.7. In this figure, the laminar burning velocity results of the database have been plotted as the abscissae while the values resulting from the equation (4.45) have been located in ordinates. For each condition, (φ, T) , a point is then obtained $(S_{L,I}(\varphi, T), S_{L,air}(\varphi, T))$. For clarity, the points corresponding to the same temperature (but with different φ) have been linked in a single curve. The two sheets that apparently appear in the figure correspond to the increase of the laminar burning velocity until $\varphi \approx 2$ (see Figure 4.2) and its subsequent reduction. For a perfect agreement every single point would have been located on the diagonal line of the first quadrant. The points positioned above this line represent an overestimation of the database values and vice versa. For temperatures sufficiently elevated, considerable differences occur depending on temperature and equivalence ratio, revealing the limitations of equation (4.45). These differences are also systematic as they grow with the increase of temperature.

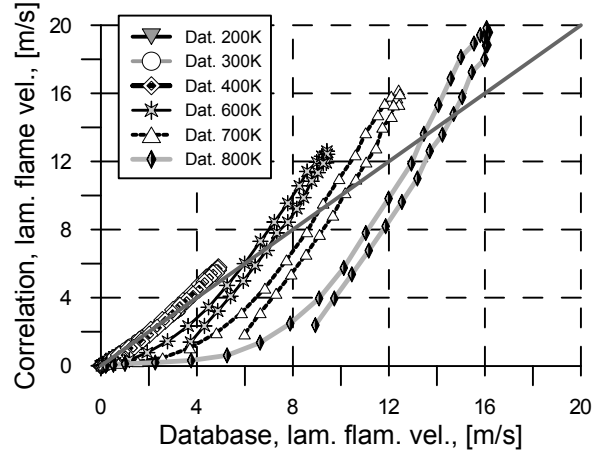


Figure 4.7: Comparison of the results of eq. (4.45) (ordinates) and INSFLA database (abscissa) at different temperatures and 1 bar.

The results represented in Figure 4.7 can also be drawn in a log-log diagram, resulting that the new chart can be approximated by two straight lines that will differ for every temperature. Using the equation (4.45) for the $S_{L,C}(\varphi, T)$, the power function

$$S_{L,C}^*(\varphi, T) = \left(\frac{1}{a_2(T)} S_{L,air}(\varphi, T) \right)^{\frac{1}{a_1(T)}}, \quad (4.48)$$

delivers a good approximation with two sets of values for a_1 , a_2 depending on φ and T . These were obtained from the data available by linear regression analysis for each temperature. The expressions (4.50) were derived using the method of least squares and resulted to be

$$a_1(T) = \begin{cases} -7.82 \cdot 10^{-4} T + 1.23 & \varphi \leq 0.3 \\ 1.95 \cdot 10^{-8} T^3 - 2.08 \cdot 10^{-5} T^2 - 8.62 \cdot 10^{-3} T - 0.20 & \varphi > 0.3 \end{cases}, \quad (4.49)$$

$$a_2(T) = \begin{cases} \exp(-4.56 \cdot 10^{-3} T + 1.40) & \varphi \leq 0.3 \\ 2.08 \cdot 10^{-8} T^3 - 3.34 \cdot 10^{-5} T^2 + 1.45 \cdot 10^{-2} T - 0.90 & \varphi > 0.3 \end{cases}. \quad (4.50)$$

Due to inaccuracies at very high temperatures, the enhanced correlation, eq. (4.50), must be still corrected for temperatures above 600 K. An adequate amendment may be performed with the formulation

$$S_{L,C}^T(\varphi, T) = [S_{L,C}^*(\varphi, T)]^{C(T)}, \quad (4.51)$$

where

$$C(T) = \begin{cases} 1 & T \leq 600K \\ -1.5 \cdot 10^{-4} \cdot T + 1.09 & T > 600K \end{cases}. \quad (4.52)$$

The results presented in Figure 4.8 show an excellent agreement between the values obtained utilizing the equation (4.51) and the database. The same representation methodology as in Figure 4.7 was repeated here. The laminar burning velocity results of the database have been plotted in the abscissa while the values resulting from the equation (4.48) have been located in ordinates. For each condition, (φ, T) a point is then obtained $(S_{L,I}(\varphi, T), S_{L,C}^T(\varphi, T))$. Very clearly, the curves collapse in a single line superimposing to the diagonal of the quadrant, a warranty of accurate prediction.

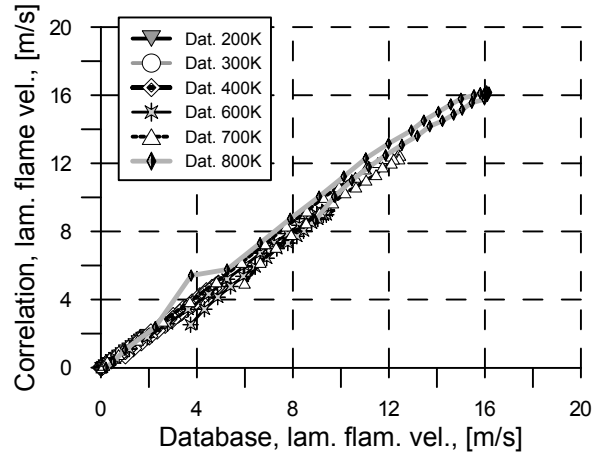


Figure 4.8: Comparison of the results of temperature dependence corrected formula, eq. (4.51), and INSFLA database at different temperatures and 1 bar after correction was applied.

A quantitative evaluation of the correctness of the results was performed using three statistic magnitudes (Martin Pliego and Ruiz-Maya Perez, 2004), namely the correlation coefficient, the mean absolute error and the standard deviation, see Table 4.4. The high value obtained for the correlation coefficient, and the small values for the standard and absolute deviation assure a good approximation.

Table 4.4: Laminar burning velocity eq. (4.51) vs. database. Statistical variables characterizing the temperature approximation: Correlation coefficient, mean error and standard deviation.

$r_{L,C}$	\bar{E} (m/s)	σ (m/s)
0.998	0.256	0.699

An interesting assessment of the quality of the correlation can be performed studying the quality of the prediction for stoichiometric H_2 -air-mixture at 1 bar over different temperatures, Figure 4.9. The results calculated with the model using equation (4.51) are very close to the INSFLA values. The maximum relative error of 8.5% occurs for 800 K.

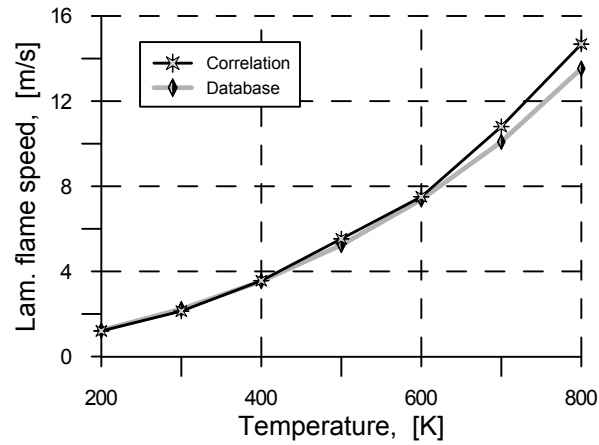


Figure 4.9: Laminar flame speed vs. temperature of a stoichiometric H_2 -air-mixture at 1 bar. Values of the database compared to the results calculated with the new correlation.

4.7 Laminar flame velocity formula: Dependence on steam dilution

Very frequently, in the praxis, a release of hydrogen is accompanied by the liberation of other gases. Those additional components may be burnable but also often non-burnable. Under the methodology we are presenting, if the accompanying gases are burnable a new laminar flame velocity correlation should be developed from experiments or calculations. In case the additional gases are non-burnable they will work, from the point of view of the chemical reaction, as dilutants of the fuel.

By its special relevance for the safety of nuclear plants, specially in the nuclear environment (Breitung et al., 2012), the effect of the dilution with steam is a very significant topic for this thesis. It could be just mentioned now that the generation of hydrogen radicals and assorted oxygen compounds, the so called radiolysis gas, by dissociation of water molecules by nuclear radiation, is a very serious issue in Boiling Water Reaction.

The dependence of laminar burning velocity on steam dilution $S_{L,C}^{T,dil}(\varphi, T, X_{H_2O})$ has been approximated utilizing equation (4.47), using the laminar flame speed corrected with the temperature $S_{L,C}^T(\varphi, T)$ object of last section, and presented in (4.51),

$$S_{L,C}^{T,dil}(\varphi, T, X_{H_2O}) = S_{L,C}^T(\varphi, T) \sqrt{\frac{\lambda_{H_2O,steam}(T)}{\lambda_{air}(T)}} \left(1 - \frac{X_{H_2O}}{X_{H_2O,flam}}\right). \quad (4.53)$$

This formula represents a second stage correction in which the effects of the temperature have been incorporated to the model.

The laminar flame speed dependence on steam dilution, see Figure 4.10, could be approximated linearly in the domain of interest following the approximation obtained by Koroll et al. (1993), with eq. (4.47).

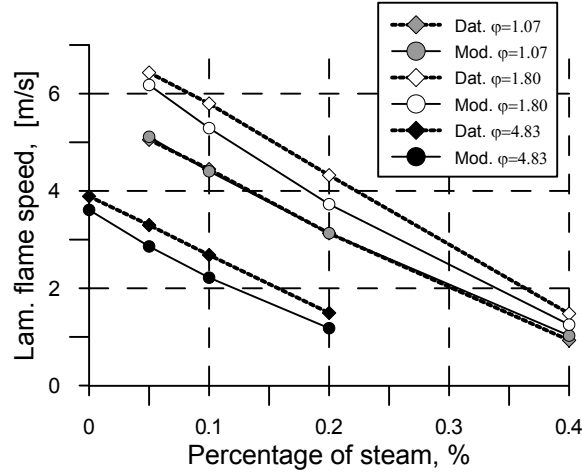


Figure 4.10: Laminar flame speed depending on steam dilution at $T = 400\text{ K}$ and $p = 1\text{ bar}$. Database and modeled values for equivalence ratio 1.07 (grey symbols), 1.80 (white symbols), 4.83 (black symbols).

In addition, the formulation of Koroll et al. (1993) has been extended to take into account the significant effect of temperature (see Figure 4.11) on the flammability limits ($x_{H_2O,flam} = x_{H_2O,flam}(T, \varphi)$).

For this purpose the laminar flame speeds of the database at different steam concentrations (some of them plotted in Figure 4.10) have been approximated by a linear function for constant equivalence ratios and temperatures. The points at which the straights cross the horizontal axis represent the locus where the burning velocity is zero being positive before, that is the flammability limits $x_{H_2O,flam}(T, \varphi)$. The results obtained by this procedure, plotted in Figure 4.11, deviate from the original formulation at 373 K by Koroll et al. (1993).

The difference is coherent with the divergences in the results for the laminar burning velocities obtained by Koroll et al. (1993) compared with those of other authors, see Figure 4.2. On one side, clearly the values for $\varphi < 4$ are overestimated by Koroll et al. (1993). On the other side, for $\varphi > 4$, the data obtained by Koroll et al. are the smallest.

Considering this, it can be inferred that the divergences in Figure 4.11 can be

attributed Koroll et al. (1993) to inconsistencies in the measurement of the laminar burning velocities. Such discrepancies are natural if we are aware of the diverse methodologies utilized by the authors of their measurements. Concretely, this is connected with the american procedure that Koroll et al. (1993) used to conduct their measurements (ASME standard), different from the utilized by other authors. The new results will modify the results obtained in eq. 4.53 significantly.

The $x_{H_2O,flam} = x_{H_2O,flam}(T, \varphi)$ resulting from our calculations has been approximated for different temperatures using the method of least squares with the result,

$$\begin{aligned} X_{H_2O,flam}(\varphi, 400) &= -2.65 \cdot 10^{-2} \cdot \ln^3(\varphi) - 9.08 \cdot 10^{-2} \cdot \ln^2(\varphi) + 0.11 \cdot \ln(\varphi) + 0.43, \\ X_{H_2O,flam}(\varphi, 600) &= -1.10 \cdot 10^{-2} \cdot \ln^3(\varphi) - 8.14 \cdot 10^{-2} \cdot \ln^2(\varphi) + 6.24 \cdot 10^{-2} \cdot \ln(\varphi) + 0.57, \\ X_{H_2O,flam}(\varphi, 800) &= -5 \cdot 10^{-4} \cdot \ln^3(\varphi) - 5.2 \cdot 10^{-2} \cdot \ln^2(\varphi) - 1.8 \cdot 10^{-2} \cdot \ln(\varphi) + 0.58. \end{aligned} \quad (4.54)$$

For intermediate temperatures, the flammability limits can be approximated by linear interpolation or extrapolation.

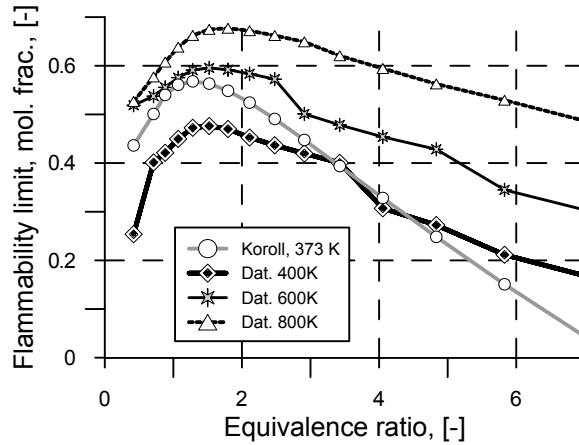


Figure 4.11: Flammability limits of steam dilution for different temperatures, $X_{H_2O,flam}$, as a function of the equivalence ratio. Database results and results with correlation for 373 K by Koroll et al. (1993). the flammability limits are given as the maximum molar fraction of steam in the gases.

The correlation coefficient of Pearson $r_{I,C}$ that describes the quality of the model qualifying the adjustement of $S_{L,C}^{T,dil}(\varphi, T, x_{H_2O})$ on the database values $S_{L,I}(\varphi, T, X_{H_2O})$, see Table 4.5, has a very large value at 400 K and decreases slightly with increasing temperature. The mean error \bar{E} and the standard deviation σ grow, too. Nevertheless, the relative errors remain moderate, due to the laminar flame speed growth with temperature, and even up to 600 K the correlation coefficient remains very large (0.979 in average), see Table 4.5. The value of \bar{E} as well as the standard deviation are sufficiently small to warrant a good approximation. For temperatures higher than 600 K the approximation degrades due to the inaccuracies on the equation describing the flammability limit at 800 K, see (Kuznetsov and Redlinger, 2008). Certainly, this temperature is too close to the auto-ignition limit and an enlarged set of concentrations will start to react without the need of an ignition source⁹.

Table 4.5: Statistical variables characterizing the correlation in presence of diluents. Correlation coefficient, mean error and standard deviation. In last line, the common values in the temperature interval from 400 °C to 600 °C

T [K]	$r_{I,C}$	\bar{E} [m/s]	σ [m/s]
400	0.992	0.167	0.172
500	0.989	0.239	0.262
600	0.969	0.587	0.608
700	0.959	0.969	0.909
800	0.934	1.698	1.365
400-600	0.979	0.335	0.438

The performance of the model can be accessed utilizing Figure 4.10. The results contained in the database predict a linear decrement of S_L with increasing steam dilution, tendency that is reproduced by the model. In spite of the general trends being well represented, the values of the database are underestimated and the relative errors reach up to 10.3% for $\phi = 1.07$, up to 15.3% for $\varphi = 1.8$ and up to

⁹Flamability limit relates to the possibility of a flame to propagate whilst auto-ignition involves the possibility of a mixture to be ignited without a punctual source. Recall that the flammability limit extents just until auto-ignition limit where the reaction will happens volumetrically.

21.0% for $\varphi = 4.83$. This can be confirmed observing the decreasing trends for the steam dilution already shown by Lamoureux et al. (2002) and Le Cong and Dagaut (2008).

4.8 Laminar flame velocity formula: Dependence on pressure

4.8.1 General

The laminar flame speed dependency on pressure has been formulated independently for pressures smaller and bigger than 1 bar. A similar methodology that was utilized for the dependence of the temperature in section 4.6.

Each curve in the $S_{L,C} - S_{L,I}$ plane corresponding to a pressure value, whose points initially show the patten shown in Figure 4.12, can be transformed in a log-log representation into two intersecting straight lines by raising the former correlation $S_{L,C}$ to the power of a pressure dependent coefficient d_2 . These lines can be corrected on the equality $S_{L,C} = S_{L,I}$ using the coefficients d_1 and d_3 in the following way,

$$S_{L,C}^{T,dil,p}(\varphi, T, x_{dil}, p) = \frac{1}{d_1} [S_{L,C}^{T,dil}(\varphi, T, x_{dil})]^{d_2} - d_3. \quad (4.55)$$

4.8.2 Pressures lower than 1 bar

The parameters d_1 and d_2 only depend on pressure and are approximated by

$$d_1(p) = \begin{cases} 0.7 \cdot p/p_0 + 0.3 & \varphi \leq 0.3 \\ 1 & \varphi > 0.3, \end{cases} \quad (4.56)$$

$$d_2(p) = 0.13 \cdot \ln(p/p_0) + 1. \quad (4.57)$$

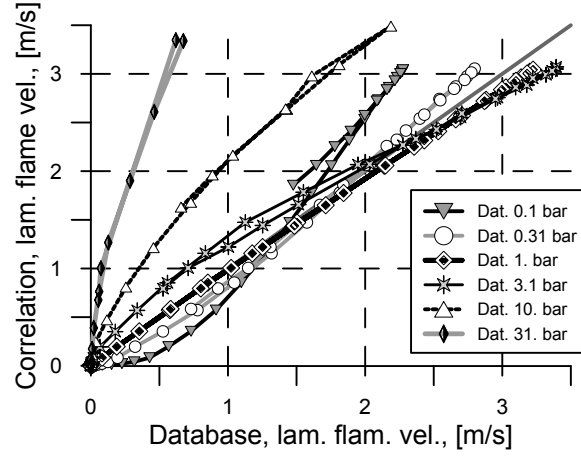


Figure 4.12: Deviations of the model due to pressure vs. database values at 300 K before modeling of the pressure effects.

d_3 depends on temperature and pressure and is calculated using

$$d_3(p, T) = \begin{cases} 0 & \varphi \leq 0.3 \\ Q & \varphi > 0.3 \end{cases}, \quad (4.58)$$

where the value of $Q(p, T)$ is given by the linear interpolation between the following formulae

$$Q(p, T) = \begin{cases} -2.26 \cdot 10^{-6} T^2 - 4.78 \cdot 10^{-4} T + 0.11 & p = 0.1 \text{ bar} \\ -4.99 \cdot 10^{-6} T^2 + 2.58 \cdot 10^{-3} T - 0.36 & p = 0.31 \text{ bar} \\ 0 & p = 1 \text{ bar} \end{cases}. \quad (4.59)$$

4.8.3 Pressures higher than 1 bar

The coefficient d_1 is obtained from the linear interpolation between the formulae

$$d_1(p, T) = \begin{cases} 4.71 \cdot 10^{-6} T^2 + 2.50 \cdot 10^{-4} T + 1.04 & p = 3.1 \text{ bar} \\ 2.52 \cdot 10^{-5} T^2 - 1.52 \cdot 10^{-3} T + 1.44 & p = 10 \text{ bar} \\ 1.80 \cdot 10^{-4} T^2 - 6.09 \cdot 10^{-2} T + 10.53 & p = 31.6 \text{ bar} \end{cases}, \quad (4.60)$$

while d_2 and d_3 are expressed with the formulae,

$$d_2 = 0.43 \cdot \ln(p/p_0) + 1, \quad (4.61)$$

$$d_3 = 0. \quad (4.62)$$

4.8.4 Summary of the pressure related corrections

In both cases these parameters were derived using linear regression analysis of INSFLA data and the method of least squares for optimal polynomial coefficients.

In Figure 4.13, the results obtained with the corrected formulation $S_{L,C}$ are correlated with the original database values $S_{L,I}$ at 300 K. The majority of the points are located close to the equality $S_{L,C} = S_{L,I}$, the correlation coefficient $r_{I,C}$ is large and as it is seen from Table 4.6 and a low standard deviation is achieved. The correlation obtained is valid in the range from 200 to 600 K.

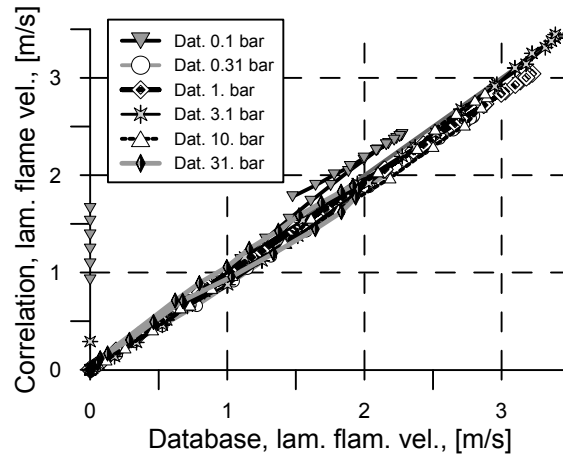


Figure 4.13: Equation (4.55) used for the modeling of the pressure deviations vs. database values at 300 K.

Table 4.6: : Statistical variables characterizing the approximation of pressure. Correlation coefficient, mean error and standard deviation. In the last row, the corresponding values considering the data for the whole interval between 200 and 600 K

T [K]	$r_{I,C}$	\bar{E} [m/s]	σ [m/s]
200	0.975	0.071	0.121
300	0.972	0.099	0.208
400	0.963	0.168	0.372
500	0.963	0.275	0.539
600	0.945	0.592	0.850
700	0.938	0.818	1.229
800	0.884	1.527	1.979
200-600	0.965	0.241	0.525

However, as can be appreciated observing data in Table 4.6, the scatter increases for high temperatures, e.g. 700 K at one bar for which the quality of the correlation severely degrades. Hence, the assumption that the exponent d_2 only depends on pressure is no longer valid for temperatures above 600 K.

The isolated points located on the vertical axis in Figure 4.13 represent very rich mixtures that the INSFLA code does not treat adequately, predicting that such mixtures lie below the flammability limit, i.e., zero flame speed.

In spite of the generally good approximation, a small systematic bias is noticeable in the correlation: the model slightly underestimates the flame speeds for pressures larger than 0.31 bar. Those deviations are almost negligible for pressures above 2 bar. With a decrease of pressure the deviations increase, see Figure 4.6.

The quality of the approximation for pressures between 0.4 and 100 bar at $\varphi = 1$ and 298 K can be visualized in the Figure 4.14 for the stoichiometric mixture.

In general, for all concentrations and for pressures between 0.1 bar and 31.62 bar, the model approximates the values obtained with INSFLA with a maximum relative error of 8.3%. The values of the database are underestimated between 0.2 bar and 31 bar and overestimated for lower pressures. Extrapolation of the model for even lower pressures is not recommended. For large pressures, up to 100 bar,

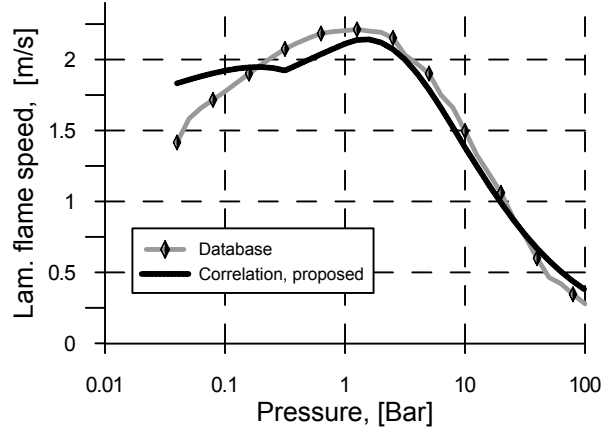


Figure 4.14: Laminar burning velocity of a stoichiometric H_2 -air-mixture at 298 K depending on pressure. Database obtained utilizing INSFLA code and the correlation proposed by the author.

the curve obtained from the approximation is in fair agreement with the values of the database. Although the absolute error is small, the relative one grows up to a maximum of 35.3% at 100 bar. For pressures lower than 0.1 bar the curves diverge because of the mentioned slope change. At 0.04 bar the large absolute error corresponds to a relative error of 29.4%.

4.8.4.1 Relation with the reaction order

The dependence of the laminar flame velocity on the pressure that has been obtained could be interpreted as an implicit reaction order n (see footnote¹⁰), if we assume $S_L \propto p^{n/2-1}$ (see e.g. Zeldovich et al. (1985)). With the previous considerations the ratio S_L/S_{L0} may be studied. On one side, from the last dependence, $S_L/S_{L0} \propto (p/p_0)^{n/2-1}$ where the sub index 0 was denoted the reference status.

¹⁰Considering a simplified chemical process described by a single reaction $X + Y \rightarrow Z$ with severe deficit of X component, the rate constant k depends on the reaction order $k \approx k_0[X]^n \exp(-T/T_a)$. Certainly, a complex system of reactions as the one that governs the combustion of hydrogen the dependence on reaction order cannot so easily be written. Still, the reaction order of the overall reaction $2H_2 + O_2 \rightarrow 2H_2O$ appears as a significant magnitude describing the dependence of the laminar burning velocity on the pressure

On the other side, from $S_L/S_{L0} \approx d_1^{-1}(S_{L0})^{d_2-1}$ valid between 3 and 31.6 bar,

$$\ln(S_L/S_{L0}) \approx (n/2 - 1) \ln(p/p_0) \ln(d_1) + (d_2 - 1) \ln(p/p_0) \ln(S_{L0}). \quad (4.63)$$

Between 3 and 31.6 bar the d_1 dependence can be approximated as

$$d_1 \approx \left(1.4 \frac{T}{T_0} - 1.2 \right) \left(\frac{p}{p_0} - 1 \right) + 1. \quad (4.64)$$

Finally, an approximated expression for the *overall* reaction order can be obtained

$$\frac{n}{2} - 1 \sim 0.43 \cdot \ln(S_{L0}) - \frac{\ln \left(\left(1.4 \cdot \frac{T}{T_0} - 1.2 \right) \cdot \left(\frac{p}{p_0} - 1 \right) + 1 \right)}{\ln(p/p_0)}. \quad (4.65)$$

In equation (4.64) the curves $d_1 = \text{const}$ represent hyperbolas centered very close to the standard conditions (p_0, T_0) . The first term in RHS of equation (4.65) is a constant. The second term contains the dependency on the pressure and temperature which resulted to be the dominating influence. The term $(1.4 \cdot T/T_0 - 1.2)$ reaches one for $T \approx 470\text{ K}$. For high pressures temperatures larger than this an increase of pressure decreases the reaction order. For temperatures below this limit and increase of pressure increases the reaction order. For 470 K the reaction order does not change.

4.9 Simultaneous influence of all parameters and restrictions in the applicability of the model

The comparison of the data contained in the database and the predictions of model final equation (4.55) is represented in Figure 4.15 for conditions in which all parameters are varied. As discussed in previous sections the corrections addressing the deviations from the database reference state are applied successively to obtain the final correlation values. The plot is representative for mixture conditions corresponding to the interval between 0.1 and 10 bar and between 200 and 600 K.

One can see that the points corresponding to the mixtures diluted up to 20 vol.

% are predicted with good accuracy. For mixtures diluted more than 20 vol. %, accuracy distortions appear due to quality reduction in both the simulations carried out for obtaining the database and the correlation approximation.

Note that in the Figure 4.15 several points appear located exactly at the axes. The points at the vertical axis represent conditions in which the mixture is considered by the model as burnable while INSFLA identify them as non-burnable. These points correspond to very rich mixtures where INSFLA does not produce reliable results. For the points at the abscissa axis the opposite situation takes place. They correspond to strongly diluted mixtures for which the new correlation eq. (4.55) has tendency to underestimate flame speed due to shortcomings of the low flammability limit model.

The weakness of the flammability limit model for both upper and lower limit is connected to the accounting for the influence of the equivalence ratio and the temperature.

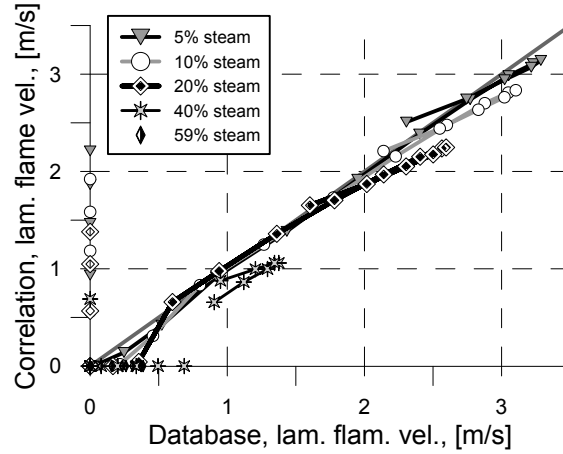


Figure 4.15: Comparison of the model eq. (4.55) and the INSFLA data for different steam dilutions at $T=400K$ and $p=0.1$ bar

Taking into account all previously discussed concerns we can conclude that the

proposed new correlation approximation can be considered reliable for temperatures between 200 and 600 K, steam dilution between 0 and 20 mol% and pressures between 0.1 and 10 bar. Undiluted hydrogen-air mixtures can still be calculated at pressures between 0.1 bar and 31.62 bar. The correlation coefficient between the proposed approximation and the values of the database in this whole area of validity is 0.97. The mean value of the absolute error is 0.34 m/s and its standard deviation is 0.59 m/s.

4.10 Transport properties of gases

4.10.1 General

The molecular transport properties of the gases are among the variables that most influence the laminar flame speed. Calculating the dynamic viscosity, μ , the diffusion, D , and thermal conductivity, χ , of the mixture is also necessary for evaluating of the formulae contained in Table 4.1. This dependence can be direct, when one of these parameters is present in the corresponding formula, or indirect through the laminar flame thickness.

Often, the molecular transport coefficients are estimated with the Sunderland's law $\mu(T)/\mu(T_0) \approx (T/T_0)^{0.76}$ e.g. Oran and Gamezo (2008), Kessler et al. (2010). In other cases, the Sunderland's law is doubtfully extended, to the diffusion and thermal diffusivity (Oran and Gamezo, 2007; Poludnenko and Oran, 2011) with the same exponential dependence, to obtain $\nu \sim \chi \sim D \propto T^n$. Also, it is not uncommon to find the approximation, e.g. (Oran and Gamezo, 2007), that $\nu = \chi = D$ in standard conditions for practical applications.

The reason for such handling is the general belief that the calculation of realistic values for the molecular transport coefficients yields an overload in the computation cost that makes realistic estimations unpractical. The candidate experience is that such concerns are excessive and has estimated the resulting overload in a 20% increase in the calculation time.

Investigation in the field of the transport properties requires insights on the

particle physics far away of the scope of this thesis. Still, accurate flame modeling requires precise transport properties prediction.

4.10.2 Dynamic viscosity

The dynamic viscosity of a gaseous pure species can be calculated utilizing the kinetic molecular theory of gases. To allow to take into account realistic interactions between the gas particles, which are described by a Lennard-Jones potential¹¹ Chapman and Cowling (1990), the collision integrals $\Omega^{(1,1)*}$ and $\Omega^{(2,2)*}$ ¹² have been utilized (see section 4.10.3). As can be found in (Hirschfelder et al., 1954), the equation for the viscosity of a single species is

$$\mu_i = 8.44 \cdot 10^{-25} \frac{\sqrt{M_i T}}{\sigma_d^2 \Omega_i^{(2,2)*}}, \quad (4.66)$$

where is M the molar mass (kg/mol), T temperature in K and σ_d the molecular diameter in m .

To estimate the viscosity of a mixture the formulation (4.67) (Wilke, 1950) could be utilized

$$\mu_{mix} = \sum_i \frac{\mu_i X_i}{1 + \sum_{j \neq i} \frac{X_j}{X_i} \Phi_{ij}}, \quad (4.67)$$

that uses the correction factors Φ_{ij} that can be obtained in turn from the equation (4.68)

$$\Phi_{ij} = \frac{1}{2\sqrt{2}} \frac{1}{\sqrt{1 + \frac{M_i}{M_j}}} \left(1 + \sqrt{\frac{\mu_i}{\mu_j} \sqrt{\frac{M_k}{M_i}}} \right)^2. \quad (4.68)$$

¹¹The Lennard-Jones potential describe the repulsion between molecules at small distances and its weakly attraction at larger distances $V(r) = A/r^{\nu-1} - B/r^{\nu'-1}$. Taking $\nu > \nu'$ the first term takes over at small distances and the second at larger. The usual values for ν ν' are 13 and 7, suggested by quantum theory, giving the famous 12-6 model. The minimum value attained for $V(r)$ is called *depth of wheel* or depth of the inter-molecular potential ϵ_ω .

¹²Represent the *cross section*, or the effective area that governs the probability of scattering or collision of the molecules considering defection, energetic level, angle...(Chapman and Cowling, 1990, Chapter 9 and 10)

4.10.3 Collision integrals $\Omega^{(1,1)*}$ and $\Omega^{(2,2)*}$

An interpolation of the tabulated data obtained by Hirschfelder et al. (1954) for the calculation of the collision integrals has been performed in order to efficiently obtain the required values.

In order to increase calculation effectiveness, instead of utilizing the Kestin et al. (1984) formulation, specific expressions for the interpolation have been developed. Two auxiliary magnitudes $T_i^* = \log(k_B T / \varepsilon_{wi})$ and $T_{ij}^* = k_B T / \varepsilon_{wij}$ have been utilized with $\varepsilon_{wij} = \sqrt{\varepsilon_{wi} \varepsilon_{wj}}$ and k_B the Boltzmann constant¹³, to increase the efficiency of the computation. The depth of the inter-molecular potential ε_w as well as the molecular diameter σ_d are included in the Table 4.7 for the species considered in large scales H_2 -air explosions. Additionally, for further acceleration the variable $Q_{ij}^* = \log(T_{ij}^*)$ was employed. The final formulation implies dependencies of $\Omega^{(1,1)*}$ and $\Omega^{(2,2)*}$ to an auxiliary variable of the type $\Omega_{ij}^{(1,1)*} = \Omega_{ij}^{(1,1)*}(Q_{ij}^*)$ and $\Omega_i^{(2,2)*} = \Omega_i^{(2,2)*}(T_i^*)$. The equations finally obtained utilizing the least squares method have been

$$\begin{aligned} \Omega_{ij}^{(1,1)*} = & 1.4435 - 1.6046 Q_{ij}^* + 1.3836 (Q_{ij}^*)^2 - 0.3307 (Q_{ij}^*)^3 - \\ & - 0.3087 (Q_{ij}^*)^4 + 0.2017 (Q_{ij}^*)^5 - 0.0332 (Q_{ij}^*)^6, \end{aligned} \quad (4.69)$$

$$\begin{aligned} \Omega_i^{(2,2)*} = & 1.5929 - 1.7870 T_i^* + 1.3662 (T_i^*)^2 + 0.1431 (T_i^*)^3 - \\ & - 0.822 (T_i^*)^4 + 0.4100 (T_i^*)^5 - 0.0627 (T_i^*)^6. \end{aligned} \quad (4.70)$$

The results of the interpolation can be seen, for the range of T^* of interest, in the figure 4.16.

¹³ $k_B = 1.3806488 \cdot 10^{-23} \text{ m}^2 \text{ kg s}^{-2} \text{ K}^{-1}$

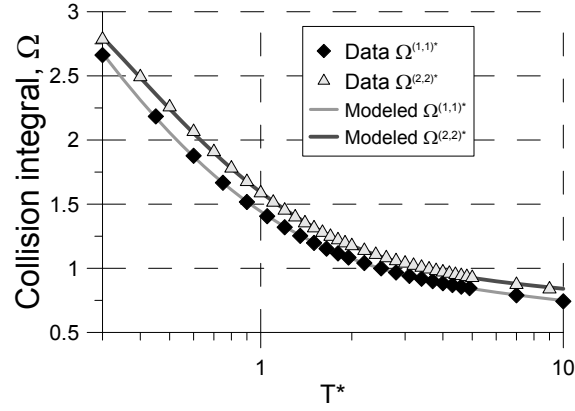


Figure 4.16: Collision integrals $\Omega^{(1,1)*}$ and $\Omega^{(2,2)*}$, real vs. modeled values.

Table 4.7: Molecular data for the calculation of the transport coefficients (Warnatz et al., 1999).

Specie	σ_d [nm]	ε_w/k_B [K]
H_2	0.292	38
O_2	0.346	107
N_2	0.362	97
H_2O	0.260	572

4.10.4 Diffusion

The binary diffusion coefficient, D_{ij} has been calculated following Bargaftik (1972) methodology,

$$D_{ij} = 5.954 \cdot 10^{-24} T \frac{\sqrt{T \frac{M_i + M_j}{M_i M_j}}}{p \sigma_{dij}^2 \Omega_{ij}^{(1,1)*}(T_{ij}^*)} \quad (4.71)$$

where p is the pressure, σ_{dij} is the arithmetic average of the molecular diameters. The diffusion coefficient of each component i in a multi-components mixture has been estimated with the equation

$$D_i = \frac{1 - Y_i}{\sum_{j \neq i} X_j / D_{ij}}. \quad (4.72)$$

4.10.5 Thermal conductivity

The conductivities of each individual species are calculated, (see Kee et al. (1989)) with the equation

$$\lambda_i = \frac{\mu_i}{M_i} (f_t C_{vt} + f_r C_{vr} + f_v C_{vv}). \quad (4.73)$$

where sub-indexes refer to t for translational, r for rotational and v for vibrational movements. The equations for the respective functions are,

$$f_t = \frac{5}{2} \left(1 - \frac{2}{\pi} \frac{C_{vr}}{C_{vt}} \frac{A}{B} \right), \quad (4.74)$$

$$f_r = \frac{\rho D_{ii}}{\mu_i} \left(1 + \frac{2}{\pi} \frac{A}{B} \right), \quad (4.75)$$

$$f_v = \frac{\rho D_{ii}}{\mu_i}. \quad (4.76)$$

The factors A and B are calculated utilizing

$$A = \frac{5}{2} - \frac{\rho D_{ii}}{\mu_i}, \quad (4.77)$$

$$B = Z_r + \frac{2}{\pi} \left(\frac{5}{3} \frac{C_{vr}}{R} + \frac{\rho D_{ii}}{\mu_i} \right), \quad (4.78)$$

where Z_r is the rotational relaxation collision number and R the universal gas constant. The translational specific heat at constant volume is $C_{vt} = \frac{3}{2}R$. The rotational and vibrational specific heat are for linear molecules, H_2 , O_2 and N_2 described by $C_{vr} = R$ and $C_{vv} = c_v - \frac{5}{2}R$ respectively, while for the case of non-linear molecules, H_2O , they can be obtained from the formulations $C_{vr} = \frac{3}{2}R$ and $C_{vv} = c_v - 3R$.

The rotational relaxation collision number is given in (Brau and Jonkman, 1970) is, for the case of impulsive collisions

$$Z_r(T) = Z_r(298) \frac{F(298)}{F(T)}, \quad (4.79)$$

being the rotational cumulative distribution function

$$F(T) = 1 + \frac{\pi^{\frac{3}{2}}}{2} \left(\frac{\varepsilon}{k_B T} \right)^{\frac{1}{2}} + \left(\frac{\pi^2}{4} + 2 \right) \left(\frac{\varepsilon}{k_B T} \right) + \pi^{\frac{3}{2}} \left(\frac{\varepsilon}{k_B T} \right)^{\frac{3}{2}}. \quad (4.80)$$

The values for the Rotational relaxation numbers at standard temperature as well as the cumulative distribution are contained in the Table 4.8.

Table 4.8: Rotational relaxation collision number and rotational cumulative distribution function for 298 K.

Species	$Zr(298)$	$F(298)$
H_2	280.	2.81
O_2	3.8	5.47
N_2	4.	5.07
H_2O	4.	28.24

The only remaining part is then to calculate the mixture properties. The thermal conductivity of a mixture has been calculated with the modified Wilke formula (Wilke, 1950) which reads

$$\lambda_{mix} = \sum_i \frac{\lambda_i}{1 + \sum_{k \neq i} 1.065 \frac{X_k}{X_i} \Phi_{ij}}. \quad (4.81)$$

The common databases dealing with the transport properties of molecules utilize two more parameters, the dipole-momentum and symmetrizing momentum of molecules. These characteristics may be of importance for water. However, the reactants are simple molecules in our reactions. Only the properties of the reactants are necessary for the calculations and for burnable mixtures the concentration of water remains moderate. Therefore, the formulation supplied is expected to provide with the sufficient accuracy.

Chapter 5

KYLCOM Model: turbulent velocity correlation and flame instability modeling

5.1 Introduction

Some aspects of combustion modeling should be treated related to some specific problem and therefore cannot be related specifically to the chapter 4. These are connected with experiments that were performed in order to add an additional refinement and accuracy to the KYLCOM methodology. Concretely, this regards the selection of the most adequate turbulent burning velocity expression and the modeling of the flame instabilities. In this chapter, we do not treat the application of the KYLCOM model to a series of particular and specific problems, an activity that will be carried out in chapter 6

In order to select, among the expressions proposed in table 4.1 in page 58, the

most accurate expression for the turbulent flame speed, such formulae have been tested against a set of selected problems. These problems correspond to moderate scale explosions for which high quality experimental data is available in the laboratory of the author.

The modeling of flame instabilities is considered in the second part of this chapter. Those appear to be significant for flames propagating in an ample domain in which turbulence is not important due to the absence of obstacles. Experimental data in such domains was available through collaboration program in the OCDE for the performance of the modeling.

5.2 The DRIVER experiment

5.2.1 General

Explosions developing in a channel filled with reactive mixture have been the object of numerous experimental, numerical and analytic investigations (e.g. (Dorofeev et al., 2000), (Chao and Lee, 2003)). Due to the relative simplicity and clearness of the interpretation of the experimental results, such type of explosions can be selected for combustion models validation.

In general, in the experiments dealing with explosion tubes, a weak ignition source, like a low energy electric spark, is used for the initiation of the combustion process. The flame starts to propagate slowly with a velocity comprised between several centimeters and several meters per second. Due to the obstacles, which generate turbulence, and the confinement, the flame suffers gradually strong accelerations. A positive feedback mechanism between burning rate and turbulence production causes flame acceleration, ensued in some cases by transition to detonation. This feedback loop may be undermined or even interrupted by the tendency of the flame to quench (see introduction 1.7) due to flame stretch and heat losses.

The experiments performed in combustion tubes can provide experimental data related to full spectrum of possible combustion regimes. Consideration of the

experimental results presented in the papers of Kuznetsov et al. (2002b), Dorofeev et al. (2000, 2001) and Yanez et al. (2011e, 2010a, 2014b, 2013a)¹ shows that three clearly identified regimes of the combustion processes were observed by these authors: slow sub-sonic, fast super-sonic (choked) and quasi detonations.

The experiments selected for the validation and evaluation of the different models are described in detail by Scholtyssek (2004). The facility is an obstructed cylindrical channel with length 12.2 m and diameter 174 mm, see Figure 5.1.



Figure 5.1: The Driver facility located at the Konevets Island, Ladoga Lake, Russia.

The selected degree of obstruction, ratio of area of the opening and the total area, is 0.6. Obstacles are made up of a set of disks with an orifice in its center. The distance between obstacles is equal to the diameter, so that a total of 68 obstacles appear in the channel. Although in the experiments, effects like venting and ignition position were tested, this study is limited to a single configuration with no venting and a single ignition position with two pre-mixed, lean, compositions with the goal to evaluate the predictive capabilities of the KYLCOM method. Taking this into account, from the wide matrix of available experiments the tests *mc003* and the *mc012* were selected, whose main characteristics are detailed in Table 5.1. Lean composition were chosen as they are more significant of the conditions found in some safety problems. Also they are more challenging for the modeling due to the Thermo-diffusive instability as would be later discussed.

A sketch of the experimental device is shown in Figure 5.2.

¹Co-authored by the candidate

Table 5.1: Main characteristics of the selected experiments.

Name	H ₂ Conc. Vol. %	Press [10 ⁵ Pa]	Temp [° C]	Regime
mc003	10	1.02	12	Unstable / slow
mc012	13	1.01	12	Choking

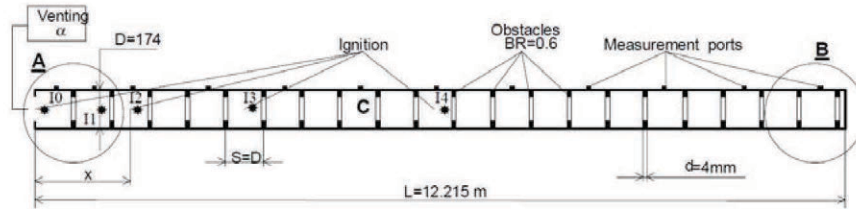


Figure 5.2: Cylindrical channel configuration. Total length 12.215 m, diameter 174 mm, length represent 68 diameters. The pitch between obstacles is equal to the diameter.

The instrumentation installed in the experiment consists on 23 light diodes and 13 pressure gauges. After the flame has passed several obstacles, a quasi-stationary choked combustion regime is reached. Matching the flame propagation speed in this stationary regime, is the main goal of this numerical experiment and allow ranking the different expressions of the turbulent burning velocity that were presented in Table 4.1 in page 61.

At this juncture, it would be appropriate to mention that the results that are going to be shown in this Chapter strictly apply just for the scales of the respective experiments. Certainly, combustion does not scale (Zeldovich et al., 1985). Nevertheless, the conclusions that will be drawn are going to be utilized in calculations involving real facilities of a size one or two orders of magnitude larger (e.g. see Chapters 6 and 7) which is certainly a significant weakness of modeling. Uncertainties in combustion related to the scaling of the experiments can only be reduced utilizing experiments as large as possible or available, as is done here, a course of action that has evident limitations involving cost, availability of the facilities, etc.

5.2.2 Modeling of the initial stage of the combustion

In all turbulence models of practical interest (k - ε , k - ω , SST, Les Eddy-viscosity-eddy-diffusivity, mixed, dynamic) an interface representing a gradient of speed triggers the generation of turbulence. Nevertheless, a planar shock evolving in a non-perturbed atmosphere does not generate turbulence. Thus, any of the turbulence models available generates a non-physical increment of turbulence in the presence of shock waves (Pope, 2000). To the difficulties mentioned it should be added the general restrictions that apply to standard turbulence models (see the review in the introduction, section 1.5) that generally consider relatively high Reynolds numbers and well developed isotropic turbulence, e.g. (Rodi and Mansour, 1993), (Sagaut, 2001).

After the ignition, and in the early stage, a spherical flame front will propagate in the laminar regime. It will develop in the unburnt mixture like a subsonic wave due to diffusive transport of mass and energy (Zeldovich et al., 1985). In the subsequent phase, the flame will abandon its perfectly spherical propagation. Initially, a crack line and afterwards some cellularity will appear in the surface of the flame (Molkov et al., 2004). This instability onset will produce some increase of the velocity of propagation that will also rise with time. This phenomenon is attributed to the thermo-diffusive and Landau-Darrieus instability. The process will culminate with the transition to the turbulent regime, or self turbulization, created exclusively by the intrinsic unstable nature of flames.

Following Bechtold and Matalon (1987) and Bradley et al. (2000, 2007a) there exist two critical Peclet numbers that limit the domain of instability. The Peclet number should be understood as the ratio of the flame radius R_d divided by the laminar flame thickness δ . The cracks begin to exist and propagate when the first critical Peclet number is reached. The larger Peclet number is connected with the formation of smaller cells that appear over the entire surface of the quasi spherical surface of the flame. The values of the critical Peclet numbers depend on the Markstein number and thus on the concentration. The critical Peclet numbers can be visualized in the Figure 5.3, where the corresponding limiting stable wavenum-

bers $n = 2\pi Pe\delta/\lambda_d$ are depicted for different Ma_{sr} , see (Bradley et al., 2007a), as a function of Pe . Bradley et al. (2000) consider that the flame stretch rate can be divided into two major parts: the part associated with aerodynamic strain and the contribution due to the curvature. The Markstein number associated with aerodynamic strain Ma_{sr} will be then measured into experimental facilities subtracting the effect of the curvature (spherical flames).

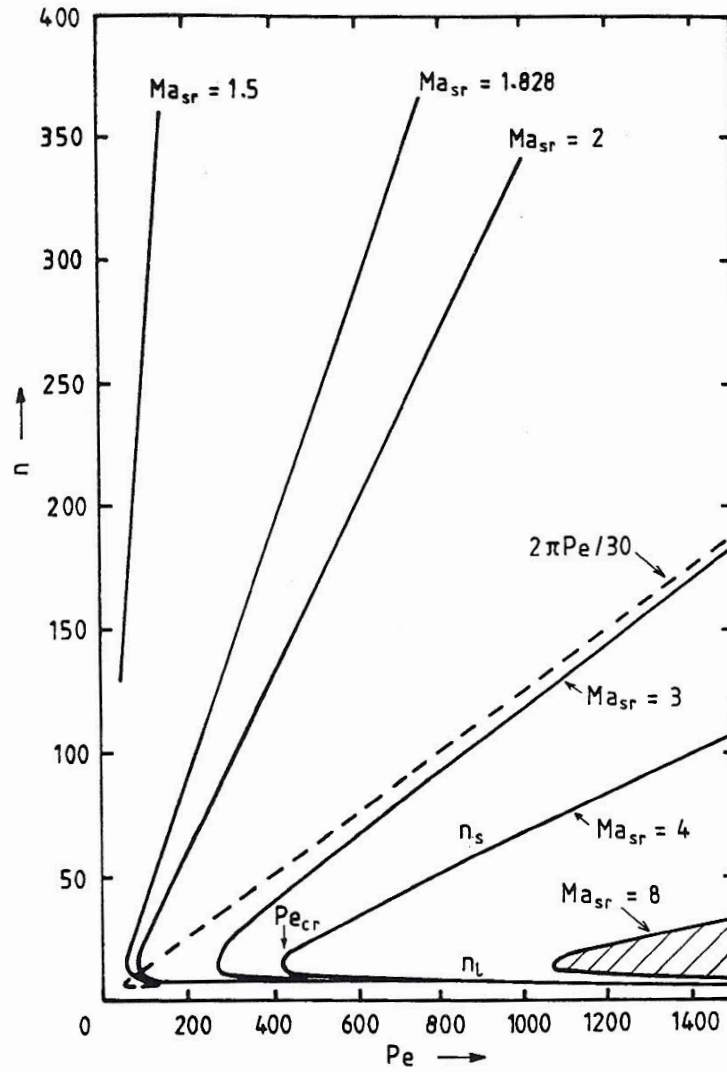


Figure 5.3: Wave numbers n (ordinates) at limits for flame stability for different Ma_{sr} as a function of Pe number. Source (Bradley et al., 2000).

The diagram contained in Figure 5.3 allows inferring the maximum flame diameter for which the propagation of the flame is expected to remain laminar. Such

value, is obtained from the corresponding laminar limit Peclet number which can be obtained considering the vertex of the instability peninsula.

In addition to the instabilities connected to the expansion of combustion products (Landau-Darrieus (Landau, 1944), diffusive (Godreche and Mannenville, 1998) and cellular (Matsukov et al., 1998)) flames suffer instabilities due to the interaction with shocks or sound waves that are promoted by the confinement in the form of reflections from walls (Bychkov and Liberman, 2000). The modeling of this laminar-transitional-turbulent behavior is very arduous. Its intrinsic complexity is not reduced in large scale simulations, where this phenomenon, partially or completely, takes place inside a single control volume, depending on the resolution.

In spite of these difficulties, some modeling can be provided. As shown in Figure 5.3 in an initial stage, immediately after the ignition (small Pe), the flame burns in the laminar regime for all wave numbers until critical Peclet number is reached (vertex of the peninsula). For the modeling, it can be considered that after this phase a sharp transition to the turbulent regime takes place.

Accurate experiments studying the flame acceleration due to its instabilities in big unconfined volumes have been performed in the Fraunhofer-Institut (Pfortner and Schneider, 1983). They involved deflagrations initiated in a 10 m diameter hemispherical balloon located in an open field and filled with a hydrogen-air mixture in stoichiometric concentration and standard conditions. In unconfined geometries, the results suggest that for the first 1.0 to 1.2 m. or first 50 to 60 ms., the combustion takes place merely in laminar regime. After that interval the flame suffers a gradual transition and evolves in the turbulent regime. In addition to its size, it is a big advantage that these experiments have been carried out in unconfined configurations so that the results could not be distorted by reflections of waves or shock waves from the walls. In spite of its closed geometry, this is of importance for the DRIVER experiment in the early stage of the flame propagation until the flame start to interact with the turbulence generated by the first obstacle.

Three strategies were taken into account to try to model this behavior by the author defining the initial stage flame propagation velocity S_i :

-
1. The first consist on introducing a defined time where the mentioned sharp transition takes place. This is suitable for calculations in which the resolution is poor. Thus, the transition to turbulence appears inside the first calculation cell even if the Peclet number corresponding to the vertex of the peninsula is quite high.
 2. The second alternative consist on substituting the time limitation by a radius limitation. This modeling is tough to be adequate for those simulations in which the ratio between Pe number for the vertex of the peninsula of stability to the dimensionless resolution is high. The ratio $Pe\delta/\Delta_x$ in which δ is the thermal flame thickness and Δ_x the resolution of the calculation, should be large enough to allow for a significant computational area in which the flame evolves as purely laminar inside the calculation domain $Pe\delta/\Delta_x = R_d/\Delta_x \gg 1$.
 3. The third option consists on comparing the chosen expression from the contained in Table 4.1 for S_t with a so-called quasi-laminar burning velocity, S_{QL} . The resulting flame propagation is provided by the smaller of them (Arntzen, 1998)

$$S_i = \min(S_t, S_{QL}), \quad (5.1)$$

in which the quasi-laminar burning velocity is defined as

$$S_{QL} = S_L (1 + a R_f)^{\frac{1}{2}}. \quad (5.2)$$

with R_f being the distance to the ignition position and a a given parameter that must be fixed comparing with experiments. The last model represents an attempt to take into account the combined effect of the Landau-Darrieus and the thermo-diffusive instabilities inside the phenomenological variable S_{QL} . This magnitude can be determined in turn from experiments adjusting the parameter a . This methodology is especially well suited for those cases

in which the calculation domain is large and free of any obstacles and obstruction.

It was already mentioned that in close geometries reflections from the walls can accelerate the flame due to flame-shock interaction (sometimes also called Richtmyer-Meshkov instability) (Bychkov and Liberman, 2000). Certainly, this phenomenon is a limitation to the rather simplistic modeling carried out in this paragraph based on unconfined (or confined in which the ratio of flame radius to container radius is very small) data. Clearly, for those geometries in which the typical length of the flame to the typical length of the container is comparable, the reflections from the wall will play a significant role in the flame wrinkling, propagation, etc. Thus, for large scale calculations these effects will not be calculable ($O(R_d) \approx O(R_{container}) \approx O(\Delta_x)$) and certainly data obtained in unconfined configurations cannot be extrapolated to confined.

5.2.3 The KYLCOM model in the initial stage of the combustion

As discussed in section 4.2 the KYLCOM model is based on defining a turbulent flame velocity. Different correlations, appearing in Table 4.1, are proposed. They will be ranked now with the help of the Driver experiment considering also the modeling of the initial combustion stages just discussed in section 5.2.2.

It is now necessary, for the sake of clarity, to clarify how the modeling of the initial stage affects the KYLCOM model.

Considering the laminar, transitional and turbulent stages of the flame we may define an effective flame burning velocity S_{eff} taking into account discussed the discussed criterion in section 5.2.2. Considering equations (4.9) and (4.40) we may rewrite the consumption rate $\bar{\omega}$

$$\bar{\omega} = \begin{cases} \frac{(A \cdot \theta + B) S_{eff}}{\Delta x} (1 - \bar{f}_{i,j,k}) & F_{i,j,k} > \left(\frac{1}{2}\right)^2 \\ 0 & F_{i,j,k} < \left(\frac{1}{2}\right)^2 \end{cases}, \quad (5.3)$$

and define,

$$S_{eff} = \begin{cases} S_i & \text{if criteria in section 5.2.2 is fulfilled, e.g., } t > t_{transition} \\ S_t \text{ from table 4.1} & \text{if criteria in section 5.2.2 is not fulfilled} \end{cases}, \quad (5.4)$$

were were the control parameter $F_{i,j,k}$ remain s as defined in (4.8).

5.2.4 Results

A structured hexahedra mesh containing 15 nodes inside the radius of the tube and a resolution of 5.8 mm was adopted for the simulation(see Table 5.2).

Table 5.2: Characteristics of the mesh used in Driver test calculations

Domain size LxWxH, cells	Resolution	Cell Number
15x15x2103	5.8 mm	473275

Test cases were performed during the development of the model to study the flame speed grid dependence. The results revealed that the sensitivity to the resolution utilized was smaller than 0.5% in case of a refinement up to eight times.

In order to improve the calculation performance only one quarter of the section of the tube was simulated.

The geometry utilized in the simulations is represented in the Figure 5.4



Figure 5.4: Geometry employed in the calculations. In the figure, one fourth of the total length of the Driver tube is represented. Additionally, the transverse section was also one fourth of the total.

The system of equations that was resolved accounted for the equations (1.14) to (1.24) for the mass, momentum, energy, species and turbulence model. The convective terms in all transport equations were calculated with the TVD (Harten, 1983) 2^{nd} order non-oscillatory scheme. Diffusive terms were calculated using 2^{nd} order central differences (LeVeque, 2007). Time integration for both convective and diffusive terms was also second order accurate. RANS-standard $k - \epsilon$ turbulent model was selected (equations (1.22)-(1.24) in chapter 1.5.4), a choice which is compatible with the aforementioned simplifications. The standard $k - \epsilon$ set of constants calibrated for tubes, see Table 1.2, was selected to ensure that the turbulence field was representative. Significant details on the numerical implementation, numerical method utilized, etc, can be found in the manual of the code *COM3D* Kotchourko et al. (2015)² utilized to obtain the results.

²Co-authored by the candidate

Both KYLCOM, see section 4.2, and a modified Zimont models (the modified Zimont Model is later described in section 5.2.4.2 in page 122) were utilized for combustion simulation. For KYLCOM the equations (4.7), (4.8), (4.9), were utilized for the propagation algorithm. The calculations were performed for each member of the list in Table 4.1. For Zimont model, also the elements of the Table 4.1 were utilized, coupled with the equation (1.41).

5.2.4.1 Experiment *mc012*: KYLCOM model

The main features of the development patterns of the flame propagation process in *mc012* experiment (see Table 5.1) can be graphically presented in the sequence contained in Figure 5.5. An initial phase of the combustion, which occurs in a *quasi-laminar* regime, is shown in the first frame in which the flame remains behind the first obstacle. The transitional regime, started mainly due to the interaction with the first obstacle, is visualized in the second frame. The acceleration phase is shown in the third and fourth. The quasi stationary propagation regime, chocking as advanced in Table 5.1, can be seen in the last two.

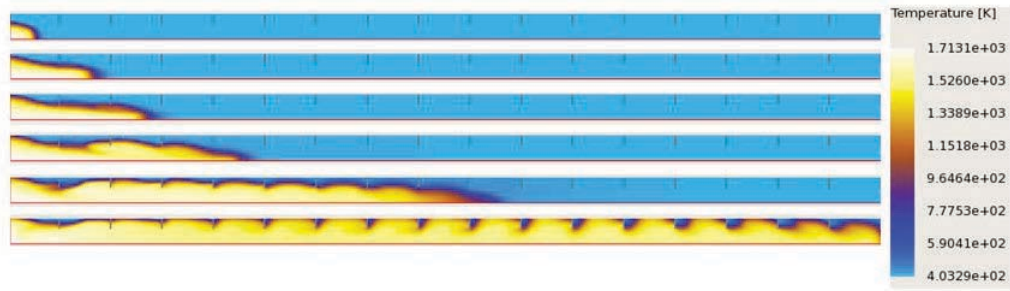


Figure 5.5: Evolution of the flame inside the tube. Temperature field cuts at $6.6 \cdot 10^{-2}$, $1.04 \cdot 10^{-1}$, $1.16 \cdot 10^{-1}$, $1.22 \cdot 10^{-1}$, $1.28 \cdot 10^{-1}$, $1.28 \cdot 10^{-1}$, $1.32 \cdot 10^{-1}$ s. Frames obtained with Schmid correlation, see Table 4.1, utilizing KYLCOM model.

For experiments carried out in combustion tubes with such or similar conditions as the Driver *mc012*, e.g. Kuznetsov et al. (2002a), the combustion regime

(flame velocities), is almost exclusively define pressure wave characteristics. Therefore comparison of simulation results has been restricted to flame velocities exclusively. The diagram describing the dependence of visible flame speeds on time for the different closure models of Table 4.1 is shown in Figure 5.6 for KYLCOM model in the Figure 5.7 and for the Zimont method.

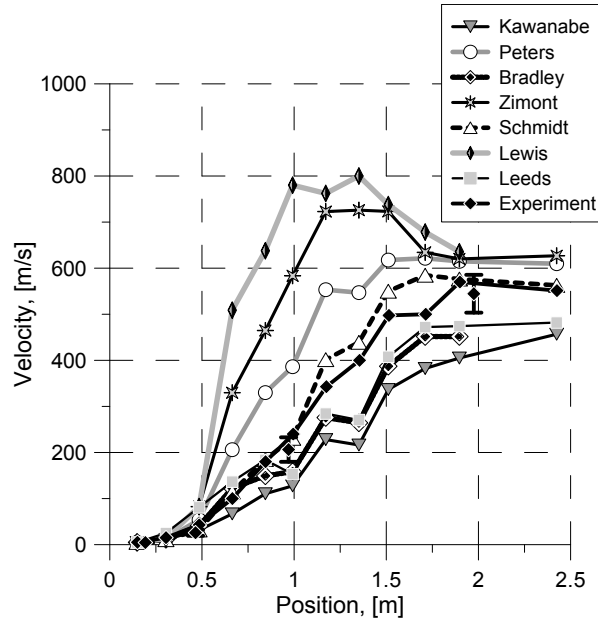


Figure 5.6: Flame speeds obtained in the simulations of *mc012* test carried out with KYLCOM model and the set of closures appearing in Table 4.1.

Similarly to the simulations frames of figure 5.5 two distinctive flame propagation regimes in the experiment appeared in Figure 5.6: an initial acceleration phase followed by a second stage in which the velocity of the propagation is quasi-constant.

The initial phase shows an exponential behavior typical of the so-called *finger flames* whose dynamics have been studied by Clanet and Searby (1996). The shape of these flames can be approximated by a cylinder plus a hemispherical surface, a combination that resembles a finger thus naming the regime. This regime hap-

pens in tubes in an intermediate stage of propagation when an initially spherically propagating flame start to disfigure in the non-confined direction of the tube and before it has reached the wall. If the time when the initial change of shape is characterized by the variable t_{sphere} the visual propagation velocity of the flame is

$$v = 2\sigma S_L \exp\left(\frac{2\sigma S_L}{R}(t - t_{sphere})\right), \quad (5.5)$$

where σ is the expansion of the gases, S_L the laminar burning velocity and R the radius of the tube. The regime is limited by the time in which the *skirt* of the flame has reached the wall (in a position near the ignition) and it is characterized by a notable increase of the flame surface and its corresponding flame acceleration.

Elongation and acceleration is a typical behavior of *finger flames* and has a simple qualitative explanation due to the motion generated by the flame before his own forehead. In the longitudinal direction of the tube the motion before the flame find no special impediment. In the transverse direction the flow finds a nearby wall. The flame begins to elongate adopting the shaped of a ellipse (the finger). Naturally the reaction also continues in traversal direction and the moment when the flame touches the wall marks the end of this phase. The result, if we would consider we have in experiment *mc012* a *finger flame* is that the flame ring would have a shape of one ring in traversal direction and ten rings in the longitudinal. Certainly, the analogy between the flame acceleration described by Figure 5.6 and the *finger flames* is arguable, as the description of the later, which is intended for flat tubes, notably does not include the obstacles which are present in the Driver experiment. The turbulence generated by them it is thus not taken into account by *finger flames* considerations. Still is notable the analogy between the exponential law of eq. (5.5) and the initial acceleration of the curves in Figure 5.6.

The second stage of the propagation of the flame starts after the flame reaches a distance of approximately 10 diameters (1.8 m) of a total length of the tube of 68. In this second phase the choked regime is established and the flame progresses in a quasi-stationary regime until the end of the tube.

For such regime, the flame speed typically obtained lays between a third and a half of the Chapman-Jouget detonation velocity (Gamezo et al., 2007). The Chapman-Jouget detonation velocity corresponds to 1293 m/s and 1436 m/s respectively for *mc003* and *mc012* tests. Therefore, for the experiment *mc003* a propagation velocity in the interval 430-650 m/s should be expected while for *mc012* tests the corresponding range is 480-720 m/s.

We may now try to understand the reason for the quasi-steady propagation velocity. In a non-obstacle one-dimensional choked flame, both the leading shock and the flame are super-sonic with respect to the pre-heated reactants. Obstacles create a more complex pattern in which both the leading shock and the flame suffer velocity changes. Consequently, the distance between them does not remain completely constant but cyclically oscillates around an average value which depends on the relative position of the leading shock, flame and obstacles.

In the simulations, the feedback mechanism between expansion, turbulence generation and burning rate saturates. A run up phenomena driving the calculation to detonation is therefore avoided and the turbulence intensity reaches a quasi-stationary value. The turbulent flame speed remains at an almost constant level after initial acceleration.

The accuracy in the prediction of the visual flame velocity in the choked regime as well as the acceleration area offers a criterion to rank the phenomenological correlations. The best fit was obtained, in order of preference, by Schmidt, the Leeds methodology modified by Arnzen, and Peters correlations (see Table 4.1 for details on closure models).

Among these three, the correlation due to Schmidt was the only one whose results stay inside the estimated experimental error-bars. A note on error-bars is pertinent. The detailed experiment whose results we are using for comparison was not repeated. The error-bars were calculated from three experiments carried out in the same facility and conditions but utilizing a fewer amount of transducers in another experimental series. Therefore, they are not symmetric (with respect to the detailed experimental data) and only three points are available.

5.2.4.2 Experiment *mc012*: Modified Zimont method

Experiment *mc012* was also simulated with the Zimont flame propagation method (Zimont, 1977; Zimont and Mesheriakov, 1988) in the same conditions utilized for KYLCOM. Results were discouraging due to the extension of the flame brush. As already mentioned in section 1.6.6, this difficulty is related to the turbulent diffusion that controls this magnitude. To eliminate this shortcoming, a modified Zimont model was employed to avoid the thickening of the flame propagation front due to diffusion. Under this formulation the mass consumption rate term adopts the form

$$\frac{\partial \bar{\rho} \tilde{f}}{\partial t} + \frac{\partial \bar{\rho} \tilde{f} \tilde{u}_i}{\partial x_i} = \rho_u S_t |\nabla \tilde{f}|, \quad (5.6)$$

where the turbulent transport is disregarded (compare with eq. (1.41)). In the reasoning included in the introduction chapter, under the section 1.6.7.3 in page 34, we mentioned that if the complete formulation had been adopted, see (1.41), the flame brush thickness, as mentioned in section 1.6.7.3 would have grown similarly to

$$\frac{\partial \bar{\rho} \bar{f}}{\partial t} = \frac{\partial}{\partial x_i} \left(\bar{D} \bar{\rho} \frac{\partial \bar{f}}{\partial x_i} \right). \quad (5.7)$$

In fact, equation (5.7) was obtained considering the behavior of the incompressible analogue

$$\frac{\partial \bar{f}}{\partial t} = \frac{\partial}{\partial x_i} \left(\bar{D} \frac{\partial \bar{f}}{\partial x_i} \right), \quad (5.8)$$

whose well known solution is

$$\bar{f}(t) = \bar{f}(0) \operatorname{erfc} \left(x / \left(2 \sqrt{\bar{D} t} \right) \right) \quad (5.9)$$

with thickness values of the order $\sqrt{\bar{D} t}$. The model was in fact intended to model this effect.

Nevertheless, this makes the calculation completely non-representative if we consider calculation cells much larger than the flame thickness and if the turbulent diffusion coefficient is very large. Suppression of the turbulent transport, like in

(5.6), reduces significantly this problematic but brings another problematic. That is, the transport of the variable f is incoherent with the transport of the other variables, for which turbulent transport is considered.

The propagation velocities are presented in the Figure 5.7. The better results were obtained for the Schmid, Zimont and Peters correlations. Taking into account the error-bars results, a significantly smaller dispersion in the results of the correlations results from utilizing this model compared with KYLCOM, see Figure 5.6. Although this reduced dispersion is clearly an advantage for the utilization of the Zimont model, the incoherent transportation of the progress variable and the enlarged flame brush, resulting in a nonphysical flame propagation pattern, amply compensates this benefit. It is remarkable that the Kawanabe correlation, due to its simplicity, is still producing neither a stationary nor a quasi stationary solution when the flame reaches the end of the simulated tube.

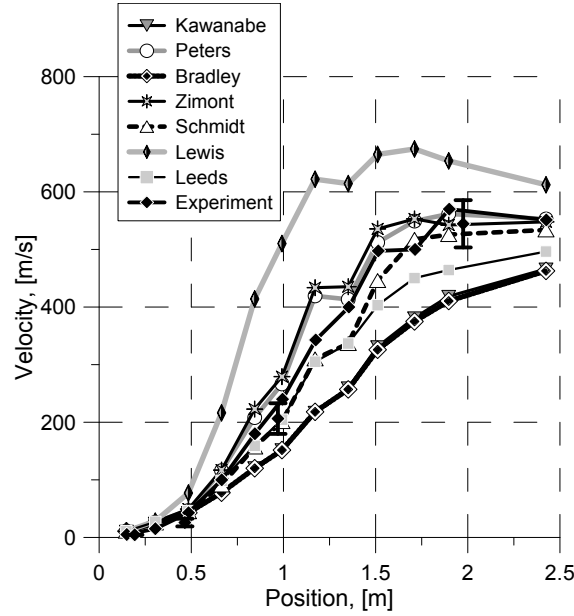


Figure 5.7: Flame speeds obtained in the simulations of *mc012* test with the modified Zimont Model.

5.2.4.3 Experiment *mc003*: KYLCOM model

In Figure 5.8 the flame velocities obtained in the experiments and simulations of the *mc003* case are depicted. The parameters for this case are shown in Table 5.2, leading to a unstable/slow combustion regime. Actually, and contrary to the *mc012* a stationary regime was never attained in the experiments. An acceleration-deceleration cycle (where deceleration is probably connected with local quenching) appears instead. It is clear from Figure 5.2 that the numerical simulations have been unable to provide accurate results for this case.

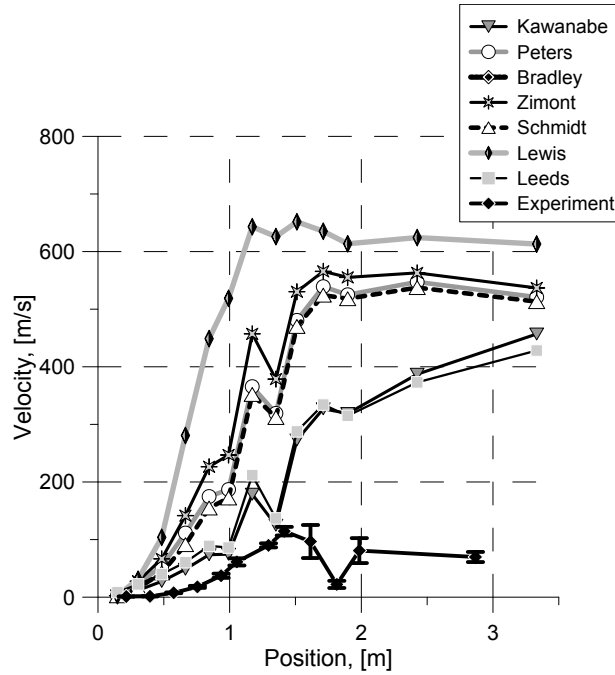


Figure 5.8: Flame speeds obtained in the simulations of *mc003* test with the KYLCOM Model.

Information about repeated attempts of this same experiments are presented in Figure 5.9. As can be appreciated, although reproducible in its main features, the details of the position-flame velocity curves are different across experiments,

indicating a significant stochastic physical behavior. This is one main reason for the difficulties found by the KYLCOM model to accurately simulate this case.

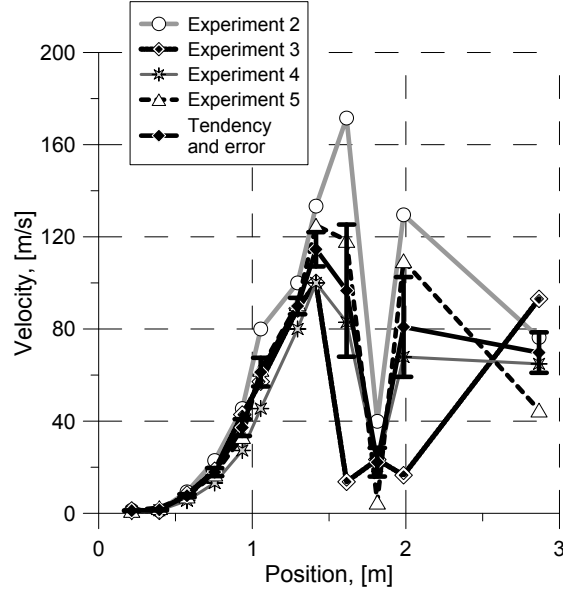


Figure 5.9: Flame speeds obtained from different experimental trials in the simulations of *mc003* test.

Let us now analyze the causes of this behavior. The Lewis number of the mixture for both problems, *mc-012* and *mc-003*, was similar and approximately 0.4. The dissimilarity of the Markstein numbers was more meaningful, -1.1 for *mc012* and -1.8 in *mc003*, and represents an explanatory parameter for the behavior difference.

Take into account that the sign of Markstein number defines the response of a flame to stretch and strain. A positive Markstein number leads to decrease of the local burning velocity while negative values stretch tends to increase the burning velocity (see e.g. Dorofeev (2008)). It is also known, that positive Ma has an stabilizing effect (Joulin and Clavin, 1978) on flame wrinkling and moderates hydrodynamics instability. Also, that flames with have negative Markstein numbers exhibit very unstably regimes as experimentally proven by (Dorofeev et al., 2001).

In this sense, it can be foreseen that the 40% difference in negative Ma between the mixtures in experiment *mc003* and *mc012* could have a significant effect on the stability of the propagation regime.

The importance and the randomness of the quenching can be studied observing the data of the five *mc003* test repetitions documented in Table 5.3. In such experiments between 40 and 88 % of the total fuel amount remained unburned depending on the experimental trial.

Table 5.3: Importance of quenching in the experiment mc-003

Experiment number	vol. % burned H_2
1	12
2	58
3	60
4	44
5	26

Certainly, heat losses and turbulence intensity are significant parameters for the quenching phenomenon (Bradley et al., 2007b). With the purpose of elucidating the importance of quenching due to heat losses we may make a comparison with other experiments carried out by Kuznetsov et al. (2002b) with the same concentration and blockage ratio but with different diameter and thus with relatively smaller heat losses leading to lower likelihood of flame extinction.

On these tests, the flame accelerates and reaches a quasi-stationary propagation after approximately ten tube diameters. Thereafter the propagation velocity obtained oscillates slightly around the value of 200 m/s. It should be recalled that this comparison is inconclusive because the change of the diameter also modifies the integral length of the turbulence, but it is a hint on the fact that even if cyclic behavior could be associated to heat losses the general behavior of the problem does not depend so significantly on it. Even if the oscillations are avoided, the deviations between the calculations that predicted a choked regime instead of slow

flame propagation (500 m/s instead of 200m/s) are very significant and cannot be explained by heat losses.

Considering these results, further model development locally taking into account a quenching mechanism (as e.g. in recent work (Bradley et al., 2007b)) is necessary to perform more realistic simulation of the considered problem. These observations are in agreement with the model limitations previously discussed, see section 4.2.3, specially those related to quenching. Those limitations were namely, that the model assumes that an increase in turbulent speed always enhances the turbulent burning velocity (flame quenching starts to dominate the combustion process for very intense turbulence). It also disregards the effect of the Markstein number on the propagation. All those shortcomings results in an spurious flame acceleration.

The behavior observed in the experimental tests (Figure 5.9) of the experiment could be more easily understood if we consider the Borghi diagram³, Figure 5.10.

In first approximation, fast propagation regimes in tubes can be easily analyzed assuming that the integral scale of the turbulence is of the same order of the diameter of the tube $L \approx D$.

On one hand, the thickness of the flame δ for the mixture of experiment *mc003* 10 % vol. H_2 is 250 μm . Thus the ratio $L/\delta \approx D/\delta$ reaches 700, and the locus of possible propagation regimes inside the Borghi diagram is reduced to a vertical line.

On the other hand, the values of u' in obstructed channels, as they can be sampled for example from the calculations carried out, are typically larger than 1 m s^{-1} . Therefore, due to the relatively small laminar burning velocity of 0.11 m s^{-1} for 10% vol. H_2 mixtures, the ratio u'/S_L is large, $\gg 1$, even for moderately large values of the u' .

Taking the previous discussion into account, the domain of flame propagation regimes was depicted in Figure 5.10 by a thick vertical black segment. The line has its lower limit in the region of thickened flames and penetrates in the domain dominated by quenching (upper grey peninsula).

³Borghi diagram was already described in the Introduction chapter in page 26

Therefore, the propagation regime is so that cyclically accelerate due to intense generation of turbulence provided by the obstacles and subsequently decelerates, thanks to extinction or local extinction, covering the domain represented by the straight black line.

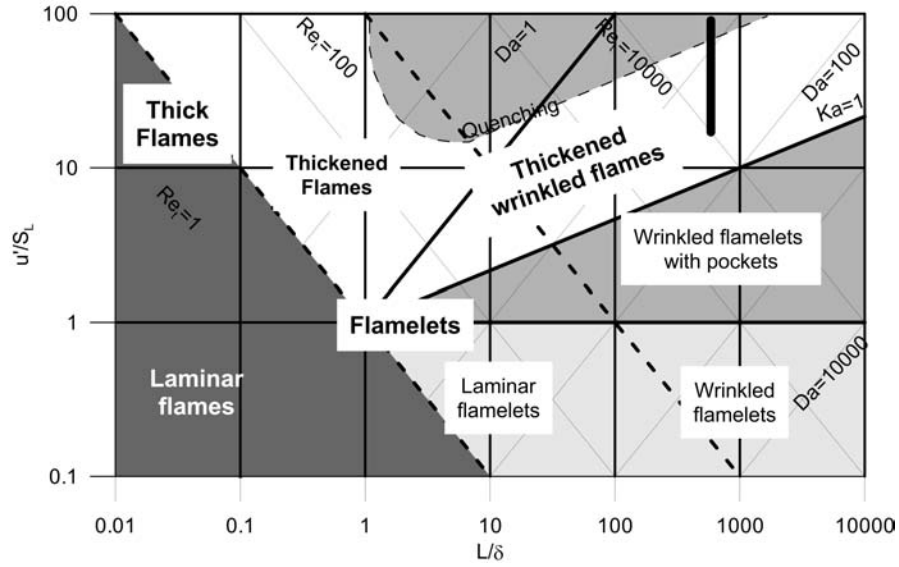


Figure 5.10: Turbulent premixed combustion diagram for test *mc003*. Note the domain of possible propagation regimes for experiment *mc003* represented by a black vertical straight line in the upper right area of the figure.

The results contained in Bradley et al. (2008) or Bradley et al. (2007b) reveal that the turbulent burning velocity increases with a growth of the turbulent flame velocity until it attains a maximum. Thereafter, it decreases as flame quenching starts to dominate the combustion process. The dependence of flame velocity on turbulence intensity for such flames is complex and is mostly determined by the strained Markstein number (Bradley et al., 2008). In the phenomenological correlations shown in Table 4.1 an augment in turbulent speed always enhances the turbulent burning velocity. Therefore, spurious flame accelerations will result from intense and unrealistic feedback between turbulence generation and products ex-

pansion. Thus, further modeling to include in the correlations the effect of the flame stretching is necessary.

5.3 THAI experiment

5.3.1 General

As a part the licensing process of the reactor containments, the threat of uncontrolled hydrogen release and combustion must be addressed. Although state-of-the-art mitigation systems can significantly reduce the risk of a combustion accident scenario, under severe circumstances low concentration deflagration processes must be assessed.

The general objective of the THAI experiments (Kanzleiter and Langer, 2008b), (Kanzleiter and Langer, 2008a) and (Kanzleiter and Langer, 2008c) was to investigate hydrogen deflagrations at low concentrations with vertical flame propagation in a sufficiently large geometry under conditions typical of severe accidents in nuclear reactors. The size and shape of the facility as well as the initial temperature, pressure and steam concentrations considered, ought to guarantee that the experiments match typical containment conditions (Yanez et al., 2012a)⁴.

In slow deflagrations propagating in non-obstructed, diluted or undiluted, very lean H_2 -air mixtures, the propagation velocity is mainly determined by the flame instabilities. This is a completely different propagation regime from the one appearing in the Driver experiments, see section 5.2.1, in which it could be considered that the flame propagation was solely determined by the turbulence⁵.

During the last decades, numerous studies performed by brilliant scientists, among others Zeldovich et al. (1985), Searby and Clavin (1986), Bychkov and Liberman (2000), have allowed to achieve a certain maturity in the understanding of flame instabilities. Nevertheless, the application of this knowledge to practical simulations for the industrial safety has only recently started (Bauwens et al., 2011).

⁴Co-authored article by the candidate

⁵In Driver experiment *mc003* quenching has a fundamental importance. Still, quenching due to stretching and strain, should be accounted for as a phenomenon, if not uniquely caused, definitely fundamentally determined by turbulence, see e.g. Bradley et al. (2007b,a)

Due to the characteristics of the problems we aim at addressing, the consideration of such phenomena becomes essential and careful assessments of the thermo-diffusive, the Rayleigh-Taylor and the acoustic-parametric instability are necessary.

5.3.2 Description of the experiment

The main component of the facility is a cylindrical steel vessel, 9.2 m height, 3.2 m diameter and with a total volume of 60 m^3 (see Figure 5.11). At the lower end a sump compartment is attached. The outer cylindrical wall has cooling/heating jackets subdivided in three vertical sections. The entire vessel is thermally insulated with a double-wall, being the inner wall 22 mm thick and the outer wall made from 6-mm stainless steel. The 16.5-mm gap between the walls is filled with thermal oil. The outside wall is insulated by the 120 mm rockwool layer.

An air-driven axial fan near the hydrogen distributor is applied to homogenize the vessel atmosphere prior to ignition. 43 fast thermocouples were installed at 13 different elevations inside the vessel to monitor flame propagation and flame temperature during the combustion (see Figure 5.12 right). In addition, the transient deflagration pressure was monitored by four fast pressure transducers of strain gauge type. The setup of the whole implementation can be observed in Figure 5.13. As a result of the experiments, detailed recordings of flame propagation, pressure transients, temperature transients and combustion completeness were obtained.

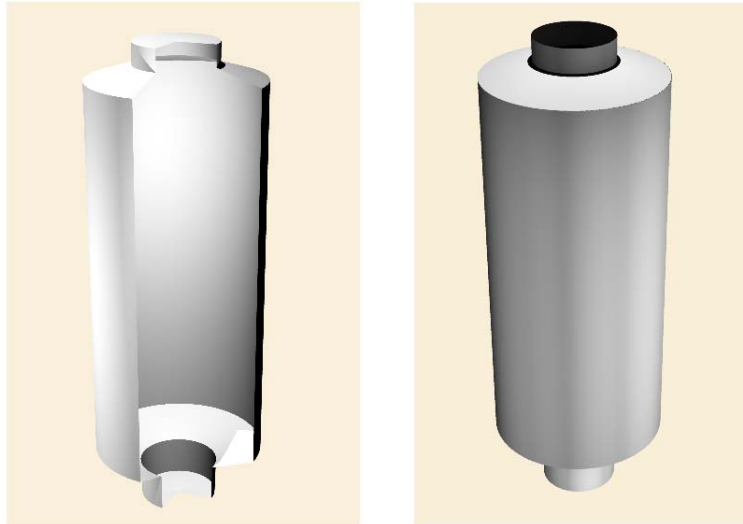


Figure 5.11: General external view of the the THAI facility generated with *Rhinoceros* software.

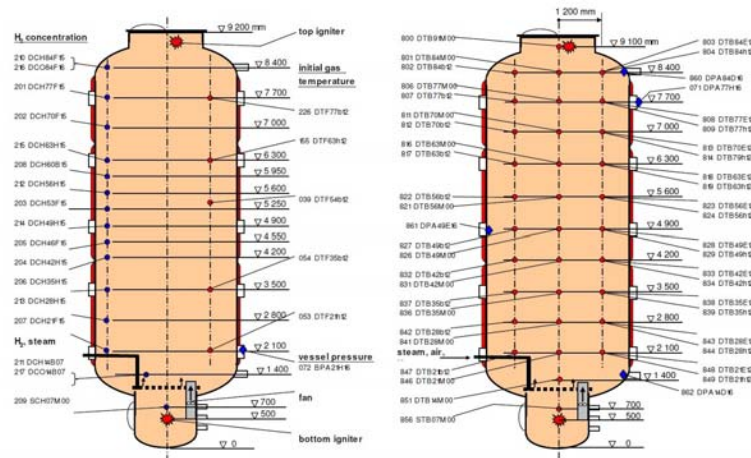


Figure 5.12: Instrumentation positions. Left, concentration measurement positions. Right, fast thermocouples location. Diagram taken from Kanzleiter and Langer (2008b)

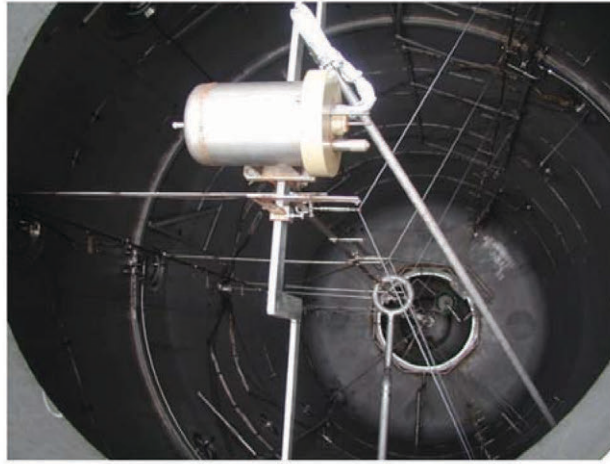


Figure 5.13: Internal view of the vessel. Igniter, instrumentation fittings and sump. Photograph appearing in Kanzleiter and Langer (2008b)

The matrix of experiments contained a total of 29 hydrogen deflagration tests. The objectives of such a wide matrix were, among others, to address mixtures with different H_2 concentrations, the presence of dilutants (steam), upwards and downwards concentrations gradients and combustion. The details of those test are contained in the references (Kanzleiter and Langer, 2008b), (Kanzleiter and Langer, 2008a) and (Kanzleiter and Langer, 2008c).

Three essays were selected for simulation purposes: the experiments HD-12 and HD-15 allow studying low-concentration combustion of hydrogen at ambient and high temperature respectively. Additionally, the experiment HD-22 was chosen to simulate the deflagration of a H_2 -steam-air mixture at superheated and saturated conditions. Some significant details of the conditions of the selected experiments are contained in Table 5.4.

Table 5.4: Selected THAI Hydrogen Deflagration Tests.

Name	Pressure [bar]	Temp. [C]	Conc. H_2 [vol %]	Conc. Steam [vol. %]	Max. Pressure [bar]	Max. Temp. [C]
HD-12	1.49	18	8.1	0	5.05	765
HD-15	1.50	93	9.9	0	4.95	950
HD-22	1.48	92	9.9	25	-	-

5.3.3 Numerical simulations

Mahaffy et al. (2007), with the support of the Nuclear Energy Organization (NEA), have given a review of the applications of CFD in safety issues in nuclear reactors, including general and not so conclusive, recommendations on the selection of the turbulence modeling in this environment. Much more concrete, Jimenez (2003) has given criteria and recommendations based on resolution achievable in calculations.

Applying the criteria of the latter author to the THAI problem, it has resulted that simulations ought to be performed with the standard $k - \epsilon$ turbulence model (Launder and Sharma, 1974) as the resolution adopted was not refined enough to allow using Large Eddy Simulation techniques.

The initial level of turbulence and dissipation was chosen with the aim of obtaining a turbulent viscosity, as appear in eq. (1.24) $\nu_t urb = c_\mu k^2/\epsilon$, with a value of the same order of magnitude of the molecular one, that for the conditions of the simulations described in Table 5.4 is of the order of 10^{-5} m s^{-2} . This choices of k and ϵ are in agreement with the criterion given by Arntzen (1998) and is representative of a initially stagnant atmosphere. Therefore, the initial values of k and ϵ were set equal to $10^{-4} \text{ m}^2/\text{s}^2$ and $10^{-4} \text{ m}^2/\text{s}^3$ respectively for all simulations.

The system of equations that should be resolved included the equations (1.14) to (1.24) for the mass, momentum, energy, species and turbulence model. The convective terms in all transport equations were calculated with the TVD (Harten, 1983) 2^{nd} order non-oscillatory scheme. Diffusive terms were calculated using 2^{nd} order central differences (LeVeque, 2007). Time integration for both convective

and diffusive terms was also second order accurate. As aforementioned, a RANS-standard $k - \epsilon$ turbulent model was selected (equations (1.22)-(1.24) in section 1.5.4). KYLCOM model was utilized for combustion simulation. For KYLCOM the equations (4.7), (4.8), (4.9), were utilized for the propagation algorithm. Taking into account the results obtained in the section 5.2 the turbulent burning velocity formulation proposed by Schmid et al. (1998) was utilized (see Table 4.1).

The grid selection was based on the previous experience trying to match the significant features of the experimental setup. The use of relatively coarse mesh (5 cm cell size) was dictated by time constraints on total completion of the simulations. The mesh used to perform the calculations cartesian as in all the thesis simulations and its characteristics are documented in Table 5.5).

Table 5.5: Characteristics of the mesh used in THAI explosions calculation.

Domain size, LxWxH, cells	Resolution	Cell Number
63x184x63	0.05 m	730,296

5.3.4 Results for test HD-12

5.3.4.1 General

The pressure time history resulting from the simulation is shown in Figure 5.14. Considering that the sound speed is much faster than the motion of the fluid, the pressure inside the vessel can be regarded as equivalent in all positions. No significant differences are found between the results of the experiments and the signal obtained from the calculation in the whole combustion stage. The divergence existing in the final phase is due to the neglect of the convective heat losses. As it will be confirmed later, during the process, the flame does not touch the external walls. The convective heat losses are proportional to temperature differences and speed of motion. Therefore, this phenomenon becomes significant only after the exhaustion of the fuel mixture and thus accounts for the final deviation. Consequently, its neglect looks absolutely justified and allows for the speed up of the calculation.

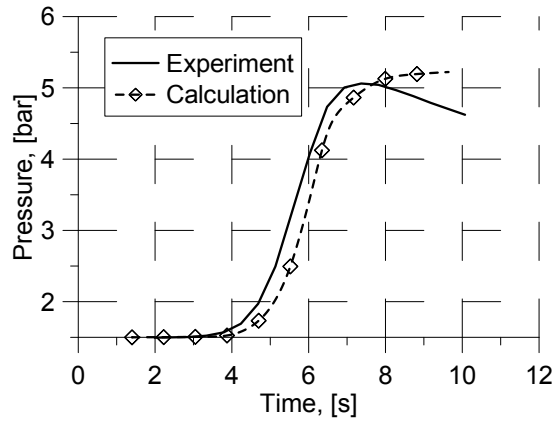


Figure 5.14: Pressure signals in the THAI, HD-12 experiment.

The position of the flame along the vessel is represented in Figure 5.15. In the experiment, the position of the flame was determined using the time of arrival of the flame to each of the fast thermocouples. An excellent agreement is shown both qualitatively and quantitatively between experiments and simulation. Both the acceleration of the flame and the constant velocity are obtained accurately

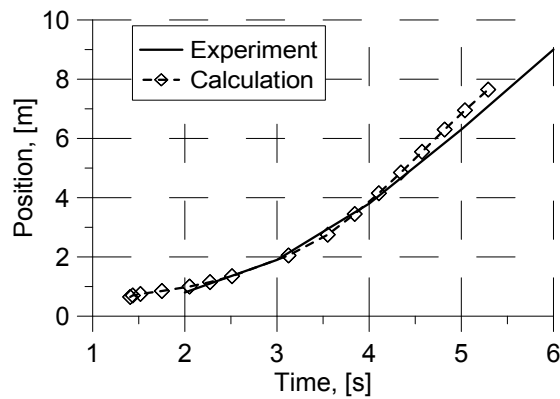


Figure 5.15: Flame position in the THAI, HD-12 experiment. Central axis of the facility selected for the calculation of positions.

Figure 5.16 shows the flame velocities obtained, $(x_{i+1} - x_i)/\Delta t$, for the same problem. An excellent agreement is also obtained from the propagation speeds if the absolute propagation values are taken into account. The divergence in the flame propagation velocity, of 0.5 m/s, should be considered of the order of approximation of the experimental magnitudes.

This low level of relative approximation, is due to the fact that the velocity derived from the experiments was obtained from the time interval that the flame takes to reach the distance between two sensors ($\approx 70 \text{ cm}$). The velocity obtained should be understood as the averaged between the sensors. Due to turbulence, non-uniform or oblique propagation, intermittency and partial quenching (usual for very lean mixtures), etc. the experimentalist consulted, Kuznetsov (2012a), considers that due to intense fluctuation, a deviation of 25% at levels of 0.5 m/s is within the approximation order of the experimental magnitudes.

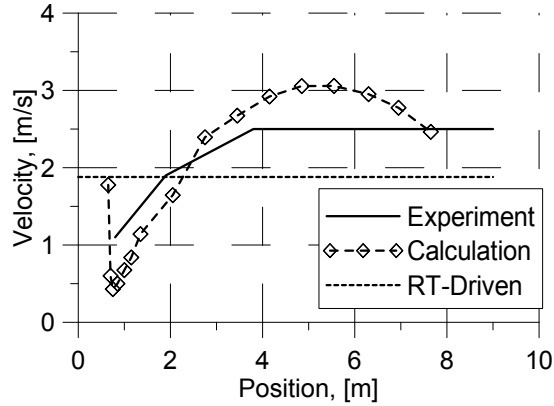


Figure 5.16: Flame velocity along the central axis of the facility in the THAI, HD-12 experiment. Comparison between experimental, calculation and Buoyancy driven (Rayleigh-Taylor (RT) driven eq. (5.10) to be later discussed) results.

5.3.4.2 General evolution of the flame.

The qualitative description of the processes appearing in the experiments can be performed utilizing the available experimental and theoretical knowledge of the

combustion science, e.g. (Zeldovich et al., 1985).

After the ignition, performed with weak energy source like hot-plugs or sparks, the flame starts its propagation in the laminar regime. After a while, but unavoidably for Peclet numbers larger than approximately 50, the cellularity starts to appear for flames with $Le < 1$. In the absence of the turbulence, obstacles, obstruction, the flame would have continued to grow until the Darrieus-Landau instability would also have contributed to the wrinkling of the flame (radius of the order of 1 m). If the Thermo-Diffusive instability would not have been present, $Le > 1$, the flame would have grown spherically just perturbed by the buoyancy effects until the Darrieus-Landau instability would have been significant. This has been already treated in the section 5.2.2. The effects of the buoyancy in the flame would have been also noticeable in the flame not only by an upwards motion, accompanied by a more or less significant deformation. Additionally, the flame interface would have suffered an enhanced, or reduced depending on the direction, wrinkling of the flame. This would have been the effect of the Rayleigh-Taylor instability.

In any case, the effects of the instability would have culminated in a significantly wrinkled flame surface, or the controversial concept of *self-turbulization of the flame*, in which the instabilities culminate generating an unstable motion or unstable flame interface with non-coherent vortical structures⁶. This qualitative behavior should be captured by the model and reproduced by the simulations.

The temperature fields in different moments after the ignition are contained in Figure 5.17 allowing to study the flame evolution in time. The post-processing of the data has been performed with routines generated by the candidate under the OpenDX data visualization software (IBM corp., 2006).

After the ignition, a quasi-laminar growth phase is followed by the transition to the turbulent regime. Following the experimental evidence found out by Pfortner and Schneider (1983) this has been set to happen when the radius of the flame surpasses one meter (approximately 2.6s after ignition, see second row of the Figure 5.17), remembering vessel diameter is 3.2 m.

⁶It is interesting to remember that, as signaled by Zeldovich et al. (1985), even if we conceive that the flow in the reactants remain irrotational, due to the wrinkling in the flame, the motion in the products is always rotational.

In the ulterior turbulent phase, the flame reaches an almost stationary propagation and expands notably laterally. Finally, the flame reaches the top of the vessel and completes the combustion of the remaining reagents propagating downwards. The turbulence model utilized in the simulation, predicts a turbulence intensity, u' , of the order of 5 cm/s with an integral scale of approximately 20cm in the reactants. This is weak turbulence, and small compared with the diameter of the container, and its doubtful whether the flame may have developed in reality in a truly turbulent regime or a significantly wrinkled one dominated by the Rayleigh-Taylor instability since the burning velocity enhancement due to the both effects would have been of the similar order.

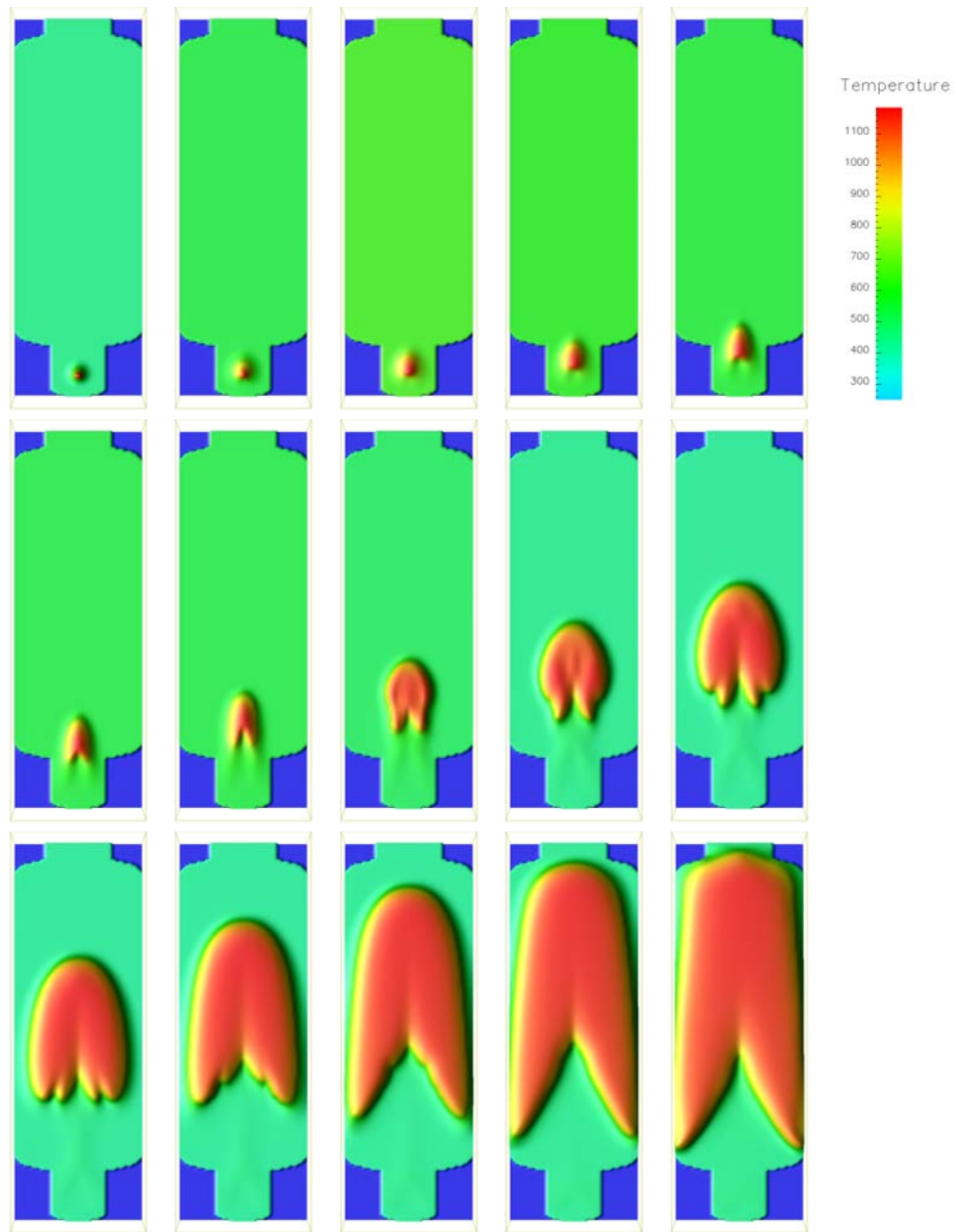


Figure 5.17: THAI-HP12. Temperature fields in different times after ignition. First row: 0.069, 0.46, 0.70, 1.09, 1.47 s. Second row: 1.84, 2.20, 2.56, 2.90, 3.23 s. Third row: 3.54, 3.86, 4.17, 4.47, 4.77 s.

During most of the process, the flame does not touch the external walls (see Figure 5.17) confirming that the divergences found between the results of the experiments and the pressure signal obtained from the calculation in the final phase (Figure 5.14) is due to the neglect of the convective heat losses.

The motion pattern that the flame generates inside the vessel traveling upwards can be seen in the Figure 5.18. While advancing upwards, the bubble of hot gases generates a toroidal vortex that can be clearly seen both in top and bottom pictures. The vorticity generated by this motion can be seen in Figure 5.19. Most notably we may need to signal the meaningful difference between the integral scale of the turbulence (of the order of 10 cm) and the big eddies generated by the global motion (of the order of the radius of the facility). This suggests that the turbulence may have an effect in the flame wrinkling but is not a determinant factor of the global motion.

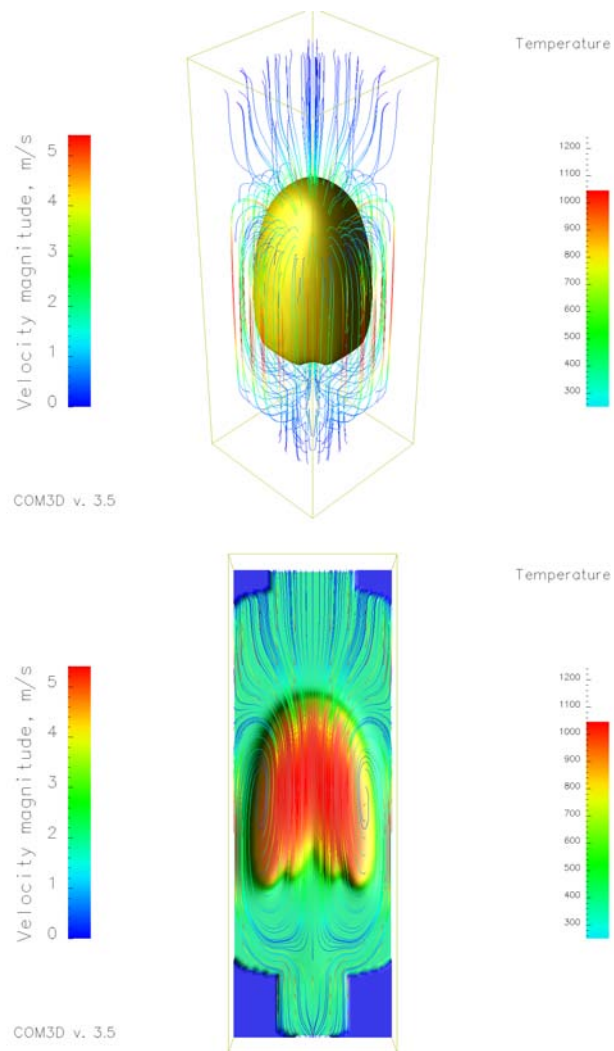


Figure 5.18: THAI-HD-12. Top: Temperature iso-surface, 800 K, and stream-lines 3.54 s after ignition. Bottom: Temperature field cut and stream-lines in the same instant.

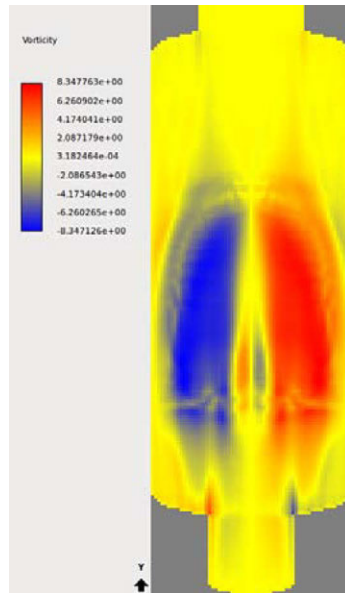


Figure 5.19: Vorticity 3.54 s after ignition

5.3.5 Results for test HD-15

5.3.5.1 General

The numerical experiment detailed in the previous section was repeated with the conditions of the HD-15 problem. The main difference between HD-12 and HD-15 is the concentration of hydrogen (from 8.1% to 9.9% vol H_2) and the temperature (from 18 °C to 93 °C). The results containing the evolution of the pressure during the combustion event are shown in Figure 5.20. The pressure readings obtained in the calculation are in good agreement with the experimental results.

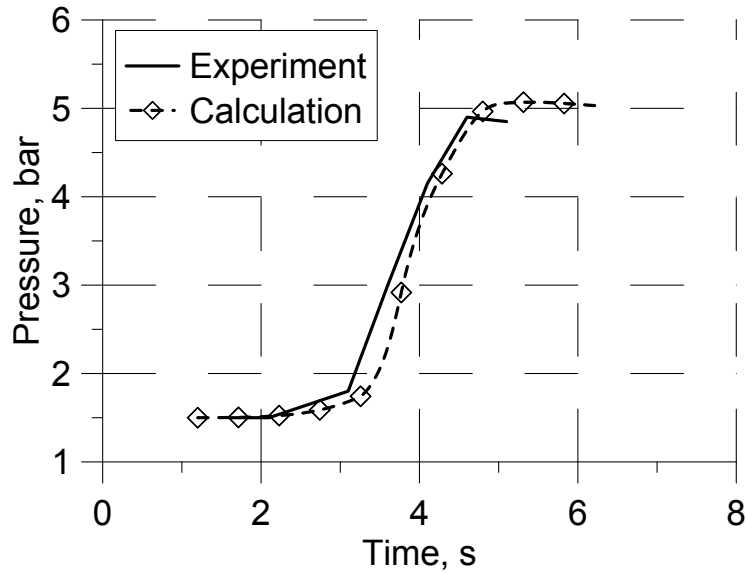


Figure 5.20: Pressure signals in the THAI, HD-15 experiment.

The position of the flame depending on the time, Figure 5.21, was calculated processing the data available from the thermocouples installed in the experimental facility. The figure shows the comparisons of the propagation of the flame along two lines of thermocouples with the results of the simulation. An additional line, measuring the flame position along an eccentric longitudinal line is included, was added to the axial location. For times smaller than 3.5 s the two lines provide the same measurements. Above that line the measurements become different probably due to flow instability.

The results of the calculations lay between the two experimental lines and since the calculation was performed without initial flow field perturbations, the results should not be able to capture the random nature of the flame evolution. Both the acceleration of the flame and the steady-state propagation regime are reproduced with high accuracy.

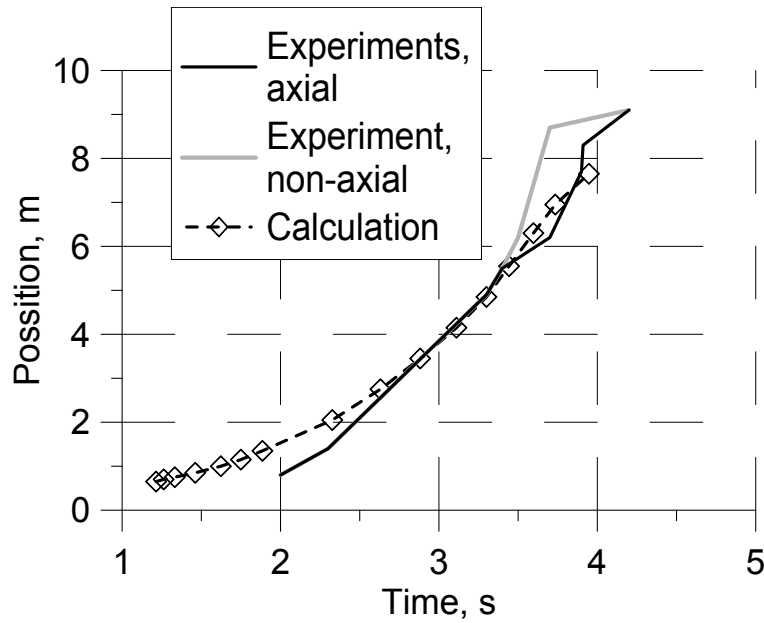


Figure 5.21: Flame position in the THAI, HD-15 experiment. Central axis and non-central line of the facility selected (full lines). Calculations, dashed lines with symbols. Both experimental lines lay superimposed until a time of 3.5 s is reached.

The flame velocity history for a set of transducers located in the axis of the facility and in an eccentric parallel line were compared with the results of the computation, see Figure 5.21 and 5.22. An assessment of the measurements errors present in the experiment can be performed comparing the experimental results of both lines. The results of the predictions are in fair agreement with the experiment until the *erratic* propagation of the flame started. A regime like that, in which for example the flame reached two transducers in different positions at the same instant, could not be reproduced in the calculation. The acceleration and the stationary regimes were though very well predicted.

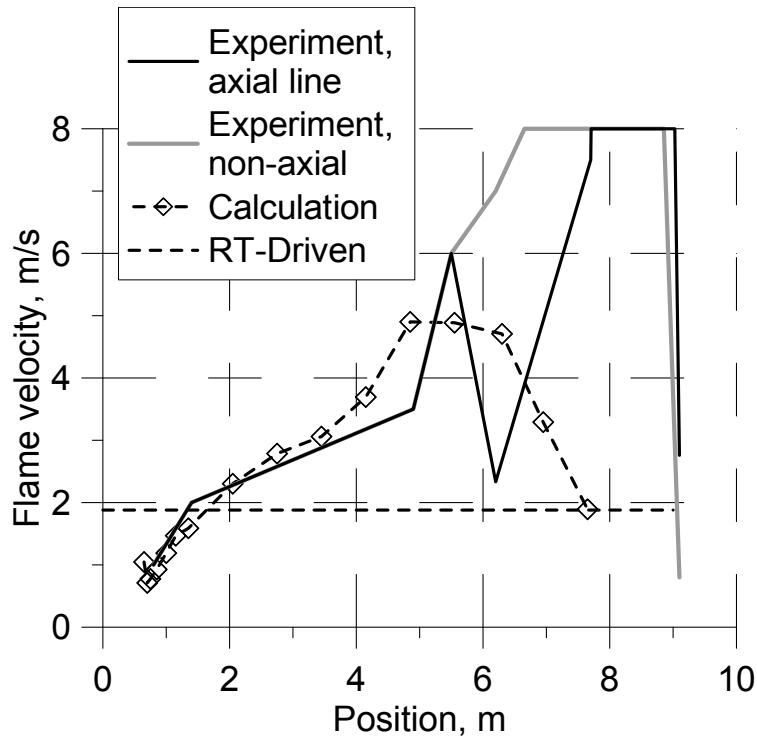


Figure 5.22: Detailed flame velocity along the central axis and non-axial transducer line of the facility in the THAI, HD-15 experiment. Velocities clipped at 6. m/s.

5.3.5.2 General evolution of the flame

The qualitative description of the processes is similar as the one described in 5.3.4.2 for the experiment HD-12.

The evolution of the flame can be studied visualizing the evolution of the temperature fields, see Figure 5.23. After the ignition, the flame suffers the transition to the turbulent regime and then accelerates upwards and laterally due to flame instabilities. Contrary to the HD-12 calculation, the flame does not detach from the sump of the facility.

In the first picture row, the flame is shown after ignition and in the phase of ac-

celeration. A recirculation pattern, shown in Figure 5.24, appears in sump creating an *stabilization* of the flame in the small cavity. The flame then continues evolving driven by the buoyancy and generates a new recirculation pattern in the upper cavity (Figure 5.25). This recirculation feeds back the combustion and generates the neck pattern that can be seen in the lower row.

From the results contained in this section, as well as the results shown for the HD-12 experiment, a general conclusion can be draw: the laminar flame velocity treatment for the concentration and temperature difference, see section 4.3.1, provides the necessary accuracy for the purposes of hydrogen safety analysis.

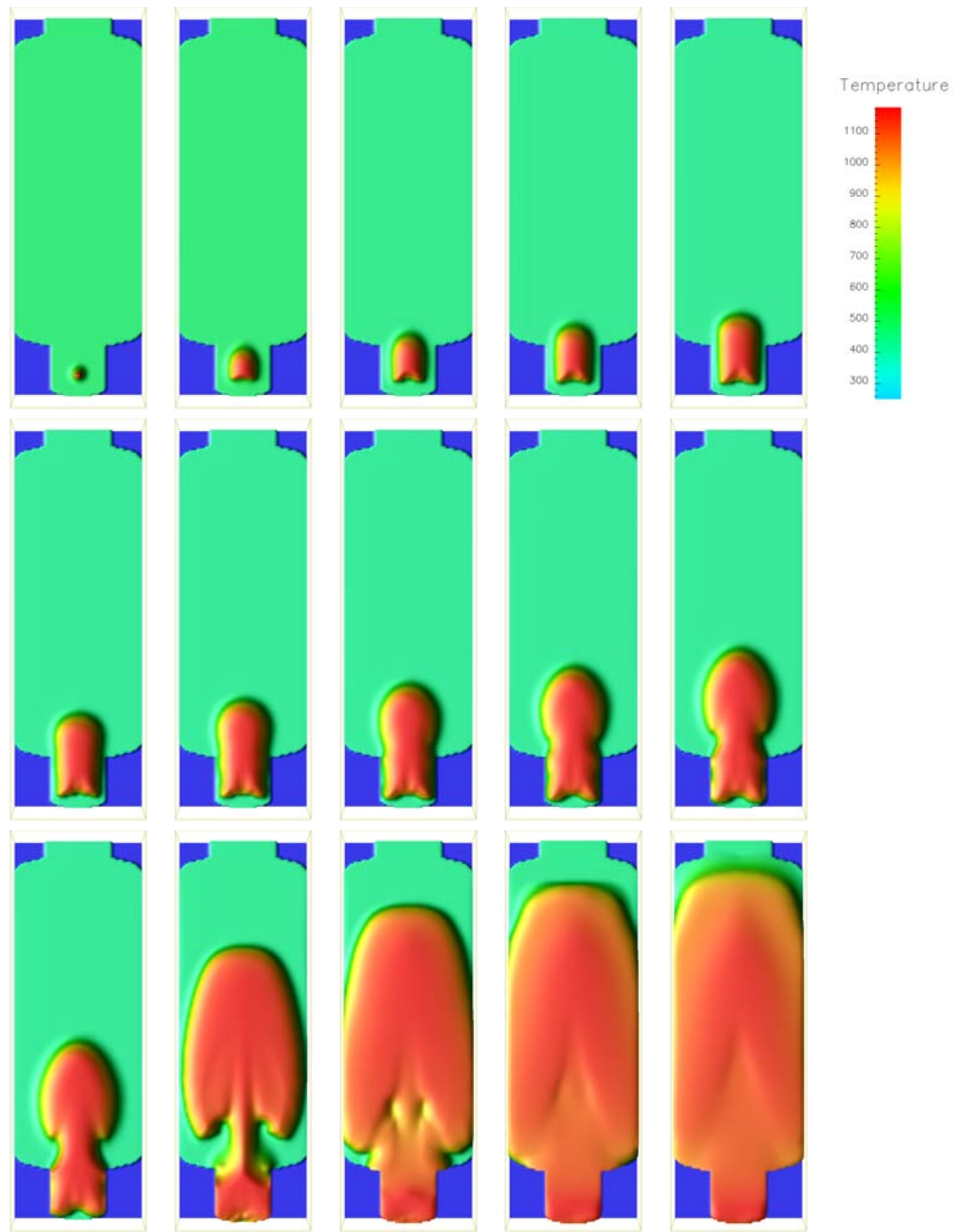


Figure 5.23: THAI HD-15 experiment. Temperature fields in different times after ignition. First row: 0.024, 0.54, 0.78, 0.93, 1.08 s. Second row: 1.23, 1.37, 1.52, 1.66, 1.81 s. Third row: 1.96, 2.45, 2.72, 2.99, 3.25 s.

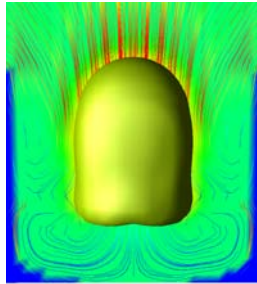


Figure 5.24: THAI HD-15 experiment. Detailed motion in the sump of the facility at time 0.5 s.

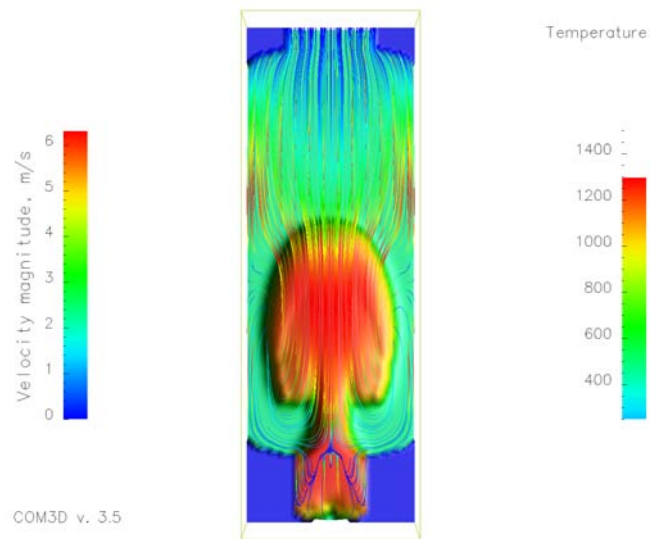


Figure 5.25: HD-15 problem. Frame taken 1.96 s after ignition. Stream lines, flow pattern. Left scale applies to stream lines.

5.3.6 Results for test HD-22

5.3.6.1 General

With the aim of testing to test the capability of the model to produce adequate results in hydrogen-air-steam atmospheres, the experiment HD-22, was chosen to simulate the deflagration of a H_2 -steam-air mixture at superheated and saturated conditions. Those are very significant conditions for the nuclear safety, concretely for a LOCA⁷ scenario, in which a saturated steam atmosphere of such kind is expected. The exact conditions in which the HD-22 test were performed are summarized in Table 5.4 and consider a wet mixture close to its inertization but still burnable.

Figure 5.26 shows the position of the flame along the vessel and displays a very good prediction. The location of the flame in the experiment was found following the same methodology as in the previous cases.

Contrary to experiment HD-15, the transducers located in the center and in an eccentric parallel lines provide similar readings. Thus, the transducers in the axis of the facility were exclusively taken into account. Certainly, as for case HD-15, the erratic irregular behavior of the flame cannot be reproduced in the calculation. This behavior is characterized by a dependence on each the experiment realization. Therefore its realistic character could only be truly analyzed statistically with a significant number of repetitions of the experiments, an experimental matrix that is nevertheless not available.

⁷Lost Of Coolant Accident, see e.g the work of Kessler et al. (2014) on Nuclear Energy Technology for further details.

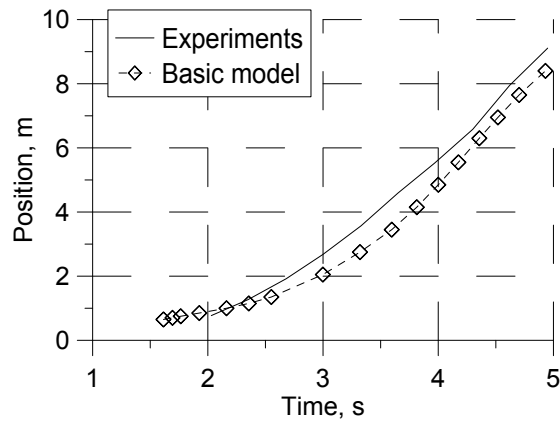


Figure 5.26: Flame position in the THAI, HD-22 experiment. Central axis line of the facility selected. Basic modeling is the same utilized for HD-12 and HD-15 experiments in sections 5.3.4.1 and 5.3.5. The extended modeling (to be shown in section 5.3.10 but not shown here) also considers the effects of sound in flame, taking into account the effects of the acoustic-parametric instability, see 5.3.9.

Figure 5.27 contains the flame velocity for a line of transducers in the axis of the facility. Experimental values are compared with the results of the computation. The agreement is good. The acceleration and the steady-state regimes were though well predicted. The deviations found in the flame propagation, of 0.5 m/s, should be considered as corresponding to the overall level of calculation accuracy.

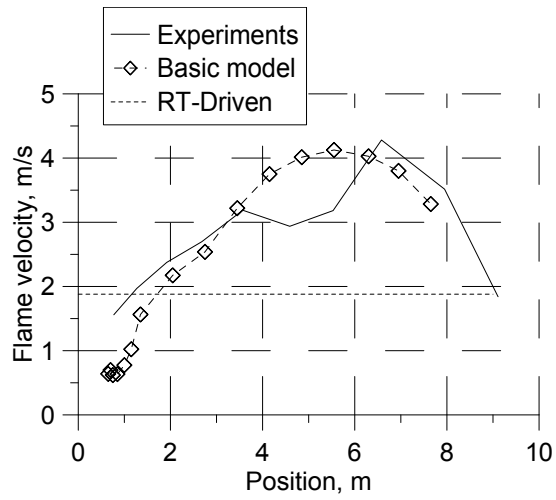


Figure 5.27: Flame velocity along the central axis and non-axial transducer line of the facility in the THAI, HD-22 experiment.

Nevertheless, it was found that the pressure computation did not provide acceptable results, see Figure 5.28 basic model, where the results of the pressure evolution during the combustion in the problem HD-22 are shown.

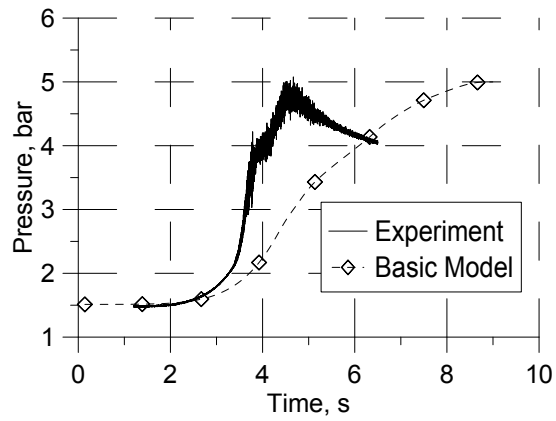


Figure 5.28: Pressure signals in the THAI, HD-22 experiment.

From the observation of the flame position and velocity results, it can be inferred that the propagation of the flame in the vertical direction was well reproduced. Thus, the pressure deviations obtained could only be connected with erroneous predictions of the transverse flame propagation. The analysis performed in the following sections is intended to provide a full understanding of this phenomenon and an adequate modeling for it. For coherency with the structure of the previous chapters, it is possible to advance here that the propagation of the flame after the additional modeling is taken into account could be visualized in the Figure 5.36 and 5.37.

5.3.7 Buoyancy driven flames analysis

Khokhlov et al. (1996) developed an algebraic flame velocity model, which was intended to describe buoyancy-driven turbulent pre-mixed flames. Its application is restricted to flames fulfilling the following conditions.

1. The flame is assumed to be thin in comparison with the largest scale of turbulence.
2. The laminar burning velocity is much smaller than the turbulent one.
3. The turbulence is driven by the Rayleigh-Taylor instability in the gravitational field.

The previous assumptions model the physical phenomenon described henceforth. After the ignition, the flame propagates vertically and, after some transient period, it becomes turbulent due to the Rayleigh-Taylor instability. Finally, the flame reaches a steady state propagation regime. The propagation speed in such a stage could be evaluated using the expression by Khokhlov et al. (1996) as

$$S_t = 0.5 \left(g H \frac{\theta - 1}{\theta + 1} \right)^{\frac{1}{2}}, \quad (5.10)$$

where H^2 represents the surface of the unperturbed flame.

The first condition is always fulfilled as $\delta \approx 10 \mu\text{m}$ in a facility with a diameter of 3.2 m.

The flame velocity registered, both in experiments and in the simulations, is one order of magnitude larger than the laminar burning velocity (see later magnitude in Table 5.6 and the registered burning velocities in Figures 5.28, 5.21 and 5.16). Thus, the second condition is accomplished. The fulfillment of the third condition, to be studied, determines whether the flame propagation regime was dominated by the Rayleigh-Taylor instability or not.

In order to determine whether the flame is driven by buoyancy processes a necessary condition to fulfill point 3, it is possible to determine the value of the Froude number of a bouyant, laminar or quasi-laminar flame. As found by Khokhlov et al. (1996), the velocity of the motion created by a flame propagating with the laminar burning velocity is of the order of S_L too. On the other hand, the characteristic velocity of propagation of the perturbations of size H due to the Rayleigh-Taylor instability is \sqrt{gH} . In first approach we may assume H as the diameter of the facility.

Ignoring in a first approach the expansion, the Froude number characterizing the relative importance of the burning and the Rayleigh-Taylor instability can be written as $Fr = S_L^2 / (gH)$, see Table 5.6. The result obtained, $Fr \ll 1$ allow stating that all experiments were buoyancy driven processes.

Table 5.6: Froude number laminar and turbulent flame velocity (following eq. (5.10)) for the different experiments

Case	Fr [—]	θ [—]	S_L [cm/s]	S_t eq. (5.10) [m/s]
HD-12	$1.2 \cdot 10^{-4}$	2.9	6.1	1.9
HD-15	$5.0 \cdot 10^{-4}$	2.7	16.8	1.9
HD-22	$5.2 \cdot 10^{-4}$	2.6	18.0	1.8

We may now evaluate the formula (5.10) for the three experiments (see Table 5.6) and compare the predictions with the results of the experiments to elucidate if condition 3 is fulfilled and determine whether the propagation regime could be

characterized as Raileigh-Taylor driven or not. The results obtained for S_T are almost the same taking into account the significant numbers of the crude approximation of equation (5.10). Notice that one of the most surprisingly characteristics of eq. (5.10) is that the S_t does not depend on S_l . Thus, as the amount of hydrogen is similar in the three experiments, so are the expansion ratios θ and thus results are very similar. Let us see now if predictions agree with experiments.

The prediction obtained for the case HD-12 was surprisingly good taking into account the crudeness of the assumptions taken into account for the obtaining of eq. (5.10). The comparison previously shown in Figure 5.16 (page 136) reveals that the experimental values were 2.5 m/s while with the use eq. (5.10) 1.8 m/s were obtained. Thus, with the certain degree of precaution, on the basis of such coincidence it can be concluded that the flame propagation regime in this experiment can be considered as driven by the Rayleigh-Taylor instability exclusively. This conclusion is somehow confirmed by the fact that the experimental results of test HD-12 exhibit a steady-state propagation regime after a certain establishing period. This is in agreement with the considerations of the theory of Khokhlov.

The results of the test HD-15 and HD-22 were also compared with the flame velocity predictions for Rayleigh-Taylor instability driven flame, see Figure 5.22, page 145, and Figure 5.27, page 151, respectively.

Experiments HD-15 and HD-22 exhibit higher divergences between the experimental flame velocity readings and theory predictions utilizing eq. (5.10). The dynamics of the curves and the values registered does not allow identifying the combustion process as being purely buoyancy driven. Therefore, condition 3 is not fulfilled. More probably, other mechanisms in addition to the Rayleigh-Taylor instability are responsible for the wrinkling and turbulence generation of the flame. Further investigation is necessary to identify the combustion regime occurring in the experiments, see further sections.

5.3.8 Analysis with the Borghi diagram

With the intention to get better insight into the processes taking place in the simulated experiments the observed flame propagation regimes can be analyzed with the help of the Borghi diagram (Borghi, 1988). For the systematic mixture examination, the Lewis, Markstein, Karlovitz and turbulent Reynolds numbers of all three conditions were calculated (see Tables 5.7 5.8). Those magnitudes as well as the other data necessary to perform such analysis were selected in the same location, far away from the flame front and at a time when the flame has reached the middle of the facility. Only qualitative comparison between cases is feasible.

Table 5.7: Flame thickness, turbulence intensity and integral scale of the turbulence.

Case	δ [m]	u' [m/s]	L [m]
HD-12	$7.6 \cdot 10^{-5}$	0.03	0.009
HD-15	$1.5 \cdot 10^{-4}$	0.10	0.12
HD-22	$3.1 \cdot 10^{-4}$	0.11	0.32

Table 5.8: Characteristics of gases mixtures. For clarity the definitions utilized are detailed henceforth. The Turbulent Reynolds number is defined as $Re_t = u' L / \nu$ where u' is the intensity of the turbulence, L the integral scale of the turbulence and ν the cinematic viscosity. The Lewis number is defined $Le = D / \chi$ where D is the diffusion coefficient and χ the thermal diffusivity. The Markstein number as is defined by Zeldovich et al. (1985) $Ma = (\chi - D) E_a (T_b - T_u) / 2 R T_b^2 \chi + D / \chi$ where E_a is activation energy, T_b temperature of the adiabatic flame and T_u the temperature of the fresh products. Karlowitz number defined by Poinot et al. (1991) $Ka = (u' / S_L) \sqrt{\nu / (u' L)}$ where S_L is the laminar burning velocity. The Damkoehler number is finally defined as $Da = (L S_L^2) / (u' \chi)$.

Case	Re_t	Ka	Da	Le	Ma	Combustion regime
HD-12	852	0.02	1500	0.36	-2.4	Wrinkled flames
HD-15	946	0.002	1068	0.35	-1.2	Wrinkled flames
HD-22	88	0.01	339	0.32	-2.8	Laminar Flamelets

The gaseous mixture of the problem HD-12 has a Lewis number approximately equal to 0.36 while the Markstein number is equal to -2.4. Both values imply an

unstable mixture prone to *erratic* propagation and local quenching. The flame is located in the flamelet regime area in the border between the wrinkled and the wrinkled with pockets formation region $u'/S_L \approx 1.0$ (see Figure 5.29).

For the HD-15 problem, the propagation regime still remains close to the line $u'/S_L \approx 1.0$. The main difference between the mixtures from the point of view of the combustion lies in the fact that the $Ma \approx -2.4$ for 8 % vol. H_2 while $Ma \approx -1.2$ for 10 % vol. H_2 , which makes second composition much more stable.

The mixture of the case HD-22 suffers a different combustion regime. The integral scale of the turbulence, evaluated during the simulations, was significantly smaller, around one order of magnitude, than for the tests HD-12 and HD-15. The level of turbulence was also smaller. The combustion regime still lies in the flamelet region but in the laminar flamelet area (see Figure 5.29). It has also to be remarked that this mixture has a Markstein number approximately equal to zero.

The Markstein number describes the sensitivity of the flame burning velocity to its curvature, $S_{L\,planar} - S_{L\,curved} \approx Ma \delta \alpha$ where the stretching can be defined as $\alpha = A_f^{-1} dA_f/dt$ with A the surface of the flame. The three gaseous mixtures involved in the tests have a Markstein number which is completely different in each of the cases. These differences may explain the cause of the different flame propagation regimes detected.

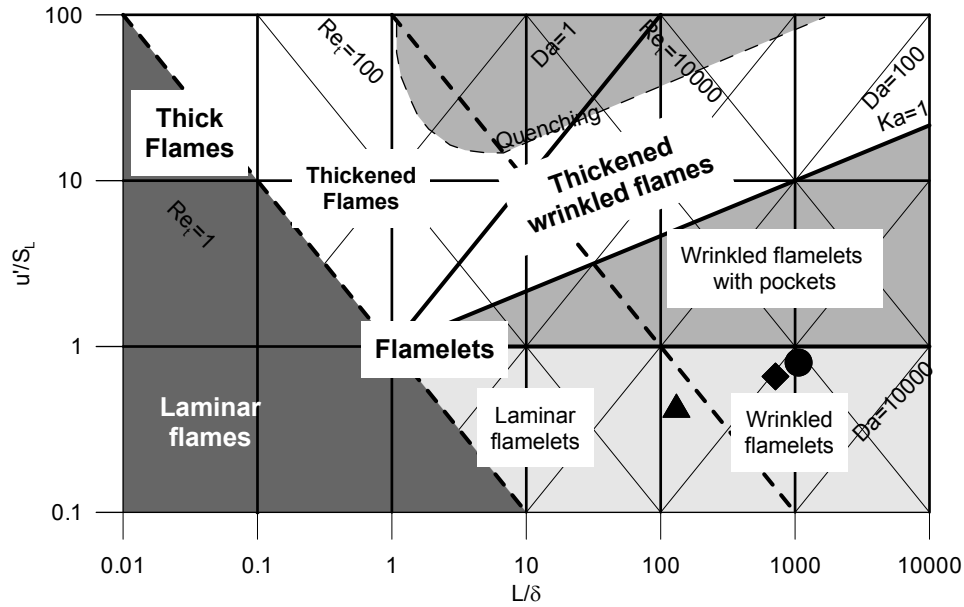


Figure 5.29: Borghi diagram. Circle denotes test HD-12, diamond HD15, triangle HD-22. Values for the turbulence, intensity u' and integral scale L , obtained in the intermediate phase of the propagation.

5.3.9 Acoustic-parametric instability analysis

The pressure readings of the HD-22 experiments, which have strong oscillations appearing soon after the flame reaches the half height of the facility (see Figure 5.28), can not be explained as caused by wrinkling of the flame due to the Rayleigh-Taylor instability or just by the presence of a strong turbulent field: the spectrum obtained by the Fourier analysis of the pressure signal, shown in Figure 5.30, shows a resonance in the first transversal harmonic (exact values are listed in Table 5.9). To calculate the transversal characteristic frequencies, the speed of sound of the cold fuel was selected.

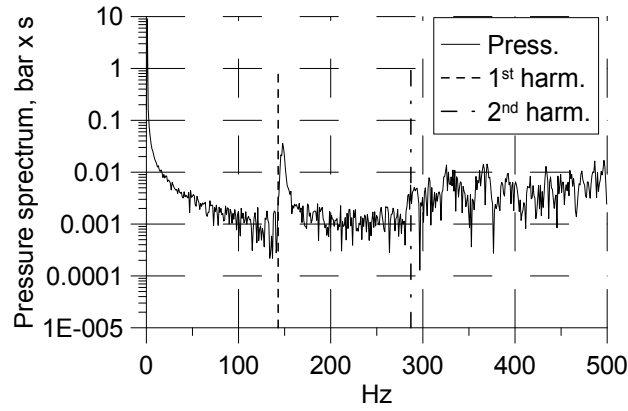


Figure 5.30: Spectrum of the pressure signal, first and second transverse harmonic. Case HD-22.

Table 5.9: Sound speed and first transverse harmonic frequency for the three experiments analyzed.

Case	Sound speed	First harmonic frequency
	[m/s]	[Hz]
HD-12	389.2	121.5
HD-15	440.5	137.5
HD-22	460.5	143.7

The generation of pressure waves by flames propagating in closed volumes is a known phenomenon. The interaction between them has been investigated for decades since the early works of Markstein (1964). The waves generated during such process can be described as weak shocks or sound waves. To be considered as weak shocks, the typical time for the sound to traverse the burning chamber must be much longer than the typical time of flame dynamics, which here can be evaluated as typical time of the Darrieus-Landau (DL) instability. In the opposite case, they can be considered as sound waves. For the problem we are dealing with, the DL typical growth rate frequency (Bychkov and Liberman, 2000) of 120 Hz and the first transversal harmonic of the chamber 143 Hz are comparable, and it was

decided to consider the waves as acoustic.

The linear theoretical results obtained by Bychkov and Liberman (2000) were applied to evaluate the enhancement of the combustion rate, see also Yanez et al. (2013c). If such theoretical results are accepted, the flame is going to be subjected to the acoustic and the parametric instabilities.

In the acoustic instability, see Pelce and Rochwerger (1999), the cellular structures of the flame front oscillate with the frequency of the acoustic alternative field. Two effects tend to muffle the instability. For large wavenumbers, it is damped by diffusive processes. For small wavenumbers, it is absorbed by the effect of gravity. For zero amplitude of the excitation velocity it corresponds to the Darrieus-Landau instability. For increased values of the alternative velocity (Pelce and Rochwerger, 1999), the acoustic instability has the notable property of being able to stabilize the Darrieus-Landau instability (Yanez et al., 2012b)⁸.

The acoustic instability may develop, for an enhanced alternative velocity, into the parametric one. Under the later, the growth rate is generally superior than in the acoustic case. The cellular structures of the flame oscillate with a frequency half of the acoustic, a fact that was recognized by Markstein as the typical sign of the Kapitsa parametrically dumped pendulum, who consequently named the instability.

The references (Bychkov and Liberman, 2000), (Searby and Clavin, 1986) (Yanez et al., 2013c)⁹ (Yanez et al., 2013b)⁹ contain the formulation for the acoustic and parametric stability limits and the growth rate. Nevertheless, the expressions contained in (Searby and Clavin, 1986) resulted inconvenient for the modeling and the equations in (Bychkov and Liberman, 2000), because of mistakes, errors or oversimplifications, were not directly applicable. Therefore, careful derivation of the equations was performed and is included in the Appendix C. The final results ob-

⁸Co-authored

⁹Co-authored

tained are, for the acoustic instability growth rate σ

$$\sigma = \frac{-B S_L \kappa}{2A} \pm \sqrt{\frac{(B S_L \kappa)^2}{4A^2} - \frac{1}{A} \left(C_1 \kappa g + C_2 S_L^2 \kappa^2 + \frac{C_1^2 U_a^2 \kappa^2}{2A} \right)}, \quad (5.11)$$

and for the parametric instability growth rate,

$$\begin{aligned} \left(A\sigma^2 - A\frac{\omega_{ac}^2}{2^2} + S_L \kappa B \sigma + \kappa g C_1 + S_L^2 \kappa C_2 \right)^2 - \left(\frac{1}{2} \kappa \omega_{ac} U_a C_1 \right)^2 + \\ + \left(A\sigma \omega_{ac} + \frac{1}{2} S_L \kappa B \omega_{ac} \right)^2 = 0, \end{aligned} \quad (5.12)$$

where A, B, C_1, C_2 , are dimensionless coefficients depending on the flame parameters and the wavenumber

$$A = 1 + \frac{\theta - 1}{\theta + 1} \kappa \delta \left(Ma - \frac{\theta}{\theta - 1} J \right), \quad (5.13)$$

$$B = \frac{2\theta}{\theta + 1} (1 + \theta \kappa \delta (Ma - J)), \quad (5.14)$$

$$C_1 = \frac{\theta - 1}{\theta + 1} \left(1 - \kappa \delta \left(Ma - \frac{J\theta}{\theta - 1} \right) \right), \quad (5.15)$$

$$C_2 = \theta \frac{\theta - 1}{\theta + 1} \quad (5.16)$$

$$\left(-1 + \frac{\kappa \delta}{\theta - 1} (h_b(\theta - 1) + (3\theta - 1)Ma - 2J\theta + (2Pr - 1)(\theta - 1)H) \right). \quad (5.17)$$

U_a and ω_{ac} are the amplitude and the circular frequency of the acoustic perturbation. Ma, J, H are defined as,

$$H = \int_0^1 (h_b - h(\vartheta)) d\vartheta, \quad (5.18)$$

$$J = \frac{\gamma_g}{1 - \gamma_g} \int_0^1 \frac{h(\vartheta)}{1 + \vartheta \gamma_g / (1 - \gamma_g)} d\vartheta, \quad (5.19)$$

$$Ma = \frac{J}{\gamma_g} - \frac{1}{2} Z e (Le - 1) \int_0^1 \frac{h(\vartheta) l n(\vartheta)}{1 + \vartheta \gamma_g / (1 - \gamma_g)} d\vartheta, \quad (5.20)$$

where $\gamma_g = (\rho_u - \rho_b)/\rho_u = 1 - 1/\theta$, $\vartheta = (T - T_u)/(T_b - T_u)$, $Le = \chi/D$ and $h(\vartheta) = (\lambda(\vartheta)C_{Pu})/(\lambda_u C_P(\vartheta)) = (\rho(\vartheta)\chi(\vartheta))/(\rho_u \chi_u)$.

The acoustic and parametric stability limits were calculated and plotted in Figure 5.31. Three independent regions resulted from the analysis. The two independent areas of instability are marked in grey. The bottom left zone represents the acoustic instability while the parametric instability is represented in upper center area.

The amplitude of the wave registered in the H-22 experiment for the first harmonic (see Figure 5.30, the first harmonic resonates) yields through $p \approx \rho U_a^2$ the coefficient $U_a/S_L \approx 65$. The observation of the Figure 5.31 with the value $U_a/S_L \approx 65$ in ordinates, allows identifying that the instability existing in the problem was the parametric.

Some detailed characteristics of the mixture utilized to perform the calculations were included in Table 5.10 and Table 5.11. The value of the molecular transport coefficients was obtained from the kinetic theory of gases, see section 4.10. The thermodynamic data was obtained from the JANAF tables (Malcolm and Chase, 1998). Special care was taken to calculate the overall activation energy using a methodology based on induction time, see Zeldovich et al. (1985) and not on the laminar burning velocity (Yanez et al., 2011c). This last magnitude was calculated utilizing the using the computer program Cantera (Goodwin, 2001).

The mixture Lewis number was calculated using the formulation proposed by Sun et al. (1999). The Le number is clearly defined for very lean mixtures $Le_1 = \chi/D_{H_2 Mixture}$ or for very rich ones $Le_2 = \chi/D_{O_2 Mixture}$ but in between is necessary

to utilize a formulation that agrees with experimentally obtained values. Sun et al. (1999) has proposed the utilization of

$$Le = Le_1 + H(Le_2 - Le_1) \quad (5.21)$$

where

$$H = n_2 G(n_1, n_2 - 1, A) / G(n_1, n_2, A), \quad (5.22)$$

and

$$G(n_1, n_2, A) = \int_0^1 \xi^{n_1} (\xi + A)^{n_2} e^{-\xi} d\xi \quad (5.23)$$

$$A = Ze(1/\phi - 1)/Le_2. \quad (5.24)$$

On these formulas n is the reaction order, ϕ is the equivalence ratio, Ze the Zeldovich number and the subscripts 1 and 2 refer to the lean and rich conditions respectively. The parameters n_1 and n_2 have been obtained from Sun et al. (1999) and tabulated.

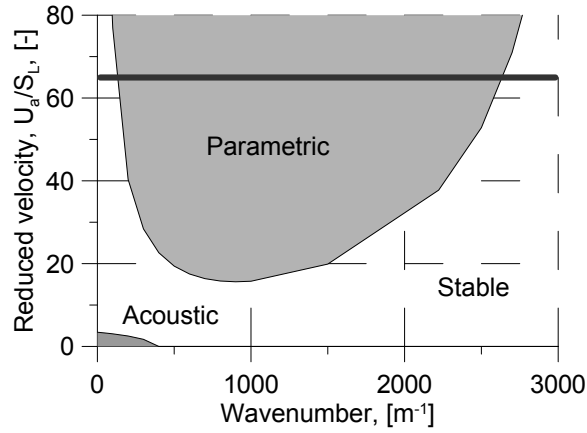


Figure 5.31: Stability limits of the gases mixture for both the acoustic and the parametric instability. Position of the $U_a/S_L \approx 65$ marked with a dark thick line.

Table 5.10: Characteristics of the mixtures selected for the calculation of the stability and instability growth rate. Markstein number was calculated as defined in (Searby and Clavin, 1986) eq. (6). this is an alternative definition to the usual one utilized previously.

Markstein Number Ma	Kinematic Viscosity $\nu [m^2/s]$	Thermal diffusivity $\chi [m^2/s]$	Diffusivity D [m^2/s]	Activation Energy $E_a/R [K]$	Temperature Products $T_b [K]$
3.18	$2.70 \cdot 10^{-5}$	$3.40 \cdot 10^{-5}$	$1.01 \cdot 10^{-4}$	7500	1179

Table 5.11: Characteristics of the mixtures selected for the calculation of the stability and instability growth rate (continuation).

Temperature Fuel	Laminar Flame Vel.	Expansion ratio	Acoustic Fre- quency	Reduced Acoustic wave Ampli- tude U_a/S_L
$T_0 [K]$	$S_L [m/s]$	θ	Hz	
430	0.18	2.6	143	65.

The mechanism leading to the final registered unstable results include several phases: in the first stage, the flame generated acoustic waves, whose amplitude could be estimated (Bychkov and Liberman, 2000) as $U_a \approx (\theta - 1)S_L \approx 0.5m/s$, that triggered the acoustic instability. Then, in a feedback process, the amplitude of such oscillations (they could be calculated following the method by Bychkov (1999)) reached a level in which the stable band between the acoustic and the parametric area was surpassed, likely in the transverse direction (the amplitude of the stable band is proportional to the frequency of the acoustic oscillations, in the longitudinal direction the frequency should be three times smaller). Then, another feed-back mechanism (parametric instability), was responsible for the transversal direction instability.

5.3.10 Effect of the parametric instability in flame dynamics in HD-22

Further model development was performed with the aim of simulating the mass consumption rate enhancement due to parametric instabilities (Bychkov and Liberman, 2000). The same procedure utilized by Bauwens et al. (2011), used by them to take into account the effects of the Rayleigh-Taylor instability, was followed. In this method, the surface wrinkling factor Ξ , defined as the ratio of the total surface of a wrinkled flame per unit of planar equivalent flame surface, characterizes flame surface enhancement due to the instability.

If we denote the planar equivalent domain as S and the flame surface is described by the function $F(x,y)$, then

$$\Xi = \left(\iint_S \sqrt{1 + (\partial F / \partial x)^2 + (\partial F / \partial y)^2} dx dy \right) / S. \quad (5.25)$$

The time of evolution of Ξ is determined from a differential equation which describes the surface dynamics taking into account the competition between its growth and its shrinking

$$\frac{d\Xi}{dt} = G_w (\Xi - 1) - R_w (\Xi - 1)^{\frac{3}{2}}. \quad (5.26)$$

With the utilization of such model, the burning velocity utilized previously in KYLCOM should be substituted by its enhanced factor ΞS_l . Finally, the effective burning velocity was evaluated as $S \approx \Xi S_T$. Take into account, that if we reformulate the expressions of Table 4.1 writings them in terms of S_t/S_l we may also define a surface wrinkling factor due to the turbulence $\Xi_{turb} \approx S_t/S_l$. If we take the flame enhancement due to turbulence and instabilities, and suposing they do not happen at the same time, we may write our effective flame burning velocity as $S_{eff} \approx \Xi_{turb} \Xi S_l$. The consumption rate $\bar{\omega}$ for KYLCOM methodology, see eq. (5.3),

can be accordingly reformulated to be

$$\bar{\omega} = \begin{cases} \frac{(A \cdot \theta + B) \Xi_{urb} \Xi_{Sl}}{\Delta x} (1 - \bar{f}_{i,j,k}) & F_{i,j,k} > \left(\frac{1}{2}\right)^2 \\ 0 & F_{i,j,k} < \left(\frac{1}{2}\right)^2 \end{cases} \quad (5.27)$$

Let us study now the terms of equation (5.26). The sub-grid wrinkling generation rate, $G_w = 2\sigma$, may be calculated from its expression in the literature, see Bychkov (1999). The expression derived in this reference contains, in the opinion of the author, some mistakes which were corrected in the Appendix C with final result already presented in eqs. (5.12), see Figure 5.32. The flame surface annihilation rate, R_w , represents the reduction of the flame surface due to cups propagation and is given by the formula

$$R_w = \frac{4\sqrt{2}S_L\kappa}{\pi}. \quad (5.28)$$

where κ represent the wavenumber with the highest amplification. κ can be estimated from the diagram for the growth rate of the parametric instability.

Even if the equation (5.26) has been utilized several times e.g. (Bauwens et al., 2011) (Yanez et al., 2011d), its derivation has been never published. Detailed obtaining of the equation 5.26 can be found in Appendix D.

For the overpressure resulting in the resonance in the first harmonic (Fig. 5.30), it is possible to obtain from the equation (5.12) the growth rate curve of the instability represented in the Figure 5.32.

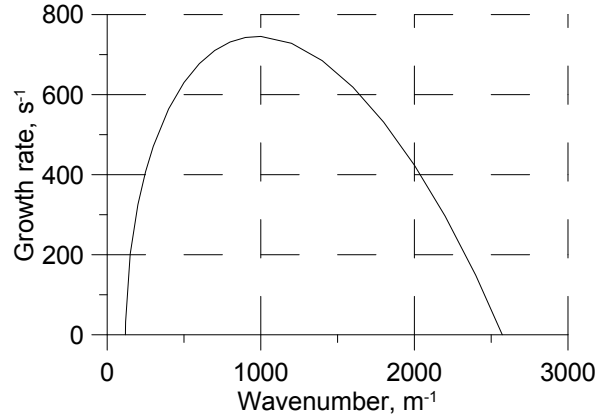


Figure 5.32: Growth rate of the parametric instability for the mixtures.

It would be now adequate to perform a clarification. The wave-number that appear in Figure 5.32 refers to the flame surface which is not the same as the wave-number of the first transverse harmonic of the facility $2\pi/3.2$.

Some limitations exist for the evaluation of R and G and the validity of the whole approach do exists: a linear model was applied in the deduction of the theoretical expressions. Therefore, the formulae are only applicable for small amplitude disturbances. Additionally, the values for R_w and G_w were considered to be constant during the whole calculations. The wavenumber κ was also considered as a constant in this formulation. For all those reasons, the values of G_w and R_w must be considered only as an estimate.

The surface wrinkling factor Ξ can be easily estimated to be approximately 1.79 in the stationary regime $d\Xi/dt = 0$.

Post-calculations for the HD-22 test were performed using the described enhancement mechanism. Good agreement between experimental results and simulation was obtained both for the pressure and for the flame position (see Figures 5.33, 5.34 and 5.35).

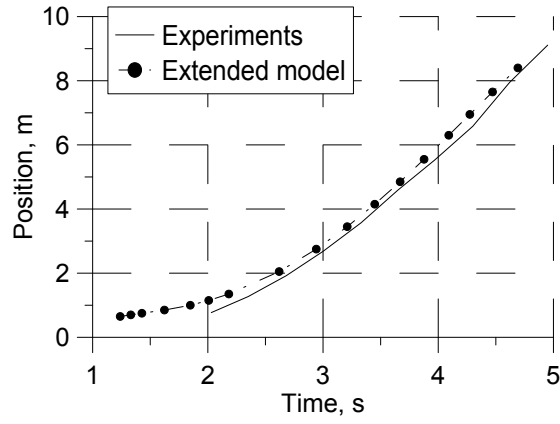


Figure 5.33: Flame position in the THAI, HD-22 experiment. The basic modeling (not shown here) is the same utilized for HD-12 and HD-15 experiments in sections 5.3.4.1 and 5.3.5. The extended modeling also considers the effects of sound in flame, taking into account the effects of the acoustic-parametric instability, see 5.3.9.

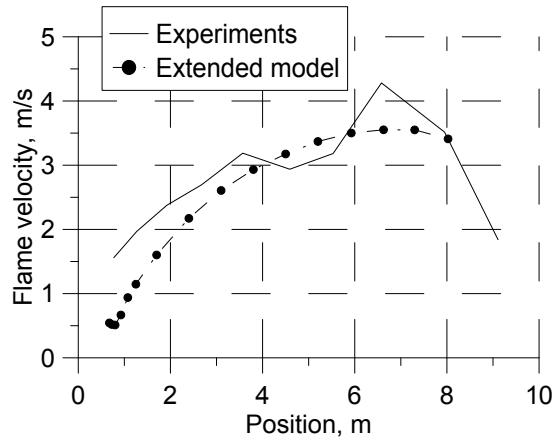


Figure 5.34: Flame velocity along the central axis and non-axial transducer line of the facility in the THAI, HD-22 experiment with extended modeling taking into account the effects of the acoustic-parametric instability.

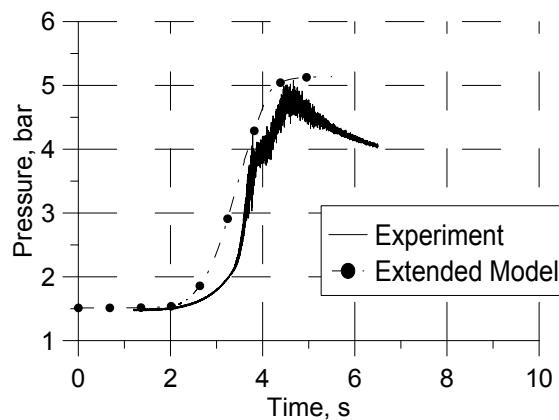


Figure 5.35: Pressure signals in the THAI, HD-22 experiment with extended modeling taking into account the effects of the acoustic-parametric instability.

The pressure built-up, Figure 5.35, is correctly predicted due to the enhanced propagation of the flame in the transverse direction (see Figure 5.36 or 5.37). The transverse enhancement is particularly visible in the second, third and fourth diagrams in the Figure 5.36 when it is compared with Figure 5.23¹⁰ and results in a flow pattern that alters completely the final combustion shape.

For the comparison with Figures 5.17 and 5.23, the general evolution of the flame was also depicted in Figure 5.37 and a comparison in Figure 5.38. The general evolution of the flame is very similar to the tendencies shown for HD-12 or HD-15. After an initial phase after ignition in which the flame burns slowly, the transition to a regime dominated by the flame instabilities happens and the flame accelerated upwards and laterally. The most significant difference is the enhanced acceleration in the transverse direction (Figure 5.38).

It is still necessary to clarify the reasons determining that the other mixtures analyzed do not suffer those parametric instabilities. A significant difference in the sound speeds between the mixtures in the experiments HD-12 and HD-22 exists (see Table 5.9). For the mixtures of the experiments HD-15 and HD-22 such

¹⁰Figure 5.23 applies to test HD-15 and not to HD-22. Dynamics without the transverse enhancement of HD-22 were similar to HD-15 ones.

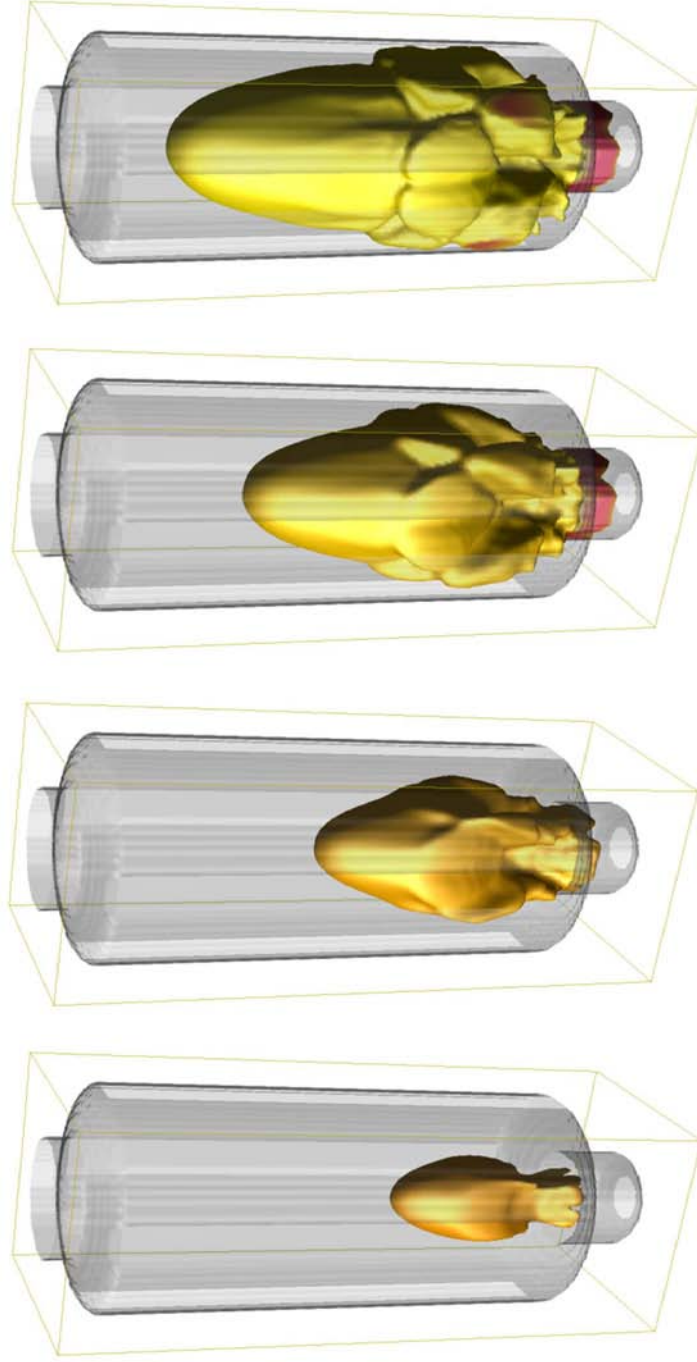


Figure 5.36: HD22 experiment. Temperature iso-surfaces taken at 800K representing the flame propagation for the simulations performed with acoustic-parametric instability modeling. The moments selected for representation were 2.83, 3.32, 3.71, 4.37 s after ignition.

difference is not as significant. Two competitive mechanisms appear: on one side HD-15 mixture has a much larger positive Markstein number (the width of the stability band between the parametric and the acoustic instability is proportional to it, Figure 5.31); on the other side, there exists a small reduction in the first harmonic frequency between the two cases. The band of stability of the problem HD-15 is finally wider and therefore the mixture does not suffer any flame surface enhancement due to parametric instability.

Following the path initiated in section 5.3.8 it is maybe of interest to compare qualitatively the results of the numerical calculations of the three experiments. In Figure 5.38, the shapes of the flames at mid-height inside the containers (different acquisition time) have been represented. The three form the typical *mushroom* shape, but the HD-12 problem does not keep continuity with the initial position of the ignition. Expansion of the HD-22 in the transverse direction is more intense thanks to the additional modeling. Its shape cannot be purely explained and it is not absolutely determined by the circulation around the walls.

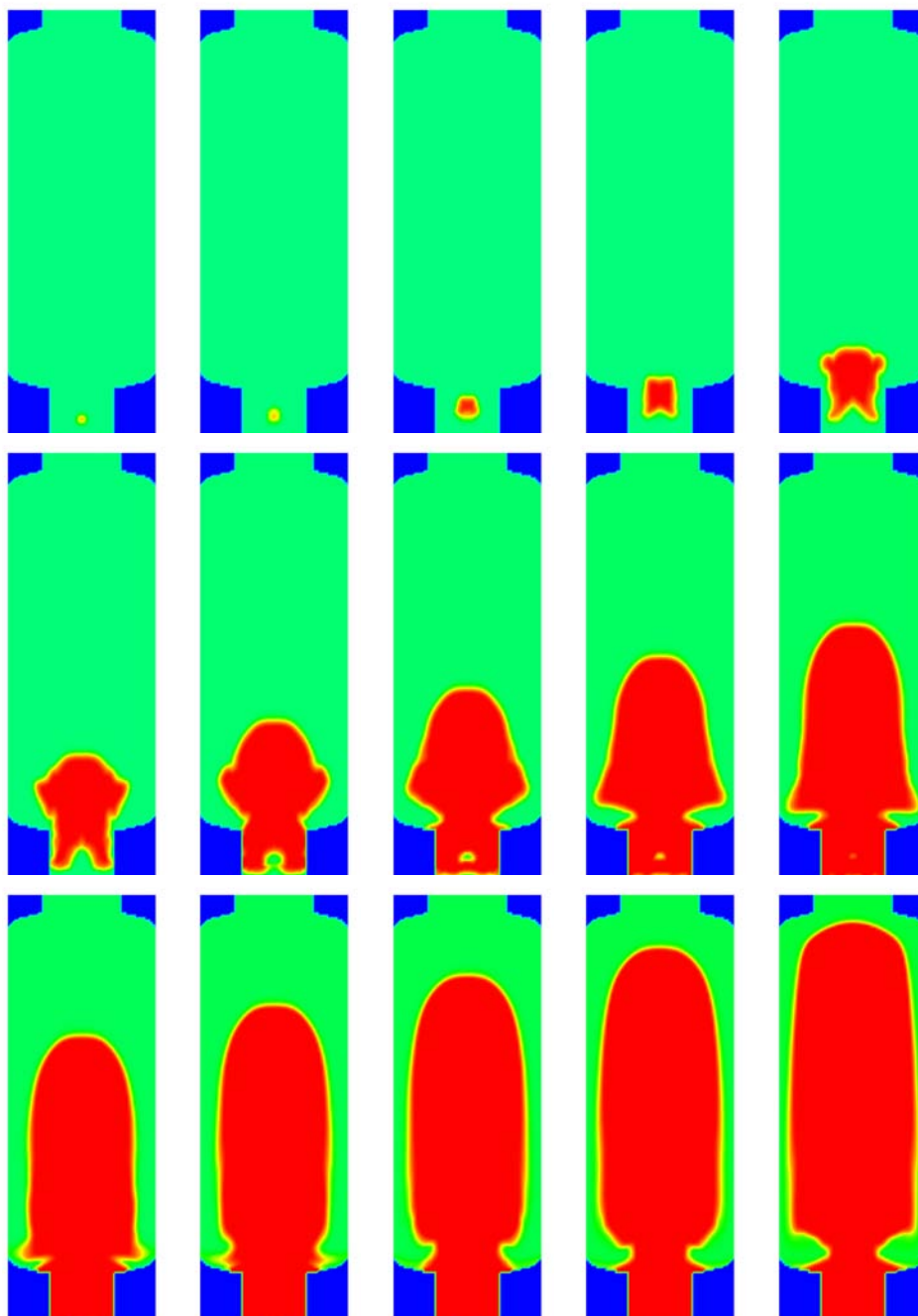


Figure 5.37: THAI-HP22. Temperature fields in different times after ignition. First row: 0.06, 0.35, 0.62, 0.88, 1.17 s. Second row: 1.40, 1.65, 1.90, 2.15, 2.40 s. Third row: 2.64, 2.89, 3.13, 3.37, 3.61 s.

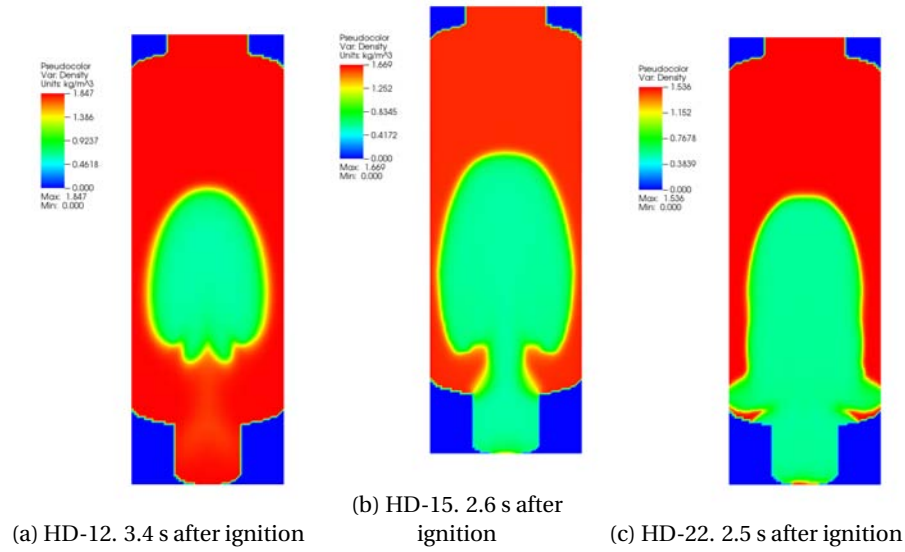


Figure 5.38: Comparison of the shapes of the flames at mid-height generated by the three different experiments analyzed. Depicted is a field representing the density.

Chapter 6

APPLICATIONS

6.1 General

This chapter contains the results of simulation activities performed by the candidate within the European HYSAFE organization workbench program (EU, 2013), (Jordan et al., 2009). The simulations were carried out utilizing the KYLCOM model (section 4.2) a variation developed during this PhD thesis. They represent different practical applications related to the hydrogen combustion in industrial safety, matters which were reviewed in section 1.8. Even if some experiments can be considered as limited in their instrumentation and validity, they represent the state of the art for large scale applications. Therefore they constitute a set of problems with the highest interest for the matter of H_2 combustion safety.

Taking this into account, the tests included in this section were selected as benchmarks within the HYSAFE project activities. Thus, simulations were performed in order to draw conclusions about the suitability of the models, numerical tools and user practices. The results of the workbenches related to the experiments contained in the sections 6.2, 6.3 and 6.4, are included respectively in the papers (Baraldi et al., 2009)¹, (Baraldi et al., 2010)¹ and (Makarov et al., 2010)¹.

¹Articles co-authored by the author of this thesis

6.2 Large scale tunnel

6.2.1 General

Among the cases of major interest for the foreseen H_2 economy, a deflagration inside a tunnel with vehicles appears as one of the most relevant hydrogen accident scenarios to foresee. Thus, evaluation to adopt the preventive measures necessary to minimize risk appears as fundamental.

Conceptually, deflagrations in tunnels constitute merely a scale enlargement with respect to the cases already studied in Section 5.2 (Driver Tube) with a more restricted influence from the blockage ratio created by obstacles. Earlier studies considering hydrogen safety in tunnels were undertaken by Breitung et al. (2000), Mukai et al. (2005), Middha and Hansen (2009) and Venetsanos et al. (2008).

6.2.2 Description of the experiment

The experiments involving hydrogen explosions in a tunnel were performed by Groethe et al. (2005) and Sato et al. (2006). The set up reproduces a vehicle tunnel whose diameter is 2.4 m, its length is 78.5 m and its cross-sectional area is 3.74 m^2 . The tunnel represents approximately a one-fifth scale of the fully realistic infrastructure and can be visualized in Figure 6.1.



Figure 6.1: Large scale tunnel experiment: facility and cross section view.

The experiment addresses an environment in which a release of hydrogen is partially confined, allowing hydrogen concentration to build up to a rich mixture. The confinement of the deflagration causes enhancement of the combustion. Additionally, the presence of vehicles in the tunnel (see Figure 6.2) represents turbulence-generating obstacles susceptible of enhance the deflagration and increase the flame front velocity.

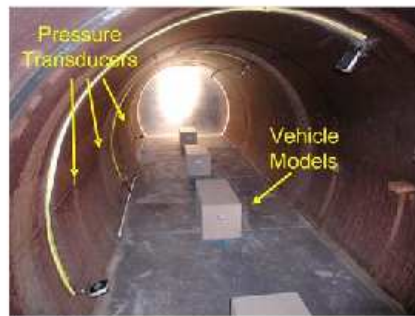
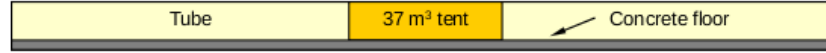


Figure 6.2: Inner view of the tunnel. Box shaped obstacles simulating vehicles.

In order to simulate the explosion of a rich H_2 release in a tunnel after an accident, an experiment in which a 30 % vol. H_2 -air homogeneous mixture contained within a 37 m^3 volume ($1\text{ kg } H_2$) located at the center of the tunnel was selected for calculations, see Figure 6.3. Two different geometrical set-ups were considered, a completely empty tunnel and a tunnel with 4 dummies simulating vehicles on the floor center-line inside the burnable mixture area. The first can be considered as a reference case while the second considers disposition of vehicles after a stop in the circulation caused by an accident. The vehicle models measured 0.94 m in length, 0.362 m in width and 0.343 m in height, representing typical vehicles at one-fifth scale, see Figure 6.2 and 6.3. The distance between vehicles was 1.52 m . The blockage ratio due to the presence of the vehicles was only 0.03 .

37 m³ Test



37 m³ Test With Obstacles



Figure 6.3: Configuration of the tunnel and the H₂ distribution. Upper: no obstacles. Bottom: 4 cars. The areas with presence of H₂ are marked in dark yellow.

Pressure transducers were mounted on the side wall along the entire length of the tunnel. The ignition position was located in the middle of the tunnel and the over-pressures generated by the deflagrations were nearly constant along the length of the tunnel. The deflagration in the empty tunnel with 30% hydrogen concentration generated an over-pressure peak of about 150 kPa. The presence of the vehicles/obstacles did not significantly increase the strength of the explosion and the overpressures were only slightly higher compared to the case without vehicles, due to the small blockage ratio.

6.2.3 Results of the simulation

The geometry of the tunnel offers several symmetries. The tunnel is symmetric both to a longitudinal plane, marked with *mirror boundary condition* in Figure 6.4, and a cross plane passing through its center signaled with blue color in the sketch. This provides the possibility of modeling just a fourth of the whole geometry.

Additionally the large volume on the right side on the picture is necessary to provide a buffer zone for the products escaping from the tunnel. Furthermore, to guarantee the absence of pressure increase due to pressure waves reflections, *open boundary conditions* (Dahoe and Cant, 2014) were implemented on the borders of the volume, colored in light pink. As the whole dynamics happens in the

interior of the tube, the volume must be interpreted a numerical *buffer* and obtain a significant discharge. Some relevant information about the grid employed on the calculation is contained in the Table 6.1

Table 6.1: Characteristics of the mesh used in tunnel calculation.

Domain size, LxWxH, cells	Resolution [cm]	Cell Number
73x70x308	9 cm	1,573,880

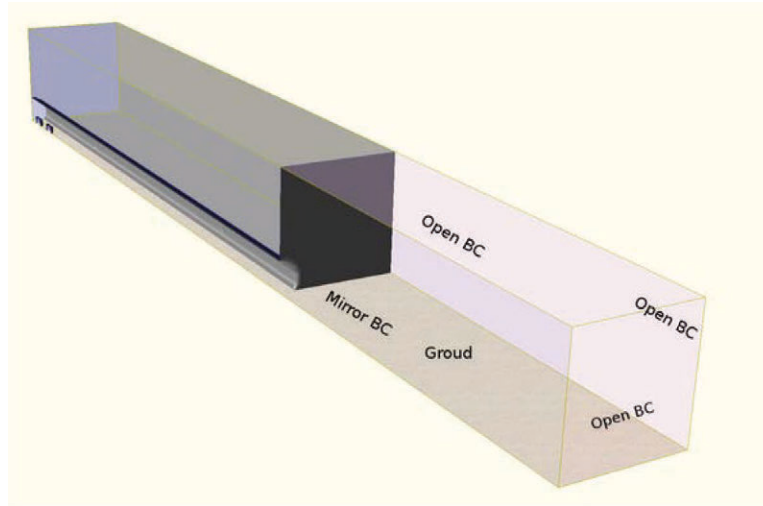


Figure 6.4: Geometry meshed for the numerical simulations of the large scale tunnel experiment.

The turbulent burning velocity utilized was the one by Schmid et al. (1998) see Table 4.1. The ignition process has been modeled by artificially forcing the initial chemical reactions in a small volume at the beginning of the calculations. The flame is considered to burn in the laminar regime in a first stage. Exact computation of the transition from laminar to turbulent burning regime is impossible for this problem. The Landau-Darrieus, thermal-diffusive, Richtmyer-Meshkov, Kelvin-Helmholtz and acoustic instabilities must be simulated in an approximate

but representative way, following the strategies and models already discussed in Section 5.2.2 and 5.3.9.

In this simulation, the laminar regime can be considered as predominant until interaction with the first obstacle is significant. AS a matter of fact, taking into account the results of the experiments performed in the Fraunhofer-Institut by Pfortner and Schneider (1983), in the initial 50 ms the mixture can be considered as completely dominated by the laminar regime. Furthermore, for stoichiometric mixtures, which corresponds to $Le \approx 1$, the thermal-diffusive instability² plays no role in the flame acceleration and no further modeling for the *quasi laminar* regime is required until the Landau-Darrieus instability is significant. Following the results obtained by the Fraunhofer-Institute, the moment in which this instability will gain preponderance (flame radius 1 m to 1.2 m) appears to be after interaction with the first obstacle and by them tunnel walls are more relevant for the dynamics. Therefore, the modeling of the Landau-Darrieus instability is also not required for these simulations.

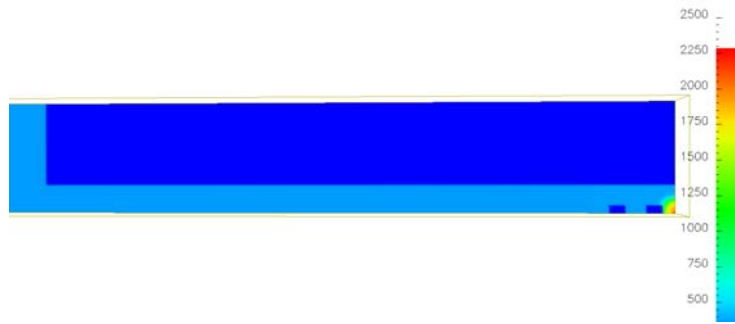


Figure 6.5: Application of the modeling to tunnel deflagration. Temperature field representing flame development in early stages. Case with obstacles. Frame taken 0.047 s after ignition.

²The thermal-diffusive instability cannot exist for $Le \leq 1$ (Zeldovich et al., 1985)

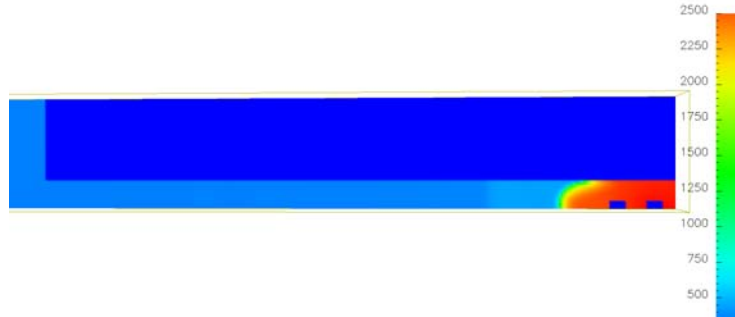


Figure 6.6: Application of the modeling to tunnel deflagration. Temperature field representing flame development in intermediate stages. Case with obstacles. Frame taken 0.087 s after ignition.

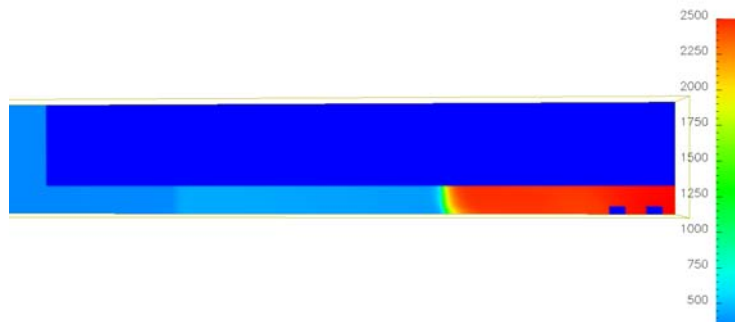


Figure 6.7: Application of the modeling to tunnel deflagration. Temperature field representing fast propagation regime, after acceleration of the flame. Case with obstacles. Frame taken 0.12 s after ignition.

Figures 6.5, 6.6 and 6.7 allow for a qualitative description of the explosion. An initial stage of slow laminar / quasi-laminar development is followed by the acceleration of the flame.

The laminar/quasi-laminar stage occurs until any interaction with the obstacles had happened, at which point the flame instabilities dominate the propagation. Figure 6.5 can be considered the maximum time limit of such an stage.

In a secondary phase, the flame acceleration of the flame occurs (see Figures 6.6, 6.7). This is due to two main reasons. On one hand, the *finger flame* mech-

anism, described by equation (5.5) and already discussed in section 5.2.4.1 takes into account the significant increase of the velocity due to the growth of the flame surface that in turn generates more (expanded) products. On the other hand, flame acceleration is due to the interaction of the flame with the boundary layers generated by the walls of the tube and the obstacles. Due to the reduced obstruction created by the cars in the tunnel (<10%), this effect is, although significant, of secondary importance compared to the *finger flames* mechanism in this problem, for the acceleration stage.

During the acceleration phase and the following fast propagation regime (see Figure 6.7), the products of the explosion push the rest of the fuel and the air contained in the tunnel to the exterior. This can be clearly seen in Figure 6.8 where the iso-surfaces corresponding to 4% vol. H_2 (approximately the flammability limits) are marked in green. The initial distribution of H_2 represented in Figure 6.3 can be compared with the status 0.24 s after ignition represented in Figure 6.8. In Figure 6.8, the leftmost iso-surface represents the position of the flame, while the rightmost shows the position of the flammability limit. The domain delimited by the leftmost iso-surface and the ignition position is filled by combustion products. The domain between the two iso-surfaces shows a concentration of H_2 in mass fraction (approximately 24% vol H_2), marked in red. This phase of fast consumption lasts until the reactants are exhausted.

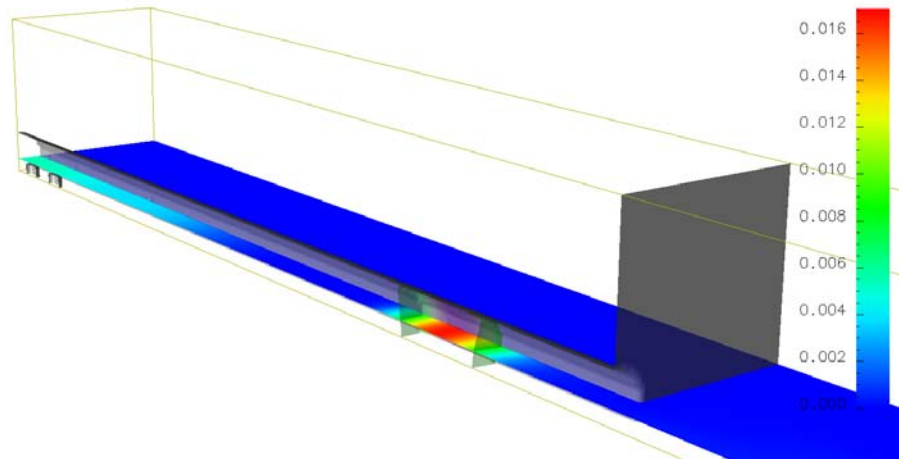


Figure 6.8: Application of the modeling to tunnel deflagration. H_2 distribution 0.24 s after ignition for the calculation with obstacles. Iso surface representing the border of the burnable area 4 vol. % H_2 . The boundary in the right constitutes the interface between the fuel and the air.

The results obtained were compared with the dynamic pressure transducers available at distances 1.0 m, 3.61 m, 10.61 m and 30.40 m from the ignition position. The results of those comparisons are shown in Figures 6.9 and 6.10 for the case in which obstacles are present. Additionally, Figures 6.11 and 6.12 contain the results of the simulation of the cases in which no obstacles were installed.

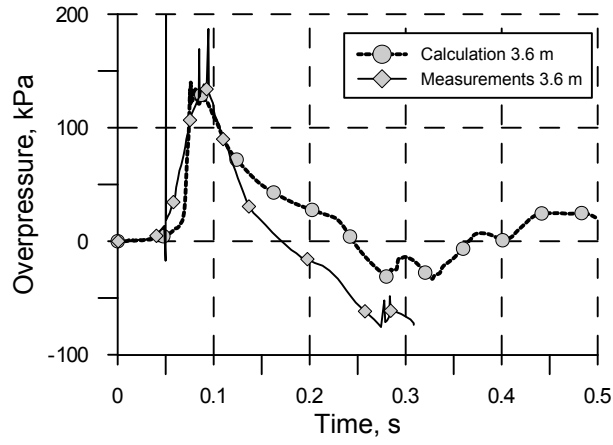


Figure 6.9: Application of the modeling to tunnel deflagration. Comparison of overpressure history for the sensor located at $x = 3.61$ m. Case with obstacles. 30% hydrogen volumetric concentration.

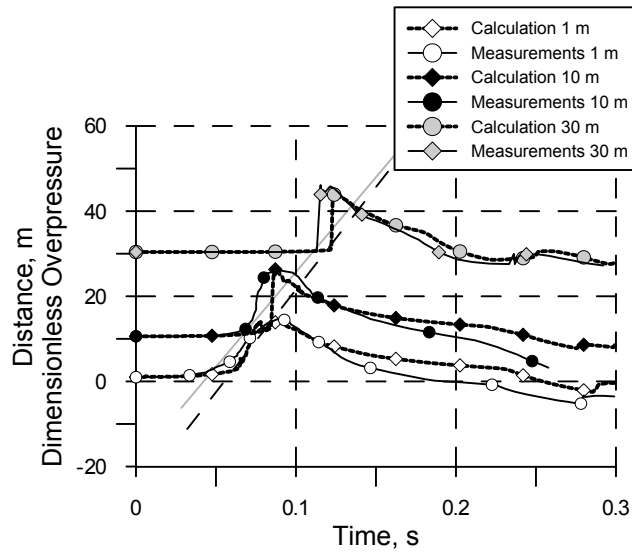


Figure 6.10: Application of the modeling to tunnel deflagration. R-t diagram. Comparison of overpressure history for the sensors located at $x \approx 1$ m, 10.6 m, 30.4 m. Case with obstacles. 30% hydrogen volumetric concentration.

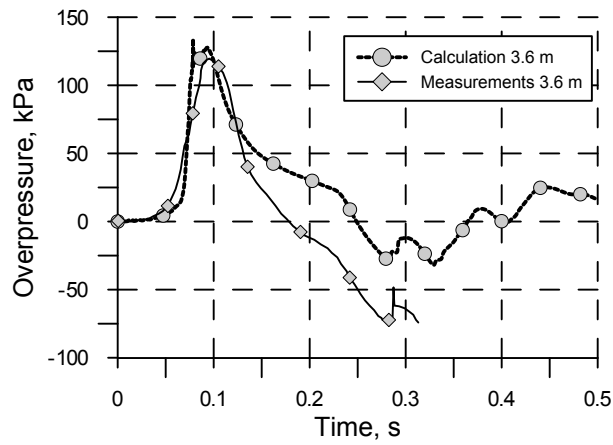


Figure 6.11: Application of the modeling to tunnel deflagration. Comparison of overpressure history for the sensor located at $x = 3.61$ m. Case without obstacles. 30% hydrogen volumetric concentration.

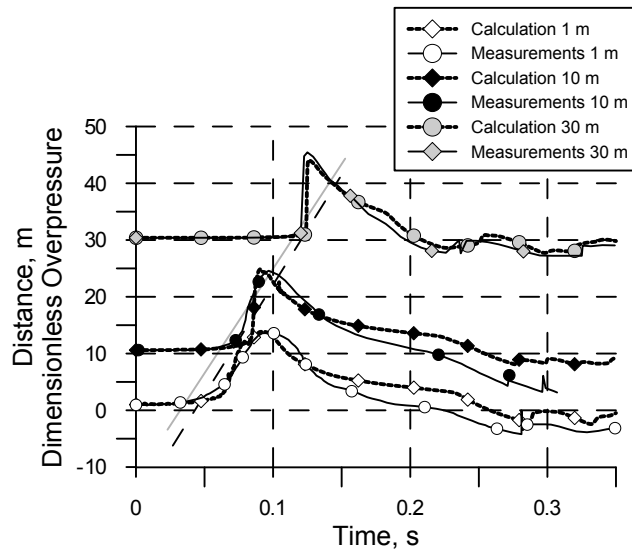


Figure 6.12: Application of the modeling to tunnel deflagration. R-t diagram. Comparison of overpressure history for the sensors located at $x \approx 1$ m 10.6 m 30.4 m. Case without obstacles. 30% hydrogen volumetric concentration.

In Figures 6.9 and 6.11 we can appreciate that the maximum over pressures are well represented in a range of 10% deviation, which is within the interval of experimental uncertainty.

In Figures 6.10 and 6.12 we may visualize the so called $R-t$ diagram. The name refers to the disposition of the axes, the distance, or radius in ordinates and the time in abscissa. In $R-t$ diagram any signal is represented, made dimensionless with the maximum instantaneous pressure, in the position where the transducer generating the signal is located. This allows for a practical graphical qualitative representation of a process, and its evolution, for its analysis.

Both in the case without obstacles and in the case with obstacles, the maximum of the blast wave pressure increases with the distance from ignition point in the early stages of propagation. The shape of blast wave profile changes also with the distance (see Figures 6.10 and 6.12³), showing a progressive steepening of the leading edge. Both behaviors are well captured by the simulations from a qualitative point of view.

The time at which the blast wave arrives at each transducer can be visualized in Figures 6.10 and 6.12. Joining with a line the instants at which the shock wave arrives for each transducer of these figures and calculating the slope, we may obtain the velocity of propagation. This is very well reproduced, even more significantly taking into account that initially the blast wave travels in a 30% hydrogen-air mixture and subsequently in air, with the significant difference in the sound velocity this represents (407 m/s and 347 m/s).

The pressure over-prediction in the tail of the profiles is expected to generate over-prediction in the calculation of the impulse in that region. The over-prediction of this magnitude is significant, as the expected potential of destruction of an explosion is in general expressed, see Baker et al. (1983), as a function of the pressure peak and the impulse. The reason for this over-prediction is that, even if heat losses were not neglected, the mesh close to the wall is too coarse to describe correctly the heat losses, producing an underestimation of their prediction.

³Peaks are normalized and therefore are of similar sizes and thus change of peak level is not to be seen in these figures. Shapes are though very recognizable.

In the early stages of the propagation, the effects of the obstacles can be analyzed comparing the curves contained in Figures 6.9 and 6.11 with the results resulting from experimental measurements or numerical analysis. We can appreciate that the maximum pressures as well as the shape of the pressure signal are very similar. This confirms that the obstacles did not play a major role in the acceleration of the flame, as previously deduced.

From the results obtained analyzing the numerical transducers located along the tube, it was also confirmed that after the early stages of propagation, the strength of the blast wave is almost constant along the whole length of the tunnel while it decays rapidly as soon as the blast wave exits from the tunnel because of the strong expansion. The negligible influence of the obstacles on the far field can be confirmed by the comparison between the results obtained in the far field, see Figure 6.13.

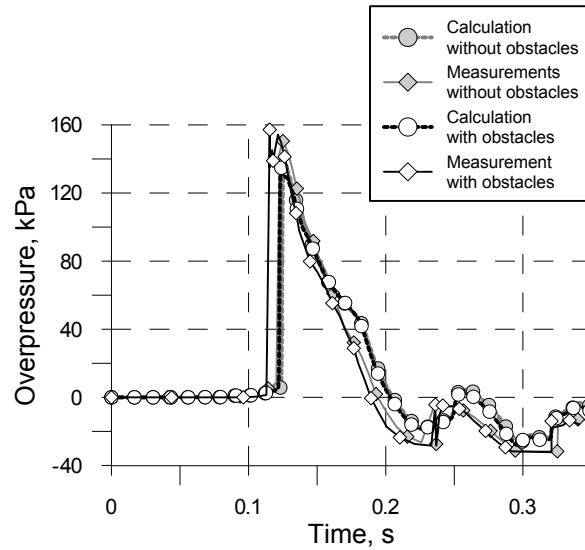


Figure 6.13: Application of the modeling to tunnel deflagration. Comparison of overpressure history for the sensor located at $x = 30.4$ m. Comparisons of the signals for the cases with obstacles / without obstacles.

6.3 Quiescent dry hydrogen-air mixtures with concentration gradient

6.3.1 Introduction

In deflagrations of hydrogen-air mixtures with gradients of concentration the flame propagation will strongly differ from well mixed regions. The experiments addressing this topic are related to a very significant issue for the prediction of deflagration of realistic hydrogen clouds (Kuznetsov et al., 2012), as in the most of accident scenarios, flame propagation will happen through non-uniform gas-mixture. The large Buncefield accident (MacDonald, G., 2013), in which liquid pool of fuel vaporized and create a vertical gradient of concentration can be given as an example of this behavior.

6.3.2 Description of the experiments

Whitehouse et al. (1996) experimentally studied the deflagration of dry hydrogen-air mixtures with concentration gradient. They tried to explain the differences in flame propagation pattern between stratified regions and well-mixed gases. To perform their study they utilized a facility which consists of a 10.7 m^3 cylinder with a diameter of 1.5 m and a height of 5.7 m . The facility has three manholes that were arranged at mid-height (see figure 6.14). The initial pressure and temperature were 1 atm and 25°C . At the bottom of the vessel three fans, mounted on a rig, were available to mix the contents. Further details on the test facility are contained in Kumar and Bowles (1990).

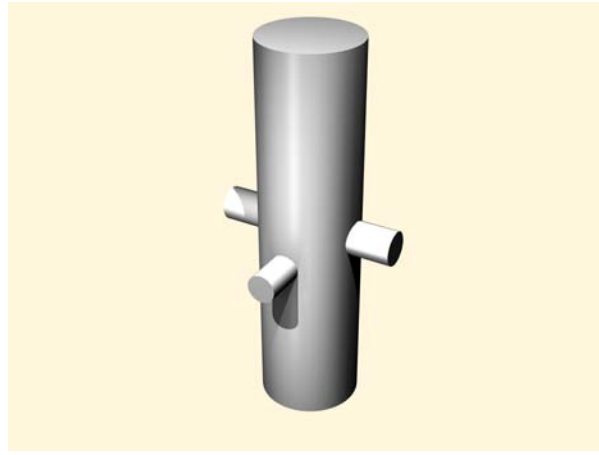


Figure 6.14: Combustion test facility geometry. Multi-purpose containment. Picture created with Rhinoceros software based in the description of the facility.

Two experiments with approximately the same amount of hydrogen were selected for the simulations. The first was a deflagration developing in a uniform 12.8 vol. % H_2 mixture. The second one was a non-uniform hydrogen mixture corresponding to an average 12.6 vol. % hydrogen which ranged from 27 vol. % at the top to 2.5 vol. % at the bottom of the vessel (see Figure 6.15).

The uniform hydrogen distribution was created by stirring the gas mixture using the fans. The stratified mixture was achieved by feeding the vessel with progressively higher hydrogen concentration. In both cases the mixture was ignited in a position close to the top of the facility.

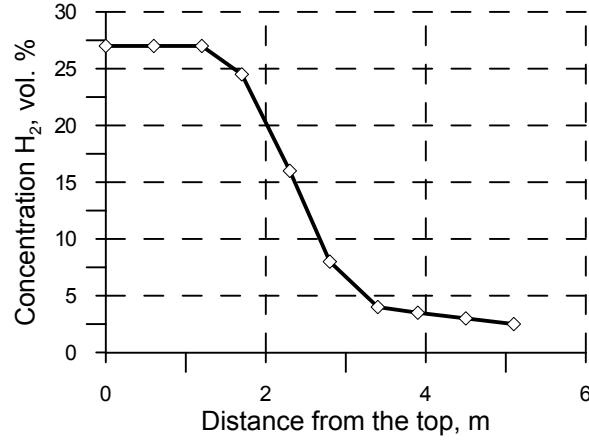


Figure 6.15: Concentration of the stratified test.

In the experiment, pressure histories were recorded using piezoelectric transducers. The flame movement was deduced from the flame arrival times, detected by an array of thermocouples, located on both sides of the vessel axis, approximately midway between the axis and the vessel wall, and pressure transducers, mounted close to the vertical center line axis.

6.3.3 Results of the simulation

In large scale calculations, the choice of a grid represents a trade-off between obtaining accurate enough results for the flow fields of interest and the availability and cost of computational power. The grid resolution was based on previous experience (Makarov et al., 2009)⁴, (García et al., 2010)⁴, (Yanez et al., 2011b)⁴(see table 6.2). The turbulence was modeled with the standard $k-\epsilon$ model (equations (1.14) to (1.24) in section 1.5.4). The turbulent burning velocity utilized was the one by Schmid et al. (1998) see Table 4.1

⁴Articles co-authored by the author of this thesis

Table 6.2: Characteristics of the mesh used in the calculation.

Domain size, LxWxH cells	Resolution	Cell Number
67x53x142	4 cm	504,242

Since the flame propagation speed is significantly lower than the speed of sound inside the tested hydrogen-air mixture, the pressure distribution could be assumed uniform and a single sensor/location is significant of the whole volume.

The results shown in Figure 6.16 allow comparing the experimental and simulated flame arrival times. Contrary to the pressure dynamics, which is an integral characteristic of a deflagration process, flame propagation is a three-dimensional process and its evolution on the centerline may deviate from the progression at the periphery of the vessel. The analysis will be built on assumption that the flame propagation along the centerline reflects its propagation in the vessel generally. This assumption is based on a simple consideration that as the vessel geometry is close to a cylinder, flame propagation should be close to one-dimensional. For the same reason, the flame propagation dynamics should correlate with the pressure dynamics. Figure 6.16 shows good agreement between simulations and the experimental data for both uniform and gradient cases. The uniform case shows an slight over prediction of the propagation speed that will also reflect in the pressure signal (Figure 6.17). For the gradient case it may be suggested that the flame propagation along the vertical axis in the lower vessel section decelerates under the combined effect of the decreasing hydrogen concentration in the mixture and decreasing volume available for the combustion products expansion.

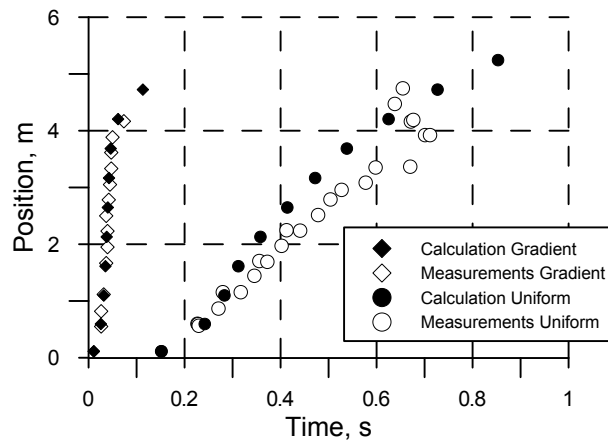


Figure 6.16: Combustion test facility geometry. The position of the flame is obtained using the ignition point as reference.

Comparison of the experimental and simulated pressure dynamics inside the vessel for the uniform 12.8 vol. % hydrogen-air mixture is shown in Figure 6.17. The experimental record indicates that there may be mass burning rate acceleration at the very final stage of combustion, leading to an increasing pressure rise rate. The most probable cause of this divergence may be differences on the facility shape, specifically on the rig supporting the ventilators. Due to the relatively old date of performance of the experiments, 1996, the exact configuration is ignored. The configuration finally adopted, shown in Figure 6.18, was deduced from the experimental paper and private communication with Atomic Energy of Canada Limited (AECL) and still contains uncertainties on the real configuration.

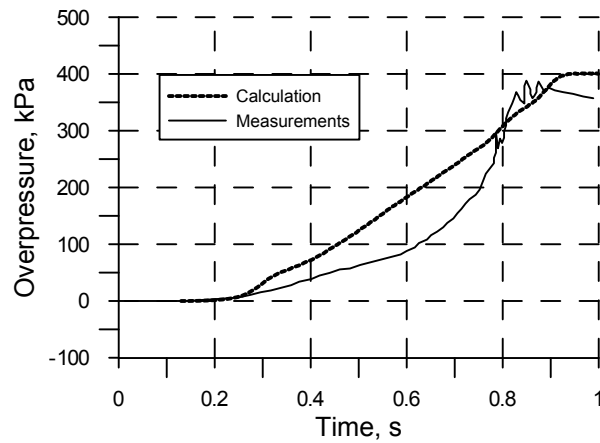


Figure 6.17: Whitehouse combustion test. Comparison of experimental and simulated pressure dynamics for the uniform 12.8% vol. hydrogen-air mixture.

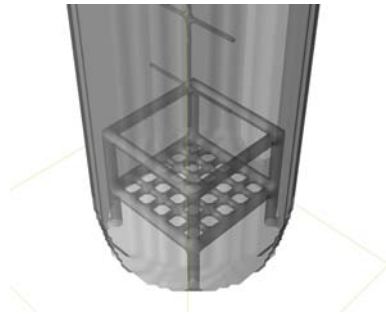


Figure 6.18: Whitehouse combustion test. Ventilators rig.

The gradient mixture deflagration, whose pressure evolution can be seen in figure 6.19, is an order of magnitude faster than that for the uniform mixture. In this case of deflagration in the gradient mixture, the simulated pressure records were closer to the experimental data. The simulation reproduced pressure oscillations similar to the experimental ones, whereas there are no comparable pressures in simulation results for the uniform mixture. It can be suggested that the propagation of the flame inside the manholes distorts the flame shape (see illustration four

in the Figure 6.20) and as a result the Richtmyer-Meshkov instability is triggered. This instability can be explicitly and directly resolved in simulations without requiring any additional modeling producing the final pressure oscillations visible in the figure. The pressure oscillations are not present in the uniform case due to the slower propagation velocity reached in this case.

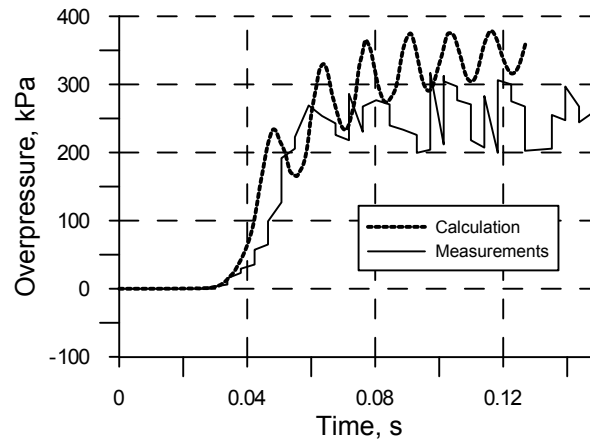


Figure 6.19: Whitehouse combustion test. Comparison of experimental and simulated pressure dynamics for the gradient (average 12.6% vol.) hydrogen-air mixture.

A general view of the development of the flame is shown in Figure 6.20. The general pattern of the stream-lines is to push downwards generating a vortex in the manhole, only significant turbulizer present in the problem, see 6.21. The flame surface in the Figure 6.20 suffers a large scale wrinkling which is caused by a low frequency mode of the Rayleigh-Taylor instability (see frame 2 in Figure 6.20) that appears completely resolved in the selected mesh.

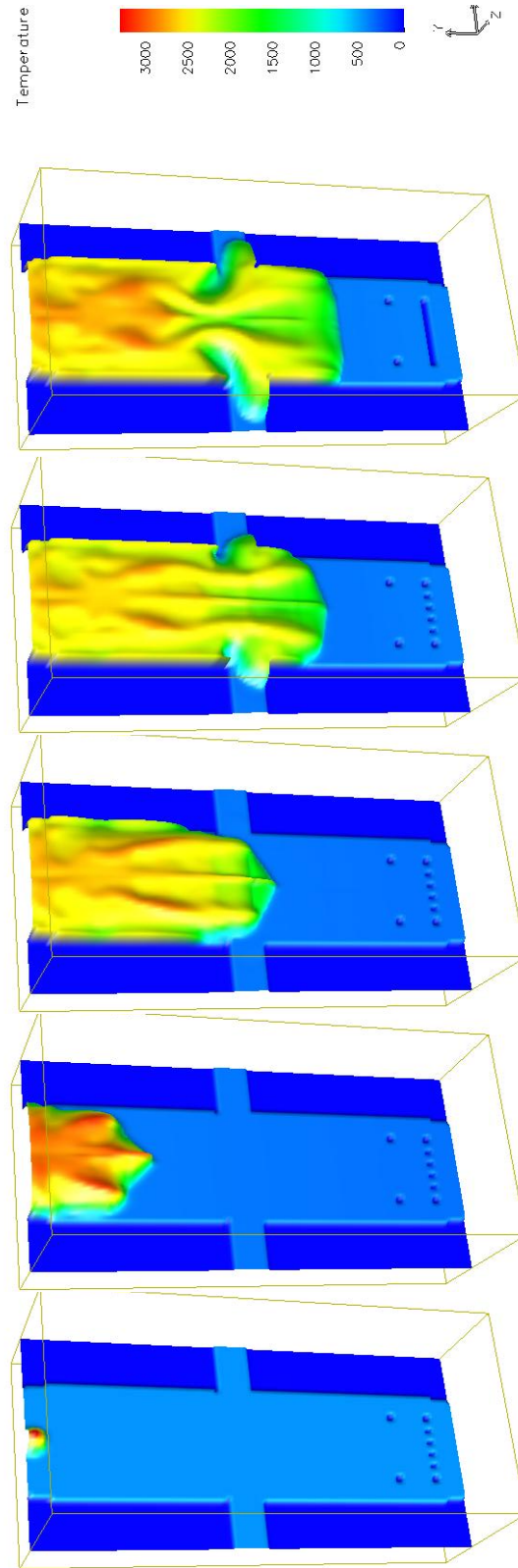


Figure 6.20: Whitehouse combustion test. Temperature fields representing flame profiles for the stratified mixture simulations. Case with composition gradient. The respective times after the ignition were 0.014, 0.03244, 0.036, 0.041 and 0.045 s.

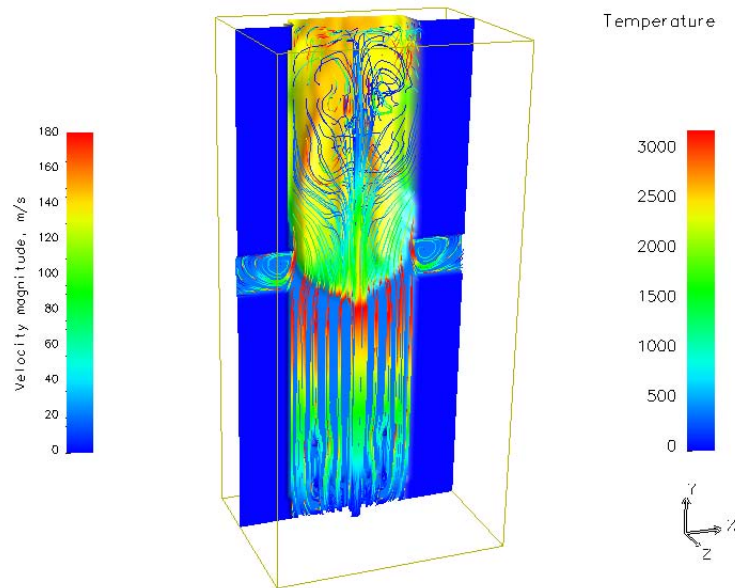


Figure 6.21: Whitehouse combustion test. Effects of the manholes as turbulizers 0.032 s after ignition. Vortex created by the manholes. Gradient (average 12.6 vol. %) hydrogen-air mixture. Right scale applies to the stream-lines while left does to the temperatures.

6.4 Vented Combustion

6.4.1 Description of the experiment

By *venting* we should understand the planned, automatically controlled or not, discharge of a container, room and any other enclosure or confinement, in order to preserve it from its bursting permitting the escape of fumes, liquids, gases, or steam or a mixture of them with the final objective of minimizing the personal and material damage.

Venting should be them considered as one of the major mitigation procedures to minimize the results of a hydrogen explosion. Therefore, validation of the code and the model utilized for the analysis of an explosion with venting is a very im-

portant issue for the hydrogen safety.

Prediction of the effects of venting in explosions is a very complex matter. It must be recalled that the strength of an explosion depends particularly on the obstruction and confinement degree. Parameters such as the mixture composition, initial pressure and temperature, pre-ignition turbulence, the size and shape of the vessel, the position of the ignition, the position, number, size and shape of the vents, the presence of obstacles and confinement inside the vessels and outside affect strongly the resulting pressure loads. Additionally, secondary mechanisms can contribute to the pressure build-up like acoustic oscillations, Helmholtz instability and flame instabilities, etc.

Many experimental and theoretical investigations about the effect of venting on flame speed and over-pressures exist, e.g. (Pasman et al., 1974) and (Razus and Krause, 2001). The classical approach to the problem (Molkov et al., 2000), (Yao, 1974), (Simpson, 1986), (Runes, 1972), (Cubbage and Simmonds, 1955), (Rasbash, 1969), (Molkov et al., 1997) is to describe venting effect with empirical correlations, evaluating the relation between maximum pressure and vent size or others characteristics of the problem. Up to now, none of the methods considered can be recommended as a general-purpose tool for vent area design, including some methods in engineering guidelines (Razus and Krause, 2001). Even more, following Bauwens et al. (2009), there exists a significant level of uncertainty in analytical and empirical-based prediction of vented combustion, resulting usually in conflicting recommendations.

The purpose of this section of this thesis is to evaluate the possibility to reproduce and study numerically the effect of the vent area on the resulting pressure loads. Several investigations of this kind have been performed by Patel et al. (2003), Ferrara et al. (2006), Karnesky et al. (2007), Molkov et al. (2006a), Molkov et al. (2007b), Makarov et al. (2007) and Di Sarli et al. (2009). To perform our study, explosions in a closed vessel versus a vented one with a vent area of 0.2 m^2 and 0.3 m^2 were compared. Experiments of hydrogen explosions in closed and vented vessels are due to Pasman et al. (1974).

The vessel represented in the Figures 6.22 and 6.23 is a container of a capacity

of 0.95 m^3 , a length of 1.5 m and an internal diameter of 0.97 m. A flange was set up in the backside (visible in Figure 6.22) to allow for the installation of rupture membranes. Piezoelectric pressure transducers were mounted on the wall of the vessel. The container was filled with stoichiometric hydrogen air mixture.

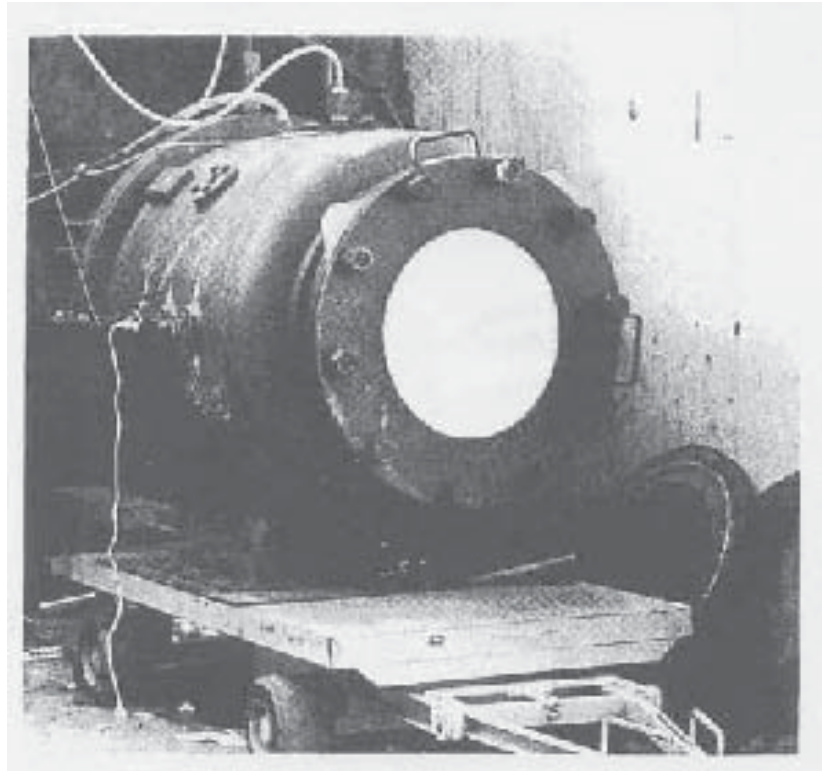


Figure 6.22: Vented combustion: photograph of the sust/gas explosion vessel.



Figure 6.23: Vented combustion: dust/gas explosion vessel. General view of the facility generated with Rhinoceros CAD program. 90° section.

6.4.2 Calculation Results

Some details about the mesh used in this numerical calculation are included in Table 6.3. The total number of numerical cells remained moderate for calculations performed with the vessel closed. For the calculation with membranes and subsequent release, a significant external volume should be simulated, becoming actually the largest region of the simulation domain. Its purpose is to be able to calculate the discharge of the deposit in an accurate way. Additionally, open, non-reflective, boundary conditions were selected for the external boundaries. The turbulence was modeled with eddy-viscosity-eddy-diffusivity LES (see section 1.5.3 and Appendixes A and B). The turbulent burning velocity utilized was the one by Schmid et al. (1998) see Table 4.1

Table 6.3: Characteristics of the mesh used in vented explosions calculation.

Case	Domain size, LxWxH, cells	Resolution [m]	Cell Number
Closed	56x83x56	0.0175	250,992
Open	100x163x100	0.035	1,630,000

The approach followed for modeling the membrane, although very simple, has produced good results. The membrane opening has been modeled as a *removable* closed wall. When over-pressure reaches a selected pre-fixed value, in this case 13 kPa, the closure is removed. To model the dynamic behavior of the process the membrane dilatation and rupture time, a delay of 5 ms. has been applied to the aperture.

In Figure 6.24 the flame propagation for the case with 0.3 m² vent is illustrated. In the first picture the early development of the deflagration is visible. The burning regime is laminar. Full development of the Landau-Darrieus instability, found to appear for flame radius 1 m to 1.2 m (Pfortner and Schneider, 1983), is not reached due to the limited size of the container and thus it can be hypothesized that this instability does not play a major role in this experiment. Due to the stoichiometry ($Le \approx 1$) the thermo-diffusive instability is not present. Therefore, no special modeling for the quasi-laminar regime has been needed. The second illustration shows the moment in which the membrane breaks and the flame suffers a sudden acceleration due to the rarefaction wave appearing in the interior of the container. Third and further frames illustrate the discharge of the products in the open atmosphere while the discharged reactants are still consumed by a turbulent flame. The eddies generated in the discharge are clearly visible creating the typical *mushroom* shape characteristic of explosions.

Figures 6.25, 6.26 and 6.27 contain a comparison of the experimental data and the simulation results. As expected, the maximum overpressure is larger in the closed vessel (about 8 bars, see Figure 6.25) and it decreases significantly in the vented configurations to 1.2 bar (see Figure 6.26) with the 0.2 m² vent and to 0.4 bar with the 0.3 m² vent.

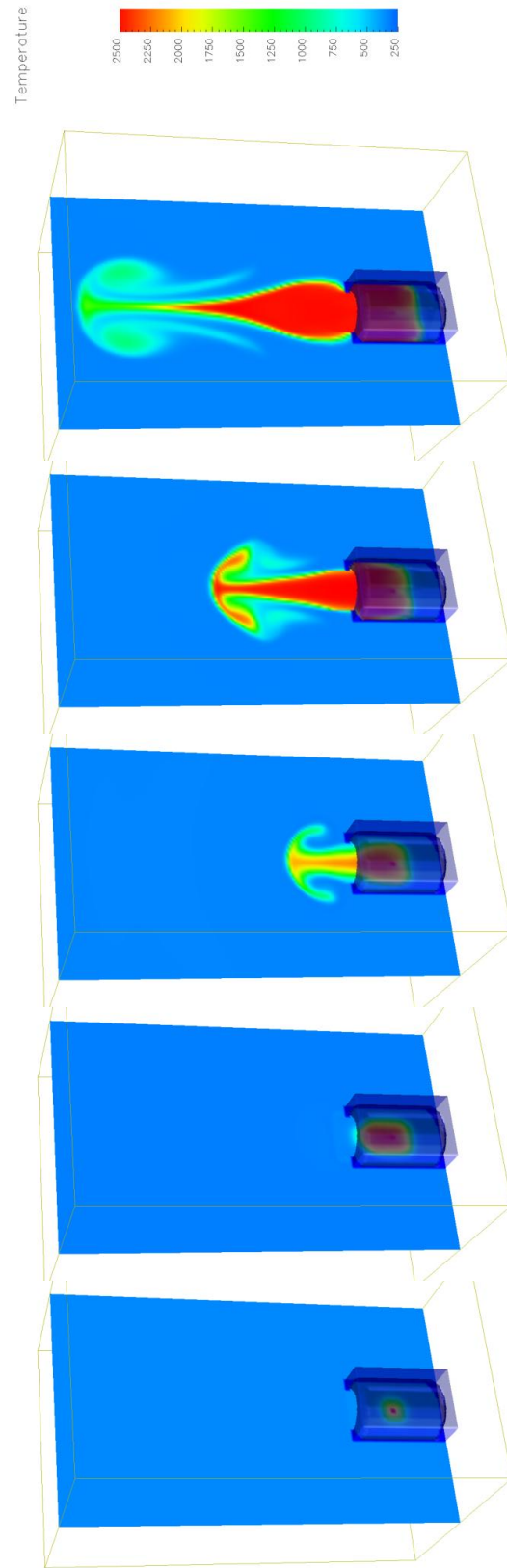


Figure 6.24: Vented combustion: temperature fields representing flame profiles for the simulations with a membrane surface of 0.3 m^2 . The times of pictures were 0.011, 0.020, 0.028, 0.051 and 0.077 s after ignition.

The level of accuracy in reproducing the maximum pressure is satisfactory. The discrepancy between the experimental data and the simulation results is below 20% for the case of the closed vessel and the case with the 0.2 m² vent. For the case with the biggest vent (0.3 m²), the discrepancy increases above 20%.

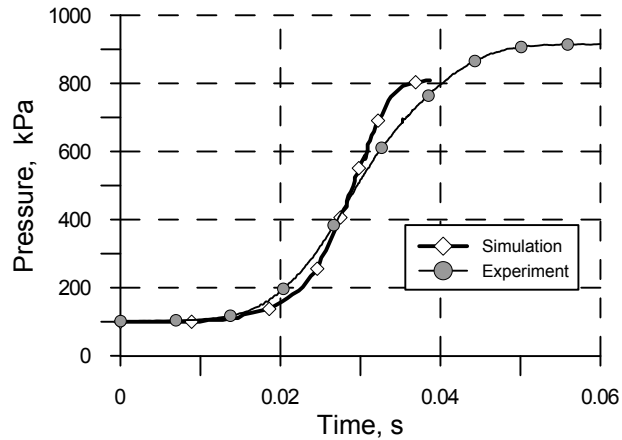


Figure 6.25: Vented combustion: Pressure signals in the dust/gas explosion vessel. Comparison of calculation and experiments for the closed case.

Surprisingly, the most significant discrepancies are found for the closed case, which conceptually represents the simplest one with complete absence of obstacles. The differences found for the closed case are thought to be due to the simplified chemical model. At high temperatures (above 1300 K), dissociation of the combustion products starts to occur, absorbing a significant amount of energy, lowering the temperature of the flame and of the burned gas and the final pressure in the vessel. If we assume the complete combustion case where the combustion products are only those given by the stoichiometric one-step chemical equation (H_2O and N_2), the theoretical adiabatic flame temperature is significantly larger than in the real case where many other species are present at the end of the combustion such as H_2 , OH , O , O_2 , NO and H . Therefore, to consider a one-step chemistry model with only steam and nitrogen as combustion products would normally over-predict the final temperature and pressure.

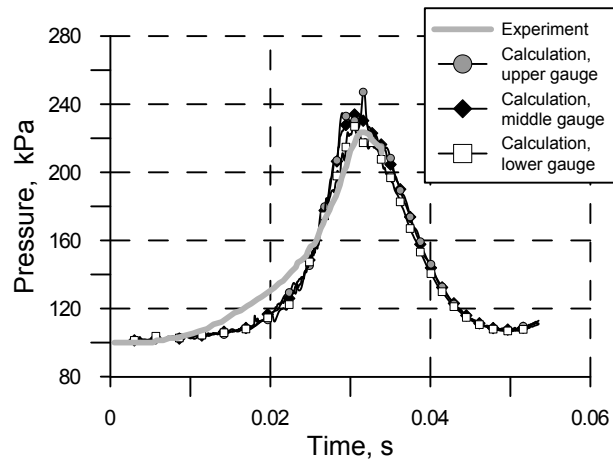


Figure 6.26: Vented combustion: Pressure signals in the dust/gas explosion vessel. Comparison of calculation and experiments for the venting (0.2 m^2) case.

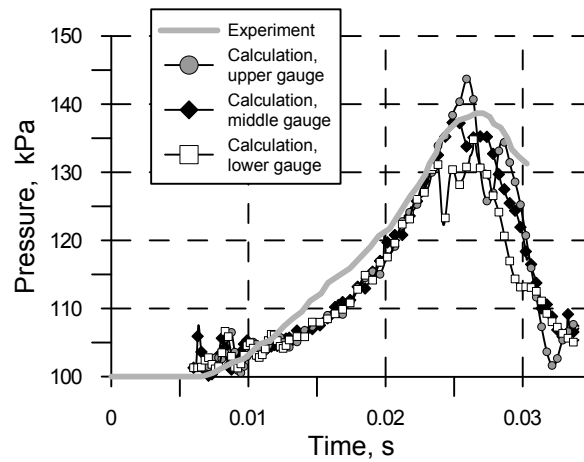


Figure 6.27: Pressure signals in the dust/gas explosion vessel. Comparison of calculation and experiments for the venting (0.3 m^2) case.

Chapter 7

Fukushima power plant analysis

7.1 Introduction

Three severe core melt down accidents have occurred in history (Kessler, 2012). The first one, the Three Mile Island disaster, happened in the United States on March 28th 1979. The second accident took place in Chernobyl, Ukraine, Soviet Union on April 26th 1986. The last catastrophe, the Fukushima Daiichi accident, occurred in Japan on March 11th 2011.

A hydrogen accumulation in the containment building may have occurred caused by several reactions following a severe accident in a nuclear reactor (Abou-Rjeily et al., 2011). The main sources of hydrogen that must be taken into account are the oxidation of Zircaloy by steam, the radiolysis of water, the reaction between water and boron carbide and the interaction of the molten core with the concrete of the containment ¹. Independently of its origin, the hydrogen released in the reactor accumulates inside the containment usually as a heterogeneous and prob-

¹The thermal decomposition of the concrete results in steam and carbon dioxide. These can further react with the metals in the melted core oxidizing them and thereby producing hydrogen and carbon monoxide

ably stratified semi-confined layer of hydrogen-air or hydrogen-air-steam mixture. The ignition of such a layer can lead to strong pressure loads and severe structural damage.

Several works consider an accident involving the combustion of a large amount of hydrogen from a nuclear engineering perspective in Boiling Water Reactors, e.g. (Abou-Rjeily et al., 2011; Breitung et al., 1999; Yanez et al., 2010b; Kessler, 2012; Sehgal, 2012; Kessler et al., 2012)². In these dedicated studies, the threat of a large scale hydrogen detonation, causing the rupture of the containment and allowing the radioactivity to be released in the environment, has clearly been identified. These sources establish that a design criterion, that must be considered for the construction of the containment building, is to withstand a large scale hydrogen detonation.

The sequence of events of the accident that can be found in the mono-graphic reports (Kessler, 2012; Kessler et al., 2012; Sehgal, 2012; TEPCO, 2012; INPO, 2011; Band et al., 2013; Borghoff et al., 2011; Repoussard and co workers, 2012) is a significant information in order to understand the catastrophe. The owner of the reactor, TEPCO (TEPCO, 2012), provides a very detailed schedule, which has been the basis of the chronology appearing in most other documents considering this issue (Band et al., 2013; Borghoff et al., 2011; INPO, 2011). The record covers in depth the development of the accident for each of the reactors independently, providing a detailed and separate timetable for each of them.

On March 11th 2011 at 14:46 an earthquake of magnitude 9.0 on the Richter Scale occurred close to the north-east coast of Japan. Following the established procedure, the Fukushima Daiichi power plant shut down automatically to initiate its cool down after suffering no apparent damage due to the earthquake. At the moment of the accident, of the six reactors available, only three were operational, units 1 to 3. Unit 4 was completely de-fueled and units 5 and 6 were shut down for maintenance. Approximately one hour later, a tsunami with a 14 m wave height reached the power plant and originated critical damage. Concretely, it disabled the emergency power supply interrupting the shut down procedure, induced a com-

²(Yanez et al., 2010b) was co-authored by the candidate

plete black-out and destroyed the sea water pumps of the station (for flooding plus blackout see e.g. (Fernandez-Cosials et al., 2015)).

The lack of electrical power disabled the delivery of cold water necessary to keep the core fully covered and cooled. The destruction of the water pumps and the blackout prevented access to the ultimate heat sink. The boil-off in the cores produced steam that raised the vessel pressure. This was relieved opening the ADS valves and bringing the steam to the suppression chamber. The water level in the reactor nucleus went down gradually until it dropped to a level of about halfway down the core. At the same time, the suppression pool started to become saturated and the pressure in the containment started to increase rapidly. Due to the lack of water, the steam generation rate became too low to cool down the fuel rods. The clad temperature increased and when the temperature reached 1400 K the Zircaloy oxidation by steam started, initiating the production of hydrogen. The temperature continued to grow and when a value of 3100 K was reached, melting point of the uranium dioxide, the melting of the core also started. Approximately 16 hours after the initiation of the event, the fuel and the control rods were completely melted. Desperate attempts to maintain the cooling of the core through battery power had proven unfruitful when they become completely exhausted after eight hours of utilization.

Meanwhile, the pressure in the suppression chamber and in the primary containment continued to increase, overtaking and surpassing the design limits. Finally, the venting was initiated twenty four hours after the initiation of the event when the pressure had risen to twice that of the design values. The gases that were vented involved steam, radioactive species and hydrogen. Additional unintended discharges through leak paths and cracks created in the primary container vessel during the pressurization event cannot be excluded.

The hydrogen finally accumulated at the roof of the reactor building, an area which was only lightly plated. The hydrogen ignited, blowing up a large section of the roof and of the lateral walls and dispersed a significant amount of volatile fission products. The explosions occurred 24.8 h after initiation of the event in Unit 1, 68.2 h after initiation of the event in Unit 3 and in Unit 4, a serious hint of

explosion in form of strong noise, has to be considered 87.9 h after initiation of the event (TEPCO, 2012).

It is most remarkable that Unit 4, which was de-fueled, also suffered an explosion. The accepted theory is associated with the back-flow of gases from Unit 3 during venting (INPO, 2011). Due to the piping arrangement, it is plausible that this backflow may have brought hydrogen into the building of Unit 4 via a reverse flow. The other two possibilities explaining this event look much less probable. They are, firstly, that the spent fuel pool of unit 4 was heated starting the oxidation of the Zircaloy and generating hydrogen. The second possibility is that the hydrogen used to refrigerate the main electric generators caused the explosion.

It is important to underline that, between the possible causes of the explosion in Unit 1 there is a consensus (TEPCO, 2012; INPO, 2011; Band et al., 2013; Borghoff et al., 2011; Repoussard and co workers, 2012) that identify it as a hydrogen deflagration or detonation. All other possible causes, like steam explosion or gasification of combustible liquids, should be disregarded following these sources. The previous studies also determine that the oxidation of Zircaloy cladding is the most intense source able to generate hydrogen (Kessler, 2012; Kessler et al., 2012; Sehgal, 2012; TEPCO, 2012; INPO, 2011; Band et al., 2013; Borghoff et al., 2011; Repoussard and co workers, 2012).

The analysis of the hydrogen explosion that happened in the Fukushima Dai-ichi accident (Unit 1), and concretely the assessment of the amount of hydrogen that reacted in the explosion of Unit 1 and the damage it caused, is the objective of this chapter. The procedure that was followed consists in performing successive analysis of increasing complexity in order to obtain results that successively converge to a most probable quantity. Section 7.2 is initiated with a review of the amount of hydrogen generated during the accidents. Next, the amount participating in the explosion is assessed algebraically considering the speed of the shock wave and the size of the products generated during the explosion. Section 7.3 contains some qualitative considerations on the hydrogen release from the point of view of combustion science. Those are mainly aimed at the estimation of the acceleration potential and combustion regime of the combustible gaseous mixtures

involved. Section 7.4 contains the refinement of previous analysis utilizing numerical computational fluid dynamics calculations. As a result, a final amount of hydrogen involved in the explosion is obtained, assessing its destructive power.

7.2 Evaluation of the amount of hydrogen participating in the explosion

7.2.1 Amount of hydrogen generated during the cooling system failure

The knowledge of the amount of hydrogen generated during the accident is a significant magnitude for the present study and represents an upper limit to the amount involved in the explosion, which could be much smaller.

In their monograph on Light Water Reactors, Sehgal et al. (Sehgal, 2012) estimated that the amount of hydrogen produced in Unit 1 during the accident, lies in the range of 800-1000 kg.

TEPCO (TEPCO, 2012) also estimated the amount of hydrogen generated through a numerical analysis considering the oxidation of the zirconium cladding, leading to the values presented in Table 7.1. Unit 1 values fit within the range set by Sehgal et al. (Sehgal, 2012).

Table 7.1: Amount of hydrogen generated in units 1 and 3 (until the explosion took place) and in unit 2 (for the whole accident) as estimated in (TEPCO, 2012)

Unit	Amount, kg
1	890
2	460
3	810

The Sandia National Laboratory also analyzed the amount of hydrogen produced during the accident (Gauntt et al., 2012) utilizing the code *MELCOR* (MELCOR, 2013), their estimations are presented in Table 7.2. The results obtained consider the amounts of hydrogen generated in units 1 to 4. For Unit 1, the analysis

included the amount generated by the oxidation of Zirconium and the interaction of the core with the concrete. The estimation performed for units 2 and 3 only include the oxidation of the cladding while the assessment carried out for Unit 4, which was de-fueled, consider exclusively the oxidation of the cladding contained in the pool. The estimation for Unit 1 (870 kg) is in fair agreement with (Sehgal, 2012; TEPCO, 2012). Deviations from (TEPCO, 2012) for Units 2, 3 are of the order of 50%.

Table 7.2: Amount of hydrogen generated in Units 1-4 following (Gauntt et al., 2012)

Unit	Cladding oxidation, [kg]	Time after initiation of event, [h]	From core-concrete, [kg]	Time after initiation of event, [h]
1	870	24	400 2650	24 82
2	0 660	24 95	- -	- -
3	0 1220 1320	40 68 95	- - -	- - -
4	1732-2098	1000	-	-

7.2.2 Methodologies for the assessment of the amount of hydrogen exploding

The velocity of the combustion wave, the propagation regime and the amount of hydrogen which have participated in the explosion registered in Unit 1 are not yet known.

It is nevertheless possible to assess the amount of hydrogen involved in the explosion studying the blast registered by several outdoor cameras and available to the public (TEPCO, 2013c). This amount may differ, being significantly smaller than the amounts generated in the core and presented in the Section 7.2.1, as clearly, not the whole inventory produced gathered under the roof of the secondary containment. This evaluation can be performed, carrying out:

-
1. The analysis of the shock wave generated by the explosion that provide the amount of hydrogen involved in a fast deflagration or detonation and represents a lower bound to the amount of reactants involved.
 2. The analysis of the size of products resulting from the combustion that provide the total inventory involved in the explosion which represents an upper bound for the total mass.

For waves and blasts propagating spherically, an analytic formulation allowing for the evaluation of the amounts involved exists, for both methods mentioned, providing a meaningful indication of the quantities of hydrogen involved.

7.2.3 Evaluation of the amount of exploding hydrogen based on the speed of the shock wave

7.2.3.1 Assessment of the velocity of the shock wave

An initial assessment of the amounts of hydrogen involved in the accident can be based on the analysis of the speed of the shock wave obtained by the outdoor video-cameras (TEPCO, 2013c). A significant difficulty in order to perform an adequate accident analysis was to find an original video with proper framing speed. Finally, two of them have been used, with an acquisition rate of 15 and 30 frames per second. As a result of the analysis of the videos, the selected frames have been displayed in Figure 7.1. The authors apologize for the quality of the pictures presented although believe they are very significant for the study of the accident. So far it has been impossible to find pictures with a better resolution. The camera that filmed the development of the explosion, from which the frames presented are obtained, was located very far away from the power plant. Thus, the photographs that appear in the image have been cut to focus in the area of the image in which the nuclear power plant appears. The shock could be traced by at least two methodologies: determining the position of the refraction created by the shock wave or tracking the steam generated by the combustion. Therefore, the images included in Figure 7.1 have been treated increasing the colors, contrast and applying filters in order to

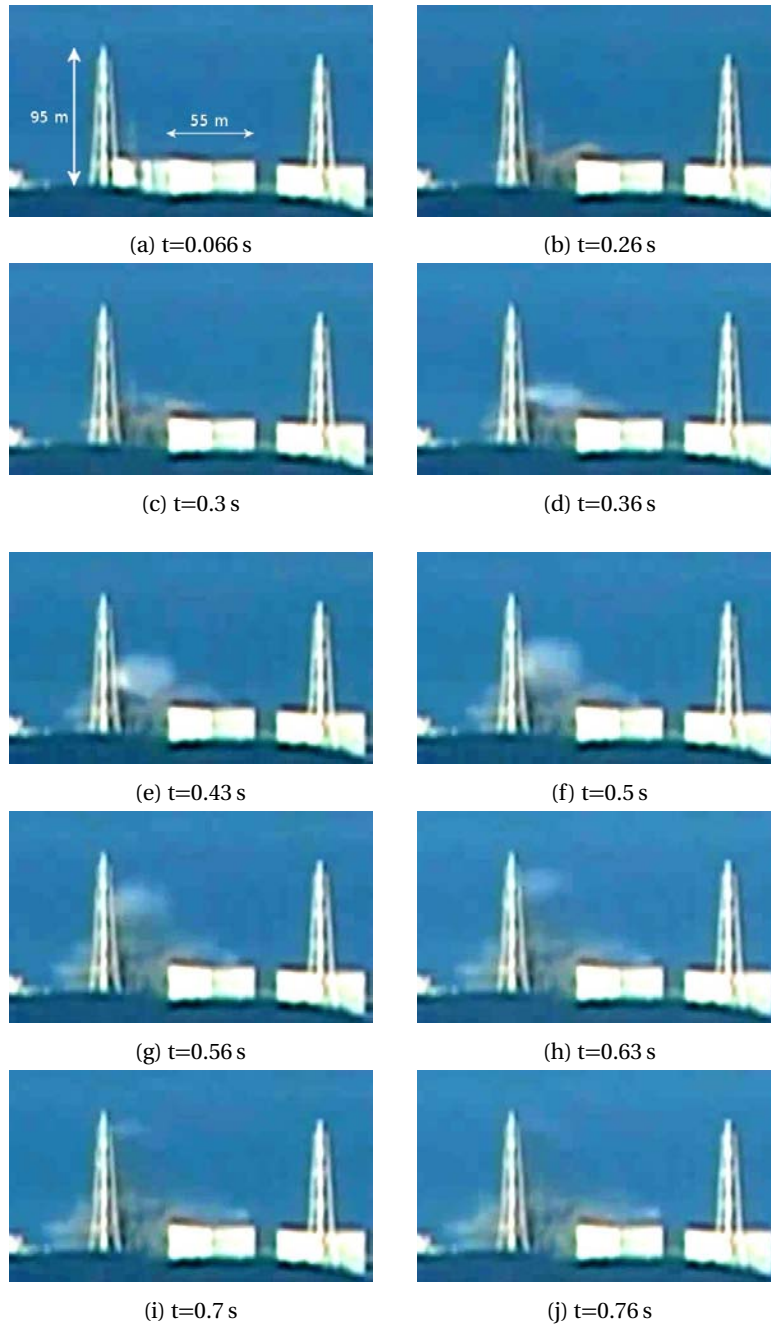


Figure 7.1: Selected frames of the hydrogen explosion and shock wave propagation. Time between frames is not uniform. The authors apologize for the quality of the pictures that are nevertheless considered very significant for the study of the accident. In frame (a) approximate sizes were included for the tower and the reactor (diagonal view).

improve the visibility of the shock wave and the combustion products. The results of one of those treatments is shown in Figure 7.2. The treatment helps to see more clearly the products of combustion, although the refraction of the shock remained invisible.

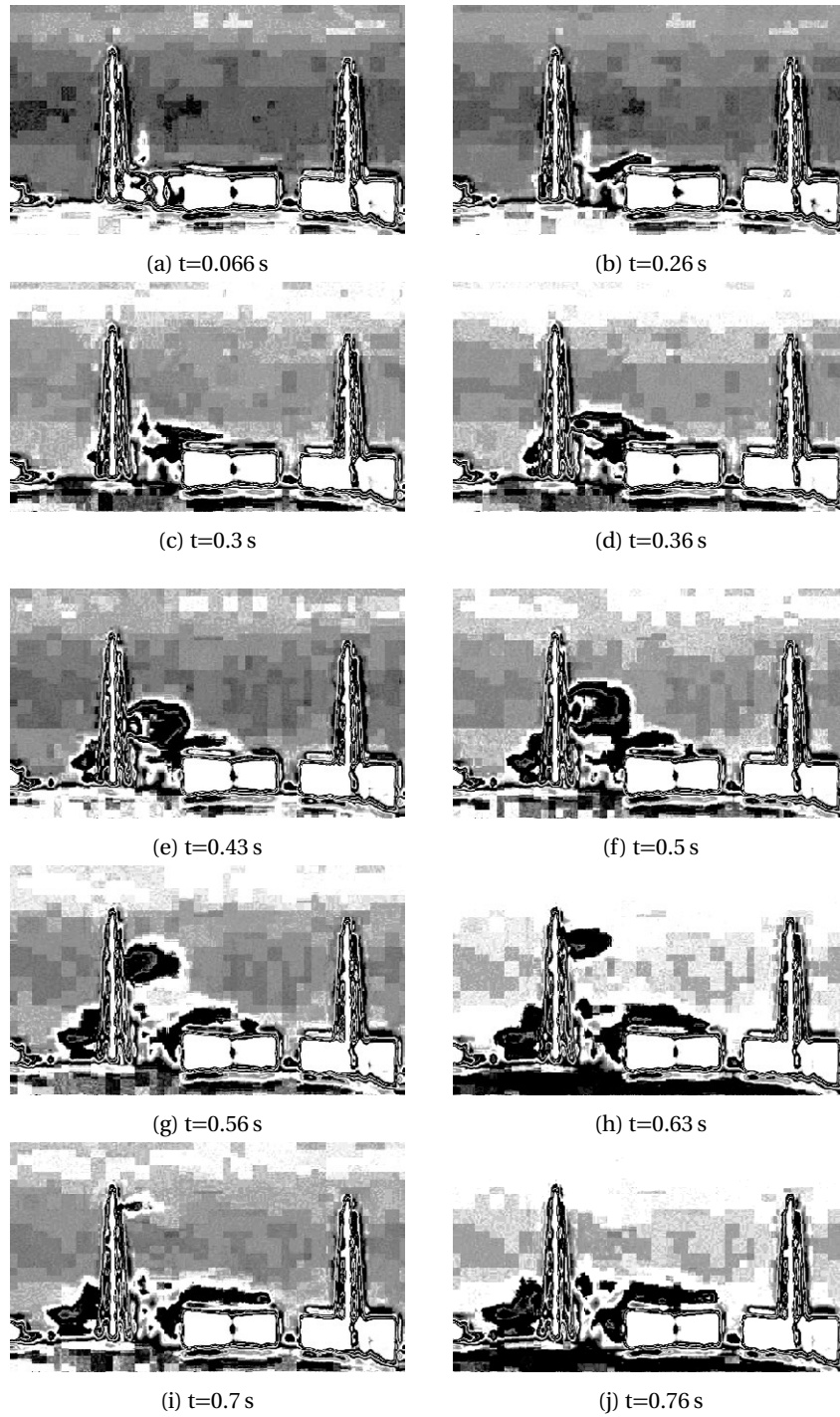


Figure 7.2: Frames in Figure 7.1 after image processing, highlighting the cloud of products and the explosion details.

In the accident, the hydrogen accumulated at the top of reactor building was finally inflamed due to an internal ignition source (likely an electric spark or a heat source). After the start of the burning reaction (frames 7.1a and 7.1b or the correspondingly 7.2a 7.2b) the combustion wave propagated relatively slowly until it accelerated. The flame reached the sonic propagation or even the detonation regime (from 7.1c or 7.2c onward) with the subsequent formation of a relatively strong shock wave. In frames 7.1c to 7.1i (corresponding to frames 7.2c and 7.2i), the steam, product of the combustion, is visible (in white) propagating upwards after the strong wave.

Such a flame behavior is similar and coherent with what is shown in combustion tests performed in flat combustible layers, e.g. (Kuznetsov et al., 2011a). As a major conclusion from those experiments, it can be stated that a significant run-up distance for effective flame acceleration, from subsonic to sonic regime or detonation, is necessary. Also, that the blockage ratio is a capital factor influencing the flame acceleration. Depending on the obstructions, the run-up distance vary between one or few meters for highly blocked space (50 % blockage ratio) reaching up to ten meters for low blocked space (less than 10 % blockage).

As a result of the analysis of the video, for which frames are shown in Figure 7.1, a shock wave speed of approximately 360 m s^{-1} , with a Mach number $M \approx 1.05$, at a distance from 50 m to 70 m from the center has been estimated.

7.2.3.2 Assessment of the amounts of fuel involved

According to the gas-dynamics formulae, e.g. (Landau and Lifshitz, 1987), the over-pressure generated by a shock of known propagation speed, P_{sh} , is

$$P_{sh}/P_0 = (2\gamma M^2 - (\gamma - 1)) / (\gamma + 1) \approx 2\gamma M^2 / (\gamma + 1) = 1.28, \quad (7.1)$$

where M is the Match number of the shock, γ the ratio of specific heats and P_0 the pressure before the arrival of the shock wave. Thus, for our case, the shock wave over-pressure turned out to be $\Delta P = P_{sh} - P_0 \approx 28 \text{ kPa}$.

The maximum pressure and impulse at different distances from the center of

the explosion can be predicted, following (Baker, 1973), as a function of the fuel mass energy of the mass of fuel. For convenience, the dimensionless dependencies in Sachs co-ordinates are utilized (Dorofeev et al., 1996). Under these coordinates, the dimensionless distance, $R^* = x(P_0/E)^{1/3}$, the dimensionless pressure, $P^* = \Delta P/P_0$, and the dimensionless impulse, $I^* = (\Delta I c_0)/(P_0^{2/3} E^{1/3})$ are used for the analysis, where x is the distance to the ignition position, P_0 the ambient pressure, E the energy of the explosive, ΔP and ΔI are the maximum over-pressure and impulse of the positive phase of shock wave. In Sachs co-ordinates, the dimensionless over-pressure and impulse may be formulated as a polynomial function of a single variable (Dorofeev et al., 1996), the dimensionless radius,

$$P^* \approx 0.34/R^{*4/3} + 0.062/R^{*2} + 0.062/R^{*3} \quad (7.2)$$

$$I^* \approx 0.0353/R^{*0.968} \quad (7.3)$$

The energy of hydrogen combustion at the distance $x \approx 60$ m may thus be obtained using equations (7.2) and (7.3) at the level of overpressure $P \approx 28$ kPa. The value of $E \approx 9200$ MJ is obtained as a result, corresponding to the combustion energy of an equivalent amount of approximately 80 kg hydrogen.

Table 7.3 summarizes the results of the calculations resulting from the image processing of the videos contained in (TEPCO, 2013c) at different distances.

Table 7.3: Results of the analysis carried out with equations (7.2) and (7.3) of the shockwave (SW) in order to obtain the amount of H_2 involved in the explosion

Distance, m	SW Radius, m	SW Speed, m/s	Over- pressure, Eq. (7.1) 100 kPa	Energy of explosion, MJ	Amount of hydrogen, kg
36-49	45	403	0.4	7850	65
49-63	55	403	0.4	14300	120
50-70	60	360	0.28	9200	80

7.2.4 Evaluation of the amount of hydrogen exploding based on the radius of the combustion products

Only a certain amount of the reactive gaseous mixture will explode in fast regime (sonic deflagration or detonation), leading to a shock wave formation. A significant amount of the reactants, at the initial stage of the combustion process, will burn relatively slowly. This is a serious restriction to the evaluation performed in section 7.2.3. An alternative possibility for the evaluation of the total amount of burned hydrogen, would be to study the radius of combustion products (Baker et al., 1983). The equation, $R_{max} \approx 3.5\Delta M_{fuel}^{1/3}$, where R_{max} is the radius of the combustion products and M_{fuel} the mass of fuel involved, that has been derived to study the detonation of propane-air gaseous mixtures can be utilized for this purpose. Utilizing this methodology, the total amount of burned hydrogen can be estimated in the range of 180-200 kg for a total maximum radius of the combustion products of $R_{max} \approx 20$ m. This radius can be estimated from the study of Figure 7.1b, in which the diameter of the explosion products can be estimated to be 40-50 m. As an indication, such an amount of hydrogen can be produced due to Zircaloy oxidation from the reaction of 4.5 ton of zirconium with 1.8 ton water ($Zr + 2H_2O \rightarrow ZrO_2 + 2H_2$).

Also, the formulation of Rakaczky (Baker et al., 1983), although devised for high explosives and thus not fully applicable, may be used for the evaluation. Under such methodology, $D_{max} \approx 3.76\Delta M_{fuel}^{0.325}$, where D_{max} is the diameter of the products and the total amount of premixed fuel oscillates between 1400 and 2800 kg, representing a final amount of hydrogen which lies in-between 140 and 270 kg. A similar $M^{1/3}$ proportionality can be also found in (Dorofeev et al., 1995). Utilizing the graphs included in this study, the total mass of premixed fuel will lie in the range of 0.5-1 tones, which may imply from 50 to 100 kg of H_2 .

7.3 Qualitative considerations on the hydrogen release from the point of view of combustion science

7.3.1 General

An estimation of the total amount of hydrogen involved in the Unit 1 explosion has been conducted in section 7.2.2. However, the combustion regime in which this event took place has not yet been discussed.

If the hypothesis, as stated in (TEPCO, 2012; INPO, 2011; Band et al., 2013; Borghoff et al., 2011; Repoussard and co workers, 2012), that the gathered hydrogen caused the explosion is accepted, the observation of Figures 7.3a and 7.3b suggests that the accumulation of fuel happened at the top of the reactor (TEPCO, 2013b, 2012).

From the point of view of the combustion, the accumulation of hydrogen under the roof of the secondary containment can be interpreted as a layer of fuel, confined or semi-confined by the roof, with a more or less heterogeneous and probably stratified concentration, in which the structural elements designed to sustain the cover may work as turbulizers that would promote flame acceleration and deflagration-to-detonation transition (DDT) (see Figure 7.3a).



Figure 7.3

The damage in the containment, resulting from a hydrogen explosion event, is proportional to the flame velocity squared. Therefore, the problem of flame propagation and acceleration, followed, or not, by a transition to detonation in semi-confined geometries appears to be very significant for Nuclear Safety.

The potential for flame acceleration can be determined utilizing criteria that segregates mixtures suffering fast propagation regime. The celebrated *Sigma Criterion* Dorofeev et al. (2001) establishes that a fast flame can only happen in tubes if the expansion ratio of the gases exceeds a certain critical value. For detonation, the *seven lambda* or simply *lambda* criterion (Dorofeev et al., 2000) establishes that the deflagration to detonation transition could only take place if the size of the burnable mixture exceeds seven times the width of the detonation cell.

In spite of its importance for Nuclear Safety, there is a serious lack of experimental data or analytic studies on critical conditions for flame acceleration and DDT in semi-confined layered geometries, both for the cases of uniform and non-uniform hydrogen-air mixtures. Extension of the criteria for tubes is not straightforward, and the existing criteria for layers, e.g. Grune et al. (2013), inferring the acceleration potential of a layered mixture (based on geometrical characteristics

such as size, pitch of obstacles, concentration, location and size of the fuel) are still very primitive.

7.3.2 Comparison with fully closed geometries

For a fully closed environment which has been studied in much greater depth, it is possible to provide the expected over-pressures depending on the flame propagation regime (Kuznetsov et al., 2011a, 2012; Ciccarelli and Dorofeev, 2008). For subsonic flame propagation, over-pressures of the order of 100 kPa may be expected. Values of the order of 400 kPa to 900 kPa are normal in the case of a sonic deflagration and over-pressures of 1 MPa to 2 MPa are achievable if detonation occurs. This means that in the cases of sonic deflagration and detonation, the maximum combustion pressure becomes sufficiently strong to damage the main reactor building and/or its equipment.

7.3.3 Acceleration and flame propagation regime in semi-confined layers

Considering the *Sigma* and *7-Lambda* criteria, the potential for acceleration of some mixtures can be examined, as reported in the experimental studies (Kuznetsov et al., 2012, 2011a; Grune et al., 2013), taking into account the thickness of the flat combustible layer, itself depending on the amount of gases discharged.

First, let us consider the most reactive hydrogen-air composition, the stoichiometric hydrogen-air mixture (30 % vol. H_2 in air). The critical (or minimum) thickness of a semi-confined layer of uniform gas composition for the effective flame acceleration and detonation initiation (Kuznetsov et al., 2011a) amounts to around 15 cm. For a concentration of 15% hydrogen in air, a 60 cm thick layer is necessary for an effective flame acceleration and a thickness of around 5 m for a detonation onset. A more realistic mixture for the nuclear safety containing a significant amount of steam (released in a loss of coolant event), namely a concentration of 15% hydrogen and 10% steam in air at 380 K, requires a thickness of around 35 cm for an effective flame acceleration and a thickness of about 8 m for the detonation initia-

tion. The experimental results shown in the previous paragraphs are summarized in Table 7.4

Table 7.4: Necessary thickness in order to obtain an effective flame acceleration and a detonation onset for some significant hydrogen-air mixtures in flat layers

H_2 [% vol.]	H_2O [% vol.]	Temperature [K]	Thickness for effective flame acceleration [m]	Thickness for detonation onset [m]
30	0	300	0.15	0.15
15	0	300	0.6	5
15	10	380	0.35	8

From the thermodynamic analysis of a steam-hydrogen release (Wagner, 2008) and (Lemmon et al., 2010), it can be inferred that, in the most probable scenario, steam condensation takes place as an iso-entropic expansion of steam from 7 MPa and 600 K, the nominal BWR conditions, to 0.1 MPa. Non condensed steam would only exist at 100 kPa for cases in which the temperature inside the containment would have been higher than 950 K. Thus, the hope of mitigation due to a strong hydrogen dilution with steam is not realistic at normal operational conditions of a BWR.

7.3.4 Size of the H_2 cloud and possibility of existence of detonation in view of the results of the first assessments

We have already enunciated the *seven lambda* criterion (Dorofeev et al., 2000), which establishes that the deflagration to detonation transition could only take place if the size of the burnable mixture exceeds seven times the width of the detonation cell. In order to utilize it, it would be necessary to know the detonation cell sizes for mixtures of significant concentrations (Kaneshige and Shepherd, 1997), which are included in Figure 7.4

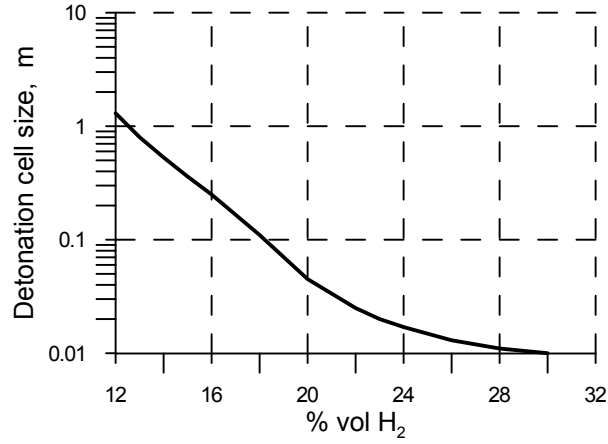


Figure 7.4: Detonation cell size obtained from the Detonation Database (Kaneshige and Shepherd, 1997)

For ulterior analysis, it is also convenient to calculate the over-pressure resulting from a detonation. Using the *Simplest theory* (Fickett and Davis, 1979), the pressure created by a detonation is directly,

$$p = (p_0 + 2\rho_0(\gamma^2 - 1)\Delta H^\oplus) / (\gamma + 1) \quad (7.4)$$

where p_0 and ρ_0 are the pressure and density of the gases before the arrival of the detonation, γ the adiabatic index and ΔH^\oplus the enthalpy of formation. The evaluation of this formula immediately yields the results contained in Figure 7.5

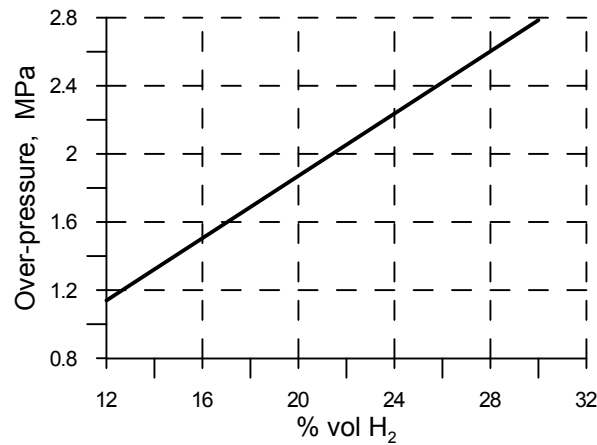


Figure 7.5: Detonation over-pressure

Due to buoyancy, the hydrogen inside the secondary containment will form a layer with different thicknesses depending on the concentration gradients it may suffer. In a building with a surface of $30\text{ m} \times 40\text{ m}$ an approximate amount of 200 kg of hydrogen may occupy a layer of significant thickness. Assuming a uniform hydrogen concentration would give an average concentration of about 7.3 % vol. H_2 . Such a hydrogen concentration is too low, according to (Kuznetsov et al., 2010), to provide a fast-sonic flame propagation regime or detonation. The hypothesis of a uniform concentration inside the secondary containment can thus be rejected. For the very significant stoichiometric concentration, an approximate thickness of 3.5 m is obtained for a uniform layer.

If we try to consider a more realistic hypothesis, a hydrogen layer significantly stratified in the vertical direction can be foreseen. A layer with a linear gradient of 1 % vol. H_2/m and maximum and minimum concentrations of 15 % vol. H_2 and 0 % vol. H_2 would have a height of approximately 14 m. According to (Kuznetsov et al., 2012), the flame propagates in such a cloud, in absence of obstructions, with a velocity of about 25 m s^{-1} and a characteristic maximum over-pressure of 20 kPa. If obstacles exist, such as beams, cranes, or any other kind of structural elements, a velocity of about 340 m/s and a characteristic maximum over-pressure of 0.55-1.2 MPa should be foreseen (Kuznetsov et al., 2012).

Applying the lambda criterion to these mixtures, the detonation scenario appears to be improbable although not impossible. The criterion establishes that a thickness of 5 to 7.5 m of combustible layer is required for the detonation. The run-up-distance for detonation transition might be too long in comparison with the size of the upper compartment.

On the other hand, the pressure of $0.5 - 1.2 \text{ MPa}$, obtained in combustion experiments with stratified layers with a maximum concentration of 15% H_2 , see (Kuznetsov et al., 2012), is comparable with the over-pressure of a lean detonation (see Figure 7.5). In fact, a sonic deflagration happening in a mixture close to the stoichiometry and a lean detonation have a comparable over-pressure $\approx 1 \text{ MPa}$.

As a conclusion of the previous disquisition, we may summarize that fast (sonic) deflagration was the most probable explosion regime, although the existence of a detonation cannot be excluded. In a closed volume, a fast deflagration may result in strong damages to the reactor building as it was seen in the photographs obtained after the Fukushima I accident (see Figure 7.3b).

7.4 Numerical simulations of the explosion

The analysis performed in Section 7.2.2 and 7.2.4 were valid for spherically propagating blast and waves. For the more realistic cases in which a flat hydrogen layer is considered and thus the propagation of the blast wave is not uniform nor isotropic, a numerical analysis must replace such analytic formulation in order to obtain more accurate results.

Calculations that have been carried out have been performed with the *in house* COM3D code Kotchourko et al. (1999b), which is a fully explicit finite differences parallelized combustion code developed in the Karlsruhe Institute of Technology intended for Nuclear Safety applications. The code resolves the compressible Euler or Navier-Stokes equations for reacting gaseous mixtures and has been widely validated in the Nuclear Engineering context Yanez et al. (2010b, 2011b, 2010c). The computations have been carried out firstly in an enlarged computational domain to capture the global features of the process, and in a subsequent stage a more

refined geometry has been utilized to refine the analysis.

7.4.1 Large computational domain calculations

The first set of numerical simulations that have been carried out, were intended to evaluate the parameters of the blast wave and their dependence on different amounts of hydrogen when the fuel forms a flat layer. Three different masses of hydrogen 10, 80 and 200 kg have been considered for the calculations of the accident scenario, based on the assessments performed in sections 7.2.3 and 7.2.4. It has been assumed that the hydrogen is uniformly distributed and that it forms a stoichiometric hydrogen-air mixture. The resulting layer has a thickness of 0.2, 1.4, and 3.5 m.

7.4.1.1 Velocity of combustion

It has been assumed that two combustion regimes were present, detonation and fast deflagration, in agreement with the qualitative analysis performed in Section 7.3. Due to the conditions of the problem, over-driven detonations can be excluded from the analysis and detonation represents an absolute maximum for the propagation of the combustion wave. The deflagration, with a flame speed of 400 m/s, is representative of the conditions discussed in Section 7.3. This corresponds to the so called *fast sonic deflagration* in a semi-confined layer of combustible mixture with a characteristic flame velocity close to the sound speed in reactants. The analysis of the pictures from Figure 7.1, shows the existence of a shock wave. This means that the propagation of the deflagration was at least sonic. The speed of sound for hydrogen-air mixtures close to the stoichiometry, lies in the vicinity of 400 m/s. Therefore, the selection of a *sonic deflagration* with a flame burning velocity of 400 m/s is representative of the weakest possible propagation regime.

Conceptually, the use of an imposed burning velocity corresponds to a very crude modeling. Concretely, it creates an analogy to a problem in which the acceleration of the flame, resulting from turbulence, flame instabilities, etc. is not representative of the reality (due to a lack of resolution) and must consequently be

disregarded . The imposed burning velocity is thus regarded as a *best estimate* of the real values of this magnitude. In spite of its crudeness, the methodology offers the possibility to analyze very low resolution problems or to allow for parametric studies, which are the main advantages that has justified its utilization in the past e.g. (Efimenko and Dorofeev, 2001). In the numerical simulations, this imposed velocity is achieved utilizing the CREBCOM combustion model, see (Efimenko and Dorofeev, 2001).

7.4.1.2 Geometrical representation

Taking into account the previous rationale and in order to perform the large scale calculations herein, an extremely simplified geometrical representation of the Fukushima I reactor (not modeling any details of the roof, etc), has been created with the intend to study the over-pressure generated by the blast of the explosion in a domain relatively distant from the contention of arround 200 m (see Figure 7.6). To speed up calculations, the symmetries present in the geometry were fully utilized, simulating just one quarter of the whole domain. The boundary conditions reflecting this simplification were signaled in the figure through light blue and pink colors, and marked as *mirror boundary conditions*. Non-reflective boundary conditions (Dahoe and Cant, 2014), were chosen in order to simulate the explosion in an open atmosphere (see faces marked *Open-BC*). The layer of pre-mixed fuel has been located at the roof of the reactor, marked in red in the figure, and will have the adequate thickness for each of the amounts of fuel considered for the simulations. Some significant details of the mesh are summarized in Table 7.5. The pressure in the far field was thoroughly studied through the installation of a significant number of numerical gauges. These were arranged forming two lines, at ground and roof levels, and were placed every ten meters.

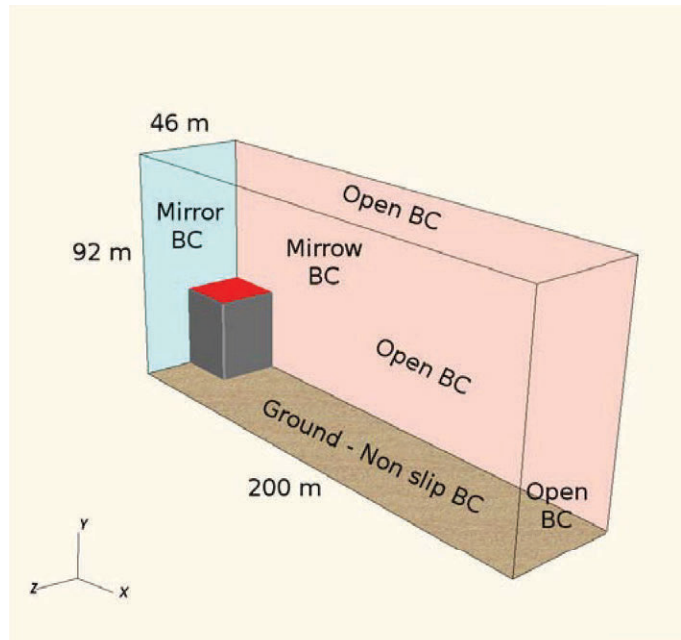


Figure 7.6: Geometry employed in the calculations. Due to symmetry, only $\frac{1}{4}$ of the total building was considered.

Table 7.5: Characteristics of the mesh used in the large scale Fukushima calculations

Domain size LxWxH, cells	Resolution	Number of Cells
46x92x200	1. m	846400

7.4.1.3 Results and discussion

7.4.1.3.1 General

Figures 7.7 and 7.8 show a sequence of screen-shots obtained as a result of the numerical calculations carried out considering the deflagration of 80 kg of hydrogen with an equivalent fuel thickness of 1.4 m and are qualitatively similar to the pictures obtained from other simulations performed with different amounts of hydrogen and propagation regimes.

In a first stage, the consumption of the fuel takes place rapidly (first snapshot

upper left in Figure 7.7). This is followed by the expansion of the shock wave. Due to the conditions of the problem, the expansion is highly anisotropic in the initial stage (upper two rows of the Figure 7.7). The momentum of the wave is much more intense in the vertical direction. The interaction of the wave with the ground creates two significant reflections. One produced by the interaction of the wave and the roof of the building. The second created by the interaction with the ground, which generates a strong reflection (last row of Figure 7.7 and Figure 7.8) and with the formation of the Mach stem, creates a significant over-pressure. In a second stage, and more significantly in the upper regions, the initial shock propagates more spherically and is followed by the reflection on the ground (snapshots in Figure 7.8).

The propagation of a blast wave can be studied plotting the so called *distance-time diagram*, a construction that allows for the following of quick processes. Figure 7.9 shows the chart corresponding to the deflagration of 80 kg of hydrogen. The sequence of dimensionless pressure histories have been plotted in the locations (vertical axes) corresponding to the position of the successive pressure sensors versus time in abscissas. The amplitude of the dimensionless pressure signals have been normalized to create a picture containing a collection of coherent signals. In order to provide the full set of information, the relative amplitude of each of the signals have been marked in the right side of the diagram. In Figure 7.9, the decay of a relative strong shock wave can be seen, with an amplitude that decreases from 20 kPa, at a point 30 m away from the building, to 3 kPa when it expands to a position 180 m away from the center of the reactor.

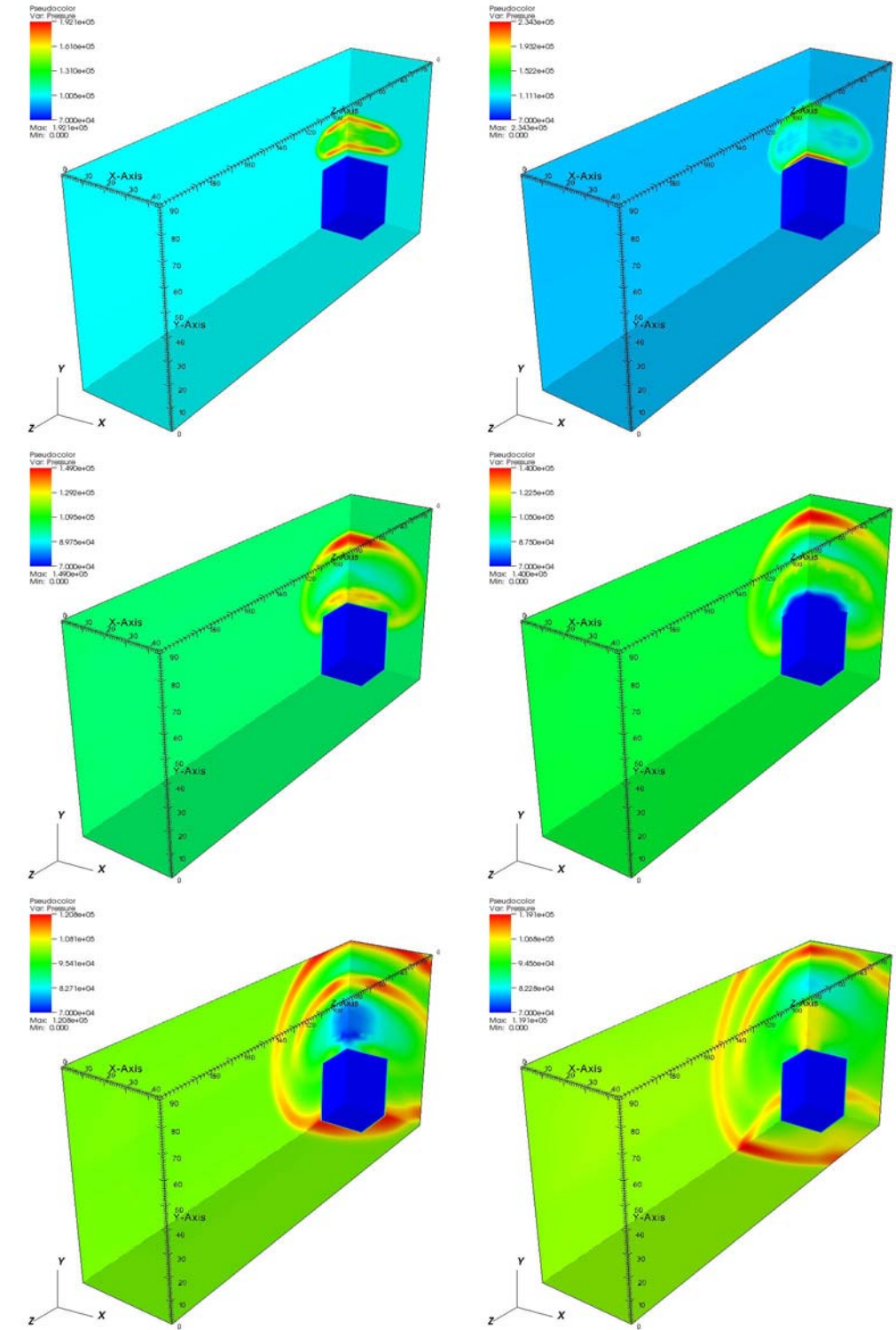


Figure 7.7: Pressure fields at different times after ignition, for the deflagration calculation considering 80 kg H_2 . First row: 0.017, 0.030 s. Second row: 0.052, 0.081 s. Third row: 0.119, 0.161 s.

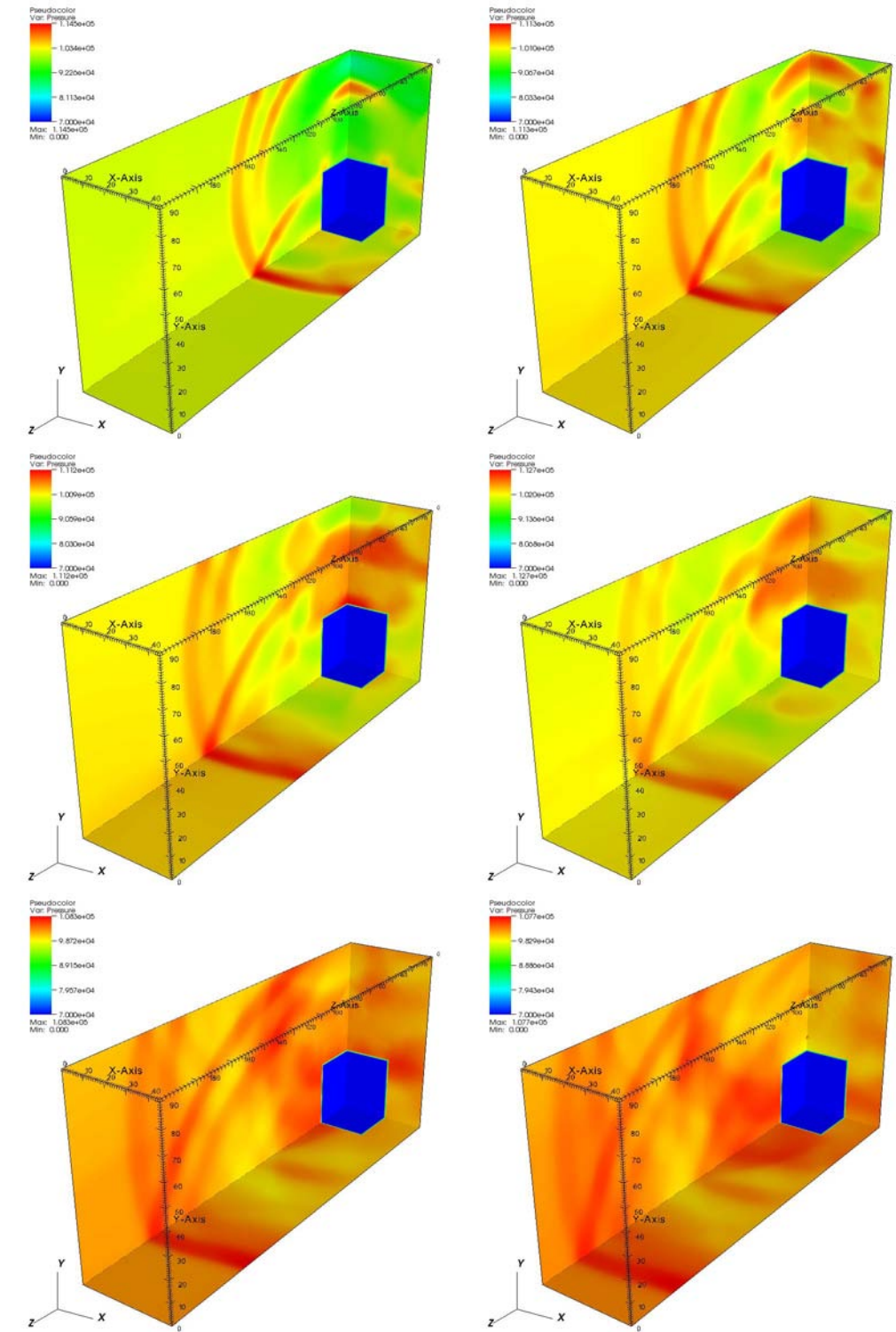


Figure 7.8: Pressure fields at different times after ignition, for the deflagration calculation considering 80 kg H_2 . First row: 0.205, 0.250 s. Second row: 0.295, 0.342 s. Third row: 0.391, 0.441 s.

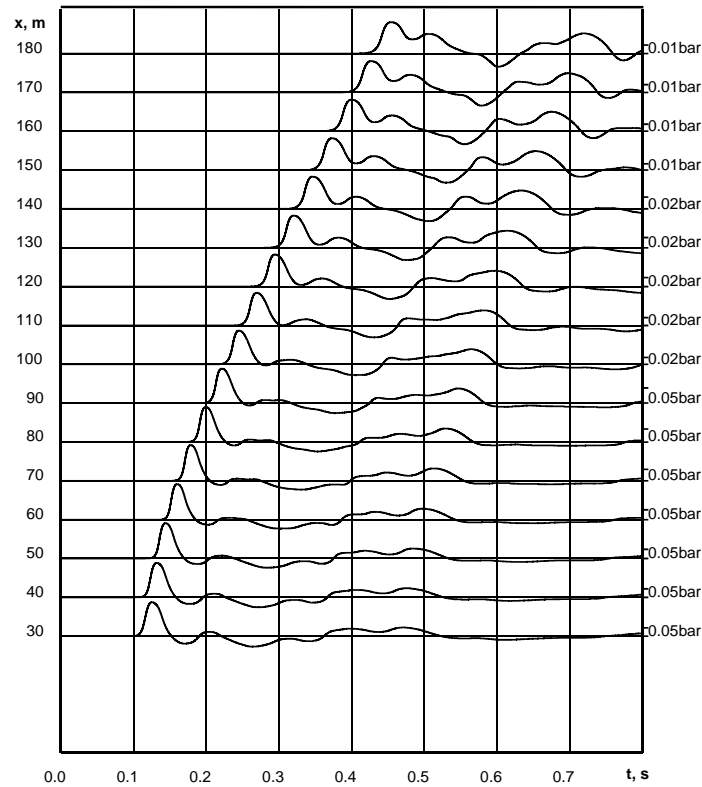


Figure 7.9: Distance-time diagram of the blast wave propagation for an 80 kg hydrogen deflagration at the top of the reactor building. The readings of each gauge have been presented at the location of the transducer. Pressure readings are dimensionless. The scale representing an equivalent (dimensional) pressure appears on the right axis for each of the gauges.

7.4.1.3.2 Estimation of the mass of fuel

The decay of the relative strong shock can be further characterized by studying the dependencies of the maximum pressure against the distance, Figure 7.10. The results of the calculation can be compared with the data obtained from the image processing, see Table 7.3 based on the results from Section 7.2.3.

The analysis of Figure 7.10, allows for the statement that the data collected in the numerical simulations of the explosion for 200 kg of hydrogen, is the closest to the results obtained by image processing. Additionally, and for the completion of the analysis, Equation (7.2), was utilized in order to predict the maximum over-pressure for different amounts of H_2 . The curves containing the dependence of the pressure on the distance have been plotted for masses of 10, 30 50, 80, 130 and 200 kg of H_2 (in gray). A best fit of the data collected in Table 7.3 utilizing equation (7.2) has been found for a mass of hydrogen of 80 kg when using this second procedure.

Analogously, Figure 7.11 summarizes the dependencies of the maximum pressure obtained in the calculations against the distance for the shock wave propagating after a detonation. The same amounts of hydrogen have been considered than in the case of the deflagration. As a result of the analysis, it can be seen that the data obtained from the image processing is, this time, located between two lines corresponding to 80 and 200 kg of hydrogen.

A comparison between Figures 7.10 and 7.11 immediately yields that the maximum pressure of the blast wave after a fast deflagration is 10-15% lower than for a detonation.

Expressing the comparisons of the two Figures 7.10 and 7.11 in terms of equivalent TNT mass, it can be seen that a detonation of 80 kg of hydrogen corresponds to an equivalent mass of 800 kg of TNT (Dorofeev, 1995; Dorofeev et al., 1996). To produce the same level of pressure loads in the case of a fast deflagration, 2-2.5 times more hydrogen than for the detonations is needed, that is, 150-200 kg of hydrogen.

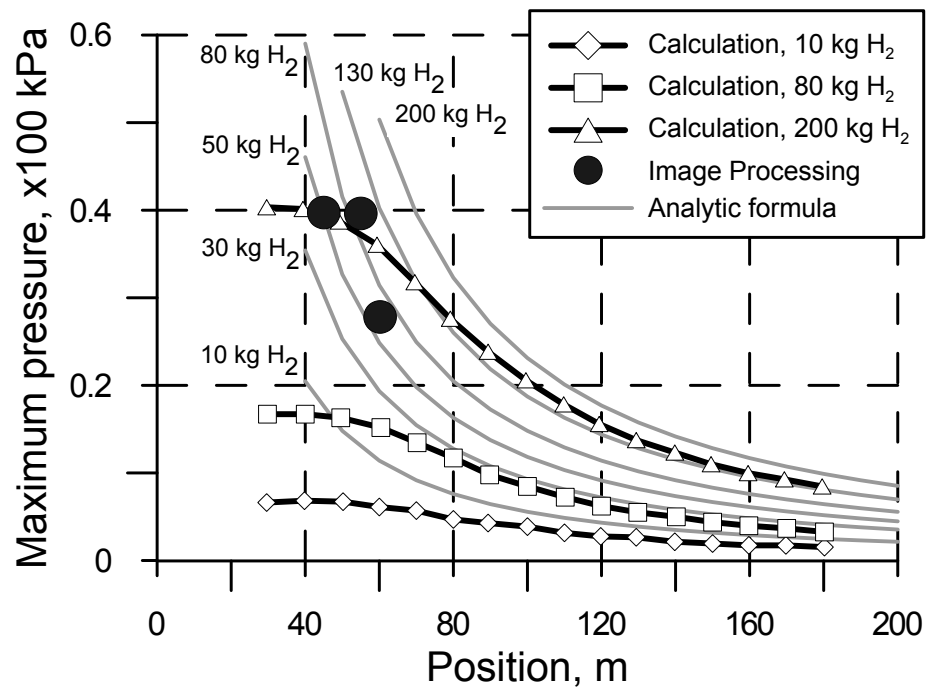


Figure 7.10: Maximum pressure vs. distance of the blast wave propagation from a fast hydrogen deflagration at the top of reactor building. Comparisons of the data obtained in the calculations versus the results from the image processing. Grey lines correspond to the application of Equation (7.2) considering the amount of hydrogen appearing in the Figure

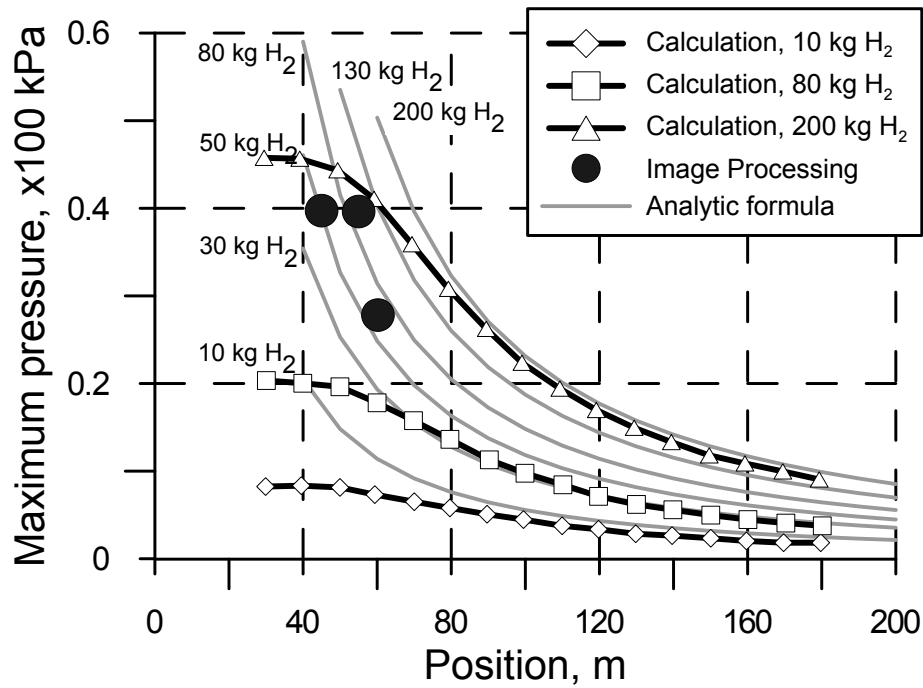


Figure 7.11: Maximum pressure vs. distance of the blast wave propagation from a fast hydrogen detonation at the top of reactor building. Comparisons of the data obtained in the calculations versus the results from the image processing. Grey lines correspond to the application of Equation (7.2) considering the amount of hydrogen appearing in the Figure

7.4.1.3.3 Estimation of the damage generated by the explosion

The over-pressure, ΔP_{max} , and the impulse, I , can be utilized to create the so called *damage diagram* (Baker et al., 1983). This chart shows the resistance to damage of significant objects, such as walls or structures or even people and human organs, to the loads generated by the pressure waves. Conceptually, the $\Delta P - I$ diagram represents a convenient methodology to mathematically relate a specific level of damage to a combination of blast pressure and impulses imposed onto a particular structural element or object.

For simplicity, if the classical shock wave profile is considered, the positive phase of the wave can be approximated as a right triangle, in which the height is the maximum over-pressure $\Delta P_{max} = P_{max} - P_0$ and the other cathetus is the duration of a positive phase $T^+ = t_i - t^+$. Therefore, the combination $\Delta P_{max} - T^+$ can be utilized as an alternative from the usual $\Delta P - I$ variables (Breitung et al., 2012) to create a simplified and more understandable *damage diagram*, see Figures 7.12 and 7.13.

Usually, the damage diagram exhibits a hyperbolic dependency on the impulse, or positive phase duration, and on the maximum over-pressure. Such a dependency has two asymptotes, ΔP^* and I^* , which characterize the two extreme cases. Those are the pure impulsive regime and the quasi-static pressure loading case.

If the maximum over-pressure ΔP and impulse I are larger than the critical ones, ΔP^* and I^* , for a given structure or organ of the human body, the object will be destroyed or the people injured.

Figures 7.12 and 7.13 show the damage diagram for brick buildings and glass windows for the cases of fast deflagration or detonation of 10, 80 and 200 kg of hydrogen respectively.

As can be observed, the windows will break at distances lesser than 150 m from the epicenter of the explosion, even for the deflagration only involving 10 kg of H_2 . For the case involving 200 kg of hydrogen, all glass windows at distances lesser than 200 m, will be broken. 50-75% of brick walls will be destroyed if the distance from the epicenter is less than 60 m.

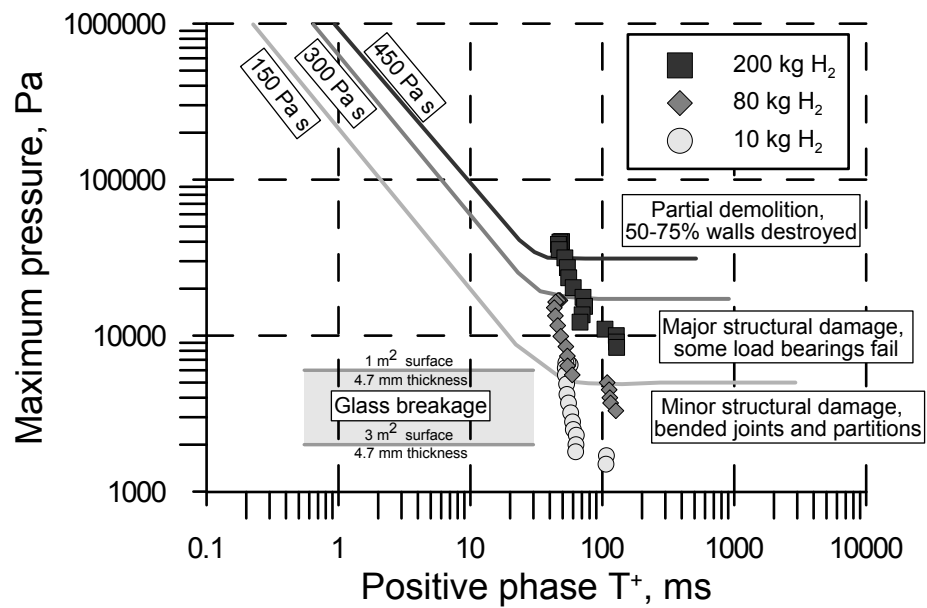


Figure 7.12: Damage diagram for a brick building and glass windows with the results of a fast deflagration simulation. Transducers are located at the roof height. For each amount of fuel, the distance to the reactor increases from upper points (the closest is located at 30 m from the center of the reactor) to lower points (the farthest is located 30 m faraway). The distance between the numerical transducers is 10 m.

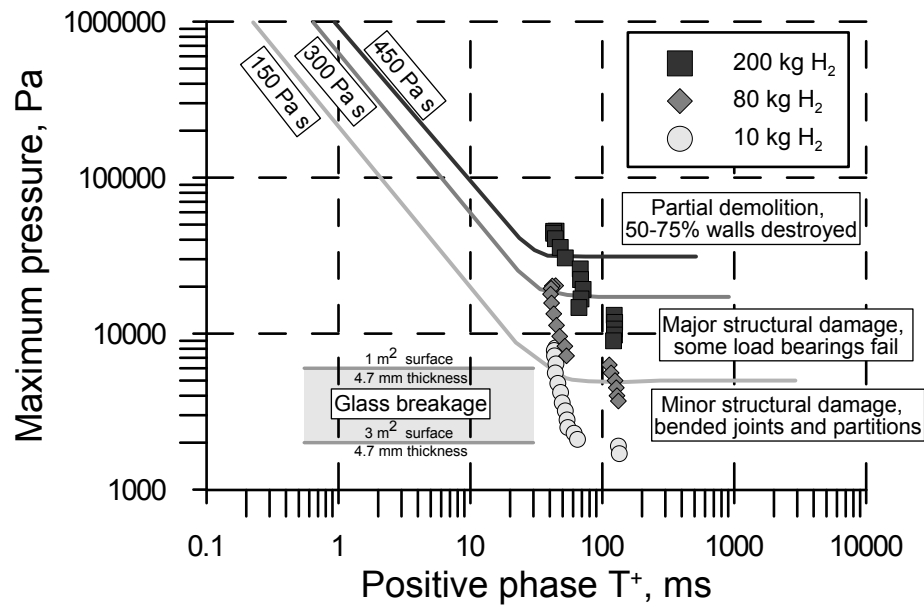


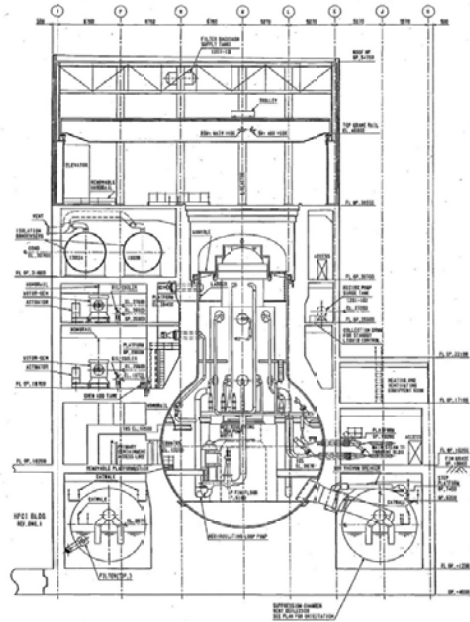
Figure 7.13: Damage diagram for a brick building and glass windows with the results of a detonation simulation. Transducers are located at roof height. For each amount of fuel, the distance to the reactor increases from upper points (the closest is located at 30 m form the center of the reactor) to lower points (the farthest is located 30 m faraway). The distance between the numerical transducers is 10 m.

7.4.2 Medium scale calculations

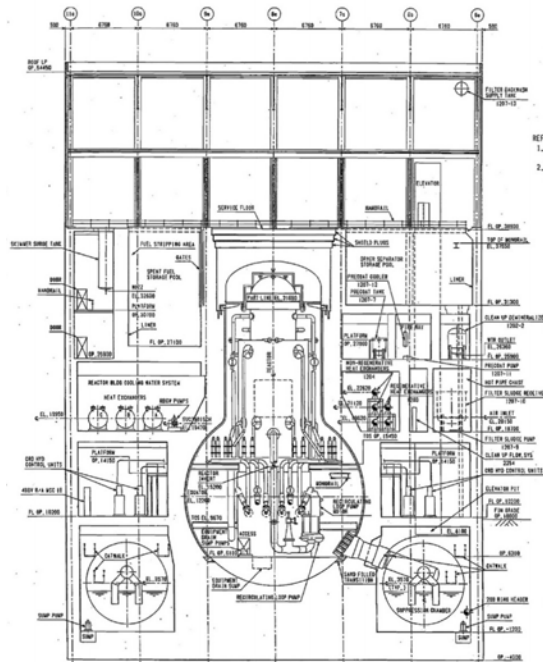
7.4.2.1 General

The evaluations carried out in section 7.4.1 may be revised considering a much refined geometry. To perform the calculations, a geometrical representation of the Fukushima I reactor has been created based on the plans (blueprints) of the Mark I reactor (TEPCO, 2013a; Kuznetsov, 2012b) (see Figures 7.14a and 7.14b).

With the purpose of achieving an improvement of the calculation efficiency, and utilizing the symmetries of the problem only one half of the whole domain of the reactor has been taken into account. In order to study the over-pressure generated by the blast of the explosion far away from the container, a very significant



(a) Front view



(b) Lateral view

Figure 7.14: BWR Mark I Containment. Detailed plan utilized for the generation²³⁵ of the mesh (TEPCO, 2013a)

free volume has been considered around the container. Additionally, and in order to take into account the surrounding atmosphere, non-reflective boundary conditions were utilized. Some significant details of the mesh are summarized in Table 7.6.

To accurately characterize the over-pressure in the far field, a significant number of numerical gauges were located every 5 meters, forming a horizontal line at two levels, namely, at the ground and at the roof level.

Table 7.6: Characteristics of the mesh used in the medium scale calculations

Domain size LxWxH, cells	Resolution, m	Number of Cells	Total volume hm^3
180x330x80	0.3	4,752,000	0.5

Based on the discussion contained in section 7.2.3, it was conceived that the burnable cloud was uniformly distributed. The results obtained in sections 7.4.1, 7.2.3 and 7.2.4 suggest that four amounts of hydrogen should be considered for the simulations, namely 50, 80, 130 and 200 kg. With regard to the results derived in section 7.4.1, only a stoichiometric concentration was accounted for. In such conditions, the inventory accumulated at the top of secondary containment formed a layer with a respective thickness of 1.7, 2.7, 4.5 and 6.9 m.

The simulations were carried out considering that hydrogen was consumed with an imposed turbulent burning velocity representative of the detonation case and of the sonic-deflagration, as discussed in section 7.4.1.1.

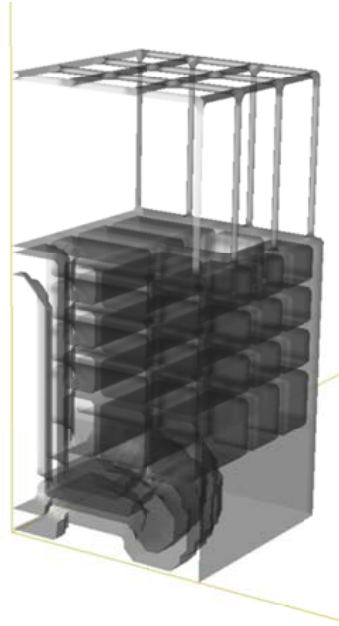


Figure 7.15: Cut of the geometry, representing the BWR Mark I Containment, employed in the medium size computational domain calculations .

7.4.2.2 Results and discussion

7.4.2.2.1 General

Figures 7.16 and 7.17 show a sequence of snapshots corresponding to the case of deflagration of 80 kg of hydrogen in air. The results show good qualitative agreement with the real process shown in Figure 7.1. The pictures, in agreement with Figures 7.7 and 7.8, show a significant non isotropy in the propagation of the shock wave in the early stage of the event (first and second lines in Figure 7.16). In this sense, it should be underline that the analyses performed in Section 7.4.1 and in this section, are based on the horizontal propagation. After this initial stage, the shock propagates more spherically (third and fourth rows of Figure 7.16 and Fig-

ure 7.17). In the whole set of pictures contained in Figure 7.17, the formation of the Mach stem can be observed. The results obtained for the rest of the Hydrogen amounts and regimes of combustion are qualitatively similar to the one chosen and are thus not reproduced.

7.4.2.2.2 Estimation of the amount of fuel

The maximum pressure registered at different distances from the center of the hydrogen layer has been plotted for different amounts of hydrogen for the case of a 400 m/s deflagration in Figure 7.18 and for the detonation in Figure 7.19 .

The numerical results were compared with the over-pressures obtained from the image processing, shown in Table 7.3. In Figure 7.18 the points obtained from the image processing lie close to the numerical results derived for the calculation involving 130 kg H_2 . In contrast, the analysis carried out with eq. (7.2) delivered a best fit of the data for a mass of hydrogen of 80 kg (gray line). The differences on the estimation of the mass by the two procedures are due to two main reasons. Firstly, that the spherical propagation of the wave was supposed in equation (7.2). Secondly, that a flat fuel distribution was taken into account in the calculations.

Analogous dependencies of the calculated maximum pressures on distance have been obtained for the case involving a detonation, Figure 7.19. The best fit of the data determined processing the photographs of the accident was also obtained for 130 kg.

The hydrogen mass of 130 kg assessed in this section is significantly smaller than the amount of around 200 kg H_2 which resulted from the analysis carried out with the coarser geometry (see Figures 7.10 and 7.11). Nevertheless, it represents a more accurate limit than the previous set of calculations and is in agreement with the total mass of hydrogen involved in the explosion. This total mass was assessed in section 7.2.4 and resulted to be from 180 to 200 kg of hydrogen. This would mean that from 65% to 75% of the total hydrogen inventory burned in a fast regime. The rest was consumed by a sub-sonically propagating flame. Of interest is also the comparison with the amounts of hydrogen generated in the accident. Taking into

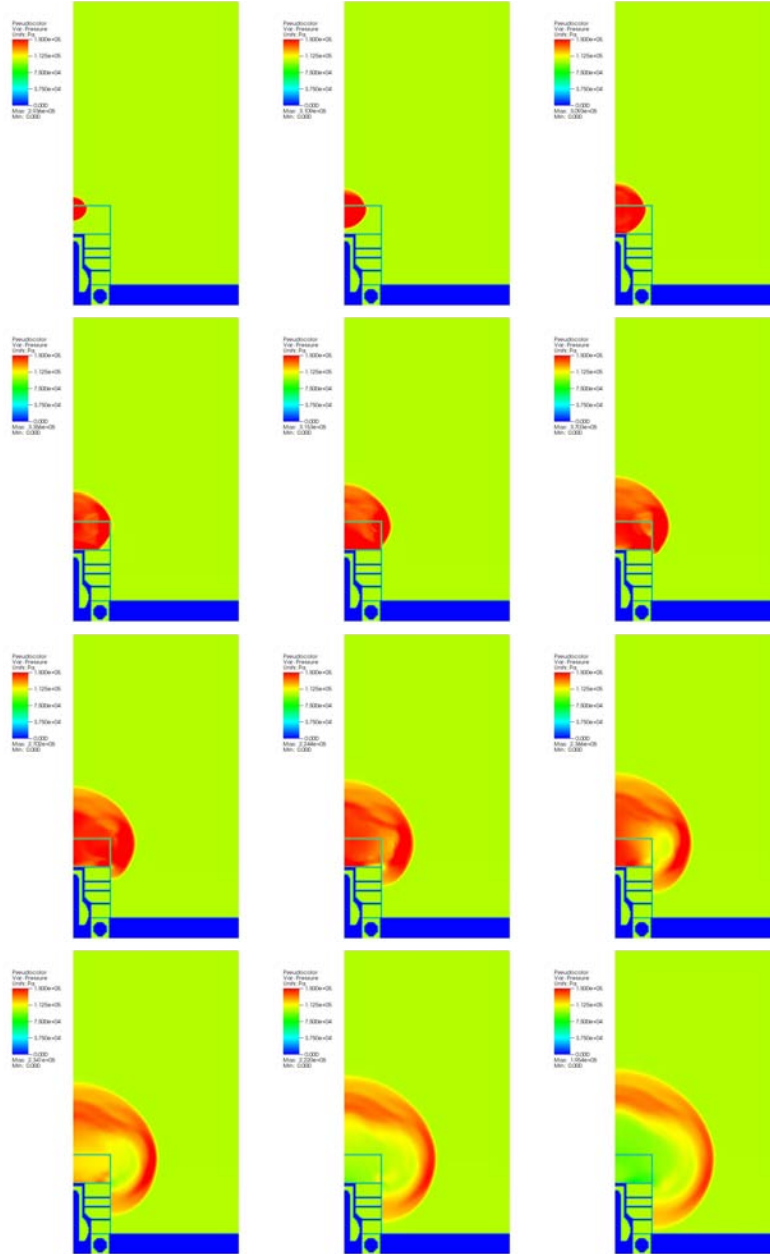


Figure 7.16: Pressure fields at different times after ignition for the deflagration calculation considering 130 kg H_2 . Interval between the snapshots is 0.01s.

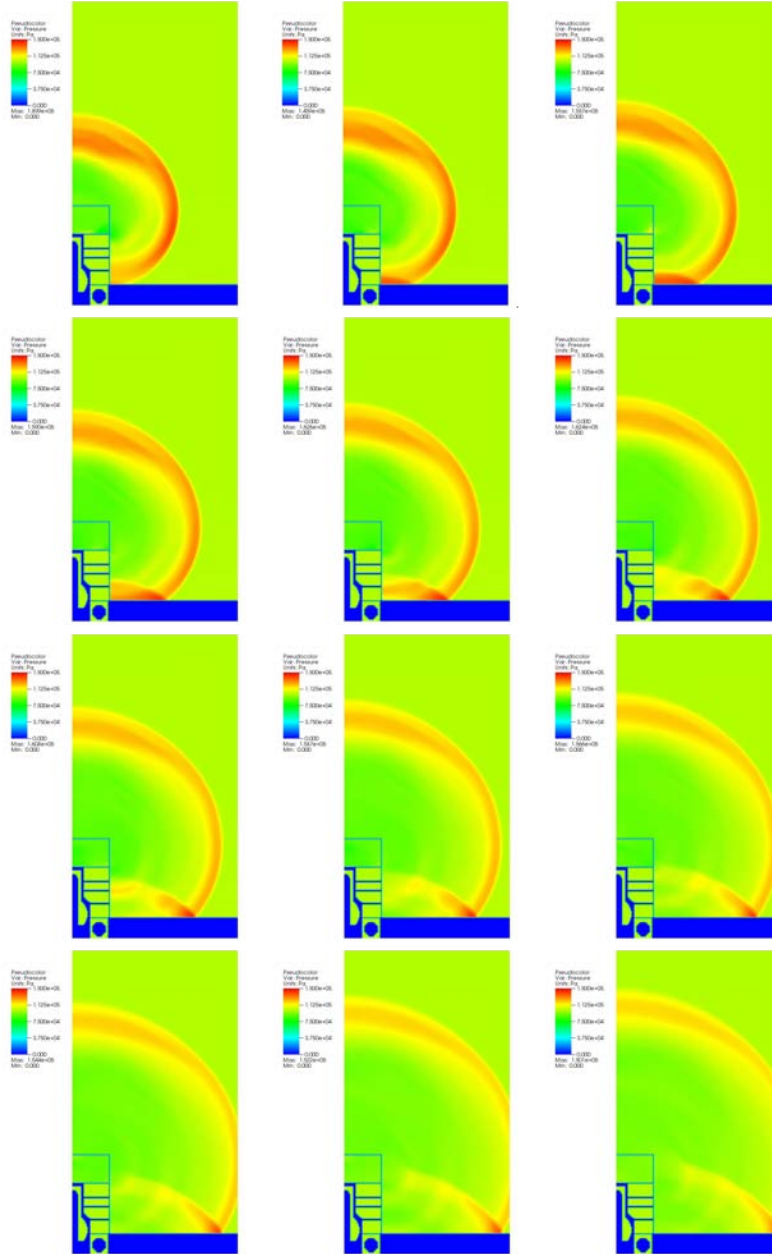


Figure 7.17: Pressure fields at different times after ignition for the deflagration calculation considering 130 kg H_2 . Interval between the snapshots is 0.01s.

account the data presented in of Table 7.1, the 130 kg estimated represents 14 % of the total amount generated, that is 890 kg. A very similar figure is obtained if the amounts summarized in Table 7.2 are utilized. If we also consider the amount estimated to have participated in the combustion at around 180 kg (based on radius), it can be concluded that 20 % of the total amount generated burned and that 14 % did it in fast regime.

It can also be stated that the restriction of the study to just two propagation regimes, the detonation and the 400 m s^{-1} sonic deflagration cases, has been correct and sufficient. The accuracy that could have been gained by further simulations of faster deflagrations is not representative. Clearly, the results obtained, calculating exclusively the detonation and the 400 m s^{-1} sonic deflagration, have approximately delivered the same amount of hydrogen, and the results that would have been obtained for faster deflagrations would have fallen in between these values.

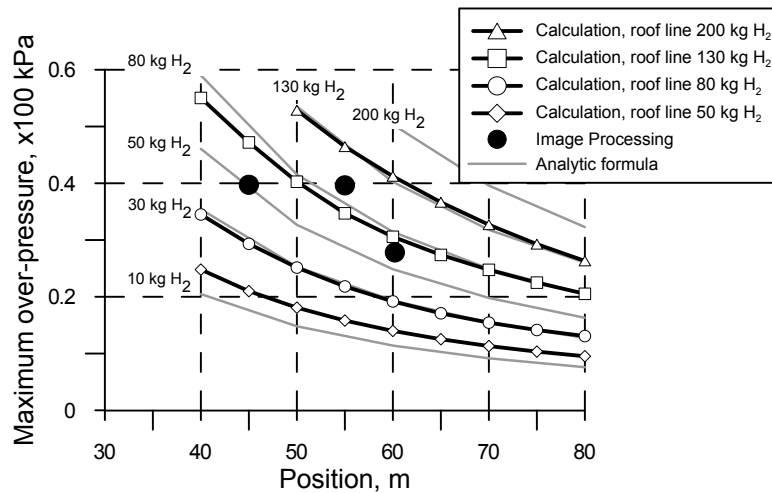


Figure 7.18: Maximum pressure vs. distance of the blast wave propagation from a fast hydrogen deflagration at the top of reactor building. Comparisons of the data obtained in the calculations against the results of the image processing. Grey lines, are the application of Equation (7.2) considering the amounts of hydrogen indicated close to each line

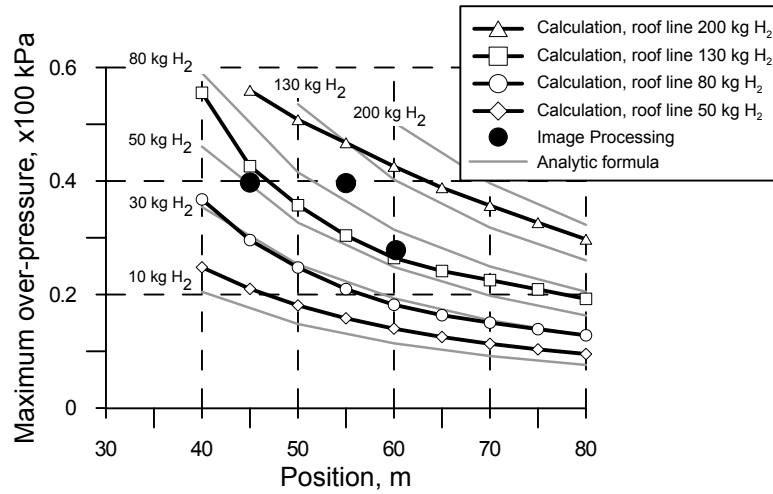


Figure 7.19: Maximum pressure vs. distance of the blast wave propagation from a fast hydrogen detonation at the top of reactor building. Comparisons of the data obtained in the calculations against the results of the image processing. Grey lines, are the application of Equation (7.2) considering the amounts of hydrogen indicated close to each line

7.4.2.2.3 Assessment of the damage generated by the explosion

The *damage diagram* (Baker et al., 1983) in terms of the maximum over-pressure ΔP_{max} and the duration of the positive phase T^+ (Breitung et al., 2012) can be used to evaluate the effect of the explosion on the structure of the plant. Figures 7.20 and 7.21 represent the *damage diagram* for brick buildings and glass windows for the cases of 400 m/s deflagration and detonation respectively. In these figures, the points obtained for different gauges accounting for the calculations involving 50, 80, 130 and 200 kg of H₂ are represented.

Significant differences exist between the Figures 7.20 and 7.21 and the analogous plots obtained from the analysis of the coarser calculation. Due to the improved resolution, the structure of the shock wave has been now resolved more accurately.

Also, the distance to the power plant at which the numerical transducers were

located was reduced compared to the coarsen analysis. These effects, and additionally the improved geometry itself, have induced a significant improvement in the obtained results.

The Figures 7.20 and 7.21 represent devastating explosions. For the case of the detonation, all the amounts of hydrogen utilized, even the case of 50 kg, have resulted in an explosion of an annihilating power. For the case of the deflagration, only the explosion involving 50 kg of hydrogen remains under demolition limit.

Nonetheless, the destructive power of the explosions, both in deflagration and detonation regime, can be even greater for structures and equipment surrounding the power plant and located on the ground. This is due to the existence of the *Mach stem* from the interaction of the shock wave and the ground (see Figures 7.16 and 7.17).

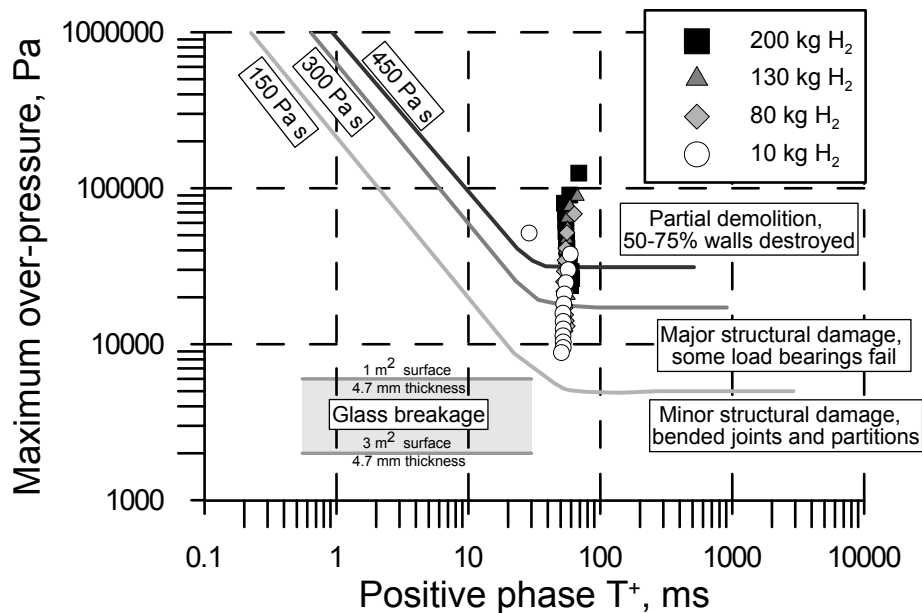


Figure 7.20: Damage diagram for brick building and glass windows with the results of the fast deflagration simulation ($U_f = 400$ m/s). Transducers are located at the roof height. For each amount of fuel, the distance to the reactor increases from upper points (the closest is located at 25 m form the center of the reactor) to lower points (the farthest is located 85 m faraway). The distance between the numerical transducers is 5 m.

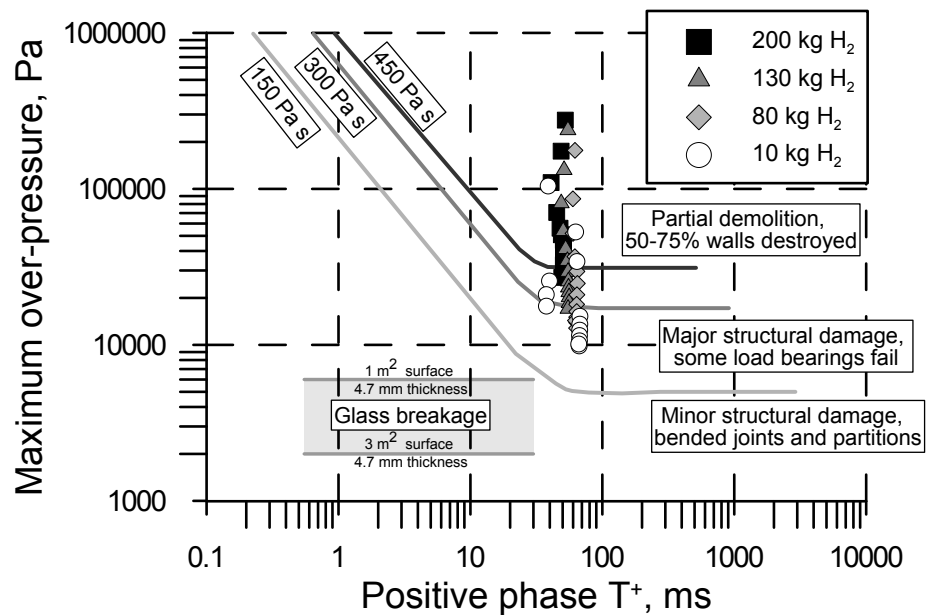


Figure 7.21: Damage diagram for brick building and glass windows with the results of detonations. Transducers are located at the roof height. For each amount of fuel the distance to the reactor increases from upper points (the closest is located at 25 m from the center of the reactor) to lower points (the farthest is located 85 m faraway). The distance between the numerical transducers is 5 m.

Chapter 8

CONCLUSIONS

8.1 Conclusions

1. Amongst the multiple options available for the simulation of combustion in large scale problems, in which severe restrictions for the resolution exist, it has been confirmed through an extensive literature review that the *flame speed modeling* methodologies represent the most adequate choice for practical problems.

The KYLCOM model, proposed in this study (see Chapter 4), allows taking full advantage of the simplification obtained with the reduction of the combustion problem to the determination of the turbulent burning rate. At the same time it allows keeping the flame brush relatively thin overcoming the most serious deficiency of the already available models.

2. A turbulent burning velocity model has been developed approximating its value with the laminar burning velocity times a factor, for which a set of formulae selected from those available in the literature have been analyzed. The performance of the model in conjunction with the different correlations for the turbulent burning velocity has been analyzed based on combustion experiments in an obstructed tube.

A quantitative ranking of the predictive capabilities of the different formulae for the turbulent burning velocity has been carried out indicating that the formula due to Schmid et al. (1998) is the most adequate for large scale problems.

3. For the evaluation of the laminar burning velocity a new formulation valid for hydrogen-air-steam mixtures has been created with two main purposes: to simplify the model and to speed-up the calculations. The proposed approximation is a generalized multi-parametric expression taking into account dependencies on equivalence ratio, temperature, pressure, and steam concentration. The correlation is based on a laminar flame speed database calculated using the INSFLA code with the detailed chemical kinetic reaction mechanism of Warnatz and Maas.
4. For completeness of the model, additionally to the considerations regarding the turbulence, an accounting of flame instabilities is necessary. This leads to additional flame wrinkling and acceleration even in presence of laminar flow. Among them, the modeling of the interaction of the flame with acoustic waves has been undertaken, as this phenomenon highly determines the combustion pattern in lean hydrogen-air-steam mixtures.
5. Multiple examples have confirmed the validity and performance of the KYL-COM model in combustion regimes ranging from near laminar to highly turbulent. The correctness of the approach has been illustrated performing a study of the accuracy of the description of hydrogen deflagrations in tubes, tunnels, realistic non-uniform hydrogen-air mixtures and mitigation effect of openings. The subsequent application of the methodology to the Fukushima Power plant accident allowed assessing the amount of hydrogen involved in the explosion event.

8.2 Contributions

1. The KYLCOM model for turbulent combustion has been developed by the author and was presented in (Yanez et al., 2010a).

It was shown that if this methodology is adopted, an accurate calculation of the laminar and turbulent burning velocities is of the highest importance for the accuracy of the results.

2. The correlation for the laminar burning velocity taking into account dependencies on equivalence ratio, temperature, pressure, and steam concentration was presented in the co-authored papers (Szabó et al., 2012b), (Szabó et al., 2012a). The approximation is found to be valid for all the equivalence ratios inside the flammability limits, for temperatures between 200 K and 600 K, pressures between 0.1 bar and 10 bar, and steam concentrations between 0 and 20 vol. %. For undiluted mixtures the formulation can be used in an extended pressure interval up to 31.6 bar. These intervals represent a wider domain than any of the previously available expressions. Some additional investigations have been carried out in order to create the previous correlation. These concerned the understanding of the laminar flame velocity dependencies on different parameters with the creation of an enhanced formulation for the laminar flame velocity based on Franz-Kamenetskii methodology, and the extraction of the one-step brutto reaction flame characteristics (Yanez et al., 2011c).

3. The performance of the KYLCOM model in conjunction with the different correlations for the turbulent burning velocity has been presented in (Yanez et al., 2010a). The selection of the appropriate expression for the calculation of the turbulent flame speed was shown to be critical and it was demonstrated that Schmidt correlation produces the best approximation.

4. Based on these results, the model has been applied to lean combustion in big containers, in conditions representative of nuclear accidents, as reported in 5.3.1 and (Yanez et al., 2010b), (Yanez et al., 2012c), (Yanez et al., 2012a).

It was ascertained that the model was able to reproduce the experiments. It was found out that the flame instabilities play a very significant role for some of the experiments.

5. Several contributions are to be reported related to the flame instabilities
 - (a) An existing model accounting of flame instabilities, that has been presented and utilized, but never mathematically derived, has been so derived (Appendix D).
 - (b) The growth rate of the acoustic instability for hydrogen-air mixtures has been theoretically analyzed by the author in Appendix C and further in the references (Yanez et al., 2011d), (Yanez et al., 2013c), (Yanez et al., 2013b) for hydrogen-air mixtures.
 - (c) utilizing the previous two contributions the acoustic-parametric instability has been modeled for the first time.
 - (d) The modeling for the instabilities has been applied to combustion in big volumes under conditions typical to severe nuclear accidents, (Yanez et al., 2010b), (Yanez et al., 2012a) in conditions that made the simulation of flame instabilities a very significant problem. The enhancement of the mass consumption rate created by the acoustic instability was successfully modeled reproducing the conditions of the experiment.
6. The validity of the KYLCOM model has been tested for different problems of interest for different branches of the industry.
 - (a) For tubes an initial evaluation was performed in (Yanez et al., 2010a). The capabilities of the model to reproduce explosions in tunnels has been reported in chapter 6.2 and in the co-authored reference (Baraldi et al., 2009). It was found out that the presence of vehicles inside a tunnel does not have a significant importance for the development of the explosion.

-
- (b) The effectiveness and accuracy of the model to reproduce explosion in an environment with severe fuel concentration gradients and very lean fuel concentrations has been ascertained in section 6.3 and presented in the co-authored reference (Makarov et al., 2010). As an interesting outcome, it was confirmed that the prediction of explosions in very lean mixtures poses a more severe problem than the variable composition.
 - (c) The capacity to replicate explosions with venting was checked in section 6.4 and co-authored reference (Baraldi et al., 2010)
 - (d) The Fukushima Power plant accident has been thoroughly analyzed. The amount of Hydrogen involved in the explosion event has been assessed successively refining the accuracy of the estimates. The final figures show that the amount of Hydrogen involved in the explosion was most probably 130 kg approximately (Yanez et al. submitted for publication).

8.3 Future work

1. The KYLCOM model has been elaborated taking into account hexahedral structured meshes exclusively. An extension to polar and multiple shaped non-structured grids will allow extending the model to non-structured meshes.
2. Although the different combustion regimes are well understood, the transition between them is described in comparatively much worse manner. Further investigation is necessary to describe thoroughly the meta-stable equilibrium status of flame propagation.

Some progress has been already achieved by the author utilizing the KYLCOM model, which has helped to postulate the existence of a new flame acceleration mechanism created by hydraulic resistance for tubes open in their rear (Yanez et al., 2010a, 2013a, 2014b). Still, further efforts are necessary.

3. The modeling of the instabilities in CFD calculations started just a few years back. Improvement of the equation (5.26), required for the determination

of the increase of the burning rate due to instabilities, is essential due to its shortcomings.

Further investigation in the theoretical research of the flame instabilities is necessary. The results reported in (Yanez et al., 2013c), already show that an improved theoretical description of the acoustic-parametric instability is indispensable.

The modeling of the Landau-Darrieus instability would be necessary specially in those problems in which the flame develops in unblocked domains of several meters (partially addressed in section 5.2.2 with the *Quasi-Laminar* burning velocity). A more *physical* model, similar to the one utilized for the Acoustic-Parametric instabilities, would be clearly beneficial for the accuracy of the calculations.

The Flame-Shock interaction, is certainly a very interesting phenomena that, known to the author, has never been modeled in problems with a restricted resolution and a complex geometry. Its effect, as pointed out already in the classic book of Markstein (1964), should be very considerable.

4. For nuclear power plant safety, the investigation of flame propagation regimes in flat combustible layers is required. Those investigations should provide run-up distances for effective flame acceleration (from subsonic to sonic regime or detonation) and a criterion describing the expected regime taking into account fuel concentration, distribution of obstacles, etc. Some progress has been already accomplished by the author in (Yanez et al., 2011a; Kuznetsov et al., 2012; Yanez et al., 2014a) but still much more improvement is essential.

Chapter 9

LIST OF PUBLICATIONS DURING PhD THESIS WORK

9.1 Journal papers:

1. YANEZ, J., KUZNETSOV, M., SOUTO-IGLESIAS, A., *An analysis of the hydrogen explosion in the Fukushima-Daiichi accident* International Journal Hydrogen Energy 40, 8261-8280, 2015.

Impact factor: 3.548, Five years impact factor: 4.086

Quartile in, Chemistry, Physical: Q2; Electrochemistry: Q2; Energy and Fuels: Q1.

2. KUZNETSOV, M., YANEZ, J., GRUNE, J, FRIEDRICHS, A., JORDAN, T. *Hydrogen combustion in a flat semi-confined layer with respect to the Fukushima Daiichi accident* Nuclear Engineering and Design 286 (2015) 36–48

Impact factor: 0.805, Five years impact factor: 0.950

Quartile in, Nuclear science and technology: Q3.

-
3. YANEZ, J., KUZNETSOV, M., REDLINGER, R. ***The acoustic-parametric instability for hydrogen-air mixtures.*** Combustion and Flame 160 (10), 2009-2016, 2013

Impact factor: 3.599, Five years impact factor: 3.643

Quartile in, Energy and fuel technology: Q1.
 4. YANEZ, J., KOTCHOURKO, A., LELYAKIN, A. ***Hydrogen deflagration simulations under typical containment conditions for nuclear safety.*** Nuclear Energy and design, 250, 678-686, 2012

Impact factor: 0.805, Five years impact factor: 0.950

Quartile in, Nuclear science and technology: Q3.
 5. SZABO, T., YANEZ, J., KOTCHOURKO, M., KUZNETSOV, M., JORDAN, T. ***Parameterization of laminar flame speed dependence on pressure and temperature in hydrogen-air-steam mixtures.*** Combustion science and technology 184 (10-11), 1427-1444, 2012

Impact factor: 1.011, Five years impact factor: 1.209

Quartile in, Engineering, multidisciplinary: Q2.
 6. YANEZ, J., KUZNETSOV, M., KOTCHOURKO, A., LELYAKIN, A., JORDAN, T. ***Theoretical considerations of laminar flame speed as a function of initial conditions and basic kinetics properties with respect to the safety problem.*** Journal of energy and power engineering 6, 849-857, 2012
 7. MAKAROV, D., VERBECKE, F., MOLKOV, V., ..., YANEZ, J. ***An inter comparison of CFD models to predict lean and non-uniform hydrogen mixture explosions.*** International Journal of hydrogen energy 35, 5754-5762, 2010

Impact factor: 3.548, Five years impact factor: 4.086

Quartile in, Chemistry, Physical: Q2; Electrochemistry: Q2; Energy and Fuels: Q1.
-

-
8. BARALDI, D., KOTCHOURKO, A., LELYAKIN, A., ..., YANEZ, J. *An inter comparison exercise on CFD model capabilities to simulate hydrogen deflagrations with pressure relief vents*. International journal of hydrogen energy, 35, 12381-12390, 2010

Impact factor: 3.548, Five years impact factor: 4.086

Quartile in, Chemistry, Physical: Q2; Electrochemistry: Q2; Energy and Fuels: Q1

9. BARALDI, D., KOTCHOURKO, A., LELYAKIN, A., ..., YANEZ, J. *An inter comparison exercise on CFD model capabilities to simulate hydrogen deflagration in a tunnel*. International Journal of hydrogen energy XXX, 1-11, 2009

Impact factor: 3.548, Five years impact factor: 4.086

Quartile in, Chemistry, Physical: Q2; Electrochemistry: Q2; Energy and Fuels: Q1.

9.2 Conference Papers

1. YANEZ, J., KUZNETSOV, M., REDLINGER, R., *The Acoustic – Parametric Instability for Gaseous Mixtures with Lewis Number Smaller than One*. International Colloquium on the Dynamics of Explosions and Reactive Systems (ICDERS) 2013. Taipei, Taiwan, 2013
2. KUZNETSOV, M., YANEZ, J., GRUNE, J., FRIEDRICH, A., JORDAN, T. *Hydrogen combustion in a Flat Semi-Confined Layer with respect to the Fukushima Daiichi Accident*. 4th Proceedings of ICAPP'12 Chicago, USA, June 24-28, 2012
3. YANEZ, J., KUZNETSOV, M., REDLINGER, R., KOTCHOURKO, A., LELYAKIN, A. *Analysis of the parametric-acoustic instability for safety assessment of hydrogen-air mixtures in closed volumes*. 4th International Conference Hydrogen Safety ICHS, San Francisco, September 2011

-
4. SZABO, T., YANEZ, J., KOTCHOURKO, M., KUZNETSOV, M., JORDAN, T. ***Parameterization of laminar flame speed dependence on pressure and temperature in hydrogen-air-steam mixtures.*** International Colloquium on the Dynamics of Explosions and Reactive Systems (ICDERS) 2011. Irvine, California, 2011
 5. YANEZ, J., KUZNETSOV, M., KOTCHOURKO, A., LELYAKIN, A., JORDAN, T. ***Theoretical considerations of laminar flame speed as a function of initial conditions and basic kinetics properties with respect to the safety problem.*** 1st International Conference for Sustainable Energy Storage (IC-SES). Belfast, February 2011
 6. YANEZ, J., KOTCHOURKO, A., LELYAKIN, A. ***Hydrogen deflagration simulations under typical containment conditions for nuclear safety.*** Computational Fluid Dynamics in Nuclear Reactor Safety (CDF4NRS), September 2010, Washington
 7. YANEZ, J., LELYAKIN, A., JORDAN, T., et al. ***Experimental and numerical Investigation of the effect of end venting on flame acceleration in an obstructed channel.*** 8th International Symposium on Hazards, Prevention, and Mitigation of Industrial Explosion (ISHPMIE), Tokio, 2010
 8. YANEZ, J., KOTCHOURKO, A., LELYAKIN, A. ***Kylcom model for the calculation of under resolved hydrogen combustion problems.*** 6th international seminar of fire and explosion hazards (ISFEH) p. 137, 11-16 April 2010, Leeds.
 9. MAKAROV, D., VERBECKE, F., MOLKOV, V., ..., YANEZ, J. ***Modeling of lean uniform and non-uniform hydrogen-air mixture explosions in a closed vessel.*** 3rd International Conference Hydrogen Safety (ICHHS) 2009

Chapter 10

Bibliography

Abou-Rjeily, Y., Cénérino, G., Drozd, A., Lee, S., Misak, J., Park, C., Preusser, G., and Vayssier, G. (2011). Mitigation of hydrogen hazards in severe accidents in nuclear power plants. Technical Report IAEA-TECDOC-1661, International Atomic Energy Agency.

Alonso-Sanz, R. (2009). *Cellular automata with memory*. Old City Pub Inc.

Argonne National Laboratory (2013). Assessing current, near-term, and long-term U.S. hydrogen markets. <http://www.dis.anl.gov/news/HydrogenMarkets.html>.

Arntzen, B. (1998). *Modeling of turbulence and combustion for simulation of gas explosions in complex geometries*. PhD thesis, The Norwegian university for science and technology. Division of applied mechanics, thermodynamics and fluid mechanics.

Arpaci, V. (1995). Micro-scales of turbulent combustion. *Energy Combustion Sci.*, 21:153–171.

Avital, E. and Luo, K. (1999). *Compressible sub-grid models for large eddy simulations of cold and hot mixing layers*, volume 7 of *Ercoftac Series: Direct and large*

-
- eddy simulations III*, Voke, Sandman & Kleiser editors, pages 175–188. Kluwer Academic Publishers.
- Bak, P., Chen, K., and Tang, C. (1990). A forest-fire model and some thoughts on turbulence. *Physical Letters A*, 147:297–300.
- Baker, W. E. (1973). *Explossions in air*. University of Texas Press, Austin, Texas.
- Baker, W. E., Cox, P. A., Westline, P., Kulesz, J., and Strehlow, R. (1983). *Explossions hazards and evaluation*. Elsevier, Amsterdam.
- Bakke, J. and Hjertager, B. (1986). Quasi-laminar/turbulent combustion modeling, real cloud generation and boundary conditions in FLACS-ICE code. Technical Report CMI No 865402-2, Chr Michelsen Institute.
- Band, S., Borghoff, S., Büttner, U., Kaulard, J., Kilian-Hülsmeier, Y., Maqua, M., Mildenerger, O., Schimpfke, T., Sonnenkalb, M., Stahl, T., Weiß, S., and Wetzel, N. (2013). Fukushima Daiichi 11. März 2011, 2. auflage. Technical Report GRS-S-53, GRS.
- Baraldi, D., Heitsch, M., and Wilkening, H. (2007). CFD simulations of hydrogen combustion in a simplified EPR containment with CFX and REACFLOW. *Nuclear Engineering and Design*, 237:1668–1678.
- Baraldi, D., Kotchourko, A., Lelyakin, A., Yanez, J., Gavrikov, A., Efimenko, A., Verbecke, E., Makarov, D., Molkov, V., and Teodorczyk, A. (2010). An inter-comparison exercise on CFD model capabilities to simulate hydrogen deflagrations with pressure relief vents. *International Journal of Hydrogen Energy*, 35:12381–12390.
- Baraldi, D., Kotchourko, A., Lelyakin, A., Yanez, J., Middha, P., Hansen, O., Gavrikov, A., Efimenko, A., Verbecke, E., Makarov, D., and Molkov, V. (2009). An inter-comparison exercise on CFD model capabilities to simulate hydrogen deflagrations in a tunnel. *International Journal of Hydrogen Energy*, 34(18):7862–7872.

-
- Bardina, J., Ferziger, H., J., and Reynolds, W. C. (1983). Improved turbulence models based on large eddy simulation of homogeneous, incompressible, turbulent flows. Technical Report TF-19, Stanford University.
- Bargaftik, N. B. (1972). *Physical and Thermodynamic Properties of Gas and Liquid*. Nauka, Moscow.
- Barley, C. and Gawlik, K. (2009). Buoyancy-driven ventilation of hydrogen from buildings: Laboratory test and model validation. *International Journal of Hydrogen Energy*, 34(13):5592–5603.
- Baurle, R. and Girimaji, S. (2003). Assumed PDF turbulence-chemistry closure with temperature-composition correlations. *Combustion and Flame*, 134:131–148.
- Bauwens, C., Chaffee, J., and Dorofeev, S. (2009). Vented explosion overpressure from combustion of hydrogen and hydrocarbon mixtures. In *3rd International Conference on Hydrogen Safety*, Ajaccio, France.
- Bauwens, C. R., Chaffee, J., and Dorofeev, S. (2011). Vented explosion overpressures from combustion of hydrogen and hydrocarbon mixtures. *International Journal of Hydrogen Energy*, 36(3):2329–2336.
- Bechtold, J. and Matalon, M. (1987). Hydrodynamic and diffusion effects on the stability of spherically expanding flames. *Combustion and Flame*, 67:177–190.
- Behrendt, F. and Warnatz, J. (1985). The dependence of flame propagation in $H_2 - O_2 - N_2$ mixtures on temperature, pressure, and initial composition. *International Journal of Hydrogen Energy*, 10:749–755.
- Bell, J. B., Day, M., Grcar J.F., L., M.J., D., and S.A., J. F. (2006). Numerical simulation of a laboratory-scale turbulent slot flame. *Proceedings of the Combustion Institute*, 31:1299–1307.
- Bentaib, A., Bleyer, A., Wilkening, H., Baraldi, D., Takasuo, E., and Huhtanen, R. (2007). Hydrogen combustion with concentration gradients in experiments and simulations : preliminary results of ENACCEF Benchmark, European Review

-
- Meeting on Severe Accident Research. In *ERMSAR-2007*, Karlsruhe, Germany. Session n° 3 , Paper n° 3.
- Berselli, L., Iliescu, T., and W.J., L. (2005). *Mathematics of Large Eddy Simulation of Turbulent Flows*. Springer, Berlin.
- Bielert, U., Breitung, W., Burgeth, B., Kotchourko, A., W., S., Pailhores, P., Petit, M., Dorofeev, S., Kuznetsov, M., and Efimenko, A. Okun, M. e. a. (2002a). Integral large scale experiments on hydrogen combustion for severe accident code validation. In *FISA-2001: EU Research in Reactor Safety*. Editors: G. van Goethem, A. Zurita, J. M. Bermejo, P. Manolatos, H. Bischoff, pages 395–407, Brussels. EURATOM, Office for Official Publications of EC.
- Bielert, U., Breitung, W., Burgeth, B., Kotchourko, A., W., S., Pailhores, P., Petit, M., Dorofeev, S., Kuznetsov, M., and Efimenko, A. Okun, M. e. a. (2002b). Large scale experiments for validation of hydrogen combustion models and criteria. In *Jahrestagung Kerntechnik*, Stuttgart, May 14 - 16.
- Bielert, U., Breitung, W., Burgeth, B., Kotchourko, A., W., S., Pailhores, P., Petit, M., Dorofeev, S., Kuznetsov, M., and Efimenko, A. Okun, M. e. a. (2003a). Application and assessment of hydrogen combustion models. In *The 10th International Topical Meeting on Nuclear Reactor Thermal Hydraulics (NURETH-10)*, Seoul, Korea, October 5-9.
- Bielert, U., Breitung, W., Burgeth, B., Kotchourko, A., W., S., Pailhores, P., Petit, M., Dorofeev, S., Kuznetsov, M., and Efimenko, A. Okun, M. e. a. (2003b). Integral large scale experiments on hydrogen combustion for severe accident code validation. In *FISA-2003: EU Research in Reactor Safety* Eds. G. van Goethem, A. Zurita, J. M. Bermejo, P. Manolatos, H. Bischoff, Brussels. EURATOM, Office for Official Publications of EC.
- Bielert, U., Kotchourko, A., Burgeth, B., and Breitung, W. (2001). Numerical simulation of large scale hydrogen explosions in complex geometries. *Journal of Applied Mathematics and Mechanics*, 81:519–520.
-

-
- Borghgi, R. (1975). Computational studies of turbulent flows with chemical reactions. In *Turbulent mixing in non-reactive and reactive flows*, S.N.B. Murphy editor, pages 163–188, New York. Plenum Press.
- Borghgi, R. (1988). Turbulent combustion modeling. *Progress in Energy and Combustion Science*, 14:245–292.
- Borghoff, S., Brück, B., Kilian-Hülsmeier, Y., Maqua, M., Mildenerberger, O., Quester, C., Stahl, T., Thuma, G., Wetzels, N., and Wild, V. (2011). Der unfall in Fukushima. Technical Report GRS-293, GRS.
- Bradley, D. (1992). How fast can we burn? *The combustion institute*, 24(1):247–262.
- Bradley, D., Gaskell, P., and Gu, X. (2005). Premixed flamelet modeling: Factors influencing the turbulent heat release rate source term and the turbulent burning velocity. *Combustion and Flame*, 143:227–245.
- Bradley, D., Gaskell, P., Sedaghat, A., and Gu, X. (2003). Generation of PDFs for flame curvature and for flame stretch in premixed turbulent combustion. *Combustion and Flame*, 135:503–523.
- Bradley, D., Lau, A., and Lawes, M. (1992). Flame stretch rate as a determinant of turbulent burning velocity. *Philosophical Transactions of the Royal Society of London*, pages A338–359.
- Bradley, D., Lawes, M., and Kexin, L. (2008). Turbulent flame speeds in ducts and the deflagration/detonation transition. *Combustion and Flame*, 154:96–108.
- Bradley, D., Lawes, M., and Kexin, L. (2009). Turbulent flame speeds in ducts and the deflagration/detonation transition. In *Proc. 5th International Seminar on Fire and Explosion Hazards*. Editors: Bradley, D., Drysdale, D., Molkov, V., Carvel, R., pages 634–643.
- Bradley, D., Lawes, M., Kexin, L., Verhelst, S., and Woolley, R. (2007a). Laminar burning velocities of lean hydrogen-air mixtures at pressures up to 1.0 MPa. *Combustion and Flame*, 149:162–172.

-
- Bradley, D., Lawes, M., Kexin, L., and Woolley, R. (2007b). The quenching of premixed turbulent flames of iso-octane, methane and hydrogen at high pressures. *Proceeding of the Combustion Institute*, 31:1393–1400.
- Bradley, D., Sheppard, C., Woolley, G., and Lockett, R. (2000). The development and structure of flame instabilities and cellularity at low Markstein numbers in explosions. *Combustion and Flame*, 122:195–209.
- Brau, C. and Jonkman, R. (1970). The classical theory of rotational relaxation in diatomic gases. *Journal of Chemical Physics*, 52(2):447–484.
- Bray, K. (1995). Turbulent transport in flames. *Proc. R. Soc Lond*, page A451:231.
- Bray, K. (1996). The challenge of turbulent combustion. In *26 symposium of Combustion the Combustion Institute*, pages 1–26.
- Bray, K. and Moss, J. B. (1977). A unified statistical model of premixed turbulent flames. *Acta Astronautica*, 4(3-4):291–319.
- Breitung, W., Bielert, U., Necker, G., Veser, A., Wetzel, F., and K, P. (2000). The challenge of turbulent combustion. In *13th World hydrogen energy conference*, Beijing, China.
- Breitung, W., Chan, C., Dorofeev, S. B., Eder, A., Gelfand, B., Heitsch, M., Klein, R., Malliokos, A. Shepherd, E., Studer, E., and Thibault, P. (1999). SOAR on containment thermalhydraulics and hydrogen distribution. Technical Report NEA/CSNI/2000/7, OECD Paris.
- Breitung, W., Dorofeev, S., Kotchourko, A., Redlinger, R., Scholtyssek, W., Bentaib, A., L'Heriteau, J., Pailhories, P., Eyink, J., Movahed, M., Petzold, K., Heitsch, M., Alekseev, A., Denkevits, A., Kuznetsov, M., Efimenko, A., Okun, M., Huld, T., and Baraldi, D. (2005). Integral large scale experiments on hydrogen combustion for severe accident code validation-HYCOM. *Nuclear Engineering and Design*, 235:253–270.
-

-
- Breitung, W., Halmer, G., Jordan, T., Kaup, B., and Vesper, A. (2012). Radiolysegas-handbook. grundlagen zur entstehung, ansammlung, zuendung, verbrennung, auswirkung und sicherheit von radiolysegas-dampf-gemischen in siedewasserreaktor-anlagen. Technical report, Simaps, Gmbh.
- Brennan, S., Bengaouer, A., Carcassi, M., Cerchiara, G., Evans, G., Friedrich, A., Gentilhomme, O., Houf, W., Kotchourko, A., Kotchourko, N., Kudriakov, S., Makarov, D., Molkov, V., Papanikolau, E., Pitre, C., Royle, M., Schefer, R., Stern, G., Venetsanos, A., Vesper, A., Willoughby, D., and Yanez, J. (2009a). Towards minimizing hazards in hydrogen and fuel cell stationary applications: key findings of modeling and experimental work in the hyper project. In *Symposium series. Hazards. IchemE*, volume 155.
- Brennan, S., Bengaouer, A., Carcassi, M., Cerchiara, G., Evans, G., Friedrich, A., Gentilhomme, O., Houf, W., Kotchourko, A., Kotchourko, N., Kudriakov, S., Makarov, D., Molkov, V., Papanikolau, E., Pitre, C., Royle, M., Schefer, R., Stern, G., Venetsanos, A., Vesper, A., Willoughby, D., and Yanez, J. (2011). Towards minimizing hazards in hydrogen and fuel cell stationary applications: key findings of modeling and experimental work in the hyper project. *International Journal of Hydrogen energy*, 36:2711–2720.
- Brennan, S., Makarov, D., and Molkov, V. (2009b). Les of high pressure hydrogen jet fire. *Journal of Loss Prevention in the Process Industries*, 22:353–359.
- Breuer, M. and Rodi, W. (1994). *Large Eddy Simulations of turbulent flow through a straight square duct and a 180 degree bend*, volume 26 of *Fluids Mechanics and its applications*. Editors: Voke, P., Kleiser, R., Chollet, J., pages 175–188. Kluwer Academic Publishers.
- Brown, N., L.A.J., B., and P.N., P. (2011). Transport properties for combustion modeling. *Progress in Energy and Combustion Science*, 37:565–582.
- Brown, W., Beeson, H., Pedley, M., Griffin, D., Bryan, C., Thomas, W., and Frazier, W. (1997). Safety standard for hydrogen and hydrogen systems. Technical Report NSS 1740.16, NASA.
-

-
- Bychkov, V. (1999). Analytical scalings for flame interaction with sound waves. *Physics of Fluids*, 11(10):3168–3173.
- Bychkov, V. and Liberman, M. (2000). Dynamics and stability of pre-mixed flames. *Physics Reports*, 325:115–237.
- Cariteau, B., Brinster, J., Studer, E., Tkatschenko, I., and Joncquet, G. (2011a). Experimental results on the dispersion of buoyant gas in a full scale garage from a complex source. *International Journal of Hydrogen Energy*, 36(3):2489–2496.
- Cariteau, B., Brinster, J., and Tkatschenko, I. (2011b). Experiments on the distribution of concentration due to buoyant gas low flow rate release in an enclosure. *International Journal of Hydrogen Energy*, 36(3):2505–2512.
- Casamirra, M., Castiglia, F., and Giardina, M. Lombardo, C. (2009). Safety studies of a hydrogen refueling station: Determination of the occurrence frequency of the accidental scenarios. *International Journal of Hydrogen Energy*, 34(14):5846–5854.
- Catlin, C. and Lindstedt, R. (1991). Premixed turbulent burning velocities derived from mixing controlled reaction models with cold front quenching. *Combustion and Flame*, 85:427–439.
- Chao, J. and Lee, J. (2003). The propagation mechanism of high speed turbulent deflagrations. *Shock Waves*, 12:277–289.
- Chapman, S. and Cowling, T. (1990). *The mathematical theory of non-uniform gases*. Cambridge university press, Cambridge, U.K.
- Charlette, F., Meneveau, C., and Veynante, D. (2002). A power law flame wrinkling model for LES of pre-mixed turbulent combustion. Part I: Non-dynamic formulation and initial test. *Combustion and Flame*, 131:159–180.
- Chaumeix, N. (2010). Personal communication.
- Chen, C. J. and Rodi, W. (1980). *Vertical turbulent buoyant jets. A review of experimental data*. Pergamon Press.
-

-
- Chen, J. (2011). Petascale direct numerical simulation of turbulent combustion-fundamental insights towards predictive models. *Proceedings of the Combustion Institute*, 33:99–123.
- Chen, K. and Bak, P. (1990). A deterministic critical forest fire model. *Physical Letters A*, 149:207–210.
- Chernyavsky, B., Wu, T., Peneau, E., Bénard, P., Oshkai, P., and Djilali, N. (2009). Formation of flammable hydrogen-air clouds from hydrogen leakage. *International Journal of Hydrogen Energy*, 36(3):2645–2655.
- Chomiak, J. and J.R., N. (1995). Modeling variable density effects in turbulent flames. some basic considerations. *Combustion and Flame*, 102:371–386.
- Ciccarelli, G. and Dorofeev, S. (2008). Flame acceleration and transition to detonation in ducts. *Progress in Combustion Science*, 34(4):499–550.
- Clanet, C. and Searby, G. (1996). On the tulip flame phenomenon. *Combustion and Flame*, 105:225–238.
- Clavin, P. (1985). Dynamic behavior of pre-mixed flame front in laminar and turbulent flows. *Progress in Energy Combustion Science*, 11:1–59.
- Cook, A. and Riley, J. (1998). Sub-grid modeling for turbulent reactive flows. *Combustion and Flame*, 112:593–606.
- Cubbage, P. and Simmonds, W. (1955). An investigation of explosion reliefs for industrial drying ovens. *Trans. Inst. Gas. Eng.*, 105:470–475.
- Dahoe, A. and Cant, R. (2014). On least-squares gradient reconstruction and its application in conjunction with a rosenbrock method.
- Damen, K., van Troost, V., Faaij, A., and Turkenburg, W. (2006). A comparison of electricity and hydrogen production systems with CO_2 capture and storage. Part A: Review and selection of promising conversion and capture technologies. *Progress in Energy and Combustion Science*, 32:215–246.

-
- Damen, K., van Troost, V., Faaij, A., and Turkenburg, W. (2007). A comparison of electricity and hydrogen production systems with CO_2 capture and storage. Part B: Chain analysis of promising CCS option. *Progress in Energy and Combustion Science*, 33:580–609.
- Damköhler, G. (1940). Der Einfluss der Turbulenz auf die Flammgeschwindigkeit in Gasgemischen. *Zeitschrift für Elektrochemie*, 46:80.
- Di Sarli, V., Benedetto, A., and Russo, G. (2009). Using large eddy simulation for understanding vented gas explosions in the presence of obstacles. *Journal of Hazardous Materials*, 169:435–442.
- Dimmelmeier, H., Eyink, J., and Movahed, M. (2012). Computational validation of the EPR combustible gas control system. *Nuclear Engineering and Design*, 246:118–124.
- Dorofeev, S. (1995). Blast effects of confined and unconfined explosions. In *20th Symposium of Shock Waves*, pages 77–86, Pasadena.
- Dorofeev, S. (2007). Evaluation of safety distances related to unconfined hydrogen explosions. *International Journal of Hydrogen Energy*, 32(13):2118–2124.
- Dorofeev, S. (2008). Flame acceleration and transition to detonation: a framework for estimating potential explosion hazards in hydrogen mixtures. In *Third European Summer School on Hydrogen Safety*, Belfast.
- Dorofeev, S., Kuznetsov, M., Alekseev, V., Efimenko, A., and Breitung, W. (2001). Evaluation of limits for effective flame acceleration in hydrogen mixtures. *Journal of Loss Prevention in the Process Industries*, 14(6):583–589.
- Dorofeev, S., Sidorov, V., Efimenko, A., Kotchourko, A., Kuznetsov, M., Chaivanov, B., Matsukov, D., Pereverzev, A., and Avenyan, V. (1995). Fireballs from deflagration and detonation of heterogeneous fuel-rich clouds. *Fire Safety Journal*, 25:323–336.

-
- Dorofeev, S., Sidorov, V., Kuznetsov, M., Dvoinishnikov, A., Alekseev, V., and Efimenko, A. (1996). Air blast and heat radiation from fuel-rich mixture detonation. *Shock Waves*, 6:21–28.
- Dorofeev, S. B., Sidorov, V. P., Kuznetsov, M. S., Matsukov, I. D., and Alekseev, V. (2000). Effect of scale on the onset of detonations. *Shock Waves*, 10:137–149.
- Dowdy, D., Smith, D., Taylor, S., and Williams, A. (1990). The use of expanding spherical flames to determine burning velocities and stretch effects in hydrogen–air mixtures. *Proceedings of the Combustion Institute*, 23:325–331.
- Driscoll, J. (2008). Turbulent premixed combustion: Flamelet structure and its effect on turbulent burning velocities. *Progress in Energy and Combustion Science*, 3:91–134.
- Duclos, J., Veynante, D., and Poinso, T. (1993). A comparison of flamelet models for turbulent premixed combustion. *Combustion and Flame*, 95:101–118.
- Efimenko, A. and Dorofeev, S. (2001). CREBCOM code system for description of gaseous combustion. *Journal of Loss Prevention in the Process Industries*, pages 575–581.
- Eidson, T. (1985). Numerical simulation of the turbulent rayleigh-benard propel using sub-grid modeling. *Journal of Fluids Mechanics*, 158:245–268.
- Ekoto, I., Merilo, E. G., Dedrick, D. E., and Groethe, M. (2011). Performance-based testing for hydrogen leakage into passenger vehicle compartments. *International Journal of Hydrogen Energy*, 36(16):10169–10178.
- Erlebacher, G., Hussaini, M. Y., Speziale, C., and Zang, T. (1990). Towards Large Eddy Simulations of compressible turbulent flows. Technical Report ICASE Rep. No. 18460, NASA.
- EU (2013). European Commission funded Network of Excellence. <http://www.hysafe.org/>.
-

-
- European Comision (2007). Special eurobarometer. energy technologies. knowledge, perception, measures. http://ec.europa.eu/public_opinion/archives/ebs/ebs_262_en.pdf.
- Evers, A. (2013). <http://www.hydrogenambassadors.com/background/worldwide-hydrogen-production-analysis.php>.
- Fardisi, S. and Karim, G. A. (2009). Characteristics of flammable, buoyant hydrogen plumes rising from open vertical containers. *International Journal of Hydrogen Energy*, 35(15):6568–6579.
- Fernandez-Cosials, M., Jimenez, G., Barreira, P., and Qural, C. (2015). External flooding event analysis in a pwr-w with maap5. *Annals of Nuclear Energy*, 76:226–236.
- Ferrara, G., Di Benedetto, A., Salzano, E., and Russo, G. (2006). CFD analysis of gas explosions vented through relief pipes. *Journal of Hazardous Materials*, 137:654–665.
- Fickett, W. and Davis, W. (1979). *Detonation*. University of California press.
- Frölich, J. (2005). Personal communication.
- Frölich, J. (2006). *Large Eddy Simulation turbulenter Stroemungen*. Teubner Verlag.
- Fureby, C. (1996). *On modeling of unsteady combustion utilizing continuum mechanical mixture theories and Large Eddy Simulation*. PhD thesis, Lund Institute of Technology.
- Gamezo, V., Ogawa, T., and Oran, E. (2007). Numerical simulations of flame propagation and ddt in obstructed channels filled with hydrogen-air mixture. *Proceedings of the Combustion Institute*, 31:2463–2471.
- García, J., Baraldi, D., Gallego, E., Beccantini, A., Crespo, A., Hansen, O., Hoiset, S., Kotchourko, A., Makarov, D., Migoya, E., Molkov, V., Voort, M., and Yanez,

-
- J. (2010). An intercomparison exercise on the capabilities of cfd models to reproduce a large-scale hydrogen deflagration in open atmosphere. *International Journal of Hydrogen Energy*, 35(9):4435–4444.
- Garnier, E., Adams, A., and Sagaut, E. (2009). *Large Eddy Simulation for Compressible Flows*. Springer, Berlin.
- Gauntt, R., Kalinich, D., Cardoni, J., Phillips, J., Goldmann, A., and Pickering, S. (2012). Fukushima Daiichi Accident Study. Technical Report SAND2012-6173, Sandia National Laboratories.
- Gerlinger, P. (2003). Investigation of an assumed pdf approach for finite-rate chemistry. *Combustions Science and Technology*, 175:841–872.
- Germano, M., Piomelli, U., Moin, P., and Cabot, W. (1991). A dynamic subgrid-scale eddy viscosity model. *Physics of Fluids*, A 3:1760–1765.
- Girimaji, S. (1991). Assumed β -pdf model for turbulent mixing: validation and extension to multiple scalar mixing. *Combustion Science and Technology*, 78:177–196.
- Glassman, I. and Yetter, R. (2008). *Combustion*. Academic Press.
- Godreche, C. and Mannenille, P. (1998). *Hydrodynamics and nonlinear instabilities*. Cambridge University Press.
- Goodwin, D. (2001). Cantera user's guide. Technical report, California Institute of Technology, Pasadena, California, USA.
- Goshal, S., Lund, T., Moin, P., and Akselvoll, K. (1995). A dynamic localization model for Large Eddy Simulation of turbulent flows. *Journal of Fluid Mechanics*, 286:229–255.
- Grimsmo (1991). *Numerical simulation of turbulent flow and combustion in a four stroke homogeneous charge internal combustion engine*. PhD thesis, Univ Trondheim.

-
- Groethe, M., Merilo, E., Colton, J., Chiba, S., Sato, Y., and H., I. (2007). Large-scale hydrogen deflagrations and detonations. *International Journal of Hydrogen Energy*, 32(13):2125–2133.
- Groethe, M., Merilo, E., Colton, J., Chiba, S., Sato, Y., and Iwabuchi, H. (2005). Large-scale hydrogen deflagration and detonations. In *1st Int. Conf. Hydrogen Safety*, Pisa.
- Grune, J., Sempert, K., Kuznetsov, M., and Jordan, T. (2013). Experimental investigation of fast flame propagation in stratified hydrogen air mixtures in semi-confined flat layers. *Journal of Loss Prevention in the Process Industries*, 26:1442–1451.
- Gulder, O. (1991). Turbulent premixed combustion modeling using fractal geometry. *Proceedings of the Combustion Institute*, 23:835–842.
- Gupta, S., Brinster, J., Studer, E., and Tkatschenko, I. (2009). Hysafe SBEP-V20: Numerical studies of release experiments inside a naturally ventilated residential garage. *International Journal of Hydrogen Energy*, 34(14):5902–5911.
- Harten, A. (1983). High resolution schemes for hyperbolic conservation laws. *Journal Computational Physics*, 49:357–393.
- Heitsch, M. (2000). Fluid dynamic analysis of a catalytic recombiner to remove hydrogen. *Nuclear Engineering and Design*, 201(1):1–10.
- Hirschfelder, J., Curtiss, C., and Bird, R. (1954). *Molecular theory of gases and liquids*. John Wiley and Sons, New York.
- Hong, Z., Davidson, D., and Hanson, R. (2011). An improved H_2/O_2 mechanism based on recent shock tube/laser absorption measurements. *Combustion and Flame*, 158(4):633–644.
- Hottinen, T. (2001). Technical review and economic aspects of hydrogen storage technologies. Master's thesis, Helsinki University of technology. Department of engineering physics and mathematics.

-
- Houf, W., Evans, G., Merilo, E., Groethe, M., and James, S. (2012). Releases from hydrogen fuel-cell vehicles in tunnels. *International Journal of Hydrogen Energy*, 37(1):715–719.
- Houf, W., Evans, G., and Schefer, R. (2009). Analysis of jet flames and unignited jets from unintended releases of hydrogen. *International Journal of Hydrogen Energy*, 34(14):5961–5969.
- Houf, W., Evans, G., Schefer, R., Merilo, E., and Groethe, M. (2010). Evaluation of barrier walls for mitigation of unintended releases of hydrogen. *International Journal of Hydrogen Energy*, 35(10):4758–4775.
- Houf, W., Evans, G., Schefer, R., Merilo, E., and Groethe, M. (2011). A study of barrier walls for mitigation of unintended releases of hydrogen. *International Journal of Hydrogen Energy*, 36(3):2520–2529.
- Houf, W. and Schefer, R. (2008). Analytical and experimental investigation of small-scale unintended releases of hydrogen. *International Journal of Hydrogen Energy*, 33(4):1435–1444.
- Hourri, A., Gomez, F., Angers, B., and Benard, P. (2011). Computational study of horizontal subsonic free jets of hydrogen: Validation and classical similarity analysis. *International Journal of Hydrogen Energy*, 36(24):15913–15918.
- House, J. E. (2007). *Principles of Chemical Kinetics*. Academic Press.
- Hu, E., Huang, Z., He, J., and Miao, H. (2009). Experimental and numerical study on laminar burning velocities and flame instabilities of hydrogen-air mixtures at elevated pressures and temperatures. *International Journal of Hydrogen Energy*, 34:8741–8755.
- IBM corp. (2006). Open data explorer. ibm's scientific data visualization software. <http://www.opendx.org/index2.php>.
- Iijima, T. and Takeno, T. (1986). Effects of temperature and pressure on burning velocity. *Combustion and Flame*, 65:35–43.

-
- INPO (2011). Special report on the nuclear accident at the Fukushima Dai-ichi nuclear power stations. Technical Report 11-005, Institute of nuclear Power Operations.
- Jarosinski, J. (1984). The thickness of laminar flames. *Combustion and flame*, 56:337–342.
- Jimenez, J. (2003). *Turbulence and Vortex Dynamics*. École Polytechnique, Palaiseau, France.
- Jones, W. P. and Launder, B. E. (1972). The prediction of laminarization with a two equation model for turbulence. *International Journal of Heat and Mass Transfer*, 15:301–314.
- Jordan, T., Adams, P., Azkarate, I., Baraldi, D., Barthelemy, H., Bauwens, L., Bengaouer, A., Brennan, S., Carcassi, M., Dahoe, A., Eisenreich, N., Engebo, A., Funnemark, E., Gallego, E., Gavrikov, A., Haland, E., Hansen, A., Haugom, G., Hawsworth, S., Jedicke, O., Kessler, A., Kotchourko, A., Kumar, S., Langer, G., Ledin, S., Makarov, D., Marangon, A., Markert, F., Middha, P., Molkov, V., Nilsen, S., Papanikolaou, E., Perrette, L., Reinecke, E., Schmidtchen, U., Serre-Combe, P., Stoecklin, M., Sully, A., Teodorczyk, A., Tigreat, D., Venetsanos, A., Verfondern, K., Versloot, N., Vetere, A., Wilms, M., and Zaretskiy, N. (2009). Achievements of the ec network of excellence hysafe. In *3rd International Conference on Hydrogen Safety*, Ajaccio, France.
- Joulin, G. and Clavin, P. (1978). Linear stability analysis of non-adiabatic flames - diffusional thermal model. *Combustion and flame*, 35:139–153.
- Kadowaki, S. and Hasegawaba, T. (2005). Numerical simulation of dynamics of pre-mixed flames: flame instability and vortex-flame interaction. *Progress in Energy and Combustion Science*, 31:193–241.
- Kaneshige, M. and Shepherd, J. (1997). Detonation database. Technical Report Technical Report FM97-8, GALCIT.

-
- Kanzleiter, T. and Langer, G. (2008a). Quick look report hydrogen deflagration tests HD-15, HD-16, HD-17, HD-18, HD-19, HD-20 and HD-24. Technical Report Reactor Safety Research Project 150 1326. THAI Project, OECD-NEA.
- Kanzleiter, T. and Langer, G. (2008b). Quick look report hydrogen deflagration tests HD-1R, HD-4, HD-7, HD-8 and HD-10. Technical Report Reactor Safety Research Project 150 1326. THAI Project, OECD-NEA.
- Kanzleiter, T. and Langer, G. (2008c). Quick look report hydrogen deflagration tests HD-2R and HD-12 and HD-24. Technical Report Reactor Safety Research Project 150 1326. THAI Project, OECD-NEA.
- Karnesky, J., Chatterje, P., Tamanini, E., and S., D. (2007). An application of 3d gasdynamic modeling for the prediction of overpressures in vented enclosures. *Journal of Loss Prevention in the Process Industries*, 20:447–454.
- Kawanabe, H., Shioji, M., Tsunooka, T., and Ali, Y. (1998). Detonation in gases. In *Proceedings of the COMODIA*, pages 287–292, Tokio.
- Kee, R., Rupley, F., and Miller, J. (1989). CHEMKIN-II: a Fortran chemical kinetics package for the analysis of gas-phase chemical kinetics. Technical Report SAND89–8009, Sandia National Laboratories.
- Kessler, D., Gamezo, V., and Oran, E. (2010). Simulations of flame acceleration and deflagration-to-detonation transitions in methane-air systems. *Combustion and Flame*, 157:2063–2077.
- Kessler, G. (2012). *Sustainable and safe nuclear fission energy*. Springer Verlag.
- Kessler, G., Veser, A., Schluechter, F., Raskob, W., Landman, C., and Paesler-Sauer, J. (2012). *Sicherheit von Leichtwasserreaktoren. Risiken der Nukleartechnologie*. Springer Verlag.
- Kessler, G., Veser, A., Schlüter, F., Raskob, W., Landman, C., and Päsler-Sauer, J. (2014). *The Risks of Nuclear Energy Technology: Safety Concepts of Light Water Reactors (Science Policy Reports)*. Springer Verlag.

-
- Kestin, J., Knierim, K., Mason, E., Najafi, B., Ro, S., and Waldman, M. (1984). Equilibrium and properties of the noble gases and their mixtures at low density. *Journal of Physical and Chemical Reference Data*, 13:229–303.
- Khokhlov, A., Oran, E., and Wheeler, J. (1996). Scaling in buoyancy-driven turbulent premixed flames. *Combustion and Flame*, 105:28–34.
- Kier, L., Seybold, P., and Cheng, C. (2014). *Modeling chemical systems using cellular automata*. Springer Verlag.
- Kikukawa, S. (2008). Consequence analysis and safety verification of hydrogen fueling stations using CFD simulation. *International Journal of Hydrogen Energy*, 33(4):1425–1434.
- Kikukawa, S., Mitsuhashi, M., and Miyake, A. (2009). A risk assessment for liquid hydrogen fueling stations. *International Journal of Hydrogen Energy*, 34(2):1135–1141.
- Kline, S., Ferziger, J., and Johnston, J. (1978). Calculation of turbulent shear flows: Status and ten-year outlook. *ASME J. Fluid Eng.*, 100(3):28–34.
- Konnov, A. (2008). Remaining uncertainties in the kinetic mechanism of hydrogen combustion. *Combustion and Flame*, 152(4):507–528.
- Koroll, G., Kumar, R., and Bowles, E. (1993). Burning velocities of hydrogen-air mixtures. *Combustion and Flame*, 94:330–340.
- Kotchourko, A. (2005). Simulation of combustion processes in lean H₂-air mixtures: Conservatism of COM3D results. Technical Report Wissenschaftliche Berichte FZKA 7115, Projekt Nukleare Sicherheitsforschung, Forschungszentrum Karlsruhe.
- Kotchourko, A., Breitung, W., and Dorofeev, S. (1999a). Test of extended eddy break up model in simulations of turbulent h₂-air combustion. In *17th International Colloquium on the Dynamics of Explosions and Reactive Systems (ICDERS)*, Heidelberg, Germany.
-

-
- Kotchourko, A., Breitung, W., and Vesper, A. (1999b). Reactive flow simulations in complex 3D geometries using COM3D code. In *Tagungsbericht Proceedings, Jahrestagung Kerntechnik*, page 173.
- Kotchourko, A., Lelyakin, A., Yanez, J., Xu, Z., and K., R. (2015). Com3d: Turbulent combustion code. tutorial guide. Technical Report Institut für Kern- und Energietechnik. Projekt Nukleare Sicherheitsforschung, Karlsruher Institut für Technologie.
- Kudriakov, S., Dabbene, F., Studer, E., Beccantini, A., Magnaud, J., Paillere, H., Bentaib, A., Bleyer, A., Malet, J., Porcheron, E., and Caroli, C. (2008). The Tonus CFD code for hydrogen risk analysis: Physical models, numerical schemes and validation matrix. *Nuclear Engineering and Design*, 238(3):551–565.
- Kumar, R. and Bowles, E. (1990). Flame acceleration in hydrogen/air mixtures in a vertical cylinder filled with obstacles. In *Proc. of 2nd International Conference on Containment Design and Operation Proceedings*, Toronto, Canada.
- Kuznetsov, M. (2012a). personal communication.
- Kuznetsov, M. (2012b). personal communication.
- Kuznetsov, M., Alekseev, V., Yankin, Y., and Dorofeev, S. (2002a). Flame acceleration in a tube with variable cross-section. *Journal de physique IV*, 7(12):317–324.
- Kuznetsov, M., Alekseev, V., Yankin, Y., and Dorofeev, S. (2002b). Flammability limits of hydrogen-oxygen-diluent mixtures. *Combustion Science and Technology*, 174:157–172.
- Kuznetsov, M., Grune, J., Friedrich, A., Sempert, K., Breitung, W., and Jordan, T. (2011a). Hydrogen-air deflagrations and detonations in a semi-confined flat layer. In *Fire and Explosion Hazards, Proceedings of the Sixth International Seminar (Edited by D. Bradley, G. Makhviladze and V. Molkov)*, pages 125–136.
- Kuznetsov, M., Grune, J., Sempert, K., and Jordan, T. (2010). Experiments for the hydrogen combustion aspects of ITER LOVA scenarios. In *Proc. of the Sixth International Seminar on Fire and Explosion Hazards*, page 1, Leeds, UK.
-

-
- Kuznetsov, M. and Redlinger, R. (2008). Flammability limits of hydrogen-air and hydrogen-oxygen mixtures at elevated temperatures. Technical Report 2nd quarter report, IceFuel Project, Forschungszentrum Karlsruhe.
- Kuznetsov, M., Redlinger, R., Breitung, W., Grune, J., Friedrich, A., and Ichikawa, N. (2011b). Laminar burning velocities of hydrogen-oxygen-steam mixtures at elevated temperatures and pressure. *Proceedings of the Combustion Institute*, 33:895–903.
- Kuznetsov, M., Yanez, J., Grune, J., Friedrich, A., and Jordan, T. (2012). Hydrogen combustion in a flat semi-confined layer with respect to the Fukushima Daiichi accident. In *Proceedings of ICAPP '12, Paper 12419*, Chicago, USA.
- LaChance, J. (2009). Risk-informed separation distances for hydrogen refueling stations. *International Journal of Hydrogen Energy*, 34(14):5838–5845.
- Lacome, J., Jamois, D., Perrette, L., and Proust, C. (2011). Large-scale hydrogen release in an isothermal confined area. *International Journal of Hydrogen Energy*, 36(3):2302–2312.
- Lamoureux, N., Djebaili-Chaumeix, N., and Paillard, C. (2002). Laminar flame velocity determination for H₂-air-steam mixtures using the spherical bomb method. *Journal of Physics IV*, 12(P7):445–452.
- Landau, L. (1944). Theory of slow combustion. *Acta Physicochimica*, 19:277–285.
- Landau, L. and Lifshitz, E. (1987). *Fluid Mechanics, Second Edition: Volume 6 (Course of Theoretical Physics)*. Butterworth-Heinemann.
- Launder, B. E. and Sharma, B. I. (1974). Application of the energy dissipation model of turbulence to the calculation of flow near a spinning disk. *Letters of Heat and Mass Transfer*, 1:131–138.
- Le Cong, T. and Dagaut, P. (2008). Effect of water vapor on the kinetics of combustion of hydrogen and natural gas: experimental and detailed modeling study. In *Proc. ASME turbo Expo*, pages 1–9, Berlin, Germany.

-
- Leckner, B. (1972). Spectral and total emissivity of water vapor and carbon dioxide. *Combustion and Flame*, 19:33–48.
- Lee, J. (2008). *The Detonation Phenomenon*. Cambridge University Press.
- Lele, S. K. (1992). Compact finite difference schemes with spectral-like resolution. *Journal of Computational Physics*, 103:16–42.
- Lemmon, E., Huber, M., and McLinden, M. (2010). Nist standard reference database 23: Reference fluid thermodynamic and transport properties-refprop, version 9.0. Technical report, National Institute of Standards and Technology, Standard Reference Data Program, Gaithersburg.
- Lesieur, M. (1997). *Turbulence in Fluids*. Kluwer Publishers.
- Lesieur, M. (2008). *Turbulence in Fluids*. Springer.
- Lesieur, M., Métais, O., and Comte, P. (2005). *Large-Eddy Simulations of Turbulence*. Cambridge University Press.
- Leslie, D. and Quarini, G. (1979). The application of turbulence theory to the formulation of subgrid modeling procedures. *Journal of Fluid Mechanics*, 91:65–91.
- LeVeque, R. J. (2002). *Finite Volume Methods for Hyperbolic Problems*. Cambridge University Press.
- LeVeque, R. J. (2007). *Finite Difference Methods for Ordinary and Partial Differential Equations*. Society for Industrial and Applied Mathematics.
- Lewis, B. and von Elbe, G. (1987). *Combustion, flames and explosions of gases*. Academic Press, 3rd edition.
- Li, J., Zhao, Z., Kazakov, A., and Dryer, F. (2004). An updated comprehensive kinetic model of hydrogen combustion. *International Journal of Chemical Kinetics*, 36:566–575.
- Liñan, A. and Williams, F. (1993). *Fundamental Aspects of Combustion*. Oxford University Press.

-
- Libby, P. and Williams, F. (1994). Fundamental aspects and a review. In *P.A. Libby and F.A., Williams editors, Turbulent reacting flow*, pages 1–61. Academic Press.
- Lilly, D. K. (1992). A proposed modification of the germano subgrid-scale closure method. *Physics of Fluids*, A4:633–635.
- Lindstedt, R. P. and Vaos, E. (1999). Modeling of premixed turbulent flames with second moment methods. *Combustion and Flame*, 116:461–485.
- Lipatnikov, A. N. and Chomiak, J. (2002). Turbulent flame speeds and thickness: phenomenology, evaluation and application in multi-dimensional simulations. *Progress in Energy and Combustion Science*, 28:1–74.
- Lipatnikov, A. N. and Chomiak, J. (2005). Molecular transport effects on turbulent flame propagation and structure. *Progress in Energy and Combustion Science*, 31:1–73.
- Lipatnikov, A. N. and Chomiak, J. (2010). Effects of premixed flames on turbulence and turbulent scalar transport. *Progress in Energy and Combustion Science*, 36:1–102.
- Liu, H. and Schreiber, W. (2008). The effect of ventilation system design on hydrogen dispersion in a sedan. *International Journal of Hydrogen Energy*, 33(19):5115–5119.
- Luo, K. (1999). Combustion effects on turbulence in a partially premixed supersonic flame. *Combustion and Flame*, 119(4):417–435.
- Luo, K. (2001). DNS and LES of turbulence-combustion interactions. In *Geurts, Bernard J. (ed.) Modern simulation strategies for turbulent flow.*, pages 263–295. R.T. Edwards.
- Lutz, A., Kee, R., and Miller, J. (1996). SENKIN: a fortran program for predicting homogeneous gas phase chemical kinetics with sensitivity analysis. Technical Report SAND87-8248, Sandia National Laboratory.

-
- Maas, U. (1988). *Mathematical modeling of transient combustion processes using detailed reaction mechanisms*. PhD thesis, University Heidelberg.
- Maas, U. (2010). Personal communication.
- Maas, U. and Warnatz, J. (1988). Ignition processes in hydrogen-oxygen mixtures. *Combustion and Flame*, 74:53–69.
- MacDonald, G. (2013). Buncefield: Why did it happen? Technical report, Control of Major Accident Hazards. Health and Safety Executive.
- Magnussen, B. and Hjertager, B. (1976). On mathematical models of turbulent combustion with special emphasis on soot formation and combustion. *16th Symp. (Int'l.) on Combustion. Technical report*.
- Mahaffy, J., Chung, B., Dubois, F., Ducros, F., Graffard, E., Heitsch, M., Henriksen, M., Komen, E., Moretti, F., Morii, T., Mühlbauer, P., Rohde, U., Scheuerer, M., Smith, B. L., Song, C., Watanabe, T., and Zigh, G. (2007). Best practice guidelines for the use of CFD in nuclear reactor safety applications. Technical Report NEA/CSNI/R(2007)5. JT03227125, Nuclear Energy Agency. Committee on the safety of nuclear installations.
- Makarov, D. and Molkov, V. (2010). Structure and concentration decay in supercritical plane hydrogen jet. In *8th International Symposium on Hazards, Prevention, and Mitigation of Industrial Explosions*, pages 1–11, Keio University, Yokohama, Japan.
- Makarov, D., Verbecke, F., and Molkov, V. (2007). Numerical analysis of hydrogen deflagration mitigation by venting through a duct. *Journal of Loss Prevention in the Process Industries*, 20:433–438.
- Makarov, D., Verbecke, F., Molkov, V., Kotchourko, A., Lelyakin, A., Yanez, J., Baraldi, G., Heitsch, M., Efimenko, A., and Gavrikov, A. (2010). An intercomparison of CFD models to predict lean and non-uniform hydrogen mixture explosions. *International Journal of Hydrogen Energy*, 35:5754–5762.

-
- Makarov, D., Verbecke, E., Molkov, V., Roe, O., Skottenne, M., Kotchourko, A., Lelyakin, A., Yanez, J., Hansen, O., Middha, P., Ledin, S., Baraldi, D., Heitsch, M., Efimenko, A., and Gavrikov, A. (2009). An inter-comparison exercise on CFD model capabilities to predict a hydrogen explosion in a simulated vehicle refueling environment. *International Journal of Hydrogen Energy*, 32(6):2800–2814.
- Malcolm, W. and Chase, J. (1998). *Nist-Janaf Thermo-chemical Tables Set*. Amer. Inst. of Physics Publ. Srvs.
- Manninen, M., Silde, A., Lindholm, I., Huhtanen, R., and Sjövall, H. (2002). Simulation of hydrogen deflagration and detonation in a BWR reactor building. *Nuclear Engineering and Design*, 211(1):27–50.
- Mao, K. and Toor, H. L. (1970). A diffusion model for reaction with turbulent mixing. *AIChE Journal*, 16(1):49–52.
- Marinov, N., Westbrook, C., and Pitz, W. (1995). Detailed and global chemical kinetics model for hydrogen. In *Eighth International Symposium on Transport Processes*, San Francisco, California, USA.
- Markstein, G. (1964). *Nonsteady flame propagation*. Pergamon Press.
- Martin Pliego, F. and Ruiz-Maya Perez, L. (2004). *Estadística I: Probabilidad*. Parainfo.
- Martinez, I. (1992). *Termodinamica basica y aplicada*. Dossat.
- Matsukov, I., Kuznetsov, M., Alekseev, V., and Dorofeev, S. (1998). Photographic study of the characteristic regimes of turbulent flame propagation, local and global quenching in obstructed areas. Technical Report FZK-INR, 315/20088504/INR, Forschungszentrum Karlsruhe.
- Matsuura, K. (2009). Effects of the geometrical configuration of a ventilation system on leaking hydrogen dispersion and accumulation. *International Journal of Hydrogen Energy*, 34(24):9869–9878.

-
- Matsuura, K., Kanayama, H., Tsukikawa, H., and Inoue, M. (2008). Numerical simulation of leaking hydrogen dispersion behavior in a partially open space. *International Journal of Hydrogen Energy*, 33:240–247.
- Matsuura, K., Nakano, M., and Ishimoto, J. (2010). Forced ventilation for sensing-based risk mitigation of leaking hydrogen in a partially open space. *International Journal of Hydrogen Energy*, 35(10):4776–4786.
- MELCOR (2013). <http://melcor.sandia.gov/>.
- Meneveau, C. and Poinso, T. (1991). Stretching and quenching of flamelets in premixed turbulent combustion. *Combustion and Flame*, 86:311–332.
- Menter, F. (1993). Zonal two equation $k-\omega$ turbulence models for aerodynamic flows. *AIAA-Paper 93-2906*.
- Menter, F. (1994). Two-equation eddy-viscosity turbulence models for engineering applications. *AIAA Journal*, 32:269–28.
- Merilo, E., Groethe, M., Colton, J., and Chiba, S. (2011). Experimental study of hydrogen release accidents in a vehicle garage. *International Journal of Hydrogen Energy*, 36(3):2436–2444.
- Middha, P. and Hansen, O. (2009). CFD simulation study to investigate the risk from hydrogen vehicles in tunnels. *International Journal of Hydrogen Energy*, 34:5875–5886.
- Modest, M. (1993). *Radiative heat transfer*. McGraw-Hill.
- Moin, P. and Mahesh, K. (1998). Direct numerical simulation: A tool in turbulence research. *Annual Review of Fluid Mechanics*, 30:539–578.
- Moin, P., Squires, K., Cabot, W., and Lee, S. (1991). A dynamic sub-grid-scale model for compressible turbulence and scalar transport. *Physics of Fluids*, A 3:2746–2757.
-

-
- Molkov, V. and Bragin, M. (2009). High-pressure hydrogen leak through a narrow channel. In *Nonequilibrium Phenomena: Plasma, Combustion, Atmosphere*, pages 332–338. Torus Press.
- Molkov, V., Dobashi, R., Suzuki, M., and Hirano, T. (2000). Venting of deflagrations: hydrocarbon-air and hydrogen-air systems. *Journal of Loss Prevention in the Process Industries*, 13:397–409.
- Molkov, V., Korolchenko, A., and Alexandrov, S. (1997). Venting of deflagrations in buildings and equipment: universal correlation. In *Proceedings of 5th International Symposium on Fire Safety Science*, pages 1249–1260, Melbourne, Australia.
- Molkov, V., Makarov, D., and Bragin, M. (2009). Physics and modelling of underexpanded jets and hydrogen dispersion in atmosphere. In *Physics of extreme state of matter - 2009*, pages 146–149. Institute of Chemical Physics, Russian Academy of Sciences.
- Molkov, V., Makarov, D., and Grigorash, A. (2004). Cellular structure of explosion flames: Modelling and large eddy simulation. *Combustion Science and Technology*, 176(5-6):851–885.
- Molkov, V., Makarov, D., and Puttock, J. (2006a). The nature and large eddy simulation of coherent deflagrations in a vented enclosure-atmosphere system. *Journal of Loss Prevention in the Process Industries*, 19:121–129.
- Molkov, V., Makarov, D., and Schneider, H. (2006b). Hydrogen-air deflagrations in open atmosphere: Large eddy simulation analysis of experimental data. *International Journal of Hydrogen Energy*, 32(13):2198–2205.
- Molkov, V., Makarov, D., and Schneider, H. (2007a). Large-scale hydrogen-air deflagrations: modelling and very large eddy simulations. In *Deflagrative and Detonative Combustion*, pages 115–132. Torus Press, Moscow.
- Molkov, V., Makarov, D., and Verbecke, F. (2007b). LES model of vented explosion: Hydrogen-air mixtures. In *Proceedings of 5th Int. Seminar on Fire and Explosion Hazards*, pages 23–27, Edinburgh, UK.

-
- Molkov, V., Verbecke, E., and Makarov, D. (2008a). Les of hydrogen-air deflagrations in a 78.5-m tunnel. *Combustion Science and Technology*, 180(5):796–808.
- Molkov, V., Verbecke, E., and Zbikowski, M. (2008b). Pressure effects of hydrogen-air explosions. In *Physics of extreme state of matter - 2008*, pages 143–145. Institute of Chemical Physics, Russian Academy of Sciences.
- Movahed-Shariat-Panahi, M. (2012). Recommendation for maximum allowable mesh size for plant combustion analysis with CFD codes. *Nuclear Engineering and Design*, 253:360–366.
- Mukai, S., Suzuki, J., Mitsuishi, H., Oyakawa, K., and Watanabe, S. (2005). CFD simulation on diffusion of leaked hydrogen caused by vehicle accident in tunnels. In *1st International conference on hydrogen safety*, page 8–10, Pisa, Italy.
- Müller, M. A., Kim, T. J., Yetter, R. A., and Dryer, F. L. (2011). Flow reactor studies and kinetic modeling of the H_2/O_2 reaction. *International Journal of Chemical Kinetics*, 31(2):113–125.
- Nallasamy, N. (1987). Turbulence models and their applications to the prediction of internal flows a review. *Computers and Fluids*, 15(2):151–194.
- O Conaire, M., Curran, H., Simmie, J., Pitz, W., and Westbrook, C. (2004). A comprehensive modeling study of hydrogen oxidation. *International Journal of Chemical Kinetics*, 36:603–622.
- Oran, E. and Gamezo, V. (2007). Origins of the deflagration-to-detonation transition in gas-phase combustion. *Combustion and Flame*, 148:4–47.
- Oran, E. and Gamezo, V. (2008). The deflagration to detonation transition in gas phase combustion. In *Third European Summer School in Hydrogen Safety*, Belfast.
- Oran, E., Jones, D., and Sichel, M. (1992). Numerical simulations of detonation transmission. In *Proc. Roy. Soc.*, volume A 436, 1, pages 267–297.

-
- Papanikolaou, E., Venetsanos, A., Cerchiara, G., Carcassi, M., and Markatos, N. (2011). On the use of hydrogen in confined spaces: Results from the internal project InsHyde. *International Journal of Hydrogen Energy*, 36(3):2597–2605.
- Papanikolaou, E., Venetsanos, A., Heitsch, M., Baraldi, D., Huser, A., Pujol, J., Garcia, J., and Markatos, N. (2010). Hysafe SBEP-V20: Numerical studies of release experiments inside a naturally ventilated residential garage. *International Journal of Hydrogen Energy*, 35(10):4747–4757.
- Pasman, H., Groothuisen, T., and P.H., G. (1974). Design of pressure relief vents. In *Prevention and Safety Promotion in the Process Industries*, editor Buschman C.H., pages 185–189. Elsevier.
- Patel, S., Ibrahim, S., and Yehia, M. (2003). Flamelet surface density modeling of turbulent deflagrating flames in vented explosions. *Journal of Loss Prevention in the Process Industries*, 16:451–455.
- Pelce, P. and Clavin, P. (1982). Influence of hydrodynamics and diffusion upon the stability limits of laminar pre-mixed flames. *Journal of Fluid Mechanics*, 124:219–237.
- Pelce, P. and Rochwerger, D. (1999). A parametric acoustic instability in premixed flames. *Journal of Fluid Mechanics*, 239:293–307.
- Peters, N. (1999). The turbulent burning velocity for large-scale and small-scale turbulence. *Journal of Fluid Mechanics*, 384:107–132.
- Peters, N. (2000). *Turbulent combustion*. Cambridge university press.
- Pfortner, H. and Schneider, H. (1983). Ballonversuche zur Untersuchung der Deflagration von Wasserstoff/Luftgemischen. Technical Report Fh-IcT-report, Fraunhofer Institut Chemische Technologie, Pfinztal, Germany.
- Pitsch, H. (2005). A consistent level set formulation for large eddy simulation of pre-mixed turbulent combustion. *Combustion and Flame*, 143:587–598.

-
- Pitts, W. M., Yang, J. C., and Fernandez, M. G. (2012). Helium dispersion following release in a 1/4-scale two-car residential garage. *International Journal of Hydrogen Energy*, 37(6):5286–5298.
- Poinsot, T. and Veynante, D. (2001). *Theoretical and numerical combustion*. Edwards.
- Poinsot, T., Veynante, D., and Candel, S. (1991). Quenching processes and premixed turbulent combustion diagrams. *Journal of Fluid Mechanics*, 228:561–606.
- Poludnenko, A. and Oran, E. (2011). The interaction of high-speed turbulence with flames: Turbulent flame speed. *Combustion and Flame*, 158:301–326.
- Pope, S. (2000). *Turbulent flows*. Cambridge University Press.
- Pope, S. and Cheng, W. (1986). Statistical calculations of spherical turbulent flames. *Proceedings of the Combustion Institute*, 21:1473–1481.
- Prabhudharwadkar, D., Aghalayam, P., and Iyer, K. (2011a). Simulation of hydrogen mitigation in catalytic recombiner: Part-I: Surface chemistry modeling. *Nuclear Engineering and Design*, 241(5):1746–1757.
- Prabhudharwadkar, D., Aghalayam, P., and Iyer, K. (2011b). Simulation of hydrogen mitigation in catalytic recombiner: Part-II: Formulation of a CFD model. *Nuclear Engineering and Design*, 241(5):1758–1767.
- Prabhudharwadkar, D., Iyer, K., Mohan, N., Bajaj, S., and Markandeya, S. (2011c). The TONUS CFD code for hydrogen risk analysis: Physical models, numerical schemes and validation matrix. *Nuclear Engineering and Design*, 241(3):832–842.
- Prasad, K., Pitts, W., and Yang, J. (2010). Effect of wind and buoyancy on hydrogen release and dispersion in a compartment with vents at multiple levels. *International Journal of Hydrogen Energy*, 35(17):9218–9231.

-
- Prasad, K., Pitts, W., and Yang, J. (2011). A numerical study of the release and dispersion of a buoyant gas in partially confined spaces. *International Journal of Hydrogen Energy*, 36(8):5200–5210.
- Ramamurthi, K., Bhadraiah, K., and Murthy, S. (2009). Formation of flammable hydrogen-air clouds from hydrogen leakage. *International Journal of Hydrogen Energy*, 34:8428–8437.
- Rasbash, D. (1969). The relief of gas and vapour explosions in domestic structures. *Fire Research Note*, 759.
- Razus, D. and Krause, U. (2001). Comparison of empirical and semi-empirical calculation methods for venting of gas explosions. *Fire Safety Journal*, 36:1–23.
- Redlinger, R. (2008). DET3D a CFD tool for simulating hydrogen combustion in nuclear reactor safety. *Nuclear Engineering and Design*, 238(3):610–617.
- Repoussard, A. and co workers (2012). Fukushima, one year later. Technical Report IRSN/DG/2012-003, IRSN.
- Rodi, W. (2000). *Turbulence models and their application in hydraulics*. Balkena Publishers.
- Rodi, W. and Mansour, N. (1993). Low reynolds number $k - \epsilon$ modeling with the aid of direct simulation data. *Journal Fluid Mechanics*, 250:509–529.
- Royle, P., Travis, J. R., and Breitung, W. (2006). Modeling and validation of catalytic hydrogen recombination in the 3D CFD Code GASFLOW II. *Proceedings of the CFD4NRS Conference, Munich*.
- Royle, M. and Willoughby, D. (2011). Consequences of catastrophic releases of ignited and unignited hydrogen jet releases. *International Journal of Hydrogen Energy*, 36(3):2688–2692.
- Runes, E. (1972). Explosion venting. *Journal of Loss Prevention in the Process Industries*, 6:63–67.

-
- Saffers, J., Makarov, D., and Molkov, V. (2011). Modelling and numerical simulation of permeated hydrogen dispersion in a garage with adiabatic walls and still air. *International Journal of Hydrogen Energy*, 36(3):2582–2588.
- Sagaut, P. (2001). *Large Eddy Simulation for Incompressible Flows*. Springer Verlag.
- Sanchez-Sanz, M. (2012). Premixed flame extinction in narrow channels with and without heat recirculation. *Combustion and Flame*, 159:3158–3167.
- Sanchez-Sanz, M., Rosales, M., and Sanchez, A. (2010). The hydrogen laminar jet. *International Journal of Hydrogen Energy*, 35(8):3919–3927.
- Sato, Y., Merilo, E., Groethe, M., Colton, J., Chiba, S., and Iwabuchi, H. (2006). Homogeneous hydrogen deflagrations in a sub-scale vehicle tunnel. In *Proceedings of 15th World Hydrogen Energy Conference*, Lyon, France.
- Schefer, R., Groethe, M., Houfa, W., and Evans, G. (2009). Experimental evaluation of barrier walls for risk reduction of unintended hydrogen releases. *International Journal of Hydrogen Energy*, 34(3):1590–1606.
- Schefer, R., Houf, W., and Williams, T. (2008). Investigation of small-scale unintended releases of hydrogen: Buoyancy effects. *International Journal of Hydrogen Energy*, 33(17):4702–4712.
- Schmid, H., Habisreuther, P., and Leuckel, W. (1998). Renormalization-group analysis of turbulence. *Combustion and Flame*, 113:79–91.
- Scholtyssek, W. e. a. (2004). Integral large scale experiments on hydrogen combustion for severe accident code validation. Technical Report FISKs-CT1999-00004, SAM HYCOM D020FIKS-1999-00004, HYCOM Final Report, EU contract.
- Searby, G. and Clavin, P. (1986). Weakly turbulent, wrinkled flames in pre-mixed gases. *Combustion Science and Technology*, 46:167–193.
- Searby, G. and Rochwerger, D. (1991). A parametric acoustic instability in premixed flames. *Journal of Fluid Mechanics*, 231:529–543.

-
- Sehgal, B. (2012). *Nuclear safety in light water reactors*. Springer Verlag.
- Shebeko, Y., Tsarichenko, S., Korolchenko, A., Trunev, A., Navzenya, V., Papkov, S., and Zaitzev, A. (1995). Burning velocities and flammability limits of gaseous mixtures at elevated temperatures and pressures. *Combustion and Flame*, 102:427–437.
- Shepherd, J. (2009). Detonation in gases. In *Proceedings of the Combustion Institute*, volume 32, 1, pages 83–98.
- Shirvill, L., Roberts, T., Royle, M., Willoughby, D., and Gautier, T. (2012). Safety studies on high-pressure hydrogen vehicle refueling stations: Releases into a simulated high-pressure dispensing area. *International Journal of Hydrogen Energy*, 37(8):6949–6964.
- Shur, M., Spalart, P., Strelets, M., and Travin, A. (2008). A hybrid RANS-LES approach with delayed-DES and wall-modeled LES capabilities. *International Journal of Heat and Fluid Flow*, 29:1638–1649.
- Siegel, R. and Howell, J. (1992). *Thermal radiation heat transfer*. Taylor and Francis.
- Simpson, L. (1986). Equations for the VDI and Bartknecht nomograms. *Plant/Oper Prog*, 5:49–51.
- Sivashinsky, G. (1977). Nonlinear analysis of hydrodynamic instability in laminar flames. -I. Derivation of basic equations. *Acta astronautica*, 4:1177–1206.
- Skjold, T., Arntzen, B., Hansen, O., Storvik, I., and Eckhoff, R. (2006). Simulation of dust explosions in complex geometries with experimental input from standardized tests. *Journal of loss prevention in the process industries*, 19:210–217.
- Smagorinsky, J. (1963). General circulation experiments with the primitive equations. *Monthly Weather Review*, 91(3):99–164.
- Spalart, P. (1997). Comments on the feasibility of LES for wing and on a hybrid RANS/LES approach. In *1st ASOSR CONFERENCE on DNS/LES*, Arlington, Texas.

-
- Spalart, P. (2009). Reflexions on RANS modeling. In *Progress in Hybrid RANS-LES Modeling. Papers Contributed to the 3rd Symposium on Hybrid RANS-LES Methods*, Gdansk, Poland.
- Spalart, P., Deck, S., Shur, M., Squires, K., Strelets, M., and Travin, A. (2006). A new version of detached-eddy simulation, resistant to ambiguous grid densities. *Theoretical and Computational Fluid Dynamics*, 20(3):181–195.
- Spalding, D. (1971). Mixing and chemical reaction in steady confined turbulent flames. In *33th Symposium of Combustion*, pages 649–657, Pittsburg. The Combustion Institute.
- Strelets, M. (2001). Detached eddy simulation of massively separated flows. In *39th ALAA Aerospace Sciences Meeting*, Reno, Nevada.
- Stroehle, J. and Myhrvold, T. (2007). An evaluation of detailed reaction mechanisms for hydrogen combustion under gas turbine conditions. *International Journal of Hydrogen Energy*, 32:125–135.
- Sun, C., Sung, C., He, L., and Law, C. (1999). Dynamics of weakly stretched flames: quantitative description and extraction of global flame parameters. *Combustion and Flame*, 118:108–128.
- Szabó, T., Yanez, J., Kotchourko, A., Kuznetsov, M., and Jordan, T. (2012a). Parameterization of laminar burning velocity dependence on pressure and temperature in hydrogen/air/steam mixtures. *Combustion science and technology*, 184:1427–1444.
- Szabó, T., Yanez, J., Kotchourko, A., Kuznetsov, M., and Jordan, T. (2012b). Parameterization of laminar burning velocity dependence on pressure and temperature in hydrogen/air/steam mixtures. In *International Colloquium on the Dynamics of Explosions and Reactive Systems (ICDERS)*.
- Takahashi, F., Mizomoto, M., and Ikai, S. (2001). Alternative energy sources III. In *Nuclear energy/synthetic fuels*, editor T. Nejat Veziroglu, volume 5, pages 447–457. McGraw-Hill.
-

-
- Tanaka, T., Azuma, T., Evans, J., Cronin, P., Johnson, D., and Cleaver, R. (2007). Experimental study on hydrogen explosions in a full-scale hydrogen filling station model. *International Journal of Hydrogen Energy*, 32(13):2162–2170.
- TEPCO (2012). Fukushima nuclear accident analysis report. http://www.tepco.co.jp/en/press/corp-com/release/betu12_e/images/120620e0104.pdf.
- TEPCO (2013a). <http://www.houseoffoust.com/fukushima/blueprint.html>.
- TEPCO (2013b). Fukushima 1 BWR containment design. General description. http://chong.zxq.net/misc/events/Daichii_BWR_Design.htm.
- TEPCO (2013c). RAW video: Smoke pours from Japan Nuclear Plant. <http://www.youtube.com/watch?v=KknHVL43YJO>.
- Trouvé, A. and Poinso, T. (1994). The evolution equation for the flame surface density in turbulent premixed combustion. *Journal of Fluid Mechanics*, 278:1–31.
- Tse, S., Zhu, D., and Law, C. (2000). Morphology and burning rates of expanding spherical flames in $H_2/O_2/inert$ mixtures up to 60 atmospheres. Alternative energy sources III. In *Proceedings of the Twenty-Eighth Symposium (International) on Combustion*, pages 1793–1800, Pittsburgh.
- Venetsanos, A., Adams, P., Azkarate, I., Bengaouer, A., Brett, L., Carcassi, M., Engebø, A., Gallego, E., Gavrikov, A., Hansen, O., Hawksworth, S., Jordan, T., Kessler, A., Kumar, S., Molkov, V., Nilsen, S., Reinecke, E., Stoecklin, M., Schmidtchen, U., Teodorczyk, A., Tigreat, D., and Versloot, N. (2011). On the use of hydrogen in confined spaces: Results from the internal project InsHyde. *International Journal of Hydrogen Energy*, 36(3):2693–2699.
- Venetsanos, A., Baraldi, D., Adams, P., Heggem, P., and Wilkening, H. (2008). CFD modeling of hydrogen release, dispersion and combustion for automotive scenarios. *Journal of Loss Prevention in the Process Industries*, 21:162–184.

-
- Venetsanos, A., Papanikolaou, E., Delichatsios, M., Garcia, J., Hansen, O., Heitsch, M., Huser, A., Jahn, W., Jordan, T., Lacomme, J., Ledin, H., Makarov, D., Middha, P., Studer, E., Tchouvelev, A., Teodorczyk, A., and Verbecke, F. Van der Voort, M. (2009). An inter-comparison exercise on the capabilities of CFD models to predict the short and long term distribution and mixing of hydrogen in a garage. *International Journal of Hydrogen Energy*, 34(14):5912–5923.
- Verhelst, S. and Sierens, R. (2007). A quasi-dimensional model for the power cycle of a hydrogen-fueled ICE. *International Journal of Hydrogen Energy*, 32:3545–3554.
- Vervisch, L. and Poinso, T. (1998). Direct numerical simulation of non-premixed turbulent combustion. *Annual Review of Fluid Mechanics*, 30:655–691.
- Veser, A., Kuznetsov, M., Fast, G., Friedrich, A., Kotchourko, N., Stern, G., Schwall, M., and Breitung, W. (2011). The structure and flame propagation regimes in turbulent hydrogen jets. *International Journal of Hydrogen Energy*, 36(3):2351–2359.
- Veynante, D., Duclos, J. M., and J., P. (1994). Experimental analysis of flamelet models for pre-mixed turbulent combustion. *Proceedings of the Combustion Institute*, 25:1249–1256.
- Veynante, D. and Vervisch, L. (2002). Turbulent combustion modeling. *Progress in Energy and Combustion Science*, 28:1–73.
- Visser, D., Houkema, M., Siccama, N., and Komen, E. (2012). Validation of a FLUENT CFD model for hydrogen distribution in a containment. *Nuclear Engineering and Design*, 245:161–171.
- Vreman, Geurts, K. (1994). Sub-grid modeling in les of compressible flow fluids mechanics and its application. In *Direct and large eddy simulation I*, Voke, Kleiser, Chollet, editors, pages 133–144. Kluwer Academic Publisher.
- Vreman, P. (1995). *Direct and large-eddy simulation of the compressible turbulent mixing layer*. PhD thesis, University Twente.
-

-
- Wagner, W. (2008). *International Steam Tables*. Springer.
- Warnatz, J., Mass, U., and Dibble, R. (1999). *Combustion*. Springer Verlag.
- Weller, H., Tabor, G., Gosman, A., and Fureby, C. (1998). Application of a flame-wrinkling LES combustion model to a turbulent mixing layer. *Proceedings of the Combustion Institute*, 27:899–907.
- Wen, J., Madhav-Rao, V., and Tam, V. (2010). Numerical study of hydrogen explosions in a refueling environment and in a model storage room. *International Journal of Hydrogen Energy*, 35(1):385–394.
- Westbrook, C., Mizobuchi, Y., Poinso, T., Smith, P., and Warnatz, J. (2005). Computational combustion. *Proceedings of the Combustion Institute*, 30:125–157.
- Whitehouse, D., Greig, D., and Koroll, G. (1996). Combustion of stratified hydrogen-air mixtures in the 10.7 m³ combustion test facility cylinder. *Nuclear Engineering and Design*, 166(3):453–462.
- Wilke, C. (1950). A viscosity equation for gas mixtures. *Journal of Chemical Physics*, 18(3):517–519.
- Wilcox, D. (1998). *Turbulence Modeling for CFD*. DCW Industries, Inc.
- Williams, D., Bauwens, L., and Oran, E. (1996). Detailed structure and propagation of three-dimensional detonations. In *Symposium (International) on Combustion*, volume 26, 2, pages 2991–2998.
- Williams, F. A. (1994). *Combustion Theory*. Westview Press.
- Wolfram, S. (2002). *A new kind of science*. Wolfram Media Inc.
- Xiao, J., Travis, J., and Breitung, W. (2011). Hydrogen release from a high pressure gaseous hydrogen reservoir in case of a small leak. *International Journal of Hydrogen Energy*, 36(3):2545–2554.
- Yakhot, A. and Orszag, S. A. (1986). Renormalization group analysis of turbulence. I. basic theory. *Journal of Scientific Computing*, 1:3–51.

-
- Yanez, J., Kotchourko, A., Kuznetsov, M., Lelyakin, A., and T., J. (2011a). Modeling of the flame acceleration in flat layer for hydrogen-air mixtures. In *4th International Conference Hydrogen Safety ICHS*, San Francisco.
- Yanez, J., Kotchourko, A., Kuznetsov, M., Lelyakin, A., and T., J. (2014a). Modeling of the flame acceleration in flat layer for hydrogen-air mixtures. *Submitted to International Journal of Hydrogen Energy*.
- Yanez, J., Kotchourko, A., and Lelyakin, A. (2010a). Experimental and numerical investigation of the effect of end venting on flame acceleration in an obstructed channel. In *8th International Symposium on Hazards, Prevention, and Mitigation of Industrial Explosion (ISHPMIE)*, Tokio, Japan.
- Yanez, J., Kotchourko, A., and Lelyakin, A. (2010b). Hydrogen deflagration simulations under typical containment conditions for nuclear safety. In *Computational Fluid Dynamics in Nuclear Reactor Safety (CDF4NRS)*, Washington.
- Yanez, J., Kotchourko, A., and Lelyakin, A. (2010c). Kylcom model for the calculation of under-resolved hydrogen combustion problems. In *Proceeding of the Sixth International Seminar on Fire and Explosion Hazards*, pages 137–148, Leeds, UK.
- Yanez, J., Kotchourko, A., and Lelyakin, A. (2012a). Hydrogen deflagration simulations under typical containment conditions for nuclear safety. *Nuclear Energy and Design*, 250:678–686.
- Yanez, J., Kotchourko, A., Lelyakin, A., Gavrikov, A., Efimenko, A. and Zbikowski, M., Makarov, D., and Molkov, V. (2011b). A comparison exercise on the CFD detonation simulation in large-scale confined volumes. *International Journal of Hydrogen Energy*, 36(3):2613–2619.
- Yanez, J., Kuznetsov, M., and Bykov, V. (2013a). Sudden acceleration of flames in open channels driven by hydraulic resistance. In *International Colloquium on the Dynamics of Explosions and Reactive Systems (ICDERS)*, Taipei.

-
- Yanez, J., Kuznetsov, M., and Bykov, V. (2014b). Sudden acceleration of flames in open channels driven by hydraulic resistance. *Submitted to combustion and flame*.
- Yanez, J., Kuznetsov, M., Grune, J., and T., J. (2012b). Flame instability of lean hydrogen-air mixtures in a smooth vertical channel with open end. In *9th International Symposium on Hazard, Prevention and Mitigation of Industrial Explosions*, Cracow.
- Yanez, J., Kuznetsov, M., Kotchourko, A., and Lelyakin, A. (2011c). Theoretical considerations of laminar flame speed as a function of initial conditions and basic kinetics properties with respect to the safety problem. In *1st International Conference for Sustainable Energy Storage (IC-SES)*, Belfast.
- Yanez, J., Kuznetsov, M., Kotchourko, A., Lelyakin, A., and T., J. (2012c). Theoretical considerations of laminar flame speed as a function of initial conditions and basic kinetic properties with respect to the safety problem. *Journal of Energy and Power Engineering*, 6(847-857).
- Yanez, J., Kuznetsov, M., and Redlinger, R. (2013b). The acoustic – parametric instability for gaseous mixtures with lewis number smaller than one. In *International Colloquium on the Dynamics of Explosions and Reactive Systems (ICDERS)*, Taipei.
- Yanez, J., Kuznetsov, M., and Redlinger, R. (2013c). The acoustic–parametric instability for hydrogen–air mixtures. *Combustion and flame*, 10:2009–2016.
- Yanez, J., Kuznetsov, M., Redlinger, R., Kotchourko, A., and Lelyakin, A. (2011d). Analysis of the parametric-acoustic instability for safety assessment of hydrogen-air mixtures in closed volumes. In *4th International Conference Hydrogen Safety ICHS*, San Francisco.
- Yanez, J., Lelyakin, A., Jordan, T., Alekseev, V., and Kuznetsov, M. (2011e). Experimental and numerical investigation of the effect of end venting on flame accel-

-
- eration in an obstructed channel. *Science and technology of energetic materials*, 72(3):86–89.
- Yao, C. (1974). Explosion venting of low-strength equipment and structures. *J. Loss Prev Process Ind*, 8:1–9.
- Yarin, L., Hetsroni, G., and Mosyak, A. (2004). *Combustion of Two-Phase Reactive Media*. Springer Verlag.
- Zabetakis, M. (1965). Flammability characteristics of combustible gases and vapors. *BuMines Bulletin*, 627:121.
- Zang, T., Dahlburg, R., and Dahlburg, J. (1992). Direct and large eddy simulations of of three dimensional compressible navier-stokes turbulence. *Physics of Fluids*, A4:127–140.
- Zbikowski, M., Makarov, D., and Molkov, V. (2010). Numerical simulations of large-scale detonation tests in the rut facility by the les model. *International Journal of Hydrogen Energy*, 181:949–956.
- Zeldovich, Y. B., Barenblatt, G., Librovich, V., and Makhviladze, G. (1985). *The mathematical theory of Combustion and Explosion*. Consultants Bureau.
- Zeldovich, Y. B. and Raizer, Y. (2002). *Physics of shock waves and high-temperature hydrodynamic phenomena*. Dover.
- Zimont, V. (1977). To computation of turbulent combustion of partially premixed gases, chemical physics of combustion and explosion processes. Combustion of multi-phase and gas systems. *Chernogolovka: OIkhF*, pages 77–80.
- Zimont, V. and Mesheriakov, E. (1988). A model of combustion of partially premixed gases. In *Structure of gas flames. Proceedings of international colloquium. Part, I.I.*, pages 35–43, Novosibirsk, SSSR.

Appendix A

CONVOLUTION OF THE NAVIER-STOKES EQUATIONS

A.1 Derivation of the convoluted equations

A.1.1 General

This section contains the derivation of the equation set for the *Large Eddy Simulation* methodology, described in section 1.5.3. The Navier-Stokes equations are convoluted to obtain the set of equations that are the core of *Large Eddy Simulation* methodology, which was summarized in equations (1.10) to (1.13) in the introduction.

The *density weighted decomposition* of the variables is usually utilized, see e.g. by Fureby (1996), Garnier et al. (2009). Under such formulation, the variables are split as $\rho = \bar{\rho} + \rho'$ and $\phi = \bar{\phi} + \phi''$, where ϕ is an arbitrary variable the over-bar and over-tilde (its separate notation will be evident in few lines) represent grid-scales quantities and the expressions marked with apostrophes stay for the sub-grid parts

to be modeled.

Any filtered variable can be denoted with an over-bar and mathematically described with the convolution

$$\bar{\phi}(\vec{x}, t) = \frac{1}{\Delta} \int_{-\infty}^{+\infty} \phi(\vec{x}, t) G\left(\frac{\vec{x} - \vec{\xi}}{\Delta}, t\right) d^3\xi, \quad (\text{A.1})$$

where G is the kernel of the filter. In the cases in which the variables are weighted with density and for simplicity, the following change of variables could be introduced

$$\tilde{\phi} = \frac{\bar{\rho}\bar{\phi}}{\bar{\rho}} \quad (\text{A.2})$$

that since $\bar{\rho}\bar{\phi} = \bar{\rho}\tilde{\phi}$, leads to a more handy notation, as will be seen below. It is also convenient at this point, as it will appear in the Navier-Stokes equations, to provide a convenient expression for the decomposition of the commonly filtered product of three variables $\overline{\rho\phi\varphi}$ where ϕ and φ are arbitrary scalars. Utilizing the previous notation we may manipulate

$$\overline{\rho\phi\varphi} = \overline{\rho(\tilde{\phi} + \phi'')(\tilde{\varphi} + \varphi'')}.$$

With the changes of variables in (A.2) the last expression transforms to

$$\bar{\rho}\widetilde{\phi\varphi} = \bar{\rho}\left(\widetilde{\tilde{\phi}\tilde{\varphi}} + \widetilde{\tilde{\phi}\varphi''} + \widetilde{\phi''\tilde{\varphi}} + \widetilde{\phi''\varphi''}\right).$$

We may now study the difference $(\widetilde{\phi\varphi} - \tilde{\phi}\tilde{\varphi})$. As we subtract the filtered variables $\tilde{\phi}\tilde{\varphi}$, that are grid size, from the common filtered $\widetilde{\phi\varphi}$, we obtain the sub-grid terms which is the object of the modeling. The following sub-grid term decomposition is also convenient:

$$\bar{\rho}\left(\widetilde{\phi\varphi} - \tilde{\phi}\tilde{\varphi}\right) = \underbrace{\bar{\rho}\left(\widetilde{\tilde{\phi}\tilde{\varphi}} - \tilde{\phi}\tilde{\varphi}\right)}_L + \underbrace{\bar{\rho}\left(\widetilde{\tilde{\phi}\varphi''} - \tilde{\phi}\varphi''\right)}_C + \underbrace{\bar{\rho}\left(\widetilde{\phi''\varphi''}\right)}_R. \quad (\text{A.3})$$

Equation (A.3) can be split in different parts for ulterior modeling purposes. The term marked with an L , the *Leonard* term, contains only variables function

of filtered quantities. The *Cross* terms, marked with C represent the interaction between filtered and unresolved quantities. Finally, the Reynolds terms, represent the interactions between purely sub-grid terms. More details about the meaning of each of them will be given in section B.1.

A.1.2 Filtering of total density

The convolution of the filter G , appearing in equation (1.9), with the density equation (A.1) gives

$$\bar{\rho}_t + (\bar{\rho} \overline{u_j})_j = 0. \quad (\text{A.4})$$

Applying equation (A.2), this last equation can be transformed to

$$\bar{\rho}_t + (\bar{\rho} \widetilde{u_j})_j = 0. \quad (\text{A.5})$$

A.1.3 Filtering of momentum equation

Similarly, the convolution applied to the momentum equation (1.2) yields

$$(\bar{\rho} \overline{u_i})_t + (\bar{\rho} \overline{u_i u_j})_j + \bar{p}_i - \bar{\sigma}_{ij,j} = 0, \quad (\text{A.6})$$

and applying (A.2) again,

$$(\bar{\rho} \widetilde{u_i})_t + (\bar{\rho} \widetilde{u_i} \widetilde{u_j})_j + \bar{p}_i - (\bar{\sigma}_{ij})_j = J, \quad (\text{A.7})$$

with

$$J = (\bar{\rho} \widetilde{u_i} \widetilde{u_j})_j - (\bar{\rho} \overline{u_i u_j})_j = [\bar{\rho} \cdot (\widetilde{u_i} \widetilde{u_j} - \overline{u_i u_j})]_j. \quad (\text{A.8})$$

Additionally, (A.7) can be transformed, summing and subtracting $\check{\sigma}_{ij}$, to

$$(\bar{\rho} \widetilde{u_i})_t + (\bar{\rho} \widetilde{u_i} \widetilde{u_j})_j + \bar{p}_i - (\check{\sigma}_{ij})_j = J + (\bar{\sigma}_{ij} - \check{\sigma}_{ij})_j, \quad (\text{A.9})$$

where $\check{\sigma} = \check{\sigma}(\tilde{u}, \tilde{\mu})$ does not contain any ensemble average. The definition of

$$\check{\sigma}_{ij} = \overline{2\mu S_{ij} - \frac{2}{3}\mu \delta_{ij} S_{kk}}, \quad (\text{A.10})$$

can be extended to,

$$\check{\sigma}_{ij} = 2\tilde{\mu} S_{ij}(\tilde{u}) - \frac{2}{3}\tilde{\mu} \delta_{ij} S_{kk}(\tilde{u}). \quad (\text{A.11})$$

A.1.4 Filtering of total energy

For the total energy equation, the application of the operator (1.9) gives,

$$\bar{\rho} \check{e} = \frac{\bar{p}}{\gamma - 1} + \frac{1}{2} \bar{\rho} \widetilde{u_i u_i}. \quad (\text{A.12})$$

This formula contains some terms that are not directly computable. Following the so called *Vreman System I* (Garnier et al., 2009), as stated in (Vreman, 1995), the equation reduces to

$$\bar{\rho} \check{e} = \frac{\bar{p}}{\gamma - 1} + \frac{1}{2} \bar{\rho} \tilde{u}_i \tilde{u}_i. \quad (\text{A.13})$$

So that

$$\bar{\rho} \check{e} = \bar{\rho} \check{e} + \frac{1}{2} \bar{\rho} [\widetilde{u_i^2} - (\widetilde{u_i})^2]. \quad (\text{A.14})$$

Furthermore it has to be considered

$$\check{q} = Q(\check{T}), \quad (\text{A.15})$$

and applying the filtering to equation (1.3)

$$\bar{\rho} \check{e}_t + [(\bar{\rho} \check{e} + \bar{p}) \widetilde{u_j}]_j - (\check{\sigma}_{ij} \widetilde{u_i})_j + \check{q}_{j,j} = S_1 + S_2 + S_3 + S_4, \quad (\text{A.16})$$

with

$$S_1 = -\frac{1}{2} [\bar{\rho} (\widetilde{u_i^2} - (\widetilde{u_i})^2)]_t, \quad (\text{A.17})$$

$$S_2 = [(\bar{\rho} \check{e} + \bar{p}) \widetilde{u_j}]_j - \overline{[(\rho e + p) u_j]}_j, \quad (\text{A.18})$$

$$S_3 = -(\check{\sigma}_{ij} \widetilde{u_i})_j + (\overline{\sigma_{ij} u_i})_j, \quad (\text{A.19})$$

$$S_4 = \check{q}_{j,j} - \bar{q}_{j,j}. \quad (\text{A.20})$$

Without the derivative, A.18 is

$$S_2 = \widetilde{u_j} \left[\frac{\gamma}{\gamma-1} \bar{p} + \frac{1}{2} \bar{\rho} (\widetilde{u_i})^2 \right] - u_j \left[\frac{\gamma}{\gamma-1} p + \frac{1}{2} \rho u_i^2 \right] = S_{21} + S_{22}, \quad (\text{A.21})$$

where

$$S_{21} = \frac{\gamma}{\gamma-1} [\bar{p} \widetilde{u_j} - \overline{p u_j}], \quad (\text{A.22})$$

$$S_{22} = \frac{1}{2} [\bar{\rho} (\widetilde{u_i})^2 \widetilde{u_j} - \overline{\rho u_i^2 u_j}]. \quad (\text{A.23})$$

Grouping

$$S_1 + S_{22} = R_1 + R_2, \quad (\text{A.24})$$

with

$$R_1 = -(\overline{\rho u_i^2})_t - (\overline{\rho u_i^2 u_j})_j. \quad (\text{A.25})$$

$$R_2 = [\bar{\rho} (\widetilde{u_i})^2]_t + [\bar{\rho} (\widetilde{u_i})^2 \widetilde{u_j}]_j. \quad (\text{A.26})$$

Then, R_1 resulted to be

$$\begin{aligned}
-R_1 &= \overline{u_i(\rho u_i)_t} + \overline{u_i(\rho u_i u_j)_j} + \overline{\rho u_i u_{i,t}} + \overline{\rho u_i u_j u_{i,j}} = \\
&\stackrel{1,2}{=} \overline{u_i(-p_i + \sigma_{ij,j})} + \overline{\rho u_i(u_{i,t} + u_j u_{i,j})} = \\
&\stackrel{1,2}{=} \overline{u_i(-p_i + \sigma_{ij,j})} + \overline{u_i(-p_i + \sigma_{ij,j})} = \\
&= -2 \overline{u_i(p_i - \sigma_{ij,j})}.
\end{aligned} \tag{A.27}$$

Moreover,

$$\begin{aligned}
R_2 &= \widetilde{u_i}[\overline{\rho \widetilde{u_i}}]_t + (\overline{\rho \widetilde{u_i} \widetilde{u_j}})_j + \overline{\rho \widetilde{u_i}}[\widetilde{u_{i,t}} + \widetilde{u_j} \widetilde{u_{i,j}}] \\
&= \widetilde{u_i}[\dots (A.7)] + Z,
\end{aligned} \tag{A.28}$$

with

$$\begin{aligned}
Z &= \overline{\rho \widetilde{u_i}}[\widetilde{u_{i,t}} + \widetilde{u_j} \widetilde{u_{i,j}}] = \\
&= \widetilde{u_i}[(\overline{\rho \widetilde{u_i}})_t - \overline{\rho}_t \widetilde{u_i}] + \widetilde{u_i} \widetilde{u_j}[(\overline{\rho \widetilde{u_i}})_j - \overline{\rho}_j \widetilde{u_i}] = \\
&= \widetilde{u_i}[(\overline{\rho \widetilde{u_i}})_t + \widetilde{u_j}(\overline{\rho \widetilde{u_i}})_j] - (\widetilde{u_i})^2[\overline{\rho}_t + \widetilde{u_j} \overline{\rho}_j] = \\
&\stackrel{(A.7)}{=} \widetilde{u_i}[-\overline{\rho}_j \widetilde{u_i}(\widetilde{u_j})_j + (A.7)] - (\widetilde{u_i})^2[-\overline{\rho}(\widetilde{u_j})_j] = \\
&= \widetilde{u_i}[\dots (A.7)].
\end{aligned} \tag{A.29}$$

Additionally,

$$\dots (A.7) \equiv -\overline{p}_i + \overline{\sigma_{ij,j}} - (\overline{\rho \tau_{ij}})_j, \tag{A.30}$$

and

$$\overline{\rho \tau_{ij}} = \overline{\rho} (\widetilde{u_i \widetilde{u_j}} - \widetilde{u_i} \widetilde{u_j}). \tag{A.31}$$

Totally, $S_1 + S_2 + S_3$, is given in equation (A.16) by

$$\begin{aligned}
&-(\check{\sigma}_{ij} \widetilde{u_i})_j + (\overline{\sigma_{ij}} \widetilde{u_i})_j + \frac{\gamma}{\gamma-1} [\overline{p} \widetilde{u_j} - \overline{p} \widetilde{u_j}]_j \\
&+ \overline{u_i(p_i - \sigma_{ij,j})} + \widetilde{u_i} \cdot [-\overline{p}_i + \overline{\sigma_{ij,j}} - (\overline{\rho \tau_{ij}})_j].
\end{aligned} \tag{A.32}$$

Collecting the pressure terms then

$$\begin{aligned}
& \frac{\gamma}{\gamma-1} [\overline{p} \widetilde{u}_j - \overline{p u_j}]_j + \overline{u_i p_i} - \widetilde{u_i} \overline{p_i} = \\
& = \frac{1}{\gamma-1} (\overline{p} \widetilde{u_j})_j + (\overline{p} \widetilde{u_j})_j - \widetilde{u_i} \overline{p_i} - \frac{1}{\gamma-1} (\overline{p u_j})_j - (\overline{p u_j})_j + \overline{u_i p_i} \\
& = \frac{1}{\gamma-1} (\overline{p} \widetilde{u_j})_j + \overline{p} (\widetilde{u_j})_j - \frac{1}{\gamma-1} (\overline{p u_j})_j - \overline{p u_{j,j}} \\
& = \frac{1}{\gamma-1} [\overline{p} \widetilde{u_j} - \overline{p u_j}]_j + \overline{p} (\widetilde{u_j})_j - \overline{p u_{j,j}}.
\end{aligned} \tag{A.33}$$

In (A.32), the terms containing σ are

$$-(\check{\sigma}_{ij} \widetilde{u_i})_j + (\overline{\sigma_{ij} u_i})_j - \overline{u_i \sigma_{ij,j}} + \widetilde{u_i} \overline{\sigma_{ij,j}} = -(\check{\sigma}_{ij} \widetilde{u_i})_j + \overline{\sigma_{ij} u_{i,j}} + \widetilde{u_i} \overline{\sigma_{ij,j}}, \tag{A.34}$$

and adding and subtracting $(\overline{\sigma_{ij} \widetilde{u_i}})_j$ the terms in (A.32) containing σ are

$$[\overline{\sigma_{ij} \widetilde{u_i}} - (\check{\sigma}_{ij} \widetilde{u_i})]_j + \overline{\sigma_{ij} u_{i,j}} - \overline{\sigma_{ij}} (\widetilde{u_i})_j. \tag{A.35}$$

A.2 Summary of results in A.1.1

The results of the previous section, in agreement with Vreman (1995), can be expressed as

$$\frac{\partial \bar{\rho}}{\partial t} = -\frac{\partial \bar{\rho} \tilde{u}_j}{\partial x_j}, \tag{A.36}$$

$$\frac{\partial \bar{\rho} \tilde{u}_i}{\partial t} = -\frac{\partial}{\partial x_i} (\bar{\rho} \tilde{u}_i \tilde{u}_j + p \delta_{ij}) \frac{\partial \check{\sigma}_{ij}}{\partial x_i} + \bar{\rho} g + S_{1,ij} + S_{2,ij}, \tag{A.37}$$

$$\begin{aligned}
\frac{\partial \bar{\rho} \check{e}}{\partial t} = & -\frac{\partial}{\partial x_i} ((\bar{\rho} \check{e} + p) \tilde{u}_i) + \frac{\partial \tilde{u}_j \check{\sigma}_{ij} - \bar{q}_i}{\partial x_i} + \bar{\rho} g_j \tilde{u}_i + \\
& + \alpha_3 + \alpha_4 + \alpha_5 + \alpha_6 + \alpha_7 + \alpha_8,
\end{aligned} \tag{A.38}$$

$$\frac{\partial \bar{\rho} \tilde{Y}_a}{\partial t} = -\frac{\partial \bar{\rho} \tilde{Y}_a \tilde{u}_i}{\partial x_i} + \frac{\partial}{\partial x_i} \left(D_t \frac{\partial \tilde{Y}_a}{\partial x_i} \right) + \bar{\omega}_a + S_9 + S_{10}, \tag{A.39}$$

where $S_{1,ij}$, $S_{2,ij}$, $\alpha_1 - \alpha_8$ & S_9 , S_{10} are the sub-grid terms. Their ordered definition and description is the object of next section.

A.3 Definition of Sub-grid Terms

This section collects the results obtained in Sections A.1.1 and A.2 expressing them in the notation from Vreman (1995)

A.3.1 Impulse equation

Left hand sides of the system (A.36) - (A.39) are equivalent to the Navier-Stokes equations but expressed in terms of the filtered variables, $\bar{\rho}$, \tilde{u}_i and \bar{p} . Right hand sides contain the so called sub-grid terms. They represent the non-resolved small scales and must be modeled because, unlike the left hand side terms, they cannot be expressed as a function of the filtered known variables.

The impulse equations contain two sub grid terms S_{1ij} , S_{2ij} . The sub-grid stress term S_{1ij} ,

$$S_{1,ij} = \frac{-\partial}{\partial x_i} (\bar{\rho} \widetilde{u_i u_j} - \bar{\rho} \tilde{u}_i \tilde{u}_j), \quad (\text{A.40})$$

appears because of the non-linearity of the convective term. Utilizing the equation (A.31), then

$$S_{1,ij} = \frac{-\partial}{\partial x_i} (\bar{\rho} \tau_{ij}). \quad (\text{A.41})$$

S_{2ij} is the sub-grid viscous stress term, that appears due to the non-linearity of the viscous stress tensors,

$$S_{2,ij} = \frac{\partial}{\partial x_i} (\bar{\sigma}_{ij} - \check{\sigma}_{ij}). \quad (\text{A.42})$$

A.3.2 Energy Equation

The sub-grid terms in the energy equation can be defined taking into account the equation (A.12), following the formulation of Vreman (1995) and of Luo (2001). The turbulent stress, on the scalar level, represents the kinetic energy transfer from resolved to unresolved scales and reads

$$\alpha_3 = \tilde{u}_i \frac{\overline{\partial \rho u_i u_j}}{\partial x_j} - \frac{\partial \bar{\rho} \tilde{u}_i \tilde{u}_j}{\partial x_j} = \tilde{u}_i \frac{\partial \bar{\rho} \tau_{ij}}{\partial x_j}. \quad (\text{A.43})$$

The Sub-grid total velocity pressure term α_4 ,

$$\alpha_4 = -\frac{1}{\gamma-1} \frac{\partial}{\partial x_i} (\overline{p u_i} - \bar{p} \tilde{u}_i), \quad (\text{A.44})$$

accounts for the effect of the sub-grid turbulence on the conduction of heat on the resolved scales.

The sub-grid pressure dilatation term α_5 contains a pure compressibility effect and vanishes in a divergence free constant density flow,

$$\alpha_5 = -\left(\overline{p \frac{\partial u_j}{\partial x_j}} - \bar{p} \frac{\partial \tilde{u}_j}{\partial x_j} \right). \quad (\text{A.45})$$

The non-linearities of the viscous stress tensor create three sub grid scales tensors, α_6 , α_7 , α_8 . The first one is the sub-grid dissipation rate term

$$\alpha_6 = \overline{\sigma_{ij} \frac{\partial u_i}{\partial x_j}} - \overline{\sigma_{ij}} \frac{\partial \tilde{u}_i}{\partial x_j}, \quad (\text{A.46})$$

which describes the amount of energy converted in internal energy due to viscous dissipation. The term α_7 is

$$\alpha_7 = \frac{\partial}{\partial x_j} (\overline{\sigma_{ij} \tilde{u}_i} - \bar{\sigma}_{ij} \tilde{u}_i). \quad (\text{A.47})$$

Additionally in the energy equation, the sub-grid heat conduction term,

$$\alpha_8 = -\frac{\partial}{\partial x_j} (\overline{\bar{q}_j} - \hat{q}_j), \quad (\text{A.48})$$

where

$$\bar{q}_j = -\bar{\lambda} \frac{\partial \bar{T}}{\partial x_j}, \quad (\text{A.49})$$

and

$$\hat{q}_j = -\bar{\lambda} \frac{\partial \tilde{T}}{\partial x_j}. \quad (\text{A.50})$$

A.3.3 Transport equation for chemical species

In the transport equation for the chemical species the sub grid terms S_9 , S_{10} appear. The Sub grid turbulent species flux term reads

$$S_9 = \frac{-\partial}{\partial x_i} \left(\bar{\rho} \left(\widetilde{u_i Y_\alpha} - \tilde{u}_i \tilde{Y}_\alpha \right) \right), \quad (\text{A.51})$$

and the sub grid viscous diffusion term is defined

$$S_{10} = \frac{\partial}{\partial x_i} \left(\overline{\rho D \frac{\partial Y_\alpha}{\partial x_i}} - \bar{\rho} \tilde{D} \frac{\partial \tilde{Y}_\alpha}{\partial x_i} \right). \quad (\text{A.52})$$

Appendix B

MODELING OF THE SUB-GRID TERMS IN LARGE EDDY SIMULATIONS

B.1 Modeling the S_{1ij} tensor

Modeling of the tensor S_{1ij} , see equation (A.40), is the main purpose of the Large Eddy Simulation methodology in incompressible flows. Comprehensive reviews on such modeling can be found in Sagaut (2001) and Frölich (2006). As discussed already, see equation (A.3), sub-grid terms can be decomposed in the Leonard, Cross and Reynolds terms. Only last two precise modeling as Leonard terms can be calculated directly from the motion.

The Cross terms are specific to the LES methodology, they do not exist for RANS approaches. Attending to the analysis of Leslie and Quarini (1979) they are responsible for the so called *back-scatter* or transfer of energy from unresolved to resolved

scales. In most approaches, as stated by Fureby (1996), and suggested by Garnier et al. (2009), they are explicitly or implicitly neglected. They could be taken into account if the *Scale Similarity* approach, pioneered by Bardina et al. (1983), is recalled. This methodology consists of assuming that the statistical structure of the tensors constructed on the basis of the sub-grid scales is similar to that of their equivalent analyzed on the basis of the resolved scales. This may be expressed in the banal equality $\overline{\phi\phi} = \bar{\phi}\bar{\phi}$, that can be used to express

$$\widetilde{\bar{\phi}\phi''} \approx \bar{\phi}\bar{\phi}. \quad (\text{B.1})$$

This relation provides the sub grid terms as a function of the resolved scales. The Scale Similarity methodology has been also applied to Reynolds terms with little success. The Reynolds terms are dissipative and through the utilization of this methodology the Kolmogorov cascade was under-estimated. The use of this model is therefore restricted to the Cross terms. If the model is applied to them, it is obtained

$$C = \bar{\rho} \left(\widetilde{\tilde{u}_i u_j'' + u_i'' \tilde{u}_j} \right) \approx \bar{\rho} \left(\widetilde{\tilde{u}_i \tilde{u}_j} - \tilde{\tilde{u}}_i \tilde{\tilde{u}}_j \right). \quad (\text{B.2})$$

The Reynolds terms are modeled, under the functional approach, following the eddy-viscosity-eddy-diffusivity methodology. Under this assumption, the scalar flux vector is modeled with the turbulent eddy-diffusivity hypothesis

$$\partial_i (\overline{u_i \phi}) = \partial_i (\zeta \partial_i (\bar{\phi})), \quad (\text{B.3})$$

where ζ is any of the turbulent transport coefficient. On the other hand, eddy-viscosity hypothesis states that the rotor part of the Reynolds stresses could be expressed as

$$\bar{\rho} \left(\widetilde{\tilde{u}_i \tilde{u}_j} - \frac{2}{3} k \delta_{ij} \right) = \rho \nu (\partial_j \tilde{u}_i + \partial_i \tilde{u}_j). \quad (\text{B.4})$$

For the rest of this section, it would be useful to recall the definition of the S_{1ij}

equation

$$S_1 = -\nabla \cdot \bar{\rho} \tau. \quad (\text{B.5})$$

where $\tau_{ij} = (\widetilde{u_i u_j} - \bar{u}_i \bar{u}_j)$.

The tensor D , representing the mean rate of strain in matrix notation is defined as

$$\tilde{D} = \nabla \vec{\tilde{u}} + \nabla^T \vec{\tilde{u}}. \quad (\text{B.6})$$

In addition, the tensor D_D which stands for the deviatoric part of D is also defined as

$$\tilde{D}_D = \tilde{D} - \frac{1}{3} \text{tr}(\tilde{D}) I. \quad (\text{B.7})$$

The tensor τ can now be modeled following the approaches contained in the so called *Eddy-viscosity-eddy-diffusivity*, *Mixed* or *Dynamic* model specified in the following sub-sections.

B.1.1 Eddy-viscosity-eddy-diffusivity model

In the *Eddy-viscosity-eddy-diffusivity* methodology the Cross terms are considered to be negligible. The τ tensor can be written

$$-\bar{\rho} \tau = \frac{2}{3} \bar{\rho} k I - 2(\mu_t) \tilde{D}_D, \quad (\text{B.8})$$

where

$$k = C_I \Delta \|\tilde{D}_D\|^2, \quad (\text{B.9})$$

and

$$\mu_t = \bar{\rho} C_D \Delta \|\tilde{D}_D\|, \quad (\text{B.10})$$

represent the sub grid kinetic energy and the turbulent dynamic viscosity respectively.

B.1.2 Mixed model

The *Mixed* model can be considered an extension of the *Eddy-viscosity-eddy-diffusivity* in which the Cross terms have been taken into account. Therefore, the modeling of τ takes care of the *back-scatter*, that is mainly due to cross terms. Under these models, the tensor adopts the formulation,

$$-\bar{\rho}\tau = \bar{\rho}\left(\widetilde{\widetilde{u_i u_j}} - \widetilde{\widetilde{u_i}}\widetilde{\widetilde{u_j}}\right) + \frac{2}{3}(k)I - 2(\mu_t)\tilde{D}_D, \quad (\text{B.11})$$

with the same definitions for the sub grid kinetic energy and the turbulent dynamic viscosity as in *Eddy-viscosity-eddy-diffusivity* methodology.

B.1.3 Dynamic model

The *Eddy-viscosity-eddy-diffusivity* methodology has a serious shortcoming. This is that the two constants C_D and C_I must be adjusted or obtained from DNS or any other methodology for each particular problem. The dynamic eddy viscosity model was originally introduced by Moin et al. (1991) to try to overcome these difficulties. The *Dynamic* method is based on minimizing an a priori estimate of the error committed locally, in space and time, in the determination of τ to deliver a point-time-wise values for C_D and C_I . The stress tensor is then modeled

$$-\bar{\rho}\tau = \frac{2}{3}\bar{\rho}kI - 2(\mu_t)\tilde{D}_D, \quad (\text{B.12})$$

where

$$k = C_I(\vec{x}, t)\Delta\|\tilde{D}_D\|^2, \quad (\text{B.13})$$

and

$$\mu_t = \bar{\rho}C_D(\vec{x}, t)\Delta\|\tilde{D}_D\|. \quad (\text{B.14})$$

The Germano-Lilly Dynamic Procedure, which was presented by Germano et al. (1991) and Lilly (1992), and extended to its compressible formulation by Moin et al. (1991), can be utilized to obtain $C_I(\vec{x}, t)$, $C_D(\vec{x}, t)$. The procedure is based on the

application of two filters, of different widths, to the equation (B.15), usually called Germano identity

$$\overline{u_i u_j} - \bar{u}_i \bar{u}_j = \overline{u_i' u_j'} - \bar{u}_i' \bar{u}_j'. \quad (\text{B.15})$$

The two filters can be defined as

$$\hat{f}(x) = \int f(x') \hat{G}(x, x') dx, \quad (\text{B.16})$$

$$\bar{f}(x) = \int f(x') \bar{G}(x, x') dx, \quad (\text{B.17})$$

where \hat{G} and \bar{G} are the kernels with different widths. Then, applying the second filter to (B.15) it is obtained

$$\widehat{\overline{u_i u_j}} - \hat{\bar{u}}_i \hat{\bar{u}}_j + \hat{\bar{u}}_i \hat{\bar{u}}_j - \widehat{\bar{u}_i' \bar{u}_j'} = \widehat{\overline{u_i' u_j'}} - \widehat{\bar{u}_i'} \widehat{\bar{u}_j'}. \quad (\text{B.18})$$

The so called sub-test-scales (secondary filter) and sub-grid-scales (primary one) may be defined and represented respectively with the variables T and ϑ :

$$T_{ij} = \widehat{\overline{u_i u_j}} - \hat{\bar{u}}_i \hat{\bar{u}}_j, \quad (\text{B.19})$$

and

$$\vartheta_{ij} = \widehat{\overline{u_i' u_j'}} - \widehat{\bar{u}_i'} \widehat{\bar{u}_j'}. \quad (\text{B.20})$$

Both magnitudes are a function of the model selected, and could be calculated utilizing different scales. On the other side,

$$L_{ij} = \widehat{\overline{u_i' u_j'}} - \hat{\bar{u}}_i \hat{\bar{u}}_j, \quad (\text{B.21})$$

is dependent on grid variables and could be directly calculated. Then the tensorial equation (B.18) can be rewritten to be

$$L = T - \vartheta. \quad (\text{B.22})$$

It must be also remarked that the expressions (B.18) to (B.22) may be generalized to any generic variables ϕ , φ .

B.1.3.1 Deviatoric part

The tensorial equation (B.22) may be split into its deviatoric and isotropic parts, which for an arbitrary variable can be expressed like,

$$\phi_{ij}^d = \phi_{ij} - \frac{1}{3}\phi_{kk}\delta_{ij}. \quad (\text{B.23})$$

The deviatoric part of the equation (B.22) can be arranged to be

$$L^d = T^d - \vartheta^d. \quad (\text{B.24})$$

The sub-grid and sub-test stress tensor may be modeled with the chosen model. Therefore, using the *Eddy-viscosity-eddy-diffusivity* model they read,

$$T - \frac{1}{3}\delta_{ij}T_{ii} = C_D \widehat{\Delta^2} \left\| \hat{\bar{D}}_D \right\| \hat{\bar{D}}_D, \quad (\text{B.25})$$

$$\vartheta - \frac{1}{3}\delta_{ij}\vartheta_{ii} = C_D \widehat{\Delta^2} \left\| \bar{D}_D \right\| \bar{D}_D, \quad (\text{B.26})$$

that combined is

$$M_{ij} = C_D \widehat{\Delta^2} \left\| \hat{\bar{D}}_D \right\| \hat{\bar{D}}_D - C_D \widehat{\Delta^2} \left\| \bar{D}_D \right\| \bar{D}_D. \quad (\text{B.27})$$

The equation (B.21) can be directly evaluated, while equation (B.27) contains the T_{ij} and τ_{ij} terms already modeled.

The Lilly (1992) procedure for the determination of $C_D(\vec{x}, t)$ lies on in evaluating the error caused in the modeling to minimize it. The error made is then evaluated with the six equation relationship

$$E_{ij} = L_{ij} - M_{ij}, \quad (\text{B.28})$$

which yields

$$C_D = \frac{M_{ij} L_{ij}^d}{M_{mn} M_{mn}}. \quad (\text{B.29})$$

In order to simplify the methodology, the utilization of the least squares method for the minimization of the error was suggested. Under this formulation the minimization of the error yields an expression for C_D

$$\frac{\partial E_{ij} E_{ij}}{\partial C_D} = 0. \quad (\text{B.30})$$

B.1.3.2 Isotropic part

In an analogous way, the isotropic part of the identity (B.22) is obtained. The isotropic sub-grid and sub-test stress tensor were modeled *Eddy-viscosity-eddy-diffusivity* model

$$T_{ii} = C_I \widehat{\Delta^2} \left\| \hat{\bar{D}}_D \right\|^2, \quad (\text{B.31})$$

$$\vartheta_{ii} = C_I \Delta^2 \left\| \bar{D}_D \right\|^2. \quad (\text{B.32})$$

Thus, the ensemble

$$M_{ii} = C_I \widehat{\Delta^2} \left\| \hat{\bar{D}}_D \right\|^2 - C_I \Delta^2 \left\| \bar{D}_D \right\|^2. \quad (\text{B.33})$$

The isotropic part of tensor L is represented by

$$L_{ii} = \widehat{\bar{u}_i \bar{u}_i} - \hat{\bar{u}}_i \hat{\bar{u}}_i. \quad (\text{B.34})$$

And by analogy with (B.29), the coefficient C_I is

$$C_I = \frac{L_{ii}}{\widehat{\Delta^2} \left\| \hat{\bar{D}}_D \right\|^2 - \Delta^2 \left\| \bar{D}_D \right\|^2}. \quad (\text{B.35})$$

B.1.4 Realizability conditions

B.1.4.1 Relation C_D to C_I

Vreman (1995) demonstrated that the turbulent stress tensor is semi-definite positive. This has several implications that can be summarized in the three following conditions,

$$\tau_{ii} \geq 0, \quad (\text{B.36})$$

$$|\tau_{ij}| \leq \sqrt{\tau_{ii}\tau_{jj}}, \quad (\text{B.37})$$

$$\det(\tau_{ij}) \geq 0. \quad (\text{B.38})$$

Additionally, the stress tensor remains positive semi-definite, if and only if, the Kernel of the filter remains positive. This implies that the computational grid could be considered as an implicit positive semi-definite filter. The test filter, defined explicitly in equation (B.16), is also of this kind. Therefore, the models for the tensor τ verify equations (B.36) to (B.38).

This has implication and significance for the constants of the models, C_D and C_I . Concretely, they must fulfill the conditions imposed by the formulas (B.36) - (B.38). The condition (B.37) implies that

$$\tau_{12}^2 + \tau_{13}^2 + \tau_{23}^2 \leq \tau_{11}\tau_{22} + \tau_{11}\tau_{33} + \tau_{22}\tau_{33}. \quad (\text{B.39})$$

Substituting equation (B.12) in (B.39) it is obtained that

$$\mu_t^2(D_{D12}^2 + D_{D13}^2 + D_{D23}^2) \leq \mu_t^2(D_{D11}D_{D22} + D_{D11}D_{D33} + D_{D22}D_{D33}) + \frac{4}{3}k^2. \quad (\text{B.40})$$

Then,

$$\begin{aligned}
& D_{D\ 11} D_{D\ 22} + D_{D\ 11} D_{D\ 33} + D_{D\ 22} D_{D\ 33} = \\
& = \frac{1}{2} (D_{D\ 11} + D_{D\ 22} + D_{D\ 33})^2 - \\
& \quad - \frac{1}{2} (D_{D\ 11}^2 + D_{D\ 22}^2 + D_{D\ 33}^2) \\
& = -\frac{1}{2} (D_{D\ 11}^2 + D_{D\ 22}^2 + D_{D\ 33}^2), \tag{B.41}
\end{aligned}$$

which in turn

$$\rho k \geq \frac{1}{2} \frac{\sqrt{3}}{\sqrt{2}} \mu_t \|D\|, \tag{B.42}$$

$$C_I \Delta \|\tilde{D}_D\|^2 \geq \bar{\rho} C_d \Delta^2 \|\tilde{D}_D\| \|\tilde{D}_D\|, \tag{B.43}$$

$$C_I \geq \frac{1}{2} \sqrt{\frac{3}{2}} C_D. \tag{B.44}$$

$$\tag{B.45}$$

This provides the area of validity for the values of the constants.

B.1.4.2 Values of the constants

The values of the constants C_D and C_I are calculated with equations (B.35) and (B.29) if the *Dynamic* model is selected. They must be obtained from the literature, from own DNS calculations or from comparison with experiments, etc, if the *Eddy-viscosity-eddy-diffusivity* or the *Mixed* models are selected. The inequality (B.44) provides, in any case, a necessary boundary to any estimation or calculation. Some values for the coefficients, which were found in the literature, are listed in Table B.1.

Procedure and/or Source	C_D	C_I
Erlebacher et al. (1990) Fureby (1996)	0.0122	0.0066
Kolmogorov Spectrum (Garnier et al., 2009)	0.022	-
Eddy Damped Quasi Normal Markovian (Lesieur, 1997)	0.014	-
RNG (Yakhot and Orszag, 1986)	0.0062	-
Zang (Zang et al., 1992)	0.092	0.066-0.0066

Table B.1: C_D and C_I Coefficients for the Eddy-Viscosity-Eddy-Diffusivity models.

For practical simulations, and based on numerical experiments, it is convenient, following Vreman (1995), to assign the value to C_I of

$$C_I = 2C_D. \quad (\text{B.46})$$

B.1.5 Stability constraints

In order to make the calculation stable and avoid numerical artifacts, the value of the constants should be limited and its variation controlled. This is necessary if the dynamic model is utilized where the constants can take different values and change in any instant. Following Sagaut (2001) a constraint for the C_D in practical calculations could be the value given for C_D by Smagorinsky and which is considered too dissipative. This yields the criteria,

$$C_D \leq C_{smag} \approx 0.2^2. \quad (\text{B.47})$$

Frölich (2005) suggests a different limitation. The value of the turbulent viscosity must remain in a range $[\nu, n \nu]$, being 'n' a multiple of the kinematic viscosity. If this approach is adopted, the constant C_D must fulfill the inequality,

$$C_D \leq n \frac{\nu}{\Delta^2 \|\tilde{D}_D\|}. \quad (\text{B.48})$$

Alternatively, Frölich (2006) suggests a time relaxation method so that the values of the C_D coefficient will not oscillate strongly between consecutive time steps.

This method was originally implemented by Breuer and Rodi (1994) and is formalized as

$$C^{n+1} = \epsilon_r C + (1 - \epsilon_r) C^n \quad (\text{B.49})$$

where ϵ_r is a small parameter. For the constant C_I , if the assumption $C_I = 2C_D$ is adopted, its values are already determined.

Lower bounds could be easily defined taking into account just taking into account the positivity of the viscosity $\nu + \nu_t \geq 0$ which is simply translated into the formulation of the *Eddy-viscosity-eddy-diffusivity* considering 0 for C_D and C_I .

B.2 Modeling the S_{2ij} tensor

The tensor S_{2ij} is recognized as negligible for high Reynolds flows in non-reactive conditions, as was discussed by Vreman (1995) and Luo (2001). It is not necessarily like that in reactive flows where the dependence of S_{2ij} on the viscosity indirectly introduces a dependence of S_{2ij} on temperature. The dependence of μ on the temperature can be approximated by the Sunderland law

$$\mu(T) = \mu(T_0) \left(\frac{T}{T_0} \right)^{\frac{3}{2}} \frac{T_0 + T_1}{T + T_1},$$

with $T_1 \approx 110 \text{ K}$, see e.g. (Chapman and Cowling, 1990). In a first approach this equation can be considered like $\mu(T) \sim T^{0.76}$. In the praxis it means an increase of six times in the values of the dynamic viscosity between products and reactants.

Recalling the definition of tensor S_2 , its dependence on temperature can be obtained to be

$$\begin{aligned} S_2 &= \partial_j \left(\frac{1}{\mu(\tilde{T})} (\overline{\sigma_{ij}} - \check{\sigma}_{ij}) \right) = \partial_j \left(\frac{\mu(T)}{\mu(\tilde{T})} S(u) - S(\tilde{u}) \right) = \\ &= \partial_j \left(\left(\frac{T}{\tilde{T}} \right)^{0.76} S(u) - S(\tilde{u}) \right). \end{aligned} \quad (\text{B.50})$$

The equation (B.50) confirms that for non-reactive mixtures $T \approx \tilde{T}$ the tensor

$S_2 \approx 0$. Also, that as stated by (Luo, 1999, 2001) the tensor S_2 no longer approaches zero for reacting flows. For the reactive mixtures, no reliable model of S_2 is nowadays available.

Nevertheless, S_2 was compared with S_1 by Vreman (1995) and the results obtained show that S_2 remains several orders of magnitude smaller than S_1 . If now we examine (B.50), we will find out that even if the tensor will be an order of magnitude bigger than in non-reactive case, it will remain small compared with S_1 , a circumstance that justifies its neglect.

B.3 Modeling the α_3 term

Recalling the definition of α_3

$$\alpha_3 = \tilde{u}_i \frac{\partial \bar{\rho} \tau_{ij}}{\partial x_j}, \quad (\text{B.51})$$

the tensor τ is already modeled in sections B.1.1, B.1.2 and B.1.3. The use of one of any of the formulations completely closes equation (B.51).

B.4 Modeling the α_4 & α_5 terms

The terms α_3, α_4 must be modeled to take into account the sub-grid-scale heat flux. Following the Eidson (1985) hypothesis ¹, the energy transfer from the resolved scales to the sub-grid scales is proportional to the gradient of the resolved temperature.

B.4.1 Eddy viscosity, eddy diffusivity

Assuming the Eison hypothesis and neglecting the *Cross* terms (A.3), the eddy diffusivity type formula,

$$\alpha_{4ij} + \alpha_{5ij} = \frac{-\partial}{\partial x_i} \left(\frac{c_p \bar{\rho} \nu_t}{\text{Pr}_t} \frac{\partial \tilde{T}}{\partial x_i} \right), \quad (\text{B.52})$$

¹Eidson (1985) was trying to close the term \widetilde{uT} and called his approach *eddy conductivity*.

is obtained, where c_p is the heat at constant pressure and ν_t and Pr_t the turbulent kinematic viscosity and Prandtl number respectively. The ratio ν_t/Pr_t represents the turbulent thermal diffusivity χ_t . Equation (B.52) establishes an analogy with the heat flux term, in equation (1.7), but utilizing turbulent magnitudes.

B.4.2 Mixed model

The methodology used in the equations (B.1), (B.2) to close the S_1 tensor has been utilized to model the α_4 & α_5 terms. The scale similarity approach has been applied to the Cross terms (Bardina et al., 1983) while Reynolds part has been modeled with the eddy-diffusivity model. The result of the application of the methodology is

$$\alpha_{4ij} + \alpha_{5ij} = \frac{1}{(\gamma-1)} \frac{\partial \widetilde{\tilde{p}} \tilde{u}_j}{\partial x_j} + \widetilde{\tilde{p}} \frac{\partial \tilde{u}_j}{\partial x_i} - \left(\frac{1}{(\gamma-1)} \frac{\partial \tilde{\tilde{p}} \tilde{u}_j}{\partial x_j} + \tilde{\tilde{p}} \frac{\partial \tilde{u}_j}{\partial x_i} \right) - \frac{\partial}{\partial x_i} \left(\frac{c_p \bar{\rho} \nu_{sgs}}{Pr_{sgs}} \frac{\partial \tilde{T}}{\partial x_i} \right). \quad (B.53)$$

B.4.3 Dynamic eddy-viscosity model

The approach used in the paragraph B.1.3 has been again employed for modeling the ensemble α_4 & α_5 . The eddy diffusivity model,

$$\alpha_{4ij} + \alpha_{5ij} = \frac{-\partial}{\partial x_i} \left(\bar{\rho} c_p \chi_{sgs} \frac{\partial \tilde{T}}{\partial x_i} \right), \quad (B.54)$$

with the sub grid thermal conductivity

$$\chi_{sgs} = C_h \cdot \Delta^2 \|D_D\|, \quad (B.55)$$

has been introduced in the Germano identity, eq. (B.15) modified to take into account the adequate variables, and strongly simplifies for scalars to $L = C_h M$. Contrary to other authors, e.g. Erlebacher et al. (1990), the Vreman (1995) system as formulation for the large eddy simulation implies the modeling, and inclusion in

the L variable, of the α_4 and α_5 tensors together. By definition, the L variable is then

$$L = \frac{\partial}{\partial x_i} \left(\frac{\widehat{\bar{\rho} R_{gas}}}{\gamma - 1} \tilde{u}_i \tilde{T} - \frac{\widehat{\bar{\rho}} R_{gas}}{\gamma - 1} \tilde{T} \tilde{u}_i \right) + \widehat{\bar{\rho} R_{gas} T} \partial_i \cdot \tilde{u}_i - \widehat{\bar{\rho}} R_{gas} \tilde{T} \partial_i \tilde{u}_i, \quad (B.56)$$

and M is

$$M = \frac{\partial}{\partial x_i} c_p \left(\bar{\rho} \Delta^2 \|\tilde{D}_D\| \partial_i \tilde{T} - \widehat{\bar{\rho}} \Delta^2 \|\tilde{D}_D\| \partial_i \tilde{T} \right). \quad (B.57)$$

Applying the least squares method of Lilly (Lilly, 1992), the solution for the model constant is obtained,

$$C_h = \frac{L \cdot M}{M \cdot M}. \quad (B.58)$$

B.4.3.1 Stability constrains

As already occurred for the constants C_D and C_I , Section B.1.5, the values of the coefficient C_h should be limited in order to make the calculation numerically stable. The methods described in section B.1.5 are also applicable for the limitation of C_h . In his formulation, Frölich (2005) suggests a limitation in the value C_h so that the turbulent thermal conductivity remains in a range $[\chi, n\chi]$ where n is multiple of the molecular conductivity. The C_h constant would be then bounded by

$$C_h \leq n \frac{\chi}{\Delta^2 \|\tilde{D}_D\|}. \quad (B.59)$$

To prevent that C_h would oscillate significantly between consecutive time steps, causing numerical instability, the relaxation method suggested in equation (B.49) could be employed. An interesting alternative proposed by Vreman (1995) is to calculate² C_h integrating over the whole calculation domain. The expression

$$C_h = \frac{\iiint L \cdot M dx^3}{\iiint M^2 dx^3}, \quad (B.60)$$

is then resulting.

²Vreman calculates directly the Turbulent Prandtl number

An interesting and alternative model for α_5 exclusively has been suggested by Vreman (1994) for the modeling of sub-grid pressure dilatation alone. According to his analysis, α_5 can be modeled utilizing the scale similarity approach. Under this assumption, the model reads

$$\alpha_5 = C_\pi \left(\overline{\bar{p} \partial_j \tilde{u}_j} - \bar{\bar{p}} \partial_j \tilde{u}_j \right), \quad (\text{B.61})$$

and the C_π constant takes the value

$$C_\pi \approx 2.2. \quad (\text{B.62})$$

B.5 Modeling the term α_6

The sub-grid turbulent dissipation rate was modeled by Goshal et al. (1995) in an attempt to provide full modeling for the sub-grid kinetic energy. In his formulation, the dissipation rate can be determined through

$$\alpha_6 = C_\epsilon \bar{\rho} \frac{k_{sgs}^{\frac{3}{2}}}{\Delta}, \quad (\text{B.63})$$

where the constant C_ϵ is susceptible of dynamic modeling. Two methods are available in the literature for the evaluation of C_ϵ . The original modeling of Goshal et al. (1995) is based on the solution of a variational problem for the sub-grid kinetic energy equation. A simplification of the complex procedure which resulted was carried out by Vreman (1995). The new methodology is based on the global balance of the terms in an integrated equation for the sub-grid kinetic energy. This allowed him to express the dynamic constant as a time dependent value which results in

$$C_\epsilon(t) = \frac{\iiint \left(\alpha_4 + \alpha_5 - \frac{\partial \bar{\rho} k}{\partial t} \right) dV}{\iiint \left(\frac{\bar{\rho} k^{\frac{3}{2}}}{\Delta} \right) dV}. \quad (\text{B.64})$$

Alternatively, the scale similarity approach could also be used (Cook and Riley, 1998). Under this assumption, a model can be formulated to provide finally

$$\alpha_6 = C_1 \left(\widehat{\tilde{\sigma}_{ij} \partial_j \tilde{u}_i} - \tilde{\sigma}_{ij} \partial_j \tilde{u}_i \right), \quad (\text{B.65})$$

where C_1 is a constant which value has been reported (Vreman, 1994) and (Cook and Riley, 1998) to be $C_1 \approx 8$.

B.6 Modeling the terms α_7 & α_8

The sub-grid heat conduction and the viscous stress non-linearities were found to be negligible in non-reactive flows. They have been neglected in the simulations carried out by Fureby and Vreman, reported in (Fureby, 1996), (Vreman, 1995) & (Vreman, 1994). Vreman (1995), evaluates them and discovers they were negligible, several orders of magnitude smaller than other modeled terms in the equations in non-reacting flows.

The term α_7 was found to be of importance in reactive flows by Avital and Luo (1999). The necessity of the modeling of this tensor is based on similar reasons as the ones that motivate the modeling of the Sub-grid viscous stress (see B.2).

From the definition of the heat flux (A.49) and of the Sunderland law, in first approach,

$$q = -\lambda \nabla T = \chi \rho C_p \nabla T \approx \mu C_p \nabla T \approx \mu(\tilde{T}) \left(\frac{T}{\tilde{T}} \right)^{0.76} C_p \nabla T. \quad (\text{B.66})$$

Thus,

$$\overline{q} - \hat{q} = \mu(\tilde{T}) \left(\frac{T}{\tilde{T}} \right)^{0.76} C_p (T) \nabla T - \mu(\tilde{T}) C_p(\tilde{T}) \nabla \tilde{T}. \quad (\text{B.67})$$

For the case of H_2 reacting mixtures, the term $(T/\tilde{T})^{0.76}$ can reach values of 3, which supports the statements of Luo about the necessity of modeling. Pitifully, no reliable simulation method is nowadays available for this term.

The viscous stress non-linearities, represented by α_8 , are poorly understood.

For non-reactive flows, e.g. (Vreman, 1995), α_8 has been evaluated by comparison with DNS data and it was found out to be small compared to other terms modeled. For the reacting mixtures, no investigation on the behavior and relevance of this term has been found to be available. Therefore no modeling has been provided for this term.

Appendix C

DERIVATION OF THE ACOUSTIC- PARAMETRIC INSTABILITY EQUATION DESCRIBING THE GROWTH RATE

C.1 General

The stability of a flame front with an arbitrary Lewis number and with transports coefficients varying with temperature has been studied in numerous investigations. Among others it is necessary to cite the work performed by Pelce and Clavin (1982) who obtained an equation for a perturbed flame front in a gravitational field

under the assumptions of high activation energy and large scale wrinkling. In their excellent review, Bychkov and Liberman (2000) recover this formulation to analyze the stability of flames and provide a generalized expression to study the hydrodynamic instabilities.

The purpose of this annex is to obtain the equations appearing in (Bychkov and Liberman, 2000) that because of misprints, errors, over-simplifications, etc. do not provide satisfactory results. In a second part, the general results are particularized to obtain the formulation necessary for the modeling of the Acoustic and Parametric instabilities.

As a starting point, the equations appearing in (Searby and Rochwerger, 1991) have been utilized. They have been made dimensionless with the length $\delta = \chi/S_L$ and time $\tau = \delta/S_L$ scales. In this chapter the notation of Searby and Rochwerger (1991) or Bychkov and Liberman (2000) is indistinctly used. Following Searby and Rochwerger (1991) the stability problem could be studied analyzing the negative solutions of,

$$A\tilde{\sigma}^2 + B\tilde{\sigma} + C = 0, \quad (\text{C.1})$$

in which $\tilde{\sigma}$ is the dimensionless growth rate.

The basic variables in dimensionless form are

$$A = 2 - \gamma_g + \gamma_g \tilde{\kappa} \left(Ma - \frac{J}{\gamma_g} \right), \quad (\text{C.2})$$

$$B = 2\tilde{\kappa} + \frac{2}{1 - \gamma_g} \tilde{\kappa}^2 (Ma - J), \quad (\text{C.3})$$

$$C = \frac{\gamma_g}{Fr} \tilde{\kappa} - \frac{\gamma_g}{1 - \gamma_g} \tilde{\kappa}^2 \left(1 + \frac{1 - \gamma_g}{Fr} \left(Ma - \frac{J}{\gamma_g} \right) \right) + \frac{\gamma_g}{1 - \gamma_g} \tilde{\kappa}^3 \left(h_b + (2 + \gamma_g) \frac{Ma}{\gamma_g} - \frac{2J}{\gamma_g} + (2Pr - 1)H \right), \quad (\text{C.4})$$

where $\gamma_g = (\rho_u - \rho_b)/\rho_u = 1 - 1/\theta$, $\vartheta = (T - T_u)/(T_b - T_u)$, $Le = \chi/D$ the Lewis number, Pr the Prandtl number, $Fr^{-1} = g\delta/S_L^2$ the Froude number, g the acceleration of the gravity and S_L the laminar flame speed. The additional definitions complete

the description of the previous equations,

$$H = \int_0^1 (h_b - h(\vartheta)) d\vartheta, \quad (C.5)$$

$$J = \frac{\gamma_g}{1-\gamma_g} \int_0^1 \frac{h(\vartheta)}{1+\vartheta\gamma_g/(1-\gamma_g)} d\vartheta, \quad (C.6)$$

$$Ma = \frac{J}{\gamma_g} - \frac{1}{2}\beta(Le-1) \int_0^1 \frac{h(\vartheta) \ln(\vartheta)}{1+\vartheta\gamma_g/(1-\gamma_g)} d\vartheta \quad (C.7)$$

where (Searby and Clavin, 1986),

$$h(\vartheta) = \frac{\lambda(\vartheta)C_{p_u}}{\lambda_u C_p(\vartheta)} = \frac{\rho(\vartheta)\chi(\vartheta)}{\rho_u \chi_u}.$$

In the derivation θ represents the expansion ratio.

Let us now try to understand the divergences between the formulations in (Searby and Rochwerger, 1991) and in (Bychkov and Liberman, 2000). To do so we will make the coefficients A , B , C dimensional. In the following pages, we denote with the sub-index Byc the variables as they appear in (Bychkov and Liberman, 2000).

The coefficient A can be transformed to

$$\begin{aligned} A &= 2 - \gamma_g + \gamma_g \tilde{\kappa} \left(Ma - \frac{J}{\gamma_g} \right) = \{ \tilde{\kappa} = \kappa \delta \} \\ &= 2 - \frac{\theta-1}{\theta} + \frac{\theta-1}{\theta} \kappa \delta \left(Ma - \frac{\theta}{\theta-1} J \right) = \\ &= \frac{\theta+1}{\theta} + \frac{\theta-1}{\theta} \kappa \delta \left(Ma - \frac{\theta}{\theta-1} J \right) = \\ &= \frac{\theta+1}{\theta} \left(1 + \frac{\theta-1}{\theta+1} \kappa \delta \left(Ma - \frac{\theta}{\theta-1} J \right) \right) = \end{aligned} \quad (C.8)$$

$$= \frac{\theta+1}{\theta} A_{Byc}. \quad (C.9)$$

Analogous treatment for the coefficient B yields

$$\begin{aligned} B &= 2\tilde{\kappa} + \frac{2}{1-\gamma_g} \tilde{\kappa}^2 (Ma - J) = \kappa\delta (2 + 2\theta\kappa\delta(Ma - J)) = \\ &= \kappa\delta \left(\frac{\theta+1}{\theta} \right) \left(\frac{2\theta}{\theta+1} (1 + \theta\kappa\delta(Ma - J)) \right) = \kappa\delta \left(\frac{\theta+1}{\theta} \right) B_{Byc}. \end{aligned} \quad (C.10)$$

The term C in the equation (C.4) can be split into two terms C_1 and C_2 . The first one contains the terms dependent of the Fr number, or in dimensional flavor, the acceleration, and C_2 will embody the remaining variables. Therefore,

$$C_1 = \frac{1}{Fr} \left(\gamma_g \tilde{\kappa} - \gamma_g \tilde{\kappa}^2 \left(Ma - \frac{J}{\gamma_g} \right) \right), \quad (C.11)$$

$$C_2 = \frac{\gamma_g}{1-\gamma_g} \tilde{\kappa}^2 \left(-1 + \tilde{\kappa} \left(h_b + (2 + \gamma_g) \frac{Ma}{\gamma_g} - \frac{2J}{\gamma_g} + (2Pr - 1)H \right) \right). \quad (C.12)$$

For the term C_1 transformation to dimensional notation yields

$$\begin{aligned} C_1 &= \frac{1}{Fr} \left(\gamma_g \tilde{\kappa} - \gamma_g \tilde{\kappa}^2 \left(Ma - \frac{J}{\gamma_g} \right) \right) = \\ &= \tilde{\kappa} \frac{\gamma_g}{Fr} \left(1 - \tilde{\kappa} \left(Ma - \frac{J}{\gamma_g} \right) \right) = \left\{ \gamma_g = \frac{\theta-1}{\theta}; \tilde{\kappa} = \kappa\delta \right\} = \\ &= \frac{\kappa\delta}{Fr} \frac{\theta-1}{\theta} \left(1 - \kappa\delta \left(Ma - \frac{J\theta}{\theta-1} \right) \right) = \\ &= \frac{\kappa\delta}{Fr} \frac{\theta+1}{\theta} \frac{\theta}{\theta+1} \frac{\theta-1}{\theta} \left(1 - \kappa\delta \left(Ma - \frac{J\theta}{\theta-1} \right) \right) = \\ &= \frac{\kappa\delta}{Fr} \frac{\theta+1}{\theta} \left(\frac{\theta-1}{\theta+1} \left(1 - \kappa\delta \left(Ma - \frac{J\theta}{\theta-1} \right) \right) \right) = \\ &= \frac{\kappa\delta}{Fr} \frac{\theta+1}{\theta} C_{1Byc}, \end{aligned} \quad (C.13)$$

while for the term C_2 , the same procedure leads to

$$\begin{aligned}
C_2 &= \frac{\gamma_g}{1-\gamma_g} \tilde{\kappa}^2 \left(-1 + \tilde{\kappa} \left(h_b + (2 + \gamma_g) \frac{Ma}{\gamma_g} - \frac{2J}{\gamma_g} + (2Pr - 1)H \right) \right) = \\
&= \left\{ \frac{\gamma_g}{\gamma_g - 1} = \theta - 1; \gamma_g = \frac{\theta - 1}{\theta}; \tilde{\kappa} = \kappa \delta \right\} = \\
&= \kappa^2 \delta^2 (\theta - 1) \left(-1 + \kappa \delta \left(h_b + \frac{3\theta - 1}{\theta - 1} Ma - \frac{2J\theta}{\theta - 1} + (2Pr - 1)H \right) \right) = \\
&= \kappa^2 \delta^2 \frac{\theta + 1}{\theta} \left(\theta \frac{\theta - 1}{\theta + 1} \left(-1 + \frac{\kappa \delta}{\theta - 1} (h_b(\theta - 1) + (3\theta - 1)Ma - 2J\theta + (2Pr - 1)(\theta - 1)H) \right) \right).
\end{aligned} \tag{C.14}$$

For H ,

$$H = \int_0^1 (h_b - h(\vartheta)) d\vartheta = h_b - \int_0^1 h(\vartheta) d\vartheta = h_b - I. \tag{C.15}$$

which in turn allows expanding

$$\begin{aligned}
(\theta - 1)((2Pr - 1)H) &= \\
&= (\theta - 1)((2Pr - 1)(h_b - I)) = \\
&= (\theta - 1)(2Prh_b - h_b - 2PrI + I) = \\
&= (\theta - 1)(2Prh_b - 2PrI + I - h_b) = \\
&= 2Prh_b(\theta - 1) - I(\theta - 1)(2Pr - 1) - (\theta - 1)h_b.
\end{aligned} \tag{C.16}$$

And,

$$\begin{aligned}
C_2 &= \kappa^2 \delta^2 \frac{\theta + 1}{\theta} \\
&\left(\theta \frac{\theta - 1}{\theta + 1} \left(-1 + \frac{\kappa \delta}{\theta - 1} ((3\theta - 1)Ma - 2J\theta + 2Pr h_b(\theta - 1) - I(\theta - 1)(2Pr - 1)) \right) \right) = \\
&= \left\{ J_3 = (\theta - 1)I \Rightarrow J_3 = (\theta - 1) \int_0^1 h(\vartheta) d\vartheta \right\} = \\
&= \kappa^2 \delta^2 \frac{\theta + 1}{\theta} \\
&\left(\theta \frac{\theta - 1}{\theta + 1} \left(-1 + \frac{\kappa \delta}{\theta - 1} ((3\theta - 1)Ma - 2J\theta + 2Pr h_b(\theta - 1) - J_3(2Pr - 1)) \right) \right) = \\
&= \kappa^2 \delta^2 \frac{\theta + 1}{\theta} C_{2Byc}. \tag{C.17}
\end{aligned}$$

The integral of J can be then changed to

$$\begin{aligned}
J &= \frac{\gamma_g}{1 - \gamma_g} \int_0^1 \frac{h(\vartheta)}{1 + \vartheta \gamma_g / (1 - \gamma_g)} d\vartheta = \\
&= (\theta - 1) \int_0^1 \frac{h(\vartheta)}{1 + \vartheta(\theta - 1)} d\vartheta = \{h(\vartheta) = h(T)\} = \\
&= (\theta - 1) \int_{T_u}^{T_b} \frac{h(T)}{(T_b - T_u) + (\theta - 1)(T - T_u)} dT, \tag{C.18}
\end{aligned}$$

where $h(\vartheta) = \frac{\rho \chi}{\rho_u \chi_u}$.

If the formula 2.8 of Bychkov and Liberman (2000), it was assumed a perfect gas at constant pressure transformation

$$\rho T = \rho_u T_u, \tag{C.19}$$

that also involved no change of molar mass and heat capacity. For the flows in

which this is valid, $\frac{\rho_u}{\rho_b} = \frac{T_b}{T_u} = \theta$. Then

$$\begin{aligned}
 J &= (\theta - 1) \int_{T_u}^{T_b} \frac{h(T)}{(T_b - T_u) + (\theta - 1)(T - T_u)} dT = \\
 &= (\theta - 1) \int_{T_u}^{T_b} \frac{h(T)}{(\theta - 1) + (\theta - 1)(T - T_u)} \frac{dT}{T_u} = \\
 &= \int_{T_u}^{T_b} \frac{h(T)}{1 + T/T_u - 1} \frac{dT}{T_u} = \int_{T_u}^{T_b} h(T) \frac{dT}{T} = J_{2Byc} \quad (C.20)
 \end{aligned}$$

which appears in Bychkov and Liberman (2000) as eq. 3.70. Nevertheless, for perfect gases

$$p = \frac{\gamma - 1}{\gamma} c_p \rho T, \quad (C.21)$$

so that the equation (C.19) is in general

$$\frac{\gamma_b - 1}{\gamma_b} c_{p_b} \rho_b T_b = \frac{\gamma_u - 1}{\gamma_u} c_{p_u} \rho_u T_u, \quad (C.22)$$

and the expansion ratio

$$\theta = \frac{\rho_u}{\rho_b} = \frac{(\gamma_b - 1)\gamma_u c_{p_b} T_b}{(\gamma_u - 1)\gamma_b c_{p_u} T_u}. \quad (C.23)$$

The approximation in equation (C.19) requires that $\gamma_u = \gamma_b$ and that $c_{p_b} = c_{p_u}$. This is not acceptable in realistic simulations of hydrogen air mixtures. Probably, the only domain in which this approximation would be acceptable would be highly steam diluted mixtures.

The derivations performed and contained in the equations (C.9), (C.10), (C.13) and (C.17) can be inserted in equation (C.1)

$$\frac{\theta + 1}{\theta} \left(A_{Byc} \tilde{\sigma}^2 + \kappa \delta B_{Byc} \tilde{\sigma} + \frac{\kappa \delta}{Fr} C_{1Byc} + \kappa^2 \delta^2 C_{2Byc} \right) = 0, \quad (C.24)$$

which introducing the Froude number $Fr^{-1} = g\delta/S_L^2$ can be transformed into

$$S_L^2 A_{Byc} \tilde{\sigma}^2 + S_L^2 \kappa \delta B_{Byc} \tilde{\sigma} + \kappa \delta g \delta C_{1Byc} + S_L^2 \kappa^2 \delta^2 C_{2Byc} = 0. \quad (C.25)$$

But the growth rate $\tilde{\sigma}$ is also non-dimensional. Transforming it, $\tilde{\sigma} = \sigma \tau = \sigma \cdot \delta / S_L$.

So that

$$S_L^2 A_{Byc} \frac{\delta^2}{S_L^2} \sigma^2 + S_L^2 \kappa \delta B_{Byc} \frac{\delta}{S_L} \sigma + \kappa \delta g \delta C_{1Byc} + S_L^2 \kappa^2 \delta^2 C_{2Byc} = 0, \quad (C.26)$$

which simplifies to

$$A_{Byc} \sigma^2 + S_L \kappa B_{Byc} \sigma + \kappa g C_{1Byc} + S_L^2 \kappa^2 C_{2Byc} = 0. \quad (C.27)$$

This equation is very similar to the equation (3.73) appearing in Bychkov and Liberman (2000). The difference, third term appears negative in the reference, can be made up for considering a different direction of the acceleration. The coefficient C_{2Byc} has opposite sign in our derivation, and therefore signs agree.

C.2 Acoustic instability

Equation (C.27) can be written in differential formulation considering that the flame front is going to be represented by the function $F(x, t) = 0$. Small perturbations could be considered in the surface of the flame utilizing the formulation $F(x, t) = F_0 \exp(\sigma t + i\kappa x)$. Deriving, it is obtained that

$$A_{Byc} \frac{d^2 F}{dt^2} + S_L \kappa B_{Byc} \frac{dF}{dt} + \kappa g C_{1Byc} F + S_L^2 \kappa^2 C_{2Byc} F = 0. \quad (C.28)$$

The acceleration g could be decomposed in a constant and an oscillatory part $g = g_a - \omega_{ac} U_a \cos(\omega_{ac} t)$ to study the case of acoustic waves instability.

In the formulation adopted the acoustic waves will be monochromatic with a

circular frequency ω_{ac} and their velocity will have an amplitude U_a . Substituting

$$A \frac{d^2 F}{dt^2} + S_L \kappa B \frac{dF}{dt} + \kappa g_a C_1 F - \kappa \omega_{ac} U_a \cos(\omega_{ac} t) C_1 F + S_L^2 \kappa^2 C_2 F = 0. \quad (C.29)$$

Utilizing the hypothesis of scale separation, a solution of this previous equation can be sought considering F as the sum of a constant and an oscillatory component, $F = F_1(t) + F_2 \cos(\omega_{ac} t)$ representative of slow and fast motion. Substituting,

$$\begin{aligned} A \frac{d^2 F_1}{dt^2} + S_L \kappa B \frac{dF_1}{dt} + \kappa g_a C_1 F_1 - \kappa \omega_{ac} U_a \cos(\omega_{ac} t) C_1 F_1 + S_L^2 \kappa^2 C_2 F_1 - \\ - A F_2 \omega_{ac}^2 \cos(\omega_{ac} t) - B S_L \kappa F_2 \omega_{ac} \sin(\omega_{ac} t) + \\ + (C_1 g_a \kappa + C_2 S_L^2 \kappa^2) F_2 \cos(\omega_{ac} t) - C_1 \omega_{ac} U_a \kappa \cos^2(\omega_{ac} t) F_2 = 0. \end{aligned} \quad (C.30)$$

If the trigonometric formula $\cos^2(\omega_{ac} t) = (1 + \cos(2\omega_{ac} t))/2$ is recalled then,

$$\begin{aligned} A \frac{d^2 F_1}{dt^2} + S_L \kappa B \frac{dF_1}{dt} + \kappa g_a C_1 F_1 - \kappa \omega_{ac} U_a \cos(\omega_{ac} t) C_1 F_1 + S_L^2 \kappa^2 C_2 F_1 - \\ - A F_2 \omega_{ac}^2 \cos(\omega_{ac} t) - B S_L \kappa F_2 \omega_{ac} \sin(\omega_{ac} t) + (C_1 g_a \kappa + C_2 S_L^2 \kappa^2) F_2 \cos(\omega_{ac} t) - \\ - \frac{1}{2} C_1 \omega_{ac} U_a \kappa F_2 - \frac{1}{2} C_1 \omega_{ac} U_a \kappa \cos(2\omega_{ac} t) F_2 = 0. \end{aligned} \quad (C.31)$$

It is possible to decompose equation (C.31) into its cosine part, sine and independent terms. This yields respectively,

$$-\kappa \omega_{ac} U_a C_1 F_1 - A F_2 \omega_{ac}^2 + (C_1 g_a \kappa + C_2 S_L^2 \kappa^2) F_2 = 0, \quad (C.32)$$

$$-B S_L \kappa \omega_{ac} F_2 = 0, \quad (C.33)$$

$$\begin{aligned} A \frac{d^2 F_1}{dt^2} + B S_L \kappa \frac{dF_1}{dt} + C_1 \kappa g_a F_1 + \\ + C_2 S_L^2 \kappa^2 F_1 - \frac{1}{2} C_1 \omega_{ac} U_a \kappa F_2 = 0. \end{aligned} \quad (C.34)$$

The condition to be able to ignore the terms in $\cos(2\omega_{ac} t)$, responsible of low-high frequencies interaction, is that their relative amplitude is negligible compared to

others modes. This provides, in the assumption of scale separation, a very significant simplification. The requisite to be able to neglect the terms in $\cos 2\omega_{ac} t$ in eq. (C.31) is that $\left| \frac{C_1 U_a \kappa}{2A\omega_{ac}} \right| \ll 1$.

Considering only the high perturbation frequencies $\left| \frac{C_2 S_L^2 \kappa^2}{A\omega_{ac}^2} \right| \ll 1$, $\left| \frac{C_1 g_a \kappa}{A\omega_{ac}^2} \right| \ll 1$, equation (C.32) simplifies to

$$-\kappa \omega_{ac} U_a C_1 F_1 - A F_2 \omega_{ac}^2 = 0. \quad (C.35)$$

Which allows finding F_2 ,

$$F_2 = -\frac{\kappa U_a C_1 F_1}{A\omega_{ac}}. \quad (C.36)$$

Introducing eq. (C.36) in the equation (C.35)

$$\begin{aligned} A \frac{d^2 F_1}{dt^2} + B S_L \kappa \frac{dF_1}{dt} + C_1 \kappa g_a F_1 + \\ + C_2 S_L^2 \kappa^2 F_1 + \frac{C_1^2 U_a^2 \kappa^2}{2A} F_1 = 0. \end{aligned} \quad (C.37)$$

This relation can be expressed in terms of growth rate just utilizing the relation $F(x, t) = F_0 \exp(\sigma t + i\kappa x)$ and deriving. Substituting,

$$A\sigma^2 + B S_L \kappa \sigma + C_1 \kappa g_a + C_2 S_L^2 \kappa^2 + \frac{C_1^2 U_a^2 \kappa^2}{2A} = 0, \quad (C.38)$$

which is a second order equation. Solving σ , it is directly obtained that

$$\sigma = \frac{-B S_L \kappa}{2A} \pm \sqrt{\frac{(B S_L \kappa)^2}{4A^2} - \frac{1}{A} \left(C_1 \kappa g + C_2 S_L^2 \kappa^2 + \frac{C_1^2 U_a^2 \kappa^2}{2A} \right)}. \quad (C.39)$$

The border separating stable and non-stable areas be easily obtained substituting

$\sigma = 0$ in equation (C.38) resulting in

$$\frac{U_a^2}{S_l^2} = -\frac{2A}{C_1} \frac{g}{\kappa S_L^2} - \frac{2C_2}{C_1^2} A. \quad (C.40)$$

C.3 Parametric instability

The second manner of interaction of flames with sound waves is the parametric instability (Bychkov, 1999; Bychkov and Liberman, 2000). A solution for the equation (C.29) for this secondary instability may be found in the form,

$$F = a \exp \sigma t \cos \frac{\omega_{ac}}{2} t + b \exp \sigma t \sin \frac{\omega_{ac}}{2} t. \quad (C.41)$$

The derivatives of such a solution may be calculated, and after simplification

$$\frac{dF}{dt} = \left(a\sigma + \frac{b\omega_{ac}}{2} \right) \exp \sigma t \cos \frac{\omega_{ac}}{2} t + \left(b\sigma - a\frac{\omega_{ac}}{2} \right) \exp \sigma t \sin \frac{\omega_{ac}}{2} t, \quad (C.42)$$

$$\frac{d^2 F}{dt^2} = \left(a\sigma^2 + b\sigma\omega_{ac} - a\frac{\omega_{ac}^2}{2^2} \right) \exp \sigma t \cos \frac{\omega_{ac}}{2} t + \left(b\sigma^2 - a\sigma\omega_{ac} - b\frac{\omega_{ac}^2}{2^2} \right) \exp \sigma t \sin \frac{\omega_{ac}}{2} t. \quad (C.43)$$

The equation (C.29) contain a term in $\cos(\omega_{ac} t)$ which will interact with the solution (C.41), with have terms in $\cos(\omega_{ac}/2 \cdot t)$ and $\sin(\omega_{ac}/2 \cdot t)$ only. For the case of high frequencies, $\left| \frac{C_1 U_a \kappa}{A \omega_{ac}} \right| \ll 1$, it can be obtained that

$$\begin{aligned} \cos \omega_{ac} t \left[a \cos \frac{\omega_{ac}}{2} t + b \sin \frac{\omega_{ac}}{2} t \right] &= a \cos \omega_{ac} t \cos \frac{\omega_{ac}}{2} t + b \cos \omega_{ac} t \sin \frac{\omega_{ac}}{2} t = \\ &= \frac{a}{2} \left[\cos \frac{3\omega_{ac}}{2} t + \cos \frac{\omega_{ac}}{2} t \right] + \frac{b}{2} \left[\sin \frac{3\omega_{ac}}{2} t - \sin \frac{\omega_{ac}}{2} t \right] \approx \frac{a}{2} \cos \frac{\omega_{ac}}{2} t - \frac{b}{2} \sin \frac{\omega_{ac}}{2} t. \end{aligned} \quad (C.44)$$

Substituting in (C.29) and grouping the cosine and sinus terms,

$$A \left(a\sigma^2 + b\sigma\omega_{ac} - a\frac{\omega_{ac}^2}{2^2} + \right) + S_L \kappa B \left(a\sigma + b\frac{\omega_{ac}}{2} \right) + \kappa g C_1 a + S_L^2 \kappa^2 c_2 a + \kappa\omega_{ac} U_a C_1 \frac{a}{2} = 0, \quad (C.45)$$

$$A \left(b\sigma^2 - a\sigma\omega_{ac} - b\frac{\omega_{ac}^2}{2^2} + \right) + S_L \kappa B \left(b\sigma - a\frac{\omega_{ac}}{2} \right) + \kappa g C_1 b + S_L^2 \kappa^2 c_2 b + \kappa\omega_{ac} U_a C_1 \frac{b}{2} = 0. \quad (C.46)$$

A linear system for a and b can be created,

$$a \left[A\sigma^2 - A\frac{\omega_{ac}^2}{2^2} + S_L \kappa B\sigma + \kappa g C_1 + S_L^2 \kappa C_2 - \frac{1}{2} \kappa\omega_{ac} U_a C_1 \right] + b \left[A\sigma\omega_{ac} + \frac{1}{2} S_L \kappa B\omega_{ac} \right] = 0, \quad (C.47)$$

$$b \left[A\sigma^2 - A\frac{\omega_{ac}^2}{2^2} + S_L \kappa B\sigma + \kappa g C_1 + S_L^2 \kappa C_2 + \frac{1}{2} \kappa\omega_{ac} U_a C_1 \right] + a \left[-A\sigma\omega_{ac} - \frac{1}{2} S_L \kappa B\omega_{ac} \right] = 0. \quad (C.48)$$

Solving the linear system of equations for the growth rate, the relation

$$\left(A\sigma^2 - A\frac{\omega_{ac}^2}{2^2} + S_L \kappa B\sigma + \kappa g C_1 + S_L^2 \kappa C_2 \right)^2 - \left(\frac{1}{2} \kappa\omega_{ac} U_a C_1 \right)^2 + \left(A\sigma\omega_{ac} + \frac{1}{2} S_L \kappa B\omega_{ac} \right)^2 = 0. \quad (C.49)$$

is obtained. This system is in general agreement with the equation appearing in the references, if the issues mentioned before are taken into account. To find the border separating the stable and non-stable regions, simply substitution of $\sigma = 0$ in the previous equation yields,

$$\left(-A\frac{\omega_{ac}^2}{2^2} + \kappa g C_1 + S_L^2 \kappa C_2 \right)^2 - \left(\frac{1}{2} \kappa\omega_{ac} U_a C_1 \right)^2 + \left(\frac{1}{2} S_L \kappa B\omega_{ac} \right)^2 = 0, \quad (C.50)$$

which can be expressed in terms of the dimensionless acoustic amplitude, U_a/S_L .

If we arrange the previous equation to look for the quotient U_a/S_L , then,

$$\frac{2^2}{\kappa^2 \omega_{ac}^2 C_1^2 S_L^2} \left(-A \frac{\omega_{ac}^2}{2^2} + \kappa g C_1 + S_L^2 \kappa C_2 \right)^2 + \frac{B^2}{C_1^2} = \left(\frac{U_a}{S_L} \right)^2. \quad (\text{C.51})$$

The digression that have been carried out in this appendix is important in order to study the effect of acoustic waves into the flame and to know if for a particular case they have a significant effect (unstable system) or is of no consideration (stable). For the cases in which it is of significance, the contents of next chapter D and the rationale carried out in 5.3.9 provide a method to take into account the effect of the sound in the modeling.

Appendix D

DERIVATION OF THE MODEL FOR THE FLAME WRINKLING EVOLUTION

D.1 General

We have already seen in section 5.3.9 that incorporating modeling of flame instabilities in our procedure can be relevant for obtaining more accurate results for the simulations reported in that chapter.

Under our approach, the effects of the flame instabilities into the flame propagation pattern was introduced into the simulations through a variable, the flame surface density, Ξ , defined as the ratio of the total surface of a wrinkled flame per unit of planar equivalent flame surface.

This variable, characterizes the flame surface enhancement due to the instability.

We have already defined Ξ denoting the planar equivalent domain as S and providing the flame position given by the function $F(x, y)$ as $\Xi = (\iint_S (1 + (\partial F / \partial x)^2 + (\partial F / \partial y)^2)^{\frac{1}{2}} dx dy) / S$.

It is still necessary to derive the differential equation (5.26), which describes the dynamics (transport, increase, annihilation) of the flame surface density, a task to which we devote this chapter.

A planar flame front is in general not stable. In first approach, the flame can be considered as a surface of discontinuity which moves with a velocity normal to itself in every position. Based on these two assumptions, a curved combustion front can be analyzed utilizing the Huygens' principle (Zeldovich et al., 1985), see Figure D.1. If the initial position and shape of the flame is known, the successive displacements of the surface can be obtained tracing the family of spheres of radius $S_L dt$ (progression of the reaction relative to the flow motion). The enveloping surface of all these spheres represents the flame position in time $t + dt$.

Observing the surface of the flame in Figure D.1, it is possible to distinguish convex and concave regions. In concave regions, the flame trajectories are convergent and ultimately focus in a single location to create a break in the surface of the flame, a cusp (marked with A).

The existence of these two separate regions, the cusp and the surface between them, suggests modeling the evolution of the front during the process in which the flame wrinkles as dominated by two competitive effects. The first is the flame destabilization created by the instability itself that we may consider in the space between cusps. The second is the suppression effect due to the enhanced velocity of the cusp propagation.

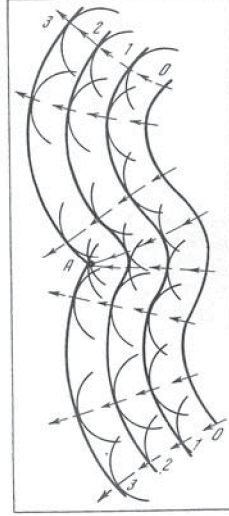


Figure D.1: Successive locations of the flame front (detonated with 0, 1, 2, 3) constructed applying the Huygens principle. Source Zeldovich et al. (1985).

The chapter is organized as follows: first, the source term in q. (5.26) is analyzed in section D.2. Recall that that eq. (5.26) reads

$$\frac{d\Xi}{dt} = G_w(\Xi - 1) - R_w(\Xi - 1)^{\frac{3}{2}} ..$$

Then, the annihilation of flame surface due to cusps evolution is taken into account in section D.3. In section D.4 the formulations obtained in sections D.2 and D.3 are rewritten in terms of Ξ for the sink in section D.4.1 and for the source in D.4.2. Finally, a result summary is provided and the limitations of the model are concisely analyzed in section D.5.

D.2 Source term

If the flame front is represented by the function $F(\vec{x}, t) = 0$ in a reference moving with the flame front, this surface divides the calculation domain in two regions

$F < 0$ for the reactants and $F > 0$ for the products. In this chapter, we restrict ourselves to two dimensional formulation (see Figure D.1).

Small perturbations could be considered in the surface of the flame utilizing the formulation $F(x, t) = A(t) \exp(i\kappa x)$. The time dependent amplitude of the fluctuations can be expressed in terms of exponential function $A(t) = A_0 \exp(\sigma t)$. Deriving, the source term representing the time dependent growth of the amplitude of the instability due to the initial perturbation, could be expressed in first approximation as

$$\frac{dA}{dt} = \sigma A, \quad (\text{D.1})$$

where σ denotes the growth rate of the instability. We may write the RHS in terms of dimensional growth rate (denoted with a tilde) as

$$\frac{dA}{dt} = \tilde{\sigma} \kappa S_L A, \quad (\text{D.2})$$

where κ is the wavenumber and S_L the laminar flame velocity.

The magnitude σ has been the subject of intensive studies and concrete formulation of this term, for any of the instabilities of interest, can be found in the literature, e.g. Bychkov and Liberman (2000).

The expression contained in equation (D.2) neglects the existence of cusps in the flame surface. In the rationale that follows, it was tried to obtain an estimate of their influence. Thus, in the following disquisitions, A will be considered the amplitude of the front between cusp and top of the cyclic surface.

D.3 Flame surface annihilation due to cusps

We may now turn our attention to the pattern of the flame in the cusp (see Figures D.2, D.3).

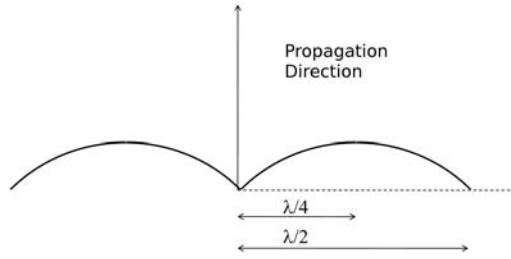


Figure D.2: Surface of a flame with a cusp in the center.

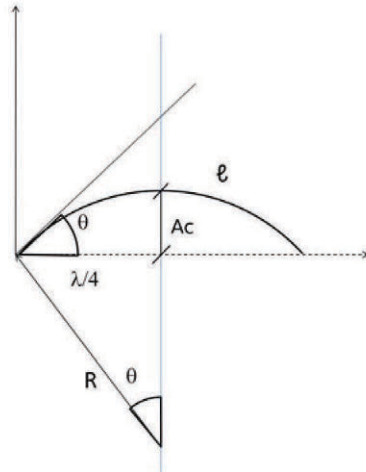


Figure D.3: Surface of a flame with a cusp and variables utilized for its description.

If θ_c is the angle of the flame in the cusp due to the interaction of the two convex areas the speed in the cusp is given by $S_L / \cos(\theta_c)$. The suppression of amplitude due to the greater velocity of the cusps $S_L / \cos(\theta_c)$ relative to the speed in convex areas S_L is

$$\frac{dA_c}{dt} = -S_L \left(\frac{1}{\cos(\theta_c)} - 1 \right). \quad (\text{D.3})$$

Out of the cusps the surface of the flame can be approximated with a parabola

$$y = ax^2 + bx + c, \quad (\text{D.4})$$

which intersects the points $(0, 0)$, $(\frac{\lambda_c}{2}, 0)$ and $(\frac{\lambda_c}{4}, A_c)$. this allows obtaining the values of a , b , c that must be

$$a = -\frac{16A_c}{\lambda_c^2}, \quad (\text{D.5})$$

$$b = \frac{8A_c}{\lambda_c}, \quad (\text{D.6})$$

$$c = 0. \quad (\text{D.7})$$

The equation of the parabola is

$$y = -\frac{16A_c}{\lambda_c^2}x^2 + \frac{8A_c}{\lambda_c}x, \quad (\text{D.8})$$

and its derivative

$$y' = -\frac{32A_c}{\lambda_c^2}x + \frac{8A_c}{\lambda_c}. \quad (\text{D.9})$$

Therefore, in the cusp, the slope is

$$tg(\theta_c) = \left. \frac{dy}{dx} \right|_{x=0} = \frac{8A_c}{\lambda_c}. \quad (\text{D.10})$$

On the other side, the secant can be expressed as

$$\frac{1}{\cos(\theta_c)} = \sqrt{tg^2(\theta_c) + 1}. \quad (\text{D.11})$$

In turn, the square root can be approximated with

$$\sqrt{tg^2(\theta_c) + 1} \approx 1 + \frac{1}{2} \left(\frac{8A_c}{\lambda_c} \right)^2. \quad (\text{D.12})$$

Introducing the last equation in equation (D.3),

$$\frac{dA_c}{dt} = -S_L \frac{8A_c^2 \kappa^2}{\pi^2}, \quad (\text{D.13})$$

is obtained.

At this stage, we have obtained an expression for the source of flame surface represented by equation (D.2). Also, an equation for the sink of amplitude of the perturbation of the flame due to the instabilities has been obtained (equation (D.13)). Those two expressions are now refereed to incoherent magnitudes. We may need to manipulate them in order to obtain a representative equation with sink and source in terms of the same variables.

D.4 Formulation in terms of Ξ

D.4.1 Annihilation due to cusp (sink contributor)

The wrinkling factor Ξ represents the relation between the surface of the wrinkled flame and the planar one. In the direction perpendicular to the paper the flame was considered as infinite, simplifying the problem to two dimensions (see Figure D.3). In this simplified model, the wrinkling factor is the ratio between the length of the arc and the chord shown in Figure D.3. The length of the chord is directly $\lambda_c/2$. The length of the arc can be easily approximated, with first order accuracy, considering that the parabola utilized in the previous section is a circle. The first order approximation is a perfectly coherent premise taking into account that the theory for flame instabilities is based in this assumption and therefore the growth

rate is obtained under these postulates. It is obtained that,

$$\frac{1}{\sin(\theta_c)} = \sqrt{1 + \left(\frac{1}{\tan(\theta_c)}\right)^2} = \sqrt{1 + \left(\frac{\lambda_c}{8A_c}\right)^2}, \quad (\text{D.14})$$

$$R = \frac{\lambda_c}{4} \frac{1}{\sin(\theta_c)}, \quad (\text{D.15})$$

$$\ell = 2\theta_c R, \quad (\text{D.16})$$

$$\theta_c \approx tg\theta_c = \frac{8A_c}{\lambda_c}, \quad (\text{D.17})$$

$$\ell = 2 \frac{8A_c}{\lambda_c} \frac{\lambda_c}{4} \sqrt{1 + \left(\frac{\lambda_c}{8A_c}\right)^2} = 4A_c \sqrt{1 + \left(\frac{\lambda_c}{8A_c}\right)^2}. \quad (\text{D.18})$$

The wrinkling factor, Ξ is then

$$\Xi = \frac{\ell}{\frac{\lambda_c}{2}} = \sqrt{1 + \left(\frac{8A_c}{\lambda_c}\right)^2}, \quad (\text{D.19})$$

which again in first order approximation reduces to,

$$\Xi \approx 1 + \frac{1}{2} \left(\frac{8A_c}{\lambda_c}\right)^2. \quad (\text{D.20})$$

Equation (D.13) can be reformulated into an expression involving different variables, the wrinkling factor and the wavenumber $\kappa = 2\pi/\lambda_c$. Under this formulation the equation (D.20) can be rewritten

$$\Xi - 1 \approx \frac{1}{2} \left(\frac{8A_c}{\lambda_c}\right)^2 = \frac{8A_c^2 \kappa^2}{\pi^2}. \quad (\text{D.21})$$

Deriving,

$$\frac{d\Xi}{dt} = \frac{8\kappa^2}{\pi^2} 2A_c \frac{dA_c}{dt}. \quad (\text{D.22})$$

On the other side from equation (D.20),

$$A_c = \sqrt{\frac{\pi^2}{8\kappa^2}(\Xi - 1)}. \quad (\text{D.23})$$

Thus,

$$\frac{d\Xi}{dt} = \frac{8\kappa^2}{\pi^2} 2 \frac{\pi}{\sqrt{8\kappa}} \sqrt{\Xi - 1} \frac{dA_c}{dt} = \quad (\text{D.24})$$

$$= \frac{2\sqrt{2}\kappa}{\pi} 2\sqrt{\Xi - 1} \frac{dA_c}{dt}. \quad (\text{D.25})$$

Therefore, substituting in equation (D.13)

$$\frac{1}{\frac{4\sqrt{2}\kappa}{\pi} \sqrt{\Xi - 1}} \frac{d\Xi}{dt} = -S_L(\Xi - 1), \quad (\text{D.26})$$

which simplifies to

$$\frac{d\Xi}{dt} = -\frac{4\sqrt{2}\kappa}{\pi} S_L(\Xi - 1)^{\frac{3}{2}}. \quad (\text{D.27})$$

The last equation represents the equation for the sink in terms of Ξ that we were looking for.

D.4.2 Source term (instability) wrinkling factor

The equation (D.2) can be also reformulated utilizing the wrinkling factor. Substituting (D.23) and (D.25) into (D.2),

$$\frac{d\Xi}{dt} = \frac{4\sqrt{2}\kappa}{\pi} \sqrt{\Xi - 1} \tilde{\sigma} \kappa S_L \sqrt{\frac{\pi^2}{8\kappa^2}(\Xi - 1)}, \quad (\text{D.28})$$

$$\frac{d\Xi}{dt} = 2\tilde{\sigma} \kappa S_L(\Xi - 1), \quad (\text{D.29})$$

which is the equation for the source in terms of Ξ .

D.5 Final equation

D.5.1 General

The annihilation and source equations (D.27) (D.29) can be combined together to generate the model sought

$$\frac{d\Xi}{dt} = 2\tilde{\sigma}\kappa S_L (\Xi - 1) - 4\sqrt{2}\frac{\kappa}{\pi} S_L (\Xi - 1)^{\frac{3}{2}}. \quad (\text{D.30})$$

The factor $\tilde{\sigma}$ (see Appendix C), dimensionless growth factor can be, for the Darrieus-Landau, Rayleigh-Taylor, thermo-diffusive or acoustic-parametric instabilities found in e.g. Bychkov and Liberman (2000) and provides a possibility for the modeling of the mentioned instabilities.

Equation (D.30) contains a free parameter, the wavenumber κ that also affects the growth rate, as $\sigma = \sigma(\kappa)$. Therefore, it is necessary to define of the wavenumber that should be considered inside the range of instability. Bauwens et al. (2011) have selected the wavenumber that produces the highest growth rate exclusively arguing that this would be the most significant wavenumber.

D.5.2 Limitations

The validity of a model based and resulting on the assumptions accepted in this appendix is doubtful. Nevertheless, it offers a possibility to introduce flame instabilities in the modeling in a very simple way.

Amongst the evident shortcomings of such an approach we could mention several points:

1. Conceptually the approach is based on establishing an analogy between combustion and optics whose validity is controversial.
2. It considers a single wavenumber as representative of the whole instability spectrum.
3. It ignores and neglects the interaction between different wavenumbers.

Probably, no further enhancements utilizing this methodology are feasible and more advanced model developments, in spite of the relatively good results of section 5.3.10, should be based on the modeling of the Kuramoto-Sivashinsky equation (Sivashinsky, 1977) to obtain a methodology of more *physical* nature.